Developing surface ionisation charge-transfer dynamics of hydrogen Rydberg atoms into an energy-resolved probe of surfaces



Mike Kohlhoff
Wolfson College
University of Oxford

A thesis submitted for the degree of
Doctor of Philosophy
Michaelmas 2016

Developing surface ionisation charge-transfer dynamics of hydrogen Rydberg atoms into an energy-resolved probe of surfaces

Mike Kohlhoff

Wolfson College
University of Oxford

A thesis submitted for the degree of
Doctor of Philosophy

Michaelmas 2016

As a Rydberg atom approaches a surface, it will eventually undergo ionisation by charge transfer into the surface at a distance of about 100 nm (for principal quantum numbers $n > 20$). The dynamics of this process are sensitive to the electronic and geometric structure of the surface and can display signature characteristics. As such, Rydberg atoms can be used to probe image-charge effects or to measure small superficial electric stray or patch fields. The charge-transfer process can be in resonance between the Rydberg energies and the energetically discrete surface states (image states) in a bandgap. Surface ionisation of Rydberg atoms is investigated for graphene, which is a zero-bandgap semiconductor and can behave either as a metal or a semiconductor. The charge-transfer dynamics observed here exhibit the characteristics of a metal with enlarged ion detection efficiency compared to a copper sample – in accordance with other properties of graphene, such as conductivity, that are enlarged compared with a regular metal. For hydrogen Rydberg atoms, surface ionisation is detected for distances up to 10 µm, with a double series of high-lying image states extending far from the graphene film possibly creating a quasi-continuum at large atom-surface separations with a density of states beyond the resolution of the Rydberg states from $n = 20$ to 40. The resonance behaviour for graphene is explored with a range of Rydberg H-atom collisional velocities whose effect on the charge transfer process introduces an additional handle on the probing of electronically discrete features of a surface. A wave-packet propagation study of a hydrogen atom incident at a free-metal surface up to $n = 20$ displays shifts in ionisation towards greater distances and over a narrower range when acceleration of the ion core is not included. The thereby significantly reduced effect of the collisional velocity of Rydberg surface ionisation is also observed in an experimental study with a limited velocity range available from supersonic expansion directed at a gold sample. This either suggests that the range of Rydberg projectile velocities is to narrow to have observable effects or that a pronounced velocity dependency is merely detected for distinct electronic resonances. With the aim to further elucidate the velocity dependence and to prospectively remove ambiguities that arise from the nature of the experiment, a chip-based decelerator is constructed and integrated into the experimental apparatus for the first time. Within the constraints of the design and the existing apparatus, the chip device is not able to produce sufficient densities of decelerated particles to be employed in surface-ionisation experiments. Extensive modelling of the deceleration process indicates that modifications to the existing design and the experimental apparatus could achieve a tunable-velocity source of hydrogen Rydberg atoms with greatly enhanced densities for future investigations.

Acknowledgements

> It is not so easy, lying here in this scrubbed hospital bed under a glass peephole with Bruno's eye in it, to give a picture of the smoke clouds that rose from Kashubian potato fires of of the slanting October rain. If I didn't have my drum, which, when handled adroitly and patiently, remembers all the incidentals that I need to get the essential down on paper, and if I didn't have the permission of the management to drum on it three of four hours a day, I'd be a poor bastard with nothing to say . . . [1].

I am extremely grateful for the experiences I have made over the last four years, the skills I have learnt, and the great people I have met along the way and have had the privilege to work with. I have to thank Tim to take me on this journey and give me the opportunity to independently carry out and explore my research projects. He has always been able to draw the big picture when doing research felt like constantly opening cans of worms and has taught me how to improve on the art of writing (British) English, with a special emphasis on the use of commas; or so I hope. Through the Marie Curie Actions, the people of the European Union need to be mentioned for providing me with the necessary funding. I want to thank Professor Frederic Merkt and Dr. Stephen Hogan for collaborating on the early design phase of the Rydberg-Stark decelerator.

A special praise goes to my helmsman Chris, whose guidance, technical prowess and passion for rabbit holes have greatly contributed to the outcome of my work and to my personal development. Atreju deserves eternal credit for introducing me to Python for ninjas. I also want to thank the whole Softley group for an enjoyable environment to work in: Brianna for proof-reading and her supportive nature, Jemma Alice for introducing me, or at least attempting to do so, to the essentials of English culture (Wimbledon and Glastonbury), Mark D for taking the time and patience to introduce me to the experiment, and Lorenzo for extremely fun times in the lab and dozens of unforgettable memes. Even Jutta.

I am indebted to the great support I got from the Electronics and Mechanical Workshops in constantly helping me to design, build and upgrade components of the experiment; many thanks particularly to Kevin, Tim, Andy and Dennis who always managed to squeeze in urgent jobs. I want to acknowledge Dr. Vitaliy Babenko and Dr. Robert Jacobs for the sample preparations.

Mostly, importantly and vitally, it is about the people I encountered throughout my time in Oxford and the COHERENCE network who immensely enriched and educated me, who I hugely appreciate in different aspects and who will continue to provide me with invaluable friendships. Lastly, I want to thank my family for their loyalty and support throughout the neverending years of education.

Contents

Abstract i

Acknowledgements ii

Atoms in Rydberg states and surface ionisation **1**

1.1 Special properties of Rydberg states 2

1.2 Rydberg atoms at surfaces and interfaces 6

1.2.1 Long-range interaction with surfaces 7

1.2.2 Short-range interaction with surfaces 9

1.3 Rydberg states in external electric fields 10

1.3.1 The Stark effect in hydrogen 10

1.3.2 Ionisation in an electric field 12

1.4 Ionisation of a Rydberg state at a metallic surface 14

1.4.1 Image-charge modelling 15

1.4.2 Surface potential modelling 16

1.4.3 Surface induced ionisation 18

1.5 Experimental studies of Rydberg charge transfer at a metal surface 20

1.5.1 Beam transmission through metallic grids 21

1.5.2 Ionisation in grazing incidence beams 21

1.5.3 Stray field influences on surface ionisation 26

1.5.4 Surface ionisation of molecules - further complexity 27

1.6 Hydrogen Rydberg atoms as surface probes 28

1.6.1 Surface induced wavefunction polarisation in hydrogen 29

1.6.2 Energy resolved probes - surface ionisation at electronically structured Cu(100) 31

1.6.3 Velocity effects on resonance behaviour 33

Modelling techniques for Rydberg atoms at surfaces and in electric fields 35

2.1 Dynamics in ionisation probability of Rydberg atoms approaching a surface . . 35

2.1.1 Time-independent perturbative and nonperturbative techniques 36

2.2 Time-dependent wave-packet propagation 38

2.2.1 Procedural outline 40

2.3 Rydberg-Stark deceleration 47

2.3.1 Electric field distributions 49

2.3.2 Numerical trajectory simulations 50

Experimental procedure and apparatus characteristics 58

3.1 Experimental apparatus to study surface ionisation 58

3.2 Molecular beam source 60

3.2.1 PID pressure control 61

3.2.2 Translational gas packet temperature 62

3.3 Rydberg excitation 65

3.3.1 VUV photon generation 65

3.3.2 Stark state selection 70

3.4 Ion extraction and detection 73

3.4.1 Revised detection system 74

3.4.2 Data recording 77

Increased efficiency and long range free-metal-like charge transfer at graphene 81

4.1 Graphene growth and sample surface topology 82

4.2 Data evaluation and surface profile integration at high extraction fields 85

4.3 Observation of increased detection efficiency at low extraction fields 87

4.4 Graphene sample robustness and reactivity 90

4.5 Increased free-metal-like behaviour 92

4.5.1 Resonance character of charge transfer 93

4.5.2 Image state density and Fermi level shifts 96

4.6 Long range surface ionisation 98

4.6.1 Excluding factors aiding enhanced detection 101

Velocity dependence of resonant Rydberg surface ionisation **104**

5.1 Ionisation distance shift of charge transfer 105

5.1.1 Probe state selection 105

5.1.2 Ionisation distance scaling 110

5.2 Experimental investigation with limited velocity ranges by supersonic expansion 113

5.2.1 Gold sample preparation 113

5.2.2 Molecular beam velocity selection 114

5.2.3 Stark state selection uncertainty 116

5.2.4 Reduced surface ionisation variability with collisional velocity 117

Towards an extended impact velocity range via a chip-based decelerator **123**

6.1 Rydberg-Stark decelerator design 124

6.1.1 Printed circuit board architecture 125

6.1.2 Oscillating potential sequence and moving traps 127

6.2 Implementation into surface experiment 131

6.2.1 Shifted Rydberg excitation 132

6.2.2 Extraction field compensation 136

6.3 Experimental performance 138

6.3.1 Parameter space dependencies 139

6.3.2 Partially reduced transmission in guiding-mode 141

6.3.3 Insufficient time of flight changes for deceleration sequences 143

Conclusions and directions **146**

References 150

Atoms in Rydberg states and surface ionisation

In 1885 Swiss mathematician Johann Balmer discovered an empirical formula that describes the wavelengths of the visible lines in the emission spectra of the hydrogen atom to a high degree of accuracy. This finding consolidated early experimental work in atomic spectroscopy by various researchers at the end of the 19th century. The formula, for the first time, provided a theoretical basis for comparing the already measured emission wavelengths and a tool to predict further spectral lines. In the case of the Balmer series, the transitioning electron moves from an energy level $n' \geq 3$ to $n = 2$, where the integer n labels discrete energy levels and was later identified as principal quantum number in the Bohr model.

In 1888 Swedish physicist Johannes Rydberg found a generalised version of Balmer's formula that described all transitions in the hydrogen atom independent of its final energy level. The energy difference in wavenumbers between an upper level n_i and lower level n_f in hydrogen is given by

$$\nu = R_H \left(\frac{1}{n_f^2} - \frac{1}{n_i^2} \right), \tag{1.1}$$

where the Rydberg constant R_H for hydrogen is $109\,678\,\mathrm{cm}^{-1}$ [2]. With the Rydberg series at hand it led to further findings of spectral series terminating at different levels n: the Lyman series ($n_f = 1$), the Paschen series ($n_f = 3$), the Brackett series ($n_f = 4$), the Pfund series ($n_f = 5$) and the Humphreys series ($n_f = 6$).

Only with the Bohr model in 1913, named after Danish physicist Niels Bohr, however, was it possible to underpin the Rydberg formula with a structural image of the atom and provide a derivation of the introduced Rydberg constant from elementary constants. In this model, the electron moves around the nucleus on circular orbits under the laws of classical mechanics with a quantum character lent by the restriction of discrete jumps in energy between the orbits. This

latter condition can be brought in accordance with the discrete energy levels of the Rydberg series in Equation 1.1. Hereby, a physical sense for high principal quantum numbers n can be attained, where a high n denotes high-lying states in energy relative to the ground state. For these highly excited states, properties of the hydrogen atom can be generalised by power laws of n; see Table 1.1 for an overview of properties encountered in the context of this text. As will emerge in later sections, the considerations for higher (principal) quantum numbers ($n \to \infty$) yield a limit in which the domains of validity of quantum and classical mechanics cross over. This reflects the contemporary understanding of Bohr's correspondence principle by which classical mechanics is recovered from quantum mechanics in the limit of high energies [3]. A Rydberg atom can thereby be treated as a semi-classical object that, when described classically, yields valid predictions if special quantum conditions are imposed (as later in section 1.3: a maximally red-shifted state).

1.1 Special properties of Rydberg states

Despite its shortcomings, the Bohr model delivers an intuitive illustration for the physical properties of a highly excited atomic state. From Table 1.1 it can be inferred that an atom in a state with high n, compared to the ground state, has a valence electron that is loosely bound to the nucleus being in an orbital of considerable size and the electron is hence easily removed in an electric field. For $n = 100$, the diameter of the orbital is about $1\,\mu\mathrm{m}$, comparable to the size of a bacterium.

In terms of experimental accessibility, Rydberg states become especially intriguing considering the lifetime of the excited state. The total lifetime at a finite temperature $\tau(K)$ of an excited atom in a collision-free environment is given by

$$\frac{1}{\tau(K)} = \frac{1}{\tau^F} + \frac{1}{\tau^{BB}}\,, \tag{1.2}$$

which is determined by spontaneous decay into the ground state or a lower state through fluorescence, given by a natural lifetime τ^F, and a decay rate $1/\tau^{BB}$ induced by black-body radiation [4]. The latter process can be separated into black-body induced transitions between bound states and beyond the ionisation limit [5]. The natural lifetime in zero electric field can be cal-

culated via the Einstein coefficients $A_{nlm,n'l'm'}$ [6], where l is the orbital angular momentum quantum number and m the magnetic quantum number referring to the projection of angular momentum onto the z axis. The overall fluorescence rate Γ_{nlm} is the sum of all coefficients A for allowed transitions from a state $|nml\rangle$ to an energetically lower state $|n'l'm'\rangle$, leading to a lifetime $\tau = \Gamma^{-1}$ and a proportionality of $\tau \propto n^3$ for low orbital momentum and $\tau \propto n^5$ for circular states with maximal orbital momentum $l = n - 1$. In a Rydberg atom exposed to an external electric field, l-states are mixed which changes the scaling of the lifetimes as $\tau \propto n^4$ for $|m| \leq 3$ [5].

Table 1.1: Dependence of atomic properties on principal quantum number n [2, 4], with the Rydberg constant R_∞, Bohr radius a_0 and elementary charge e. Unless noted otherwise, all quantities in the text are expressed in atomic units (a.u.) in which $\hbar = m_e = e = 1$.

Property	n scaling
Classical orbital radius	$a_0 n^2$
Binding energy	$-R_\infty n^{-2}$
Ionisation field	n^{-4}
Radiative lifetimes	$n^3 \ldots n^5$
Polarisability	n^7
Maximum induced dipole moment	$e a_0 n^2$

Since the energetic spacing between adjacent n manifolds is small, scaling as n^{-3}, and the photon energy required for surpassing the ionisation threshold is small as well, the thermal environment can easily induce transitions between different n manifolds or lead to ionisation. Therefore, it is advantageous to operate experiments under cryogenic conditions when they involve the trapping of Rydberg species [7]. The maximum of the Planck distribution, which characterises the spectrum of a black body, shifts to lower frequencies as the temperature of the body in thermal equilibrium with its environment decreases. For example, if the environment is cooled to 11 K the photon energy of the corresponding radiation field is not sufficiently high to ionise the Rydberg atom and merely induces transitions to neighbouring n manifolds, while at the same time stimulated emission and absorption processes are less likely, leaving radiative decay as the main mechanism for loss of Rydberg population over time [5], which allows for experimentally achievable lifetimes of up to milliseconds [8, 9].

The ability to easily remove the valence electron combined with long lifetimes make highly excited (Rydberg) states suitable for spectroscopic applications in investigating chemical dynamics. Pulsed-field techniques in which a Rydberg state acts as an intermediate towards forming an ion has led to the development of zero electron kinetic energy (ZEKE), mass-analyzed threshold ionization (MATI), photo-induced Rydberg ionization spectroscopy (PIRI) or resonance-enhanced multiphoton ionisation (REMPI) [10, 11]. These techniques, close to the ionisation threshold, have been employed to study the electronic structure of molecules with very high resolution below the bandwidth of the lasers involved in the experiments [12, 13]. In those methods, it is taken advantage of the fact that all neutral atoms and molecules have Rydberg states with structure and behaviour akin to the H-atom. In addition, detecting ions, as in MATI, is comparatively uncomplicated via electric fields and can be conducted with high detection efficiency that allows for a mass-separation of the involved species.

Outside the field of spectroscopy, Rydberg atoms hold a great promise based on another significant property: tunable long-range interactions. As Table 1.1 shows, the (permanent) dipole moment arising from the first-order Stark shift of the Rydberg states scales with n^2, which lets the dipole-dipole interaction V_{dd} scale with n^4/R^3. The interaction potential V_{dd} in (Hartree) atomic units between two atoms in different internal states when assumed as two classical dipoles being separated by a distance $R = |\boldsymbol{R}|$ is given by

$$V_{dd} = \frac{\mu_1 \mu_2}{R^3} \left(1 - \cos^2 \theta\right), \tag{1.3}$$

where θ defines the angle with the quantisation axis so that μ_i is the z-component of the dipole moment operator $\boldsymbol{\mu}$ [14, 15]. An applied electric field is defined as being parallel to the quantisation axis. Note, that if the externally applied electric field is stronger than all other fields, *e.g.* the fields originating from the dipoles themselves, the dipole interaction as stated in Equation 1.3 corresponds to two classical, permanent dipoles which are aligned in the field and able to exchange energy [16]; the angular dependency in that case has been confirmed experimentally in an approximately one-dimensional cloud of Rydberg atoms [17]. This always-resonant interaction needs to be distinguished from the resonant dipole-dipole interactions originating from the large transition dipole moment of Rydberg states. In this case, when no permanent field is present, the average dipole moment of a pair vanishes and V_{dd} has no effect in first order.

However, the second-order perturbation is the basis for an energy shift of the pair state, the van der Waals interaction which scales as n^{11}/R^6 [14, 18]. The induced interaction gives rise to a dipole blockade mechanism, the Rydberg blockade, which is a collective feature of a dense Rydberg sample. This blockade is a mechanism in which excitation of another Rydberg atom close to a given excited atom is collectively suppressed within a specific volume according to a blockade radius [19, 20, 21, 22, 23].

Yet, when the atomic pair is tuned into degeneracy by applying a small electric field so that the energy levels converge, the resonant dipolar interaction creates a first-order effect that has a $1/R^3$ dependence. At this point, the internal atomic states can be exchanged in the form of $np+np \longleftrightarrow ns+(n+1)s$, by which energy can be transferred between an s and a p state. This process is called a Förster resonance, borrowing from Förster resonance energy transfer (FRET), or fluorescence resonance energy transfer, a photochemical phenomenon widely employed in biological research. The analogue mechanism, a resonant transfer of energy between a pair of states in a Rydberg gas has been studied extensively [24, 25, 26, 27, 28, 29, 30]. It should be noted that the electric fields required to tune the energy levels into resonance are not sufficiently strong to change the l-character of the pair states and induce a permanent charge distribution [15].

The dipole and van der Waals interactions between Rydberg states are significantly stronger compared with the ground state. For instance, the interaction of a rubidium atom in the $100s$ state, which is dominated by the dipole-dipole interaction at short range and by the van der Waals interaction at large distances, is 10^{12} times stronger than the interaction of the ground state atoms [31].

Interestingly, the discussed properties of Rydberg atoms are not exclusive to atomic or molecular systems in the gas phase. Strong dipole-dipole interaction have been observed between excitons with giant wavefunctions in copper oxide, equivalently leading to an excitation blockade mechanism [32]. Also, it has been shown that positronium can be prepared in a Rydberg state with the aim to exploit the resulting dipole interaction with external electric fields for controlling their motion [33].

1.2 Rydberg atoms at surfaces and interfaces

Their range of exotic properties makes Rydberg atoms an interesting subject in various fields of research. They are utilised in cavity quantum electrodynamics [34, 35], in controlled chemical reactions and formation of giant exotic molecules [36, 37, 38, 39, 40], serve as a model system for dipole-mediated energy transport in biological systems [41], can be used as a non-linear medium to mediate single-photon interactions [42, 43] and have been proposed in several ways for quantum information processing [21, 22, 31, 44, 45]. However, their properties are such that their strong interaction will not be limited to surrounding atoms but that they also couple to condensed matter, bulk surfaces, in the vicinity. See Figure 1.1 for an overview of Rydberg-surface interactions.

It has been suggested that the long-range interaction of Rydberg states may be facilitated by enclosing a Rydberg gas at room temperature in wedge-shaped glass cells with the attempt to implement integrable gates for quantum information processing and single-photon devices [46]. Other proposals have concentrated on combining Rydberg atoms in the gas phase with a solid-state coplanar waveguide [47], where the waveguide can hold a superconducting qubit which is a highly promising candidates for the successful large-scale implementation of quantum information [48]. This hybrid approach combines the advantages of the two different quantum systems: the strong coupling of the macroscopic solid-state device and the long radiative lifetimes of the Rydberg atoms. Here, the Rydberg atom in the hybrid system can enhance the comparatively short coherence times of the superconducting qubit of a few tens of μs [49, 50] and also act as a memory or transmitter by transferring information from one part of the device to another.

Even though the special characteristics of these high lying states offer a unique degree of control and manipulation, it comes at the price of them being easily perturbed by their environment. When atoms are excited into states of high principal quantum number n, their exaggerated properties give rise to to long-range interactions which result in a strong coupling with their environment. Likewise, the greatly expanded electron cloud results in a large polarisability for a Rydberg state causing a strong response to electric fields. If the aim is to implement Rydberg atoms for a practical application in quantum information processing or quantum simulation, miniaturisation will be a key factor, and closer interfacing of a Rydberg gas to metal

and dielectric components of the apparatus is inevitable.

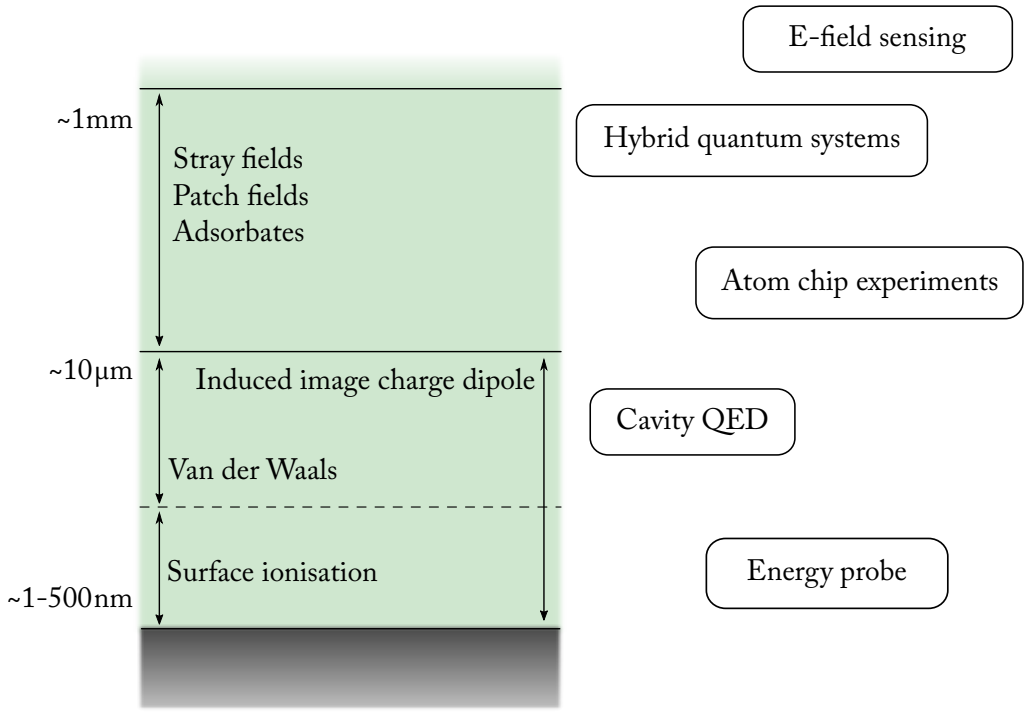

Figure 1.1: Different interaction types for neutral Rydberg atoms interfaced with a metallic surface and the distance ranges spanned by these interactions. The relevance of these distance regimes for typical applications and fields of research is noted on the right side.

1.2.1 Long-range interaction with surfaces

For the aforementioned schemes to be feasible, understanding the interplay of Rydberg atoms with small electric fields arising near surfaces becomes crucially important. The fields can be produced by the roughness and geometric structure of nearby surfaces, or they may originate from patch charges on them. In the context of information processing, the effect of adsorbates has been investigated by a number of groups over the last few years. In a seminal work, Tauschinsky *et al.* investigated energy-level shifts of rubidium Rydberg atoms above the gold-coated surface of a permanent magnetic substrate via electromagnetically induced transparency (EIT) [51]. They found the level shifts to be distance-dependent and caused by spatially inhomogeneous electric fields originating from adatoms adsorbed on the chip surface. The magnitude of these fields scales with the height as $\propto z^{-0.7}$, contrary to the fields due to randomly distributed patch potentials which scale with z^{-2} [52]. In this experiment, the Rb-atoms are excited to Rydberg states and held in micron-sized traps 10 μm above a patterned magnetic film [53] and are lost

from the traps over time, depositing as mounds on the substrate. Work on the adsorption of neutral atoms onto the surface of an atom chip was further complemented by Hattermann *et al.* who also used EIT to probe an atom cloud released from optical tweezers onto a copper surface. They were able to determine that electrostatic fields arising from the adsorbed Rubidium are about $1\,\mathrm{V\,cm^{-1}}$ in magnitude and that these fields were formed after a mere 100 repetitions of their experimental cycle [54].

In atom-chip experiments the detrimental effects of Rydberg-surface interactions prevent the trapping of atom clouds at distances closer than $\sim 100\,\mathrm{nm}$ to the substrate due to perturbation of the trapping potential [55]. In the proposal for using wedge glass cells for housing a Rydberg vapour at room temperature, the goal is to construct the spacing of the glass cells to accommodate a Rydberg blockade. To match the blockade radius, the confining compartment needs to extend several micrometres for a state in principal quantum numbers $n = 30$ to 50 [46]. The potentially significant interactions of a Rydberg atoms with surfaces must be well understood to achieve, in the context of quantum information, maximum fidelity and a deterministic scheme that preserves atomic coherence.

In contrast to a metal as a conductor, an insulator builds up a dielectric polarisation when placed in an electric field where this charging-up effect is expected to enhance the dipolar interaction of an atom with a dielectric surface, especially when adsorbates are deposited on the surface. The enlarged response of a Rydberg state to a dielectric surface can be explained by a resonant coupling to polariton and plasmon modes of the material [34, 56, 57]. Even though fused silica glass is a common material used in cold atom experiments it has only been studied marginally. In work by Kübler *et al.* and Abel *et al.* it was found that the shift of the Rydberg state energies deviates from the expected scaling in the presence of a dielectric by modifying the electric field response [46, 58, 59, 60]. In reference [46] the principal quantum number of the Rydberg state is specifically chosen to minimise the coupling to polariton modes in the quartz glass. Other ways to inhibit the interaction with the substrate are to use specially designed coatings.

The extreme sensitivity to minuscule electric fields in surface architectures leads to an undesired response in the form of, *e.g.*, Stark shifts, but this can also be used as a probe. Employing high-resolution spectroscopy of the Stark shift of Rydberg states, the magnitude of electric fields can be determined; in this way measurements of field inhomogeneities down to $\pm\,20\,\mu\mathrm{V}$ have

been demonstrated [61]. Similarly, it has been shown how to detect nonresonant broadband radio-frequency electrical noise affecting Rydberg states of helium [62].

1.2.2 Short-range interaction with surfaces

Complications of using chip or hybrid designs for, *e.g.*, quantum information applications are the energy shifts of the atomic state and altered excited state lifetimes by changes in the spontaneous emission rates [35], which are of relevance at comparatively large atom-surface separations. After the effect of stray electric fields, the next strongest coupling is the interaction of a Rydberg atom with its induced image charge in the surface. Within the classical treatment of the conduction electrons in a metal as a (perfectly) polarisable fluid, the large dipole moment of a Rydberg state ($\propto n^2$) induces a charge polarisation in the metallic bulk that is accounted for with the method of image charges and brings about an attractive net force of the van der Waals type outside the surface [63]. At the smaller end of the range of separations the influence of the image-charge interactions get more drastic, and the Rydberg electron is able to pass over or tunnel through the potential barrier into the conduction band and thus is ionised [11, 64].

At the closest distances to the surface, the shape of the potential landscape gains importance and it has been proposed that Rydberg atoms could be used for controlled deposition in nanolithography [65]. Surface orbitals are in general not fully occupied, which renders the surface reactive to any element or compound present in the gas phase. If the surface is exposed to a controlled environment, as when it is placed in a (ultra-) high vacuum, it becomes possible to control the exposure to potential reaction partners which makes it a model system for the study of surface chemistry.

In the following, the focus will be on the interplay of an highly-excited atomic state with a metallic surface, particularly the process of ionisation, which has been a subject of several investigations over the last three decades in experimental studies [64, 66, 67, 68, 69] as well as in theoretical studies [70, 71, 72, 73]. In section 1.3 the properties of Rydberg states in external fields will be described, and then in section 1.4 these will be compared to the properties of Rydberg states close to a solid.

1.3 Rydberg states in external electric fields

To understand the ionisation of a Rydberg state in front of a surface, as is addressed later, it is useful to consider the effects of a homogeneous electric field. As the electron in a Rydberg atom is distributed over a large orbital, and far removed from the core, it has a low binding energy and the atom is highly polarisable. This makes it possible to easily remove the electron from the core with modest electric fields which renders the remaining ion detectable by charged particle detectors.

1.3.1 The Stark effect in hydrogen

The eigenstates of hydrogenic Rydberg orbitals at zero electric field can be described by the quantum numbers $|nml\rangle$ where n is the principal quantum number, l the orbital angular momentum quantum number, and m the magnetic quantum number referring to the projection of angular momentum onto the z axis.

If a static electric field of magnitude F is applied along the z-direction, a perturbing term is added to the (hydrogenic) zero-field Hamiltonian H^0

$$H = H^0 + H^{\text{Stark}}(F) \tag{1.4}$$

where the Stark term can be expressed (in atomic units) as in Equation (1.5) when spherical coordinates are chosen and the z-axis is the quantization axis to describe the symmetry of the problem, with μ_z as the z-component of the dipole moment operator as in Equation 1.3.

$$H^{\text{Stark}}(F) = -\boldsymbol{\mu}F = -\mu_z F_z = Fr\cos\theta \tag{1.5}$$

This leads to a shift in energy that varies linearly with the applied field and thereby to a lifting of the degeneracy of the $|lm\rangle$ states. The splitting of the energy levels for a hydrogen atom is depicted in Figure 1.2. In this symmetry, angular momentum l is no longer a good quantum number and the resulting wavefunctions can be described by the principal quantum number n and the magnetic quantum number m. The problem remains separable with newly-introduced

parabolic quantum numbers n_1 and n_2 obeying the relation given in Equation (1.6).

$$n = n_1 + n_2 + |m| + 1 \tag{1.6}$$

A Stark state is usually labelled by the quantum number $k = n_1 - n_2$, where k ranges from $-(n - |m| - 1)$ to $(n - |m| - 1)$ in steps of two with the total number of distinct Stark states for a given n and m being $n - |m|$.

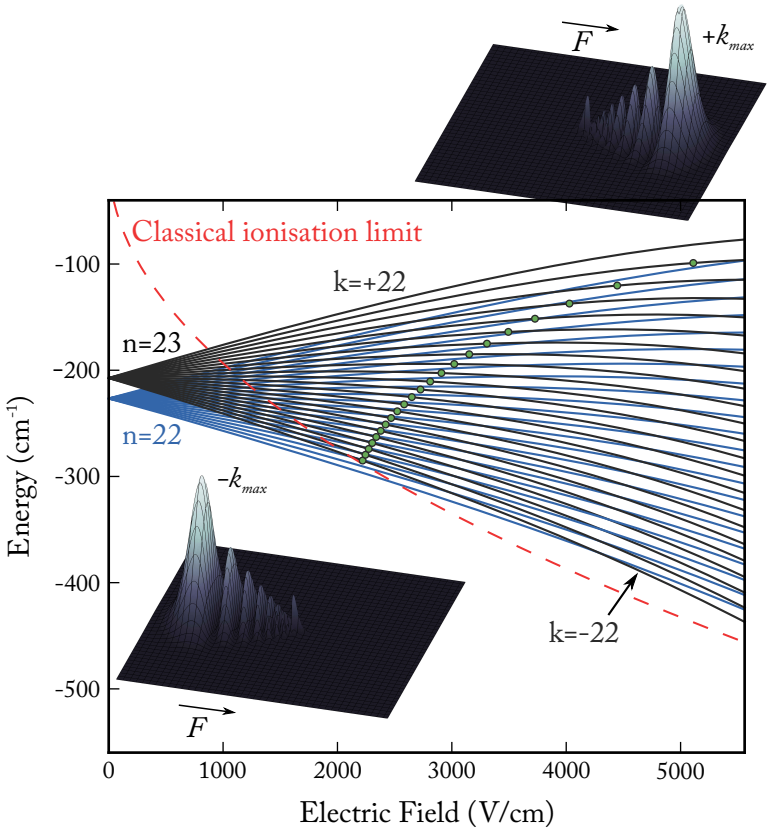

Figure 1.2: Stark effect in hydrogen for $n = 23$ and $n = 22$, maximally polarised parabolic k states are labeled for $n = 23$. The crossing point of the two manifolds is the Inglis-Teller limit, beyond which no avoided crossings are observed in hydrogen. Also shown is the energy of the saddle point $V = -2\sqrt{F}$ (dashed red line) at which field ionisation is classically expected. Green circles mark field values for the different Stark states at which the ionisation rate Γ exceeds $1 \times 10^6\,\mathrm{s}^{-1}$, which is the typical experimental timescale over which ionisation occurs. Note that only in the case of the most red-shifted state the classically expected field value coincides with the calculated rate. Also shown are the electron probabilities for polarisation parallel to the direction of the field ($+k$, blue-shifted) and in the opposite direction to the electric field ($-k$, red-shifted). The positive core is located in the middle of the plane of the wavefunction.

These states have a permanent dipole moment, which manifests in a permanent polarisation along the direction of the field. A positive Stark shift corresponds to a polarisation of the electron density along the positive direction of the electric field towards higher energies

(blue-shifted, $+k$) and a negative shift in the opposite direction towards lower energies (red-shifted, $-k$); exemplary probability distributions for two different maximally polarised k states are shown in Figure 1.2. Wavefunctions for extreme members of the Stark manifold in Figure 1.2 illustrate that the electron distribution is highly asymmetric with the majority of the electron probability furthest away from the core. This large separation gives the maximally polarised k states a large dipole moment ($3/2nk$) which offers a handle to exert a force on a Rydberg atom making the maximal $+k$ states an ideal candidate for spatial manipulation.

First order perturbation theory is valid for small fields that produce the linear shift of the split energies. If higher order contributions are taken into account, the energies for a specific Stark state can be calculated by the expansion in Equation (1.7) [74]; the higher order effects are discernible at higher fields. For the hydrogen atom, the energies including second order corrections are

$$E^{\text{Stark}}(F,n,m,k) = -\frac{1}{2n^2} + \frac{3}{2}nkF - \frac{n^4}{16}\left(17n^2 - 3k^2 - 9m + 19\right)F^2 + \mathcal{O}(F^3) + \dots \quad (1.7)$$

Energies calculated from Equation (1.7) are plotted in Figure 1.2 for two different principal quantum numbers.

1.3.2 Ionisation in an electric field

While for modest electric fields the effect on the atom may be just an energy level shift, at higher fields, ionisation can occur. This can be understood by considering the potential for the electron in the field.

If a Rydberg atom is placed in a constant external electric field along the quantisation axis, the z-axis, the combination of the Coulomb potential (for an electron) and the linear Stark perturbation as seen by an electron has the form

$$V = -\frac{1}{r} + Fz\,. \quad (1.8)$$

This combined potential has, as depicted in Figure 1.3, a saddle point on the anode side of the ion core at $z = -1/F$ with energy $V_{\text{saddle}} = -2\sqrt{F}$; as the magnitude of the field increases the energy of the saddle point decreases. Classically, at a field value of $F = 1/(16n^4)$ a Rydberg

state would be expected to ionise, as the electron can escape the Coulomb potential. For a maximum red-shifted state, the threshold field for ionisation is $F = 1/(9n^4)$, accounting for the Stark shift of the level [4].

As shown in Figure 1.2 it would be expected that red-shifted Stark states ionise at higher fields than blue-shifted states of the same n manifold since, at the same field value, a blue-shifted state is higher in energy. However, this is not observed experimentally. For the H atom, and for other Rydberg atoms using fast-ramped fields, blue states ionise at higher fields than red states for high principal quantum numbers n [2].

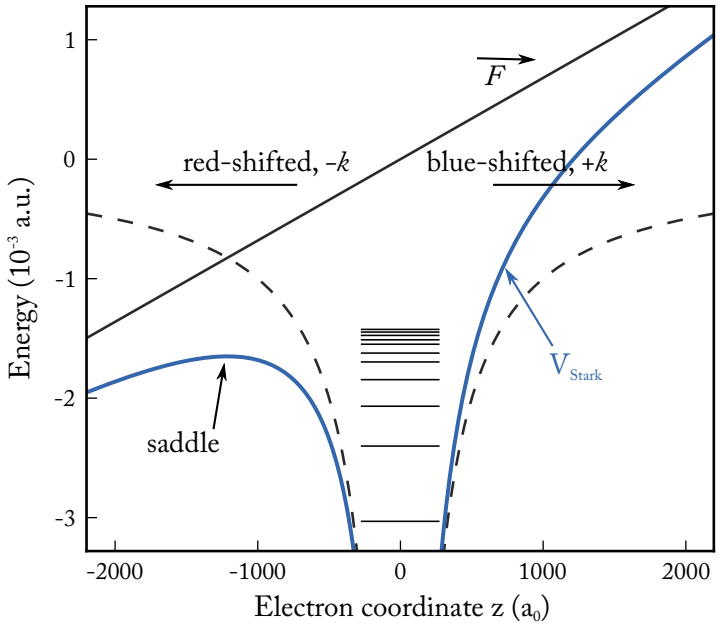

Figure 1.3: Combined Stark potential (full blue line) of the perturbed Coulomb potential (dashed line) with the core positioned at $z = 0$ that forms a saddle point forming in the negative direction of the electric field; potential energies are given in atomic units (a.u.). Arrows mark the direction relative to the core in which the red- and blue-shifted wavefunctions are polarised. Compare the maximally polarised wavefunctions as depicted in Figure 1.2 in respect to the position of the ion core. Complementing the classical intuition, schematic energy levels are added to the plot to demonstrate the lowering of the saddle below the energy of the Rydberg state; these levels have no spatial relationship here.

In the classical approach to understanding the field ionisation behaviour, the spatial extent of the electronic charge polarisation is not considered for different Stark states. In the case of a blue state, the majority of the electron density is located on the opposite side of the core to the saddle point as illustrated in Figure 1.2, which makes these states kinetically more stable, leading to longer lifetimes until the ionisation event occurs. In order to achieve the same ionisation rates Γ for a blue state as for a red state, fields of higher magnitude have to be applied. A

representation of the ionisation rate for different Stark states is shown in Figure 1.2; the rates were calculated with a semi-empirical formula for Γ as used by Damburg and Kolosov [75].

The field-ionisation behaviour of a Rydberg state may be derived for a hydrogen atom; in the case of a nonhydrogenic species, a different behaviour is observed. For an electron in a low orbital momentum state l, which classically has a strongly elliptic orbit, the inner part of the wavefunction is highly penetrating, causing the shielding of the core to be reduced and thereby a deviation from the Coulomb potential. The difference in energy to the hydrogen Rydberg formula is expressed through an effective quantum number $n^* = n - \delta_l$, where δ_l is the l dependent quantum defect which is 0 for a hydrogenic one-electron ion. With the Rydberg constant R_∞ the energy levels of the Rydberg series are then determined as

$$E = -\frac{R_\infty}{(n-\delta_l)^2}\,. \tag{1.9}$$

For other species, such as alkali atoms or molecules, the spherical symmetry is broken which allows coupling between red and blue states resulting in avoided crossings beyond the field value where neighbouring n manifolds cross, the Inglis-Teller limit at $1/(3n^5)$. The field ionisation behaviour may be 'adiabatic' or 'diabatic' (hydrogen like) according to how rapidly the field is ramped up, and hence whether the system passes adiabatically or diabatically through the level crossings [11]. For hydrogen atoms the behaviour at level crossings should be strictly diabatic as the crossings genuinely occur.

1.4 Ionisation of a Rydberg state at a metallic surface

As remarked in section 1.2, at a distance of about 1 µm to 10 µm from the surface, the dominant net-attractive dipole interaction of a Rydberg state and the surface can be described by the classical method of electric images if the orbital size for a given *n* is smaller than the distance to the surface. The conduction band electrons are assumed to be mobile within the metal surface so that the material can be treated as being perfectly polarisable. Then, when an atom is brought adiabatically from an infinite distance to a large finite distance in front of the conductor, the effect can be compared to the interaction with the electric mirror image of opposite charge at same distance beyond the surface boundary image plane [63].

1.4.1 Image-charge modelling

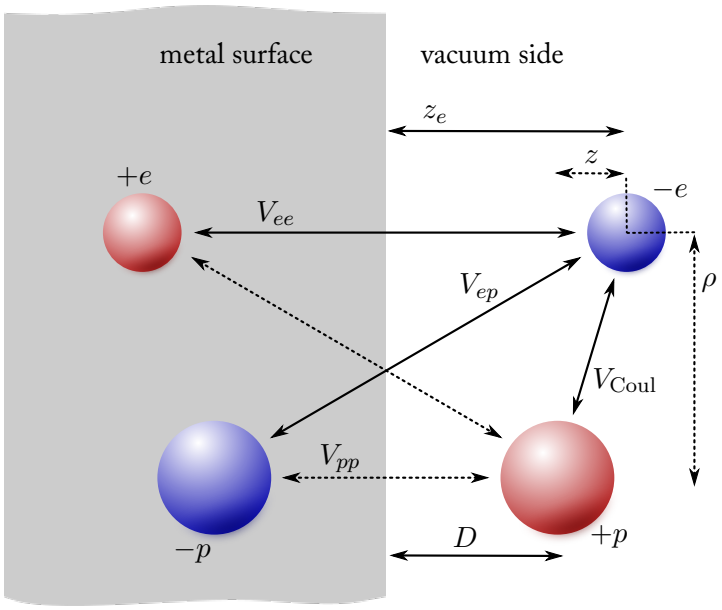

Figure 1.4: Image-charge model for an atom in front of a metallic surface. The dipole on the vacuum side of the interface system induces a mirrored charge distribution in the metal that can be described by point charges. Different potential terms are labelled according to Equation (1.10). The real electron is described in cylindrical symmetry by (z, ρ). The shape of the various potential contributions are further elaborated in Figure 1.5.

The contribution of the point-charge potentials for the interaction between the electron, ion core and their images can be isolated as depicted in Figure 1.4. Choosing the surface normal as the symmetry axis, the position of the electron can then be described by (z, ρ) relative to the ion core at height D above the image plane. The total one-electron potential is then a sum of the Coulomb potential and a surface potential that is composed of an interaction between the electron and image-electron V_{ee}, an interaction V_{ep} between the electron and image-proton as well as a term V_{pp} describing the interaction of the proton and image-proton.

In the asymptotic long-range limit, for a charge of $q_p = e = 1$ and with $z_e = z + D$, the surface potential as the sum of the respective V_{ii} components for the Rydberg electron becomes

$$\begin{aligned} \lim_{D,\, z_e \to \infty} V_{\text{surface}} &= \lim_{D,\, z_e \to \infty} (V_{ee} + V_{pp} + V_{ep}) \\ &= -\frac{1}{4 z_e} - \frac{1}{4D} + \frac{1}{\sqrt{(2D + z)^2 + \rho^2}} \,. \end{aligned} \tag{1.10}$$

where the attractive V_{pp} term is cancelled by a repulsive term from the expansion but can be

omitted because it lowers the energy of both the Rydberg state and the energy states of the surface equally and therefore does not affect the surface ionisation dynamics [73]. To avoid handling the square root denominators, the components of the surface potential can be treated with a binomial expansion [76] given by

$$V_{\text{surface}} = \overbrace{-\frac{1}{16D^3}\left(\rho^2+2z^2\right)}^{D^2\gg r^2} \underbrace{+\frac{3}{32D^4}\left(zr^2+z^3\right)+\dots}_{D^2\not\gg r^2}. \tag{1.11}$$

The total potential would additionally contain the Coulomb potential, $V_{\text{tot}} = V_{\text{surface}} + V_{\text{Coulomb}}$, where $V_{\text{Coulomb}} = -1/r$ and the distance r is the separation between ion core and electron. This potential can then be used in the Hamiltonian for calculating the energy levels of the system quantum mechanically; Ganesan and Taylor included terms up to 8th order to achieve convergence in their quantum calculations of the energy levels for a $n = 20$ Rydberg state.

If the atom is much further away from the surface than its orbital size, the quadratic terms are sufficient, which gives the instantaneous D^{-3} dependent van der Waals potential [77]. However, the size of a Rydberg atom grows as n^2 and the assumption that $D^2 \gg r^2$ loses its validity and Equation (1.11) needs to include higher order terms in the expansion.

The van der Waals contribution introduces a perturbation that couples the hydrogenic spherical basis functions $|nlm\rangle$ with $\Delta l = 0, \pm 2$ and $\Delta m = 0$, similar to the Stark effect described above; this lifts the lm degeneracy and causes a strong polarisation of the electronic wavefunctions. A series of differently polarised states is formed where a red-shifted state is oriented towards the surface whereas a blue-shifted state is oriented towards the vacuum side of the interface system in the absence of an external field. These effects lead to strong deviations from the over-the-barrier model especially for the more blue-shifted states.

1.4.2 Surface potential modelling

As Equation (1.10) is only valid for the asymptotic limit, it is unsuitable for small distances or large atom sizes since it exhibits a singularity for V_{ee} at $z = -D$, *i.e.* at the surface boundary. To alleviate these shortcomings, a free-electron Jellium potential as proposed by Jones *et al.* [78,

79] can be introduced which treats the electrons as moving within a background of (positive) charge density of the ion cores in the metal. The potential is then given as

$$V_{ee}(z, D) = \begin{cases} \frac{-1+\exp(-\lambda(z_e-z_0))}{4(z_e-z_0)} & \text{if } z_e > z_0 \\ \\ \frac{V_0}{A\exp(B(z_e-z_0))+1} & \text{otherwise} \end{cases} \tag{1.12}$$

$$\text{with } A = -1 - 4V_0/\lambda,\ B = -2V_0/A$$

A and B are chosen to match V_{ee} and its derivative at the image plane position z_0. This barrier model has three further parameters to create a continuous transition from the vacuum to the bulk; λ determines the width at which the modelled potential is saturating towards U_0 where U_0 is the inner potential of the metal related to the work function of the material. The resulting Jellium surface potential system and its components are depicted in Figure 1.5; it can be seen that a barrier with a saddle point is formed towards the surface.

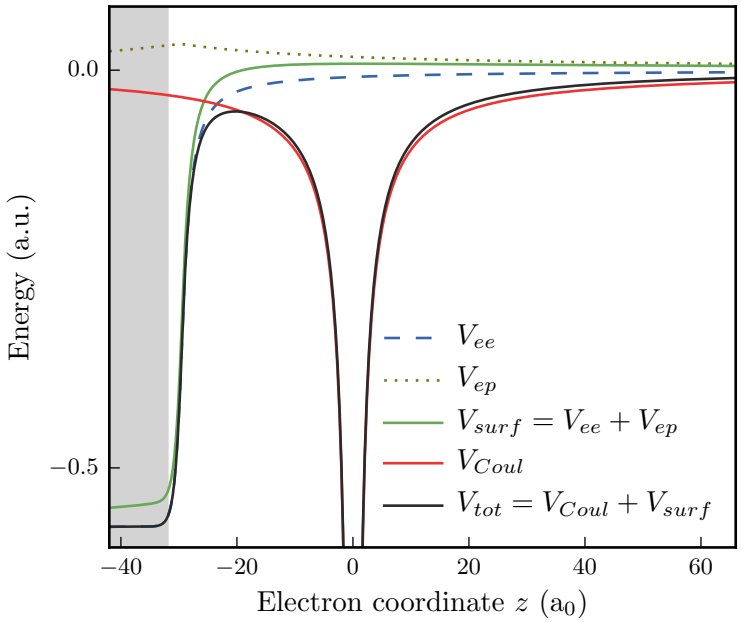

Figure 1.5: Perturbation of the atomic potential induced by the presence of a surface. As explained in the text, the Jellium model for V_{ee} ensures a smooth transition of the potentials when crossing the vacuum surface boundary. The surface sits at a position of $-30\,a_0$ relative to the center of the electronic potential at $z = 0$. Note that this reference system is chosen in various calculations discussed in the text as performed by So *et al.* [73]. Here, the symmetry center of the atom is selected to lie statically at $z = 0$ and the surface is moved towards the atom. The parameters for the Jellium model are selected for aluminium. The figure is adapted with permission from reference [73], copyrighted by the American Physical Society.

1.4.3 Surface induced ionisation

This effect of the saddle point is similar to the behaviour for ionisation in an electric field, in that the saddle is lowered and the barrier is decreased in width when the surface is approached by the atom. The position of the saddle point in the frame of the ion core is given in [80] as $z_s(D) \approx -0.69D$ and the height as $E_s(D) \approx 1.74/D$. Here, the perturbation of the Coulomb potential of the atom is increased as the distance between the atom and surface gets smaller as shown in Figure 1.6. Analogous to the effect of a homogeneous field, the originally bound electron can escape over the potential barrier or tunnel through it into the conduction band of the metal.

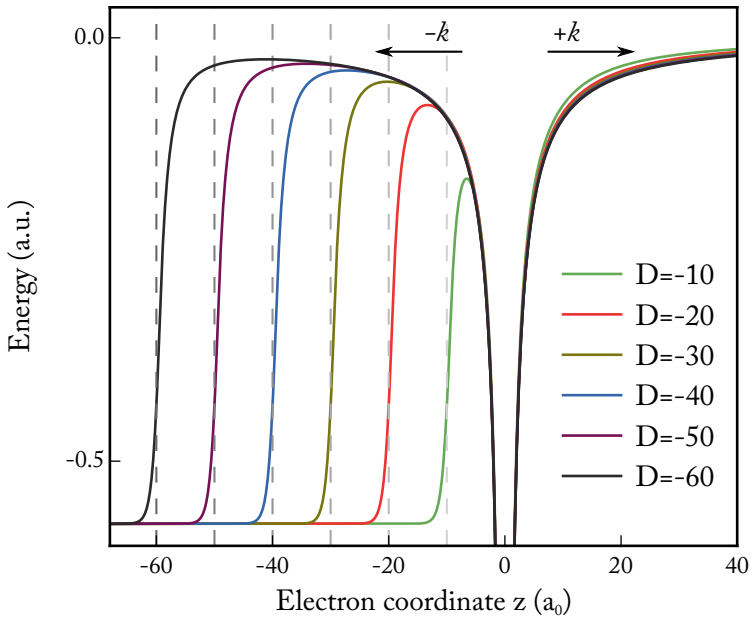

Figure 1.6: Total potentials for the combined system of atom and surface with decreasing separation, which causes a saddle point to be formed towards the surface which decrease in height and width until the electron can escape the Coulomb potential into the metal. Akin to the polarisation of the Rydberg wavefunctions in an homogeneous field as shown in Figure 1.2, a polarisation of the electron density of the atom relative to the core likewise occurs in front of the surface. They are equally labelled with the parabolic quantum number k, with the electron cloud either polarised towards the surface ($-k$) or towards the vacuum side ($+k$); compare Figure 1.7 for a depiction of these polarised atomic wavefunctions.

When comparing the energy of the saddle point with the energy of a Rydberg state, as given in Equation (1.7), the ionisation distance for the classical over-the-barrier model (OTB) can be derived in terms of n as $D_{\mathrm{OTB}} \approx 3.48n^2a_0$ [81]. For a Rydberg atom in a state $n = 30$ this predicts an ionisation distance of about 165 nm. The usefulness of the OTB model has been shown by Burgörfer *et al.* to characterise the reverse case, the neutralisation of an ion by

charge transfer from the surface to an impinging ion [81].

This classical approach delivers a useful intuition and a good first approximation for the process of charge transfer into the metal, but cannot fully account for the actual complexity of the composite system. For example, the dynamics of resonant tunneling through the barrier are not explicitly accounted for. In the OTB approach the probability for ionisation steps from zero to one at a critical atom-surface separation whereas this step will have a finite width when the process is considered as tunneling through a barrier into a vacant level in the metal. As the surface is approached and the potential barrier decreased in width the ionisation probability increases exponentially. On the other hand, the height and width of the potential barrier displayed in Figure 1.5 are not dependent on an external field, albeit such a field is usually present experimentally as discussed later.

The model also assumes that for every energy of the Rydberg state there will be an empty level in the conduction band of the metal at the same energy for transfer, however the model will not be appropriate if surfaces other than free-electron metals are of interest.

Importantly though, the reduced geometry of the OTB model to one dimension ($\rho = 0$) does not account for spatial effects, like polarisation of the Rydberg wavefunctions by the surface perturbation or the treatment of more complex species like molecules or nonhydrogenic atoms. Akin to the homogeneous field case, the lm degeneracy is lifted by the perturbation of the surface resulting in the formation of surface Stark states. Here, the quantisation axis is the surface normal, with states lower in energy that are oriented towards the surface ($-k$) and higher-energy states that are oriented towards the vacuum side ($+k$). However, the surface-perturbed energy levels within a n manifold can undergo many level crossings as the surface is approached. This has has been shown by So *et al.* by calculating energy levels of a Rydberg state in front of a surface using a complex scaling method [73], where the crossings are attributed to breaking of parity in the z-direction. Complex scaling is a coordinate transformation method used as a tool to study resonance and ionisation processes for weakly bound states. Results of such a calculation and how the energy levels cross are shown in Figure 1.7.

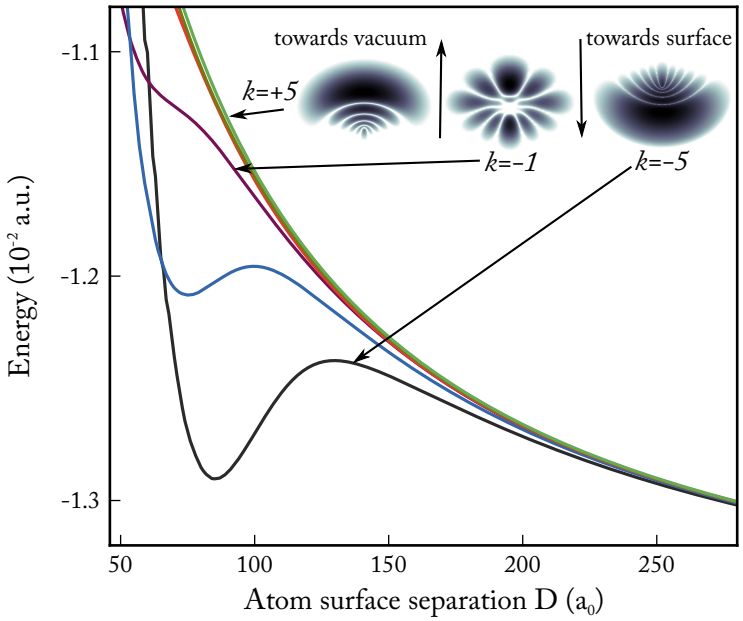

Figure 1.7: Energies of hydrogen in $n = 6$, $m = 0$ as a function of distance between the atom and the surface in atomic units, calculated from a complex scaling method with no extraction field present. In contrast to the homogeneous field Stark splitting, energy levels cross as the distance to the surface is reduced. But similarly, the wavefunctions are polarised, with the electron density directed either towards the surface ($-k$) or towards the vacuum ($+k$) as in the examples shown on the top. The wavefunctions are calculated with a grid based Coulomb-wave discrete variable representation (CWDVR) method.

1.5 Experimental studies of Rydberg charge transfer at a metal surface

In order to investigate the short range perturbation of a surface on an atom, the standard technique is to use atoms travelling in a beam directed at a surface of interest, which allows the atoms to be brought very close to the target by choosing a suitable experimental geometry.

Rydberg charge transfer has been experimentally observed with metal surfaces and with intrinsic and doped semiconductor surfaces. For the latter case, Dunham *et al.* found that the surface ionisation behaviour of a Si(100) sample is similar to a Au(111) sample [82] while Sashikesh *et al.* investigated the ionisation of hydrogen molecules at a silicon surface, observing different sensitivities to surface charge distributions caused by different dopant densities of either p-type or n-type silicon semiconductors [83, 84]. In the context of this review, the emphasis is on the transfer of an electron from a Rydberg orbital to the conduction band of a metal.

1.5.1 Beam transmission through metallic grids

The earliest study of Rydberg ionisation at a solid surface was conducted by Fabre *et al.* [66] where sodium atoms in a beam were excited to a Rydberg state and directed at a gold foil with micrometre sized slits. The measured transmission through the slits displayed a cutoff at $n \sim 65$ at which the orbital diameter is about 100 times smaller than the slits. Evidently, the transmission is not just reduced by collision of Rydberg atoms with the gold sieve as if the atoms are assumed to behave like hard spheres; the loss of transmission is attributed to ionisation into the sieve.

Kocher and Taylor also measured the transmission of lithium Rydberg atoms through a gold mesh and over time observed a decreased survival probability. They attributed the reduced transmission to the formation of an adlayer onto the mesh material, which was formed from water molecules and lithium adsorbed on the mesh. The adlayer can form surface dipoles that are able to produce local electric fields exceeding the field ionisation threshold for a Rydberg state and atoms are thereby lost to detection since they do not pass through the mesh. The Rydberg atom experiment proved to be sufficiently sensitive to probe the orientation of these submonolayer adsorbates alongside density variations that correspond to a surface coverage ranging from 10^{-4} to 10^{-5} monolayers [85].

In both of the aforementioned experiments the event of ionisation was inferred indirectly from the detection of Rydberg atoms travelling close to a substrate at a constant distance. In order to get access to distances near $D = 0$ in a controlled manner an atom beam can still be used, but directed at the surface at an angle. At a shallow angle this enables access of the atom beam to the surface target from the side, while leaving space in front of the target for the extraction of ions produced in the process. At the same time, this approach reduces the perpendicular component of the kinetic energy of the Rydberg atom projectile.

1.5.2 Ionisation in grazing incidence beams

The first experiment to directly observe the ionisation of Rydberg atoms at a solid surface was performed by Gray *et al.*; for a representation similar to their experimental geometry, see Figure 3.1. Here, a beam of (nd) potassium atoms was excited to principal quantum numbers 17 to 30 and directed at a plane gold mirror at an angle of 2°. The Rydberg atoms that are ionised

are detected by using a fine-mesh electrode located 2 mm above and parallel to the surface that creates a homogeneous electric field to accelerate ions away from the surface, and direct them at a position-sensitive detector with the aid of further extraction electrodes. In the absence of such a field the ions would travel further towards the surface and be neutralised via Auger neutralisation and not be available for detection. In that Auger process, an electron from the conduction band of the metal is transferred at close range to the ground state of the ion in the gas phase [86].

The applied electric field must counteract the momentum of the ion after the ionisation event occurs and the attraction of the ion by its own image charge to the surface, otherwise the ion will collide with the surface; the higher the velocity of the ion, or the further away the ion from the surface at the point of formation, the higher the magnitude of the extraction field needs to be to reverse the ion trajectory. As shown below, the minimum extraction field at which ions are observed can be translated into a distance of the ion from the surface at its point of formation and thereby the position of the Rydberg atom immediately before the event of ionisation.

In the experiment the ion signal is measured over a range of extraction fields up to the value required for field ionisation, as shown in Figure 1.8 (b); the information about surface ionisation is then extracted from the magnitude and shape of a surface ionisation profiles (SIP). These profiles are composed of a normalised ionisation signal at a constant extraction field where the ionisation signal represents the detected ions integrated over time gates that respectively separate ions stemming from field and surface ionisation. Typically, the magnitude of the profiles is increasing with increasing extraction field until the field-ionisation threshold, at which all Rydberg atoms undergo field ionisation and no surface ionisation is detected.

In an alternative configuration (by reversing the direction of the applied field), it is also possible to extract the electrons that are formed during surface ionisation [87]. McCormack *et al.* demonstrated the experimental detection of an electron signal that was proposed to be the result of 'backscattered' electrons ejected away from the surface during the process of surface ionisation [73].

Assuming a perfect conductor, the field necessary to pull an ion away from its own image charge can be calculated. By considering the perpendicular components of kinetic and potential energy of the mirror system, a point charge at a distance D and with charge Z_i ($= 1$ for a proton)

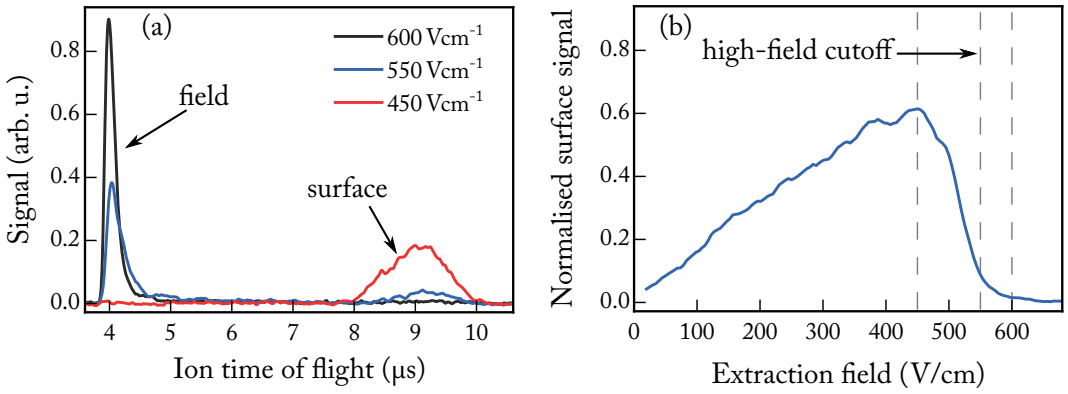

Figure 1.8: Typical time of flight (TOF) traces for ions produced in the process of field and surface ionisation for $n = 35$, $k = 0$ in (a). If the extraction field is lowered below the value necessary to field-ionise a Rydberg atom, the onset of surface ionisation in the TOF can be observed. With the earlier field signal in the TOF than the surface signal, the flight time of the Rydberg atom towards the surface, with an extraction field present, can be deduced. The gated and integrated surface signal in (b) from the TOF trace in (a); the maximum field value to extract ions from surface ionisation is marked as the high-field cutoff.

requires a minimum extraction field of

$$F_{\text{min}}(D, T_\perp) = Z_i \left(\frac{1}{2D} + \sqrt{\frac{T_\perp}{D}} \right)^2 , \tag{1.13}$$

where the perpendicular component of the kinetic energy of the projectile is given by $T_\perp = 1/2mv_\perp^2$. This can be rearranged into Equation (1.14) to give the minimum distance (in atomic units) from which a positive ion can be extracted with a given field,

$$D_{\text{min}}(F, T_\perp) = \frac{T_\perp + \sqrt{F} + \sqrt{T_\perp^2 + 2T_\perp\sqrt{F}}}{2F} . \tag{1.14}$$

If no field is present, the time from the event of ionisation and the subsequent acceleration of the remaining ion into the surface is very short ($\sim$1 ns) whereas modern high voltage pulsed electronics typically have a rise time of multiple ns, hence the electric field needs to be permanently present during the process of surface ionisation. The field might have effects on the surface itself and the process of surface ionisation that are not accounted for; the effects of a surface bias field are discussed in [73].

As $T_\perp \to 0$ and incorporating the distance dependence from the OTB model, $D \propto n^2$, in

the asymptotic limit of Equation (1.13) the minimum detection field for hydrogen becomes

$$\lim_{T_\perp \to 0} F_{\min}(D, T_\perp) = \frac{1}{4D^2} \propto n^{-4} .$$

Thereby, Gray *et al.* were able to infer a distance to the target for surface ionisation and to predict a field at which appreciable ion detection should occur. In the recorded traces Gray *et al.* observe a discernible magnitude of ion surface signal at drastically lower fields than predicted but also a significant rise in signal at the field ranges corresponding to $\sim (4-5)n^2 a_0$; the overall shape of the ionisation traces are in stark contrast to what would be expected theoretically.

In the experimental configuration, it is inevitable that (non excited) potassium atoms travelling in the beam will be deposited on the substrate even remaining after routinely baking the surface regularly above the melting point; the deposition is minimised by collimating the beam before and after laser excitation. The difficulty arising from this is the possible neutralisation of potassium ions in the presence of an electrostatic field by collective interaction with adsorbed potassium atoms [88] since these adsorbates can locally generate high fields. The sharp onset at low extraction fields, which is independent of n, was attributed to this neutralisation process.

Despite the difficulty to account for the influences of stray fields in the previously described experiment, the results are reported with high reproducibility. In order to circumvent the adsorption of the atoms that are intended to be excited into a Rydberg state, elements can be chosen that are either less likely to react with the surface or less likely to deposit as irregular mounds of adsorbate; an obvious choice are rare-gas elements. In their subsequent experiments, Dunning and coworkers switched to the use of xenon in surface ionisation experiments with a Au(111) gold surface [68, 89, 90, 91].

Under these stable and well-defined conditions Hill *et al.* excited xenon atoms contained in a supersonic expansion to the lowest (red-shifted) state for $13 \leq n \leq 20$ and directed the beam at a gold target at an angle of $\sim 4°$. They recorded highly efficient surface ionisation over a range of extraction voltages and found, as before, a gradual rather than a sudden rise in ionisation as the extraction field increased. The scaling of the distances for the onset of ionisation is determined as n^2, which possibly matches intuition since this is approximately the scaling of the atomic radius with principal quantum number. The distance over which ionisation occurs was derived from the experiment to be $D = (4.5 \pm 0.9)n^2 a_0$, which is in agreement with

a predicted value of $\sim 3.8n^2a_0$ from complex scaling theory that examines the broadening of Rydberg levels in the presence of a surface and bias fields [92].

Since possible large-scale contamination of the surface sample can be eliminated from this version of the experiment, other reasons have to be considered as to why the surface signal still follows a shallow rise rather than a step-like trend. Hill *et al.* discussed the influence of the velocity distribution of the incoming atoms as well as mixing of neighbouring Stark states to partly account for the observed trace shapes. The surface preparation was further considered by comparing the surface geometries of a gold target prepared by epitaxial growth, which is near to atomically flat, to a rough machined copper surface. The latter target shows an earlier onset of surface ionisation pointing again at the importance of the shape of surface potentials.

To elucidate the influence of state changes as the surface is approached by a Rydberg atom, Dunning *et al.* initially prepared xenon atoms in the most red-shifted and most blue-shifted state before interacting with the surface sample [71]. The surface-ionisation profile shapes for originally red-shifted and blue-shifted states show no significant differences and the original polarisation during preparation in a static electric field is barely discernible after ion collection. This was in contrast to initial expectation given that the red-shifted states are polarised towards the surface whereas the blue shifted ones away from the surface. These authors argued that the minimum field applied for ion detection F_{min} is mixing states of neighbouring n manifolds and by surface perturbation the approaching Stark states lose their initial identity. In contrast to hydrogen, this is due to wholly or partially adiabatic traversal of crossings in the Stark energy map as the electric field magnitude is increased; avoided crossings lead to a loss of the initial polarisation of Stark states.

Based on these findings, which cannot explain the broad shape of the ion collection signal, Wethekam *et al.* then focussed on investigating the ionisation rates for the lowest state in the $n = 17$ and $n = 20$ manifolds [89]. In this study it was shown that the experimental traces can be fit by modelling the ionisation expressed by a tunneling rate Γ into the metal, and by the manner in which the ionisation rate varies when the distance to the surface is decreased. First, the fraction I of incident atoms in an extraction field F with a known perpendicular component

of the velocity distribution $f(v_\perp)$ that survive up to a critical distance D_c can be calculated as

$$I(F) = 1 - \int_0^\infty f(v_\perp) \times \exp\left(- \int_{D_c(F,v_\perp)}^\infty \frac{\Gamma(D', F)}{|v_\perp|} \, \mathrm{d}D' \right) \mathrm{d}v_\perp \, . \tag{1.15}$$

Tests by Wethekam *et al.* showed that the broad onset in the ionisation traces could not be accounted for when incorporating an experimental velocity distribution. Since the velocity distribution does not fully explain the broadness of the ionisation onset, an ionisation rate Γ is modelled which increases exponentially with decreasing distance D'; thereby it is possible to fit the data for the most red-shifted states with

$$\Gamma(D', F) = \Gamma_0 \exp\left(- \frac{D'(1 - kF_0)}{D_{\mathrm{decay}}} \right) , \tag{1.16}$$

where $F_0 = n^4 F$ is the classically scaled ion extraction field, Γ_0, k and D_{decay} are constants to describe the decay of Rydberg population by ionisation. Note that the chosen characteristic decay length $D_{\mathrm{decay}} \sim 230\, a_0$ is much larger than the expected $\sim 30\, a_0$ from hydrogenic theory.

1.5.3 Stray field influences on surface ionisation

While the previous model delivers a good fit to the experimental shape of the ionisation traces, it does not clarify explicitly what the reasons for this behaviour are. The possible influence of stray fields on the ionisation dynamics has been indicated several times before but not quantitatively assessed. Even though the Au(111) sample is atomically flat, it nonetheless might contain contaminants that can be a source for field inhomogeneities where any stray or patch field generated from these irregularities can reach far into the vacuum.

An approach to further investigate the effect of fields emanating from the surface is to vary the collisional angle of the incident atom beam. Considering the surface potential landscape to be (regularly) modulated along the surface by its geometric structure or surface irregularities it produces field inhomogeneities that decay rapidly with distance from the surface which lead to a range of effective incident angles relative to the surface normal [93], where the incident atom trajectories are effectively exposed to lower fields (shallower angle) and higher fields. Varying the angle, and thereby the exposure to different parts of the surface potential, can have an impact on the onset and the shape of rising surface ionisation.

With the same apparatus as described in reference [90] Neufeld *et al.* investigated stray fields associated with surface inhomogeneities by varying the angle of the atom beam between $\sim 5-16$ degrees. They observed that the distance at which surface ionisation occurs is dramatically increased with increasing collisional angle, which is also expressed in large, and unphysical, decay lengths D_{decay} in the modelled ionisation rate in Equation (1.16) that are mitigated by the effects of the inhomogeneities. The potential variations across the surface were modelled by the assumption of a simple periodic variation since the actual potential landscape of the gold surface is not known.

To conceptually grasp the magnitude of modulation and different domains of the surface potential Pu *et al.* measured the surface potentials directly via Kelvin probe force microscopy [91]. When using the measured patch fields in trajectory simulations they were able to reproduce surface ionisation for xenon with high accuracy when using a simple over-the-barrier model. Eventually, Pu *et al.* used an array of patterned electrodes to create a highly regular surface potential that would emulate a perfectly flat and homogeneous sample. The bias of these regularly spaced electrodes was chosen to be higher than that generated by an actual surface patch charge so that these fields dominate the atom surface interaction rather than the actual surface potentials of the electrode array. When a modest (positive) bias is applied to the electrodes the ion signal is significantly larger at lower extraction field, implying that direct field ionisation can be achieved with stray fields originating from a structured solid sample paving the way to surface detection of low n Rydberg atoms.

1.5.4 Surface ionisation of molecules - further complexity

As hinted at in section 1.4.3, the symmetry of the (classical) modelling for surface ionisation does not account for the behaviour of the Rydberg states of more complex species like molecules. A series of experiments studying the ionisation of hydrogen molecules at evaporated gold and aluminium surfaces was performed by Softley and coworkers [67, 87, 93, 94]. Whereas for xenon the non-vanishing quantum defect creates a deviation from the hydrogenic behaviour, for molecules rotational (quantum number N^+) and vibrational (quantum number v^+) degrees of freedom for the core are further introduced to the problem and these might add to the dynamics of surface induced ionisation.

The first ionisation of hydrogen molecules at a surface was observed by Lloyd *et al.* with molecules excited to a Rydberg state with a core rotational state of $N^+ = 2$. They found that the ionisation distance scales with the size of the Rydberg orbital, as in the case of xenon ($\propto n^2$), but that the distance scaling varies with an effectively higher quantum number ν_0 that is calculated with respect to the ionisation threshold of the $N^+ = 0$ state [67]. With this effective quantum number, the distance range for surface ionisation could be determined as $D \sim (3-5)\nu_0^2 a_0^2$ which is in agreement with the results for xenon atoms.

Here, the detected onset of ionisation is more characteristic of the $N^+ = 0$ states that have a higher principal quantum number but are close in energy to the state in the $N^+ = 2$ series, suggesting a state transition such that core rotational energy is transferred to the Rydberg electron. While rotational states N^+ are generally not coupled to each other in a homogeneous electric field, field inhomogeneities or perturbations by the surface image-charge interaction can introduce a coupling and facilitate a population transfer between two states of different rotational quantum numbers. In consecutive studies it was confirmed that the surface induces a coupling between different rotational channels of the form $|N^+ = 2, n\rangle \rightarrow |N^+ = 0, n'\rangle$, where $n' > n$, leading to a forced rotational autoionisation [93, 94].

Furthermore, it was found that the observed surface ionisation does not differ with the surface material, either gold or aluminium, but shows differences associated with the roughness of the material; a machined instead of evaporated aluminium surface exhibits a marked change in the ionisation behaviour. In the latter case the size of surface structures was $\sim 230\,\mathrm{nm}$ and thereby comparable to the size of the Rydberg orbitals.

1.6 Hydrogen Rydberg atoms as surface probes

In order to alleviate ambiguities in the experimental assessment of surface ionisation that are due to the adiabatic energy level crossings in the excited species as described in the previous section, the use of atomic hydrogen is an evident but challenging choice. Theoretically, it allows the direct comparison of the results from *ab initio* calculations to the experimental outcome. With other species, the nonhydrogenic effects had to be estimated to account for uncertainties in experimental observations [68, 89]. As explained in section 1.3.1 hydrogen has the advantage of traversing the Stark map without undergoing avoided crossing beyond the Inglis-Teller limit.

The difficulty, however, of exciting atomic hydrogen into a Rydberg state compared to an alkali metal is the large energy difference of the $1s \rightarrow 2p$ transition (Lyman alpha line L_α) which lies in the vacuum ultraviolet part of the electromagnetic spectrum and is easily absorbed in ambient air. So *et al.* investigated the charge transfer from hydrogen atoms to a gold surface for the first time [69].

1.6.1 Surface induced wavefunction polarisation in hydrogen

So *et al.* measured surface ionisation profiles (signal versus extraction field) for hydrogen in selected Stark states for a range of principal quantum numbers; by applying a small bias voltage to the surface a specific state can be selected spectroscopically from the Stark manifold. The bias field ($\ll F_{\text{extraction}}$) is present during Rydberg excitation and chosen so that the initial orientation of the electron polarisation matches the wavefunction polarisation due to the surface perturbation, as illustrated in Figure 1.7, *i.e.* a red-shifted state is oriented towards the surface and a blue-shifted state is oriented away from the surface along the surface normal.

Similar to the surface ionisation traces for xenon, a shallow rise in signal with a low-field onset can be observed as well as as a high-field cutoff, as can be seen in Figure 1.9. Both onset and cutoff of surface ionisation shift towards higher fields when going from the maximum red-shifted ($-k_{\text{max}}$) to the maximum blue-shifted state ($+k_{\text{max}}$). The shift of the field-ionisation signal (high-field cutoff) follows the expected diabatic behaviour as demonstrated previously and illustrated in Figure 1.2, but more interestingly, this behaviour also manifests itself for the surface signal.

With respect to the position at which the ion core is formed it would be expected that a red, surface oriented, state ionises furthest from the surface and can be detected at lower fields and a blue, vacuum oriented, state ionises closest to the surface and is detected by higher fields. This expectation is based on the assumption that the approaching atom does not undergo avoided crossings leading to a change in polarisation which was confirmed theoretically in earlier studies [73, 95, 96]. This is precisely what can be recognised in the surface ionisation profiles in Figure 1.9 and, contrary to xenon or the hydrogen molecule, it can be concluded that hydrogen atoms diabatically pass through level crossings as the distance between atom and surface is decreased such that the Stark polarisation is maintained from excitation to the event of ionisation.

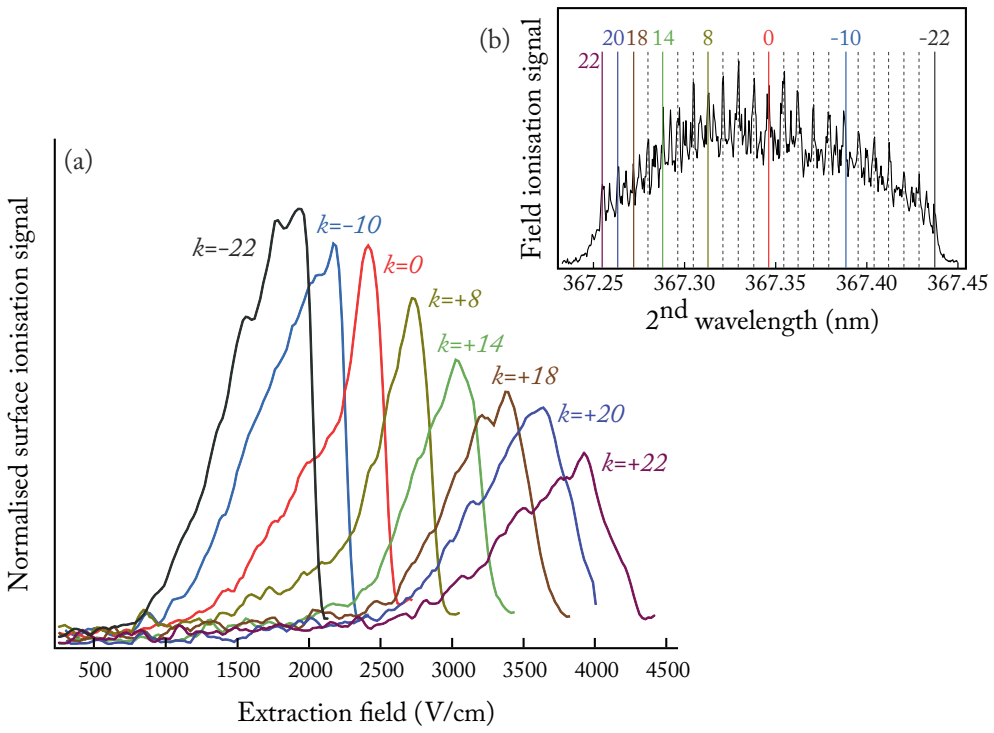

Figure 1.9: Surface ionisation profiles for H atoms in $n = 23$ and a range of Stark states are shown in (a). The Stark spectrum obtained by scanning the second laser for excitation from the *2p* state is shown in (b), from which selected states are populated by wavelength selection in a homogeneous field. The surface traces are normalised to the magnitude of the same state during field ionisation. The figure is adapted with permission from reference [69], copyrighted by the American Physical Society.

When considering only the most red-shifted states, the low-field onset of surface ionisation can be modelled as critical field $F_{\min}$ for ion extraction with Equation (1.14) as a critical distance $D_{\min}$ from the OTB approach. When the velocity distribution is convoluted with a step function at the critical distance it does not account for the continuous rise in the surface signal. So *et al.* used a model that empirically accounts for the shift and broadening of ionisation distances by incorporating a mean critical ionisation distance $\mu(F) = D_{\min}(F) - n^2$ and a spread around this mean $\sigma = 2.5n^2$ into the OTB model to derive a cumulative ionisation probability Φ at distance D,

$$\Phi(D, F) = 1 - \frac{1}{2}\left(1 + \operatorname{erf}\left(\frac{D - \mu(F)}{\sqrt{2\sigma^2}}\right)\right). \tag{1.17}$$

That equation, when again convoluted with an experimental velocity distribution $f(v_\perp)$, gives

an ion detection probability P as

$$P(F) = \int_0^\infty f(v_\perp)\Phi(D_{\min}, F)\,\mathrm{d}v_\perp\,, \tag{1.18}$$

which provides a very good agreement for the experimental traces from $n = 20$ to 36.

Overall, in this experiment it was demonstrated that hydrogen atoms can be successfully employed in the study of surface ionisation which creates the possibility to directly compare theory to experiment. It also demonstrates that a unique control over the charge polarisation of the Rydberg state can be achieved with atomic hydrogen.

1.6.2 Energy resolved probes - surface ionisation at electronically structured Cu(100)

The focus of the previous work with atomic hydrogen at a Au sample was how varying the properties of the Rydberg state itself affected the surface ionisation dynamics. The energies of the conduction band in gold are continuous, so that any energy of a Rydberg state will be degenerate with a state in the metal that can act as an acceptor for charge transfer. When an electronically structured surface is introduced it is conceivable that surface ionisation via charge transfer is enhanced at discrete resonances.

A Cu(100) surface has a band gap at the energy of the Rydberg states, in which a series of so called image states is set. They arise from the image charge interaction of an electron outside the metal at distance z_e resulting in a Coulomb like potential $V_{ee} = -1/4z_e$ that forms a series of bound states along the surface normal. This image state series, which resembles the Rydberg series but with a different periodicity, is of the form

$$E(n_{\mathrm{img}}) = -\frac{1}{16}\,\frac{1}{2(n_{\mathrm{img}} + a)^2}\,, \tag{1.19}$$

where n_{img} is the index of the image state and a the quantum defect parameter for a given surface. In the direction parallel to the surface the wavefunctions of surface states are similar to the bulk states that form (non-discrete) energy bands so that only the perpendicular component of the velocity is physically relevant.

With the same apparatus as described in 3.1 and used in reference [69], Gibbard *et al.*

studied surface ionisation at a Cu(100) surface with hydrogen excited to Rydberg states approximately in the middle of the Stark manifold for a range of principal quantum numbers n=25 to 34. As a co-author of this paper, early work in this thesis involved sharing in the work of data recording for this study.

The surface is mounted on a translation stage that can transfer the sample into a separate chamber where the copper sample is treated with an ion gun and annealed by repeated heating cycles to ensure a clean and flat sample before Rydberg measurements are conducted. The surface ionisation traces are normalised to the field ionisation signal and integrated from the minimum extraction field to the high-field cutoff as described in 3.4 and plotted over the principal quantum numbers in Figure 1.10; example surface ionisation traces are shown in Figure 1.11. The integrated signal displays non-monotonicity over the principal quantum number and a strong difference compared to a gold surface which possesses no discrete surface energies. These results were explained in terms of resonant enhancement of the ionisation process when the Rydberg energy for $n = 26$, 31 and 33 matches one of the image states of the surface.

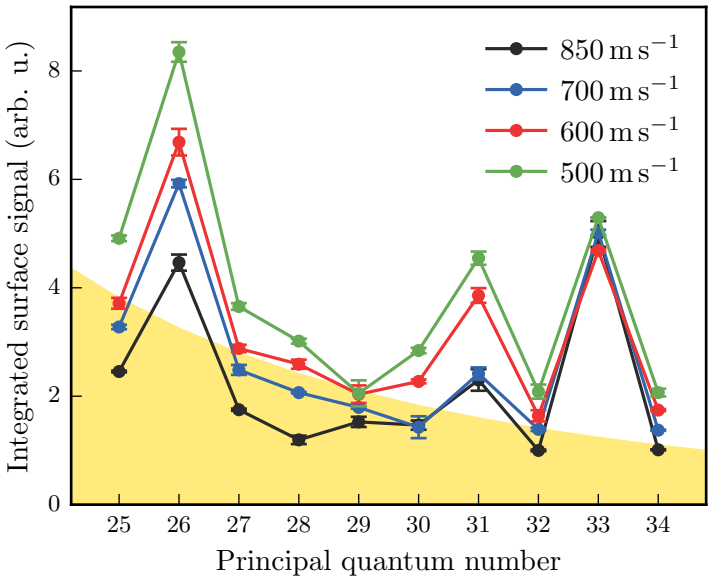

Figure 1.10: Integrated surface ionisation profiles for Rydberg atoms impinging on a Cu(100) surface over a range of principal quantum numbers for different collisional velocities as shown in Figure 1.11 for approximately mid-manifold Stark states; stated is the perpendicular component of the velocity. The normalised surface ionisation profiles are recorded per state at a constant velocity of the Rydberg projectile and then integrated over the range of extraction fields and displayed as a single data point for the principal quantum number n. The yellow background shows the integrated surface ionisation signal for a gold surface at a constant velocity which displays a monotonic behaviour. Note that the integrated signal for the gold surface is not a continuous function but merely plotted as filled line. Figure reproduced from reference [97].

1.6.3 Velocity effects on resonance behaviour

Additionally, as described in 1.6.2, the velocity in this experiment is adjusted to repeat the measurements at a range of collisional velocities, which introduces another handle on probing resonant charge transfer.

First, the collisional velocity will affect the ion detection efficiency; from Equation (1.13) it can be seen that at a lower velocity of the ion projectile a lower field F_{min} will be necessary for extraction. Second, this variation with velocity becomes more pronounced for an increased ionisation distance. With greater distance D in Equation (1.13), the $\sqrt{T_{\perp}/D}$ term will become more dominant and lead to greater shifts in the ionisation onset F_{min} over respectively constant $T_{\perp}$ and thus velocities. This shifts the low-field onset in the surface ionisation traces to lower fields and thereby increases the overall amount of integrated signal. These effects can be observed in Figure 1.11 for a resonant ($n = 26$) as well as for a nonresonant case ($n = 27$); the magnitude of surface signal is increasing with decreasing collisional velocity which in turn leads to the variations shown in Figure 1.10.

Another effect is that a slower atom will spend more time at a certain distance and thereby be more likely to be ionised further away from the surface, also shifting F_{min} to lower fields. The latter is expected to be more important in the case where a Rydberg state is resonant with an image state [98].

In conclusion, it could be demonstrated that Rydberg atoms display a sensitivity to the discrete surface states by enhanced surface ionisation and it illustrates the ability of such studies to probe the electronic structure of surfaces. The application of this technique can complement previous experimental approaches aimed at the detection of low lying image states [99, 100, 101]. By populating different Rydberg states this probe can be adjusted accordingly to the energetics of the system of interest.

With the results presented for a Cu(100) surface it becomes intriguing to explore other systems that are of a confined and discrete nature. Currently, investigations of Rydberg surface ionisation into thin films and nanometre sized particles deposited onto a substrate are being carried out in our group [102]. For thin films it has been shown theoretically that tunneling from atomic levels into a film deposited on an insulating material displays quantum effects and that these are able to strongly influence ionisation rates [103, 104].

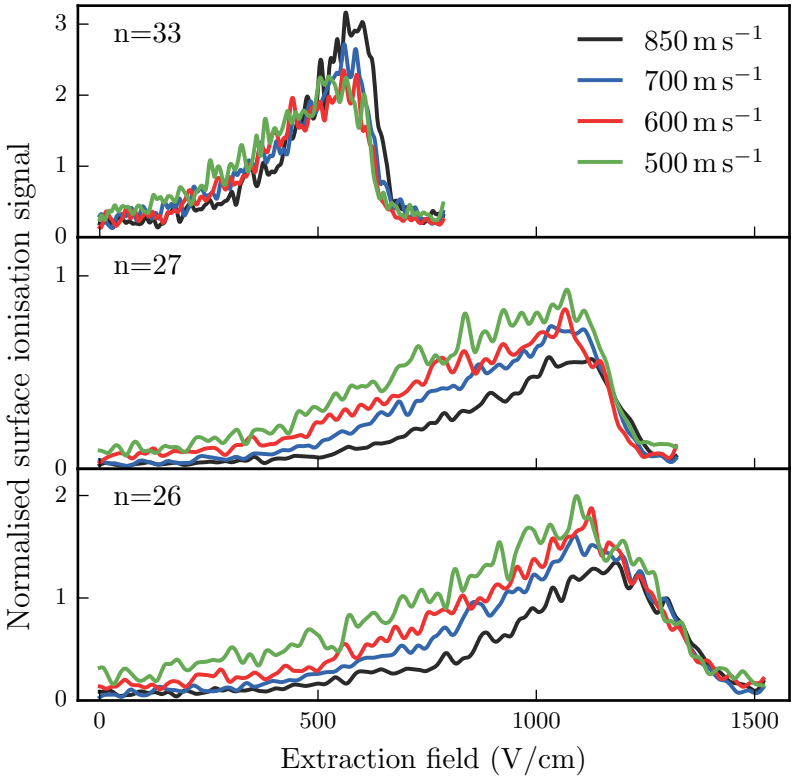

Figure 1.11: Surface ionisation profiles (ion signal from surface ionisation at a constant extraction field value) for hydrogen Rydberg atoms incident on a Cu(100) surface for different collisional velocities for $n = 26, 27, 33$; the color coding for the different velocities are identical for all plots. The magnitude of the surface signal is normalised with the magnitude of the corresponding, and separately recorded, field ionisation signal. Figure reproduced from reference [97].

Following the argument from above, a further decrease in the collisional velocity would increase the time an atom spends at a certain distance from the surface. By spectroscopic means, the uncertainty of a measurement could be decreased by maximising the interaction time with the system in question, *e.g.* for a discrete energy as the image state of a band gap material.

In the following chapters it will be assessed how the process of surface ionisation is influenced as the collisional velocity of the Rydberg atoms is varied and how the velocity dependence can be utilised for surface studies. The process of ionisation at a graphene surface is also investigated in chapter 4.

Modelling techniques for Rydberg atoms at surfaces and in electric fields

To predict the behaviour of a single Rydberg atom being ionised in close proximity to a surface or moving collectively in an electric field, different approaches have to be chosen. The change in position and velocity by forces exerted on the Rydberg atom dipole in an electric field can be calculated classically by integrating the equations of motion for a point mass, whereas the surface ionisation process needs to be modelled quantum mechanically in a way that accounts for the spatial extension of the Rydberg wavefunctions. In the latter case, a single instance of an atom can be considered to be representative for all of the atoms in an ensemble whereas in the former case a statistically created set of atoms is explored.

2.1 Dynamics in ionisation probability of Rydberg atoms approaching a surface

As laid out in section 1.4, the ionisation of a hydrogen atom in proximity to a surface can be approached by considering it to be a problem akin to the ionisation in an external electric field. The comparability of the two problems, in essence the hybridisation of atomic states by surface interaction [95], is demonstrated in Figure 1.6 where a potential barrier of decreasing width is formed between the core of the Rydberg atom and the surface boundary. For the situation in an electric field F, as governed by the Hamiltonian in Equation 1.5, there will be a non-zero probability for the electron to tunnel through it. This case can be described with a probability current w (flow of probability per unit time per unit area) through a plane perpendicular to the

z-axis is given by the Landau formula [105]

$$w = -\frac{4}{F}\exp\left(-\frac{2}{3F}\right); \tag{2.1}$$

for a hydrogen atom in the ground state with a finite barrier this results in a resonant character, where w can also be read as the *width* of an energy level $\Gamma \sim \hbar/\tau$, with lifetime τ. When studying resonant interactions between surfaces and particle projectiles, the energy and width of a level become quantitative characteristics by which to compare the processes in question.

2.1.1 Time-independent perturbative and nonperturbative techniques

In a variety of phenomena that involve the interaction between a surface and particles in the gas phase, the transfer of an electron is often explored as the key process. Due to its prevalence in surface science this mechanism has been treated theoretically early on, where the shift and broadening of alkali-atom valence levels in the vicinity of a metal surface have been studied [106, 107]. Here, by invoking the perturbing Hamiltonian based on the image-charge interaction as introduced in section 1.4, the probability for the transition of an electron from an atomic level into the conduction band of the metal could be calculated. The thereby finite lifetime of a discrete atomic level describes the resonant charge transfer into a continuum of states in the metal surface. A simple system to study the transfer of an electron is to have negatively charged ions colliding with a surface [108, 109].

This, after all, only represents a very limited case in which the surface energy levels are merely comprised of the free-metal continuum. When adsorbates are added to the treatment, more energy levels are introduced, significantly complicating the problem [110]. Since the manifolds of high lying states in a Rydberg atom are close in energy and expected to mix under perturbation, using them to represent the multi-level character of this compound problem becomes appealing. Due to the large spatial extension of a Rydberg atom, the interaction of surface and atomic level occurs at greater distances from the surface. For one, this should allow for a simpler treatment of the surface potentials in question but needs a different approach than perturbation since its validity is only given for smaller distances and requires otherwise large corrections to the classical image-charge Hamiltonian [76].

In order to overcome these limitations, various nonperturbative techniques have been in-

troduced. Among them are the complex scaling method of Nordlander and Tully [111], as used in section 1.3, and the coupled angular mode (CAM) method of Teillet-Billy and Gauyacq; in CAM the mixing of angular scattering modes is treated to calculate the position and width of negative ion ground and excited states [112]. When comparing results obtained with the nonperturbative methods they were found to be quite different from those obtained with perturbation when studying an aluminium surface [113, 114]. Nonetheless, for excited states, Nordlander argues that the direct comparison between the techniques is not possible since the perturbative procedure neglects the hybridisation between the atomic orbitals induced by the surface [115]. It was demonstrated in these calculations that the hybridisation leads to levels that display greatly varying level shifts and widths as a function of surface separation D from each other.

In the Rydberg atoms considered, one electron is in an excited state, which can be considered as having only one channel for electronic transition if the energy of the state lies above the Fermi level of the solid. Usually, as in the two accurate methods above, the transition process is treated as deriving from an adiabatic quasi-stationary state. In these terms, the electron-surface interaction can be related to basic notions of atomic scattering with which Borisov *et al.* extracted energy levels and widths from the scattering S-Matrix as function of D [113, 114]. In discussing the wavefunction of a resonant state of width Γ, the boundary conditions for solving Schrödinger's equation become critical to the physical interpretation of the problem. For the quasi-stationary problem, a simple approach would be to facilitate their resemblance to bound stationary states [116]. This assumes localisation in space at $t = 0$ and a time evolution of the wavefunction ψ given by

$$\psi(t) = \exp\left(-iEt/\hbar\right)\psi(t=0) \tag{2.2}$$

with complex energies E and real energies E_0

$$E = E_0 - i\Gamma/2\,, \tag{2.3}$$

where the $-i\Gamma/2$ term results in an exponential decay of the state. The stationary problem $H\psi(\boldsymbol{r}) = E\psi(\boldsymbol{r})$ can be solved with the Siegert boundary condition $\psi(r \to \infty) = \exp(ikr)/r$, which does not account for a dynamic evolution of the initial state but assumes to follow a given energy level adiabatically. In order to examine the dynamics of the electron transfer in a system

that has multiple levels close to each other, as in an excited electronic state, another approach has to be chosen to capture the potential nonadiabatic effects.

2.2 Time-dependent wave-packet propagation

To elucidate the experimental results of surface ionisation of dense energy manifold Rydberg states approaching a surface, a wave-packet technique has been used in several studies to investigate the quantum mechanical evolution of the electron, *e.g.* see references [72, 73], that have been developed from studies of the charge transfer from a negative hydrogen into a metal surface [109, 117], comprehending all dynamical effects.

The attractiveness of the wave-packet propagation (WPP) approach becomes clear when considering the inherent advantages of the method, which will be of importance to the calculations for the Rydberg surface experiment. For one, it allows to equally regard the static and dynamic aspects of a problem, in which the latter can include fast and strongly nonadiabatic processes. Additionally, this approach permits to treat continuous and discrete spectra of a system in the same way. It furthermore allows to visualise the progression in *real-time* which intrigues as an effective way to demonstrate and discern the dynamics of the evolving system.

The WPP procedure is a numerical method that is based on the solution of the Cauchy problem for the time-dependent Schrödinger equation [70]

$$\begin{aligned} i\frac{\partial}{\partial t}\psi(\boldsymbol{r},t) &= H(\boldsymbol{r},t)\psi(\boldsymbol{r},t)\,, \\ \psi(\boldsymbol{r},0) &= \psi_0(\boldsymbol{r})\,. \end{aligned} \tag{2.4}$$

The time dependence is apparent since the Cauchy conditions constitute an initial-value problem having initial conditions in time rather than on a boundary in space. The stationary problem could be solved by calculating the autocorrelation function for an arbitrary initial state and the resonance features could subsequently be extracted via the Laplace transform.

The importance of the time dependence becomes evident when looking at the Landau-Zener model, or effect, for an avoided crossing of two eigenstates $|1\rangle$ and $|2\rangle$ whose Hamiltonian depends on a parameter, *e.g.* an (increasing) electric field F, exhibiting an intersection of the energy levels at some value of the field F_c in first approximation. These eigenstates, the diabatic

states, could be the most blue-shifted ($|1\rangle$) and most red-shifted ($|2\rangle$) state of neighbouring n-manifolds, as shown in Figure 1.2. The unrepelled energy levels beyond the crossing point extend monotonically increasing or decreasing as $|1'\rangle$ and $|2'\rangle$, respectively. If the levels are coupled by a perturbing interaction $\boldsymbol{\nu}$, the degeneracy of the energy levels will be lifted at F_c resulting in the two levels not crossing each other. Beyond the crossing point, the energy levels will then reverse their monotonicity with increasing field.

The probability P for a system starting in one state, to end in the *diabatic* state after, for example, a field sweep is given by [118]

$$P = \exp\left(-2\pi \frac{|\nu_{12}|^2}{\hbar(dF/dt)}\right) , \tag{2.5}$$

where ν_{12} denotes the matrix element of $\boldsymbol{\nu}$ connecting the two concerning states. If the system does not undergo a transition to an eigenstate of the initial unperturbed Hamiltonian it follows the energy curves of the coupled Hamiltonian *adiabatically*. Here, the outcome of the transition, either $P \to 0$ or $P \to 1$, depends on the coupling strength $|\nu_{12}|$ and the slew rate of the electric field dF/dt, *i.e.*, how quickly the field is ramped through the avoided crossing. The rate of change qualifies how gradual the system is changing; in an adiabatic process the eigenstate probability density adapts to a slowly changing environment.

Following the evolution of the Rydberg eigenstates in time as they approach the surface should be of great significance discerning the surface ionisation dynamics. Representatively, Sjakste *et al.* applied the wave-packet propagation technique to explain the apparent loss of electron polarisation in experimental results for Xenon [68, 71], which was not accounted for in former theoretical investigations. In general, as before, the newly introduced wave-packet technique is designed to calculate the ionisation distance as a Rydberg atom is brought close to a surface.

Another advantage of this method is the reduced computational time. Whereas complex scaling relies on a matrix diagonalisation (of size N) at every distance step with a N^3 dependence, the wave-packet propagation consists of matrix multiplications at every step whose number of computational operations only scale by N^2.

2.2.1 Procedural outline

In this time-dependent approach, the wave function $\psi(\boldsymbol{r}, t)$ at any time t can be calculated by the initial wavefunction, or wave-packet, $\psi_0(\boldsymbol{r})$ from Equation 2.4 by integrating the time-dependent Schrödinger equation. By finding a sufficiently accurate representation of the time evolution operator U, the discretised wavefunction $\psi(\boldsymbol{r}, t)$ can be obtained by numerically integrating $\psi(\boldsymbol{r}, t + \Delta t) = U(t + \Delta t, t)\psi(\boldsymbol{r}, t)$ [119].

A first approximation to simplify the overall symmetry of the problem is to explicitly consider the evolution and eventually transfer of one electron from the atom to the surface during the course of an collision process; what is usually referred to as a resonant charge transfer. In this one-electron treatment many-body effects are neglected, as is the possible Auger neutralisation for the remaining ion core. With this, the Hamiltonian in Equation 2.4, $H = T + V$, can be separated into

$$H(\boldsymbol{r}, t) = T(r) + V_H(r) + V^{(P)}(\boldsymbol{r}, t)\,, \tag{2.6}$$

where $T(r)$ is the radial kinetic energy operator, V_H the potential energy operator for the hydrogen atom and the perturbing potential energy operator $V^{(P)}$. The potential energy operator for the hydrogenic state is composed of the centrifugal potential expanded over a spherical basis, and the Coulomb potential V_C,

$$V_H(r) = \frac{l(l+1)}{2r^2} + V_C(r)\,. \tag{2.7}$$

Here, the eigenstates of the systems in solution of the hydrogen atom problem are separated as $\psi(r, \theta, \phi) = R(r)\Theta(\theta)\Phi(\phi) = R(r)Y_{lm}(\theta, \phi)$ with the normalised spherical harmonics Y_{lm} as solution for the spherical angles θ and ϕ, and a radial solution $R(r)$. The perturbing potential is comprised of an external field $V_F(z) = Fz$ and a cylindrically symmetrical surface potential $V_{surf}(z, \rho, t)$ as described in section 1.4,

$$V^{(P)}(\boldsymbol{r}, t) = V_F(z) + V_{surf}(z, \rho, t)\,. \tag{2.8}$$

This two-dimensional problem can be further simplified by fixing the atomic frame. Thereby, the motion of the ion core is fixed in place and the evolution of the electron interacting with the surface potential over time is translated into a function of distance where the distance D

between the surface and the fixed ion core is decreased in successive numerical steps,

$$D(t) = D_0 - v_\perp t\,, \tag{2.9}$$

where $v_\perp$ is the speed at which the surface approaches the atom as the perpendicular component of the collisional velocity of the atom; the surface is approached perpendicularly by the Rydberg atom. The advantage of this fixed frame is the reduced size of the grid that is necessary to capture the surface and atom together.

In the following, a technique will be introduced that was used by So *et al.* in [73]. In this work, the authors have developed a more efficient representation of the wave-packet as implemented by Sjakste *et al.* in [72]. So and co-authors have used a Coulomb-wave discrete variable representation (CWDVR) that will be presented in its outlines, for more information and further references to the details of implementation see reference [120].

Initial wavefunction discretised on a grid

The initial distance D_0 at time $t = 0$ is the separation of atom and surface with the initial wavefunction from (2.4) as $\psi_0(\boldsymbol{r}) = \psi_0(D_0)$. In the performed calculations the initial distance is chosen to be $D_0 = 6n^2a_0$, which is sufficiently large for no significant surface ionisation to occur as well as not mixing energy levels of the Rydberg state. The initial wavefunction is obtained by finding the eigenvalues through diagonalisation of the Hamiltonian in (2.4) before the onset of propagation, where the problem is discretised with a two-dimensional grid for r and θ. During this preceding step the angular coordinate is described through Legendre polynomials $P_l(\cos\theta)$ for $m_l = 0$ in a finite basis representation (FBR) which has been shown to be appropriate for large scattering distances [121]. In this representation, through a finite number of irreducible basis functions, the operator V_H is constructed from the eigenfunctions of the angular momentum, which are normalised spherical harmonics, and displays a diagonal form in it.

On the other hand, the perturbing operator $V^{(P)}$ is diagonal is in a discrete variable representation (DVR) which is appropriate for smaller scattering distances. In a DVR, the integrals of matrix elements that are represented through a set of basis functions have some relationship that allows to express these integrals as a finite sum over quadrature points. This is usually a

Gaussian quadrature, a numerical technique which factors an integral into a sum of weighted higher order polynomials over non-uniform (grid) points. The vector of values at these grid points can then be used as an equivalent representation to the basis expansion. From this viewpoint, it is evident that a (Gaussian) DVR is as accurate as a potential operator dependent on coordinates expressed in a FBR representation, the matrix elements are then given by the potential at the grid points. For an extensive review on the technique, see reference [122]. The $V^{(P)}$ operator is then transformed into the FBR representation by

$$V^{(P),\,FBR} = UV^{(P),\,DVR}U^{\dagger}\,, \tag{2.10}$$

where U is the transformation matrix which corresponds to the recurrence relation that generates the characteristic polynomial from a symmetric tridiagonal matrix [123].

For a lower number of grid points necessary than in the later introduced CWDVR grid, the radial component is expressed through a regularised Lagrange-mesh based on the zeros of Laguerre polynomials [124]. Here, with increasing radius from the ion core, the density of grid points decreases, treating the singularity at the center efficiently. After the initial eigenstates have been found, they are projected onto the CWDVR grid and propagated over time.

Coulomb-wave discrete variable representation

The novelty introduced by So *et al.* was to carry out the calculations more efficiently by choosing a grid that requires fewer grid points than the grids in previous studies [72]. The employed CWDVR grid is chosen to treat the singularity of the Coulomb potential similar to the DVR grid from before, with a variable density of grid points. The technique has been proposed by Dunseath *et al.* and is applied to treat the electron wavefunction in its radial coordinate [125].

Here, the grid points are defined as the positive roots of a positive energy reference function $v(r)$ that is a solution to the Coulomb differential equation,

$$0 = v(r)\left(\frac{d^2}{dr^2} - \frac{l(l+1)}{r^2} + \frac{2z}{r} + 2E\right)\,. \tag{2.11}$$

For convenience $l = 0$, $\kappa = \sqrt{E}$ and the center of the potential excluded; the solution $v(t)$ of

(2.11) can be expressed as [126]

$$v_\kappa(r) = \frac{1}{\sqrt{\kappa}} F_0(-z/\kappa, \kappa r)\,, \tag{2.12}$$

with the regular Coulomb wave function F_0. The positive zeros of $v_\kappa(r)$ represent a non-uniform sequence with a higher concentration of points towards the center and an almost regular distribution at large distances, the parameters κ and z vary the density of the grid. The parameter z can be interpreted as an effective charge of the ion core and alters the distribution of grid points around the singularity whereas varying the parameter κ is related to the energy of the Coulomb-wave and changes the near-uniform spacing of the grid points at larger distances; the radial grid is exemplified in Figure 2.1. Thereby, this grid is appropriate for the treatment of the process of surface ionisation, where bound wavefunctions close to the surface as well as free wavefunctions after ionisation of highly excited states, whose size scales with n^2, occur. With this gain in efficiency, it is possible to attain higher principal quantum numbers compared to the previous investigations.

In the CWDVR, the kinetic energy $T(r)$ matrix in (2.6) is given by a simple expression [125] and the potential energy matrix, which is diagonal in the radial coordinate, is given by the potential at the grid points $\{r_i\}$. The matrix elements are

$$T_{ij}^{CWDVR} = -\delta_{ij}\frac{W(r_i)}{6} + (1-\delta_{ij})\,\frac{1}{(r_i - r_j)^2}\,, \tag{2.13}$$

$$V_{ij}^{CWDVR} = -\delta_{ij} V(r_i)\,, \tag{2.14}$$

where $W(r_i) = \kappa^2 + 2z/r_i$. The Coulomb wavefunction and its first derivative, which constitutes the quadrature weights for the CWDVR, are computed by the `COULFG` subroutine by Barnett [127] through Steed's method. The zeros of the Coulomb wavefunction, which correspond to the grid points, are calculated with the Newton-Raphson method [128]. The whole FORTRAN code can be found on GitHub/softleygroup. Modifications to the original source used in [73] have been made to allow for running the code for different parameters without re-compiling and in an automated fashion looping through a set of parameters.

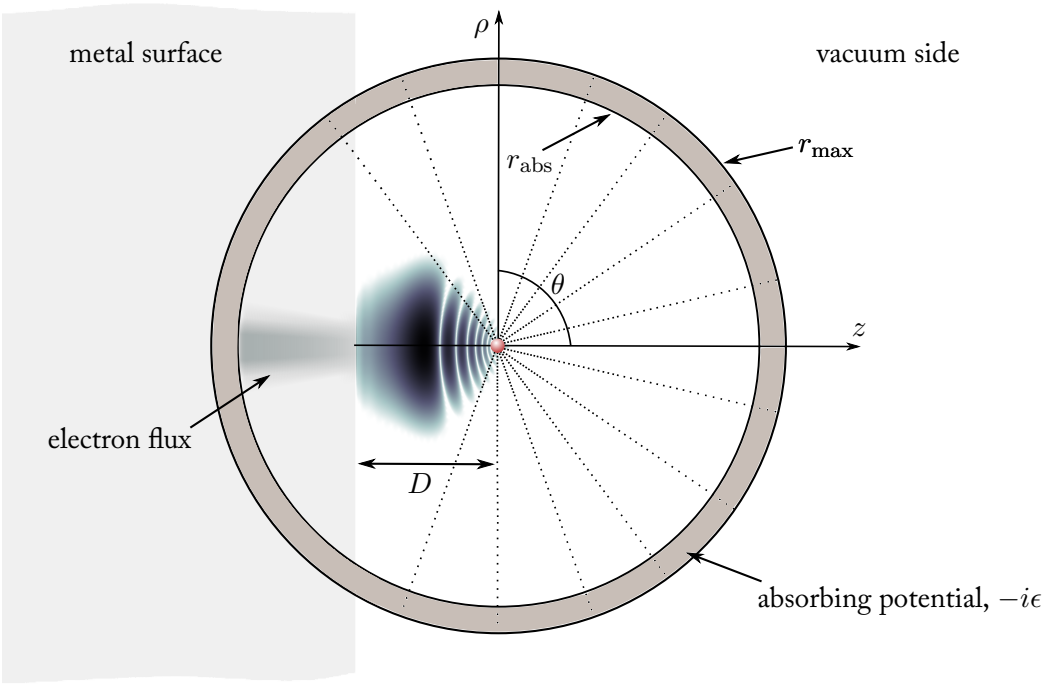

Figure 2.1: Schematic illustration of the CWDVR grid used for propagating a Rydberg electron wavepacket over time by decreasing the distance D between the fixed ion core (in red) and the surface approaching the Rydberg atom, so that $D < D_0$ with initial distance D_0. The radial points have a non-uniform distribution being spaced more closely towards the core. Depicted is a snapshot of a maximum red-shifted wavefunction for $n = 10, k = -9$ for $D \ll D_0$. It can clearly be seen, how the electron density is transferred into the surface. It also shows that the electron flux is not transmitted beyond the lower bound of the absorbing potential r_{abs} with the overall grid being truncated at r_{max}.

Time propagation

The formal solution to the time-dependent Schrödinger equation in (2.4) is

$$\psi(t + \Delta t) = e^{-iH\Delta t}\psi(t)\,, \tag{2.15}$$

with $\psi(t)$ being the initial wavefunction and $e^{-iH\Delta t}$ the propagator whose action generates the wavefunctions $\psi(t + \Delta t)$ at later times. For small time steps, as used in the WPP code ($\Delta t = 1\,a.u. = \hbar/(\alpha m_e c^2)$, with fine-structure constant α) where the time step equals the orbital period for the Bohr radius, the propagator can be approximated by the symmetrised split operator [129] based on Strang's representation of the exponential function of a sum of operators [130]

$$e^{-i(H-i\epsilon)\Delta t)} = e^{-i(V^{(P)}/2)\Delta t}\, e^{-i(T+V_H-i\epsilon)\Delta t}\, e^{-i(V^{(P)}/2)\Delta t} + \mathcal{O}(\Delta t^3)\,, \tag{2.16}$$

with the operators from Equation 2.6 in matrix representation and $-i\epsilon$ as the absorbing boundary potential, which is defined to fulfil the boundary conditions of the differential equation problem.

Absorbing boundary condition

Despite large grid sizes due to the orbital size of the involved Rydberg atoms, the grids have to be truncated. This artificial and non-physical boundary of the grid at r_{max} can lead to reflections of electron wavefunctions instead of a decay while propagating away from the ion core towards the vacuum. Mathematically, the Cauchy problem in (2.4) implies an outgoing boundary condition being imposed on the solution. To maintain the correct boundary condition and to suppress wavelets being reflected off the edge of the grid, an auxiliary absorbing potential can be added to the Hamiltonian which is in close vicinity to the numerical grid [131, 132, 133],

$$H = H - i\epsilon(r)\,, \tag{2.17}$$

where $-i\epsilon$ is the boundary potential as in Equation 2.16. The matrix elements of this potential with radial coordinate r are $-i\epsilon(r)h(r-r_{abs})$, with the lower boundary of the absorbing region r_{abs} and the Haeviside step function h. The complex potential in (2.17) has the form

$$-i\epsilon(r) = -i\frac{y(x)}{2}\left(\frac{2\pi}{\Delta r}\right)^2\,,\; x = \frac{c(r-r_{abs})}{\Delta r}\,, \tag{2.18}$$

where $\Delta r = r_{max} - r_{abs}$ is the width of the absorbing boundary region, r_{max} being the boundary of the numerical grid. The approximate form of $y(x)$ in (2.18) is given by

$$y(x) = \frac{4}{(c-x)^2} + \frac{4}{(c+x)^2} - \frac{8}{c^2}\,, \tag{2.19}$$

with $c \approx 2.62206$ [132, 133]. The width Δr is dependent on the momentum, the De-Broglie wavelength, of the outgoing wave. As in reference [73], Δr for a transmission-free boundary potential is set to $30\,\mathrm{a_0}$ for all calculations, which has been found to remove spurious wavefunction reflections. An illustration of the absorbing boundary region and the other grid parameters are shown in Figure 2.1

Full implementation and detection

Inspecting Equation 2.16, it becomes clear where the advantage of using a radial DVR and an angular DVR-FBR lays. Summing up the sections above, the time-independent matrix V_H is diagonal in the radial DVR and the angular FBR given as the potential at the radial grid points can be calculated before the propagation, T in the CWDVR is given by the simple expression in (2.13) and the absorbing potential is diagonal in the radial DVR. The time-dependent perturbation terms V^P which are dependent on both radial and angular coordinate is diagonal in either radial and angular DVR can be calculated by the FBR-DVR transformation matrix U from Equation 2.10 via

$$e^{-iV^P/2} = UD_V^e U^\dagger \,, \tag{2.20}$$

where D_V^e is a diagonal matrix with elements $D_{V_{ii}}^e = \exp\left(V_{ii}^{(P),\,DVR}\right)$ given by the exponential of the potential at the radial and angular grid points. After all components of the split operator in (2.16) have been evaluated the wavefunction representation is propagated by Δt.

The overall objective of these calculations is to capture the proportion of the electron density that is transferred into the approaching surface. For that, the whole electron density is monitored within the absorption region defined by r_{abs} and the surface boundary. When the derivative of this confined electron density is taken, it can be interpreted as an ionisation probability per unit length with respect to the atom-surface separation D,

$$P(D, v_\perp, F) = \frac{\Gamma(D,F)}{v_\perp}\, n(D, v_\perp, F)\,, \tag{2.21}$$

with the width Γ of a state, the population n of a state, the perpendicular component of the collisional velocity $v_\perp$ and at an electric field F. The change in population is monitored via flux autocorrelation relations [134].

With these representations, So *et al.* performed calculations for hydrogen up to principal quantum numbers of $n = 10$. Even though this is an improvement, it still doesn't permit a direct comparison of calculations and experimental data, since, as shown later, the lowest accessible principal quantum numbers in the Rydberg surface experiment are $n \geq= 20$.

2.3 Rydberg-Stark deceleration

Following the argument from section 1.6 when studying electronic properties of a surface material, the collisional velocity of the Rydberg atoms approaching a surface can have a twofold effect on the detected signal. First, the extraction efficiency of the resulting ion core is dependent on the momentum of the projectile, increasing the amount of detected ions when reducing the collisional velocity and secondly, the slower the projectile the longer it will be exposed to possibly higher ionisation rates at certain distances away from the surface that also increase the amount of detected ions.

With the experimental apparatus from section 1.6, the velocity of the impinging hydrogen atoms can be varied via selection from a distribution generated by the supersonic expansion. Another possibility is to have probe *and* target moving, leading to a low relative collisional velocity which has been successfully demonstrated for merged supersonic beams, achieving sub-Kelvin temperatures [135, 136]; collisional velocity and temperature for (scattering) particles can be related by $E_{kin}/k_B \sim T$ with Boltzmann constant k_B. This however, is not a viable approach for the Rydberg surface experiment since translating the surface sample at the velocity of the molecular beam is not permissible.

Even though the outer electron of a Rydberg atom is far removed from the ion core, the overall atom is still a neutral particle. Thereby, Rydberg atoms cannot be manipulated with a mere potential gradient, a uniform electric field [137], neither can their motion be controlled via laser cooling which requires cycling transitions [138]. However, particles with a dipole moment μ possess different potential energies

$$E_{\text{Stark}} = -\boldsymbol{\mu} \cdot \boldsymbol{F} \,, \tag{2.22}$$

that vary with the magnitude of the electric field F, so the energy of a certain eigenstate varies spatially if the electric field is inhomogeneous. The change in potential energy then results in a force K_{Stark} in the direction of decreasing energy of the eigenstate,

$$\mathbf{K}_{\text{Stark}} = -\nabla E_{\text{Stark}} = -\nabla(\boldsymbol{\mu} \cdot \mathbf{F}) \,. \tag{2.23}$$

For an eigenstate whose energy decreases with decreasing field, a low-field seeking state (LFS), a

decelerating force is exerted in the direction of decreasing field and, respectively, in the direction of increasing field for a high-field seeking state (HFS).

Hence, to remove kinetic energy from a moving LFS particle, the field distribution needs to be designed in a way that it increases in the forward direction of the projectile.

The principle of this Stark-deceleration has been first demonstrated for neutral dipolar molecules by Bethlem *et al.* in which a multitude of electrode stages at $\pm 10\,\mathrm{kV}$ are employed to slow down a beam of ground state CO from $225\,\mathrm{m\,s^{-1}}$ to $98\,\mathrm{m\,s^{-1}}$ [139]. Over the following years a number of groups have employed Stark decelerators with the aim, *e.g.*, to study cold ion-molecule reactions [140, 141].

Compared to the ground state, a Rydberg state exhibits an appreciable Stark shift at much lower fields, as can be seen in Figure 1.2 since the dipole moment scales with n^2. Theoretically, it has been proposed to employ Stark deceleration for atoms in Rydberg states by exploiting the large electric dipole moment, Rydberg-Stark deceleration, by Breeden and Metcalf [142]. It was first shown by Townsend *et al.* that a beam of Rydberg Krypton atoms can be deflected with potentials over an order of magnitude smaller than in a Stark decelerator [143]. The deflector in this case consisted of a pair or rods applied with opposite potentials. Following these first experiments, devices were developed that managed to reduce the velocity of a beam of hydrogen atoms by time-dependent fields so that they can subsequently be trapped [7, 144, 145]. Usually, these experiments are performed with highly polarised LFS states, as the blue-shifted $+k_{max}$ Stark state depicted in Figure 1.2, since Earnshaw's theorem does not allow for a maximum in an electric field whereas a minimum can be designed to facilitate trapping [146]. The magnitude of the dipole moment of a Stark state $|nk\rangle$ is given by

$$|\boldsymbol{\mu_{nk}}| = \frac{3}{2} nk\,. \tag{2.24}$$

Despite the aforementioned advantages of Rydberg-Stark deceleration, significant drawbacks exist that make this technique challenging. The finite lifetime of a Rydberg state does not permit to employ these states in very long deceleration cycles or storage times. The potential sequences have to be tailored so that the lifetime is not exceeded but also that the involved field strengths do not exceed the critical value for field ionisation which translates into a minimum time to remove excess kinetic energy. Also, the field strength cannot exceed the Inglis-Teller

limit. Beyond this field value, avoided crossings can exist if non-hydrogenic species are used which results in a loss of polarisation in an electric field. Experimentally, the excitation in a dense manifold requires laser systems with low bandwidth and the sensitivity to electric fields correspondingly demands a high accuracy of the involved electronic components to generate field distributions as conceived.

2.3.1 Electric field distributions

When designing electric fields in free space for a static distribution of charges, they must obey Maxwell's equations, particularly the divergence theorem or Gauss' law $\mathrm{div}F = \vec{\nabla} \cdot \vec{F} = \rho/\epsilon_0$ by which the electric field F is related to the charge density ρ with permittivity of free space ϵ_0. The electric field can be written as the gradient of a potential $\vec{F} = -\nabla V$ and by combining these two the potential in free space $V(x, y, z)$ can be found as a solution to the Laplace equation

$$\Delta V = \vec{\nabla}^2 V = \frac{\partial^2 V}{\partial x^2} + \frac{\partial^2 V}{\partial x^2} + \frac{\partial^2 V}{\partial x^2} = 0\,. \tag{2.25}$$

The calculation of an electric field would however require a potential to be expressed in an analytical form which is mostly not the case in an arbitrarily chosen geometry, it is therefore necessary to solve (2.25) numerically. For this, the commercial software SIMION® is used, employing finite difference methods in order to find solutions to boundary value problems for partial differential equations in which the electrode (charge distribution) is discretised on a finite element mesh. During the solving of (2.25) for a given set of defined electrode points, optimized successive overrelaxation (OSR) and multimesh methods are used to determine the potential on the non-electrode points. The linearity of the Laplace equation ensures that the solution remains valid when different potentials are set to the electrode grid points.

During the modelling of the geometries every set of grid points belonging to a single electrode j is assigned a potential value of $j \cdot 1$ V where the solver generates a corresponding potential array file per electrode. The respective potential array files are read into a Python object from which the potential and field values can be extracted in Cartesian coordinates. The respective potential arrays are scaled for a set electrode potential and summed to get the overall potential in free space at position (x, y, z).

Principally, a lot of the desired calculations, such as numerical particle trajectory simulations

for ions, can be done within the SIMION® workbench environment but it should be evident that the versatility and capabilities of a programming language cannot be matched. The author explicitly encourages the use of the Python programming language.

2.3.2 Numerical trajectory simulations

To assess the experimental performance of a decelerator geometry that is to be combined with the Rydberg surface apparatus, the path of the Rydberg atoms is simulated as they pass through the device and interact with the electric fields generated by it. For these calculations, the essential parts of the surface experiment, the electrode holding the extraction mesh and the surface mount, and the decelerator construction are included in the geometry that is built in SIMION®. Here, due to RAM constraints of the software, the spatial resolution is set to one grid unit per 0.1 mm.

The discretised electrode grid includes all relevant components of the apparatus from the point of laser intersection onwards where the hydrogen atoms are excited to a Rydberg state. Parts of the apparatus which generate the gas packet are not included and the spatial and velocity distribution of the Rydberg atoms will be generated separately from the potential grid calculations based on a statistical approximation.

Initial supersonic gas packet

In the trajectory simulations an initial cloud of particles is generated with a Monte Carlo approach for a uniform distribution of positions with the constraints of the capillary into which the seeded ammonia expands. The velocity distribution is created with a normal distribution where the mean velocity is only non-zero for the forward (z) direction of the gas packet which is set to the maximum value determined experimentally for the different carrier gases of the supersonic expansion. The standard deviation in each orthogonal direction is set equally according to a previously determined temperature where the predominantly used carrier gas helium has a temperature of 20 K [120].

It needs to be noted that the chosen normal distribution does not accurately describe the physical process during expansion of a gas through a nozzle. Here, two separate cases can be treated dependent on the size of the orifice D and the mean free path of the gas λ_0 [147,

148]. When $\lambda_0 \gg D$ the number of collisions while escaping the reservoir at temperature T_0 reaches zero. The resulting velocities are described by a Maxwell-Boltzmann distribution which is characterised by the molar mass m and temperature T_0. In this case, the internal degrees of freedom of the escaped molecules, rotational and vibrational, are equal to the molecules in the container. In the other case, when $\lambda_0 \ll D$, the escaping molecules undergo a multitude of collision leading to an adiabatic transfer of the enthalpy of the gas in the reservoir into kinetic energy of the mass flow under ideal conditions of a stationary flow. Under these conditions the mass flow has a velocity v that is greater than the local speed of sound a of an ideal gas, hence supersonic, expressed by the Mach number

$$M = v/a = v/\sqrt{\gamma k_B T/m}\,, \tag{2.26}$$

with $\gamma = C_P/C_V$ as the ratio of heat capacity at constant pressure and volume. For a reservoir at constant pressure and temperature, the mean longitudinal velocity $\overline{v_z}$ of the gas packet at a distance L from the orifice can then be expressed as

$$\overline{v_z} = M(L)\sqrt{\frac{\gamma k_B T(L)}{m}}\,, \tag{2.27}$$

where $T(L)$ is the translational temperature [149]. The Maxwell-Boltzmann distribution from the effusive beam is extended by the mean forward velocity which leads to a narrowing of the half-width of the distribution of velocities v, for $n = 2$ expressed by

$$f_n(v) = N_n v^n \exp(-(v - \overline{v_z})^2/\alpha^2)\,, \tag{2.28}$$

with a normalisation factor N_n and $\alpha = \sqrt{2k_B T(L)/m}$ [149]. For the index $n = 3$ the distribution pertains to the flux density.

The dependence of the centerline Mach number M for a free flow on the distance L from the orifice was empirically determined as

$$M(L) = A\left(\frac{L}{D} - B\right)^{\gamma-1} - C\left(\frac{L}{D} - B\right)^{-\gamma+1}\,, \tag{2.29}$$

with $A = 3.26$, $B = 0.075$, $C = 0.61$, $\gamma = 5/3$ for a monatomic gas and $A = 3.65$, $B = 0.4$,

$C = 0.82$, $\gamma = 7/5$ for a diatomic gas [150]. The translational temperature of the expansion can be expressed in terms of the Mach number as [148]

$$\frac{T(L)}{T_0} = W^{-1}\,,\; W = 1 + \frac{\gamma - 1}{2} M(L)^2\,. \tag{2.30}$$

The temperature reduces until a terminal Mach number M_∞ given by

$$M_\infty = 133\,(\rho_0 \cdot D)^{(\gamma-1)/\gamma} \tag{2.31}$$

is reached [151]. As for the translational temperature in Equation 2.30, other quantities can be derived as a function of the position of the expanding Mach disk, such as the number density

$$\frac{n(L)}{n_0} = W^{-1/(\gamma-1)}\,. \tag{2.32}$$

For a sufficiently cooled expansion when $T \ll T_0$ is reached, the maximum of the velocity distribution, the terminal velocity is [147]

$$v_\infty = \sqrt{\frac{2k_B}{m}\left(\frac{\gamma}{\gamma-1}\right) T_0}\,. \tag{2.33}$$

The equations above are applicable for the expansion of an atomic or diatomic gas. If the species of interest is comparatively light, an effective expansion can be achieved by adding a fraction of it to a gas mix mainly made up of a heavier carrier gas which has a lower longitudinal velocity; this process is called *seeding*. The seeded species is then cooled by collisions with the carrier gas and, under the condition of high source pressure, the supersonic expansion can be equally described with the formalism for a pure gas when molecular weight and heat capacity of the gas mixture are taken as weighted averages [152].

Depending on the pressure of the source chamber, the terminal Mach number for a seeded beam of helium in the Rydberg surface experiment varies from ∼75 to 100 whereas at the position of photolysis in the capillary a Mach number of ∼20 is reached. At the same position the temperature of the beam is ∼2 K which is in stark contrast to the experimentally determined 20 K. A further discussion on this follows in the subsequent chapter. The number density n at that point is about $5 \times 10^{16}\,\mathrm{cm}^{-3}$, n_0 was estimated for an ideal gas.

To attain realistic conditions for the cloud of Rydberg atoms that will serve as a starting point for the trajectory simulations in an electric field at discrete time steps, the gas expansion is simulated before the onset of the time-stepping and then loaded into the potential array. The gas packet with number density n is used for the initial distribution in the capillary which is propagated through the skimmer ($1\,\mathrm{mm}$ diameter) towards the interaction region where the final exclusion of particles is done for the cylinder that is formed by the counter propagation laser beams which intersects the beam axis non-orthogonally. With this method, the resulting number of particles at the point of intersection is roughly 10^1 to 10^2 ($< 0.001\%$ of N_{init} for helium seeded) which is too low to receive a satisfactory amount of particles for the consecutive propagation in an electric field, to low to attain a meaningful analysis. Therefore, the resulting particle probability distribution was estimated and reconstructed to receive a significantly higher number of particles within the same laser excited volume and with the same spread in positions and velocity.

The following scheme is demonstrated for the x-component of the gas packet but is analogous for (y, z) and was implemented in MATLAB®. First, the position and velocity data is transformed to the copula scale by estimating the probability density function using a kernel smoothing estimator of the cumulative distribution function (cdf), where a copula is the joint distribution of random variables.

```
x = rLasersIntercept(1,:);
vx = vLasersIntercept(1,:);

u = ksdensity(x, x, 'function', 'cdf');
vu = ksdensity(vx, vx, 'function', 'cdf');
```

The next step is to fit the copula to the transformed positions and velocities as a multivariate t-distribution returning a matrix $\hat{\rho}$ of the estimated linear correlation parameters and a scalar parameter $\hat{\nu}$ for the estimated degrees of freedom. The fitting is performed with a maximum likelihood method.

```
[rhohat, nuhat] = copulafit('t', [u v w vu vv vw], 'Method', 'ML')
```

From these linear correlation parameters, a random distribution with N samples is created and transformed back to the original scale of the position and velocity data in three dimensions.

```
r = copularnd('t', Rho, nu, N);
ur = r(:,1);
vur = r(:,4);

xn = ksdensity(x, ur, 'function', 'icdf');
vxn = ksdensity(vx, vur, 'function', 'icdf');

rLasersIntercept = zeros(3, N);
vLasersIntercept = zeros(3, N);

rLasersIntercept(1,:) = xn;
vLasersIntercept(1,:) = vn;
```

With this procedure the number of initial particles for the time stepping sequence is set to 1 to 5×10^4 particles.

Time stepping method

The decelerator device for Rydberg atoms in chapter 6 operates with a time-dependent potential sequence. Since no analytical solution exists to the electric field distribution in space and the differential equations of motion in time, the problem is discretised also on the time scale and solved numerically. With the initial conditions ($\mathbf{r_0}$, $\mathbf{v_0}$) from the gas expansion, the positions $\mathbf{r}$ and velocities $\mathbf{v}$ are updated with the Störmer-Verlet method with a single coordinate given by

$$\begin{aligned} r_i(t+\Delta t) &= 2r_i(t) - r_i(t-\Delta t) + \frac{K_i(t)}{m}\Delta t + \mathcal{O}(\Delta t^4)\,, \\ v_i &= \left(r_i(t+\Delta t) - r_i(t-\Delta t)\right)/2\Delta t\,, \end{aligned} \tag{2.34}$$

where K_i is calculated by (2.23). This method for determining the positions numerically has the advantage of being very accurate and easy to implement as well as being *symplectic* which means that the algorithm preserves the phase-space structure of the Hamiltonian, the nearby Hamiltonian in time is approximately conserved [153, 154].

The force at every time step and hence the electric field distribution is calculated by adjusting (scaling) the individual electrode potentials in the potential array so that per time step the electric field is static. The time step is set to 10 ns and found to be sufficient for convergence. The electric field at an arbitrary position is derived from the potential that is interpolated between

grid points with a central difference scheme. Since the force exerted on the dipole is calculated as the gradient of the electric field, the second derivative of the potential, it takes considerably more time than merely extracting the electric field distribution from the potential array object.

The great advantages of Python in its ease of use and comprehensiveness for scientific usage comes at a price by its inherent makeup as an interpreted language. In contrast to a compiled code, as in C/C++ for example, where the high-level source code is translated into machine/binary code as a whole into an executable, an interpreter translates the source code one statement at a time. The downside of this is the greater time of executing the instructions of the source code.

Here, the calculation of the forces contributes the majority to the runtime when the array of particles is propagated. In order to reduce the execution time, the majority of the code, like file handling and setting up and dealing with particle arrays, is kept in Python whereas the parts intense in CPU load are ported to C. This is done via the Python module `ctypes` which allows to call foreign functions and dynamic-link libraries (DLL) that are compiled in the C language. The code in this manner will be outlined briefly for a single coordinate `x` and can be found in full under GitHub/softleygroup.

The potential array object is initiated and the corresponding files read into the object in Python and methods necessary to retrieve information from it are remapped in C by calling functions defined in a `.c` file via C data types on the `acc` object that holds pointers to memory (re-)allocated to the single potential arrays.

```
import ctypes
from ctypes import c_double, c_ulong, c_uint
c_double_p = ctypes.POINTER(c_double)

self.potArray = EField(folder, nElectrodes, scale)

acc = accelerator()
acc.set_npas(len(voltages))
acc.set_pasize(self.nx, self.dx)
for n, p in enumerate(self.pas):
    acc.add_pa(n, p.potential.ctypes.data_as(c_double_p), voltages[n])

def helper(xx):
    dE = np.zeros((xx.shape[0]), dtype=np.double)
    a.getFieldGradient(xx.shape[0], xx.ctypes.data_as(c_double_p), \
                       dE.ctypes.data_as(c_double_p))
    return dE

self.getFieldGradient = helper
```

When the `acc` object is created the code in the `.c` file gets compiled into `.so` shared object files and the data types declared.

```
class accelerator(object):

call([compiler, '-shared', target + '.o', '-o', target + extension], \
     cwd=localdir)

self.acc = ctypes.cdll.LoadLibrary(libpath)

self.acc.getFieldGradient.argtypes = [c_uint, c_double_p, c_double_p, \
                                      c_double_p, c_double_p]
self.acc.getFieldGradient.restype = None
self.getFieldGradient = self.acc.getFieldGradient
```

The calculation of, for example, the field gradient for a single particle position is then determined in C and returned to the main loop in Python to calculate the forces on an array of particles that gets propagated over time.

```
static void getSingleFieldGradient(const double x, double * result)
{
    double E0[1];
    double dx1[1], dx2[1], dy1[1];

    getSingleField(x, &E0[0]);
    double normE = sqrt(E0[0]*E0[0]);

    getSingleField(x+hx, &dx2[0]);
    getSingleField(x-hx, &dx1[0]);

    result[0] = (E0[0]*(dx2[0] - dx1[0]))/normE/dx;
}
```

With this approach, the runtime of a simulation for $\sim 5 \times 10^4$ particles could be reduced by a factor of ~ 300 which introduced a significant convenience simulating diverse parameters of the decelerator device over a finer range of values.

The wave-packet procedure discussed here is applied to propagate a hydrogen atom towards a gold surface for a set of collisional velocities and the results reported in chapter 5. The particle trajectory simulations are used in chapter 6 to characterise the performance of the decelerator device.

Experimental procedure and apparatus characteristics

When the process of surface ionisation is assessed for a range of quantum numbers to determine a possible sensitivity to the electronic structure of a surface, as in section 1.6, it is of importance to maintain constant experimental conditions and signal magnitudes over time for accuracy and reproducibility. This is especially crucial when data recording is run for a range of values for one parameter over extended periods. A strong motivation in the context of this work was therefore to reduce ambiguities that might arise from one surface ionisation signal measurement to another. This was done by replacing or optimising specific components of the experiment. The other focus in this chapter will be on the measures that were taken to duplicate the excitation scheme for Rydberg states at a different position in the apparatus to accommodate the decelerator design as introduced in section 6.1.

3.1 Experimental apparatus to study surface ionisation

In the hydrogen Rydberg atom surface experiment, H atoms are produced by photodissociation of a supersonic beam of ammonia. In a supersonic expansion, or molecular beam, a high pressure reservoir equipped with a small orifice (valve) is briefly opened ($\sim$100 µs) towards a high vacuum chamber. When the high pressure gas passes through the valve the molecules undergo frequent collisions which results in an adiabatic cooling of the expanded gas which has a narrow velocity distribution around a mean [155]. This velocity distribution is characterised by a possible temperature of less than 1 K while the lab-frame velocity is controlled by seeding in a rare gas.

The expansion in this experiment is released into a quartz capillary that is mounted in front of the pulsed supersonic valve [156] at the focus of an ArF excimer laser operating at 193 nm

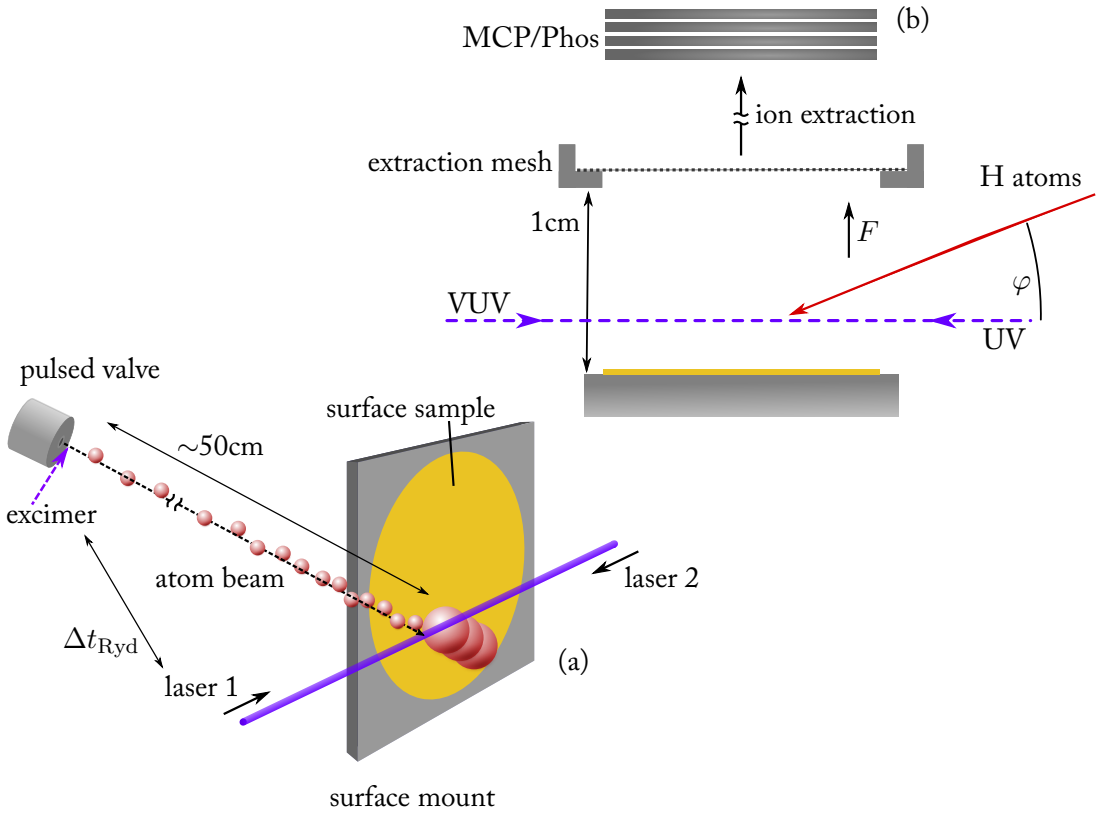

Figure 3.1: Experimental apparatus as described in the text. Counter propagating laser beams for Rydberg excitation intersect a beam of hydrogen atoms from supersonic expansion in front of the surface at a distance of $\sim 2-3$ mm in (a). The atom beam is directed towards the surface at an angle of $\varphi = 20°$ and the pulsed supersonic valve located at approximately 50 cm from the interaction region. The capillary for photodissociation of ammonia mounted to the pulsed valve and the skimmer placed at 3 cm behind the capillary are not shown in the drawing; see Figure 3.3 for the capillary mounted to a plate in front of the pulsed valve. The velocity of the Rydberg H atoms can be set by varying the delay of the Rydberg excitation relative to the excimer for photolysis (Δt_{Ryd}). The surface can be applied with a potential bias for Stark state selection in an electric field F in the interaction region in (b). A mesh grid electrode sits parallel to the surface mount for ion extraction towards a micro-channel plate/phosphor-screen detector (the full electrode stack used for ion extraction is not not included for clarity).

which dissociates ammonia to produce hydrogen atoms. After the expansion, which cools the H atoms to the carrier gas temperature, the beam passes through a skimmer mounted between two differentially pumped chambers and travels for about 0.5 m towards the interaction region.

In outline, Rydberg excitation is achieved with two counter propagating (pulsed) lasers using a two-photon resonant transition via the $2p$ intermediate state to Rydberg states in the range $n = 20$ to 40. The two lasers are frequency doubled dye lasers that are pumped by a Nd:YAG laser where the second photon (UV) wavelength of the transition ranges from 365 nm to 379 nm. The vacuum ultraviolet light (VUV) is produced by focussing one laser beam into a mixture of krypton and argon. This rare gas mixture enables third harmonic generation to pro-

duce the L_α radiation at $121.6\,\mathrm{nm}$ that is collimated into the interaction region with a lithium fluoride lens. The time delay between the photodissociation and the Rydberg excitation can be adjusted which allows selection of different parts of the velocity distribution. The long path between the capillary and the interaction region and the width of respective laser pulses $<10\,\mathrm{ns}$ gives a velocity resolution of $\sigma \sim 1\%$. An overview of the experimental apparatus is shown in Figure 3.1, for further details on the experimental procedure see sections 3.2 to 3.4.

The molecular beam is directed at the surface at an angle of 20°, in principle this can be varied but was kept fixed here. The counter propagating laser beams cross the hydrogen beam about $2\,\mathrm{mm}$ to $3\,\mathrm{mm}$ in front of the target. Ions are extracted by a mesh electrode that is parallel to the surface at a distance of $1\,\mathrm{cm}$, followed by a stack of electrodes to direct the collected ions towards a multichannel plate and phosphor-screen detector. The field and surface ionisation signals are separated in time by integrating TOF traces like the example shown in Figure 1.8 over the different arrival times. The extraction field is scanned from near-zero to above the onset of field ionisation and the maximum magnitude of the gated and integrated field ionisation signal above threshold is used to normalise the surface signal.

3.2 Molecular beam source

The pulsed nozzle that creates the supersonic cloud of atoms is operated at a frequency of 10 Hz where the synchronised trigger pulse for this event serves as the initial time reference t_0 for all other devices of the experimental sequence at t_0. The vacuum chamber into which the gas from a (high pressure) reservoir is released during the supersonic expansion, the "source chamber", is pumped by a turbomolecular pump and operated at a base pressure of $10^{-8}\,\mathrm{mbar}$. It is connected to a differentially pumped chamber separated by the skimmer before accessing the main sample chamber. All vacuum chambers in the experiment are pumped separately by respective turbomolecular pumps.

Any potential optimisation for an experimental parameter is usually done by monitoring the magnitude of the signal received from field ionisation of a Rydberg state. The optimal compromise of signal magnitude and stability, and pressure in the sample chamber was found for an operating pressure of the source chamber at $10^{-5}\,\mathrm{mbar}$ at a fixed current pulse width that is applied to the coil which retracts the poppet from the orifice. The pressure of the source chamber

is used here as an indirect measure of the molecular beam density. With the existing control unit however, it proved impossible to operate the valve so the source pressure remains constant; noticeable fluctuations of the field ionisation signal were observed over the course of minutes and hours which means that the density of each gas pulse is fluctuating. This becomes particularly problematic when single scans take several minutes or when a set of scans is launched where the data recording and evaluation presumes a uniformity in the experimental conditions.

3.2.1 PID pressure control

Figure 3.2 illustrates how the pressure is varying over time when the current control is fixed, also showing how this affects the magnitude of the field signal over time. In order to overcome this issue, the controller for the pulsed valve was replaced with an instrument that can be interfaced with the analogue voltage output of a data acquisition (DAQ) device. The output of the DAQ device is then programmed to act as feedback controller that regulates the analogue output by comparing the reading of a pressure gauge to a setpoint via a PID algorithm. With this approach, the output of the controller $u(t)$ is determined through the error ϵ, the difference between the setpoint and the current pressure, by calculating the integral and derivative of the error signal,

$$u(t) = K_P\epsilon(t) + K_I \int \epsilon(t)\,\mathrm{d}t + K_D \frac{d\epsilon(t)}{dt}\,, \tag{3.1}$$

with the proportional (K_P), integral (K_I) and derivative (K_D) gains. The PID controller was tuned to quickly adjust to the setpoint for a range of pressure by finding the gains heuristically. A satisfactory performance was achieved for the gains set to $K_P = 0.02$, $K_I = 0.02$ and $K_D = 0.008$. The typical behaviour for a PID controlled pressure source can also be seen in Figure 3.2, combined with a large reservoir for the seeded gas and operated at a pressure of $5\,\mathrm{bar}$, signal stability could be achieved over the course of hours before being limited by other factors. The long-term stability gets more important during measurements for a sequence of collisional velocities as carried out in sections 5.2 and 4.5, allowing more conclusive comparison between single data sets.

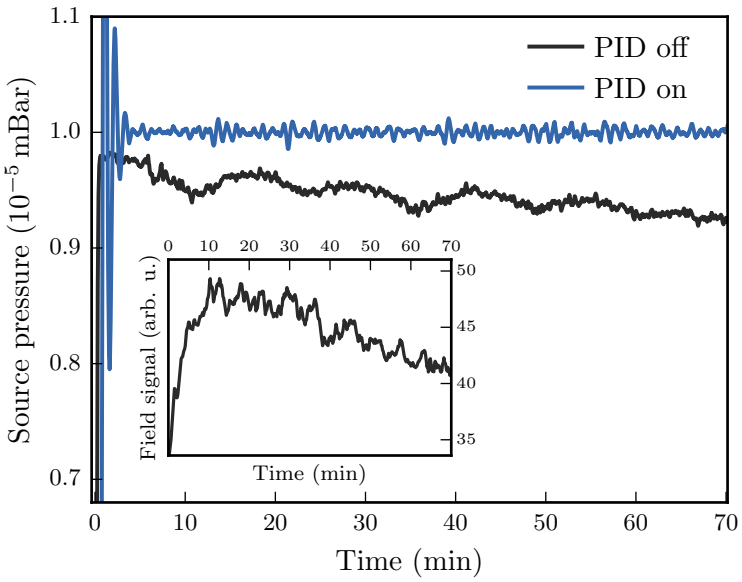

Figure 3.2: Vacuum pressure of the (source) chamber that is exposed to the supersonic expansion of a pulsed nozzle. The magnitude of the field ionisation signal is maximised by adjusting the amount of gas being released from the valve. Without the PID control loop being engaged to regulate the current driving the valve current, the source pressure is not constant over time (setpoint: 10^{-5} mbar). How this in turn affects the amount of integrated surface signal is exemplary shown in the inlet. In the initial phase for the activated control circuit (in blue) it can be seen how the feedback mechanism is settling the pressure adjustment.

3.2.2 Translational gas packet temperature

As laid out in section 2.3, the translational temperature for a beam of ammonia seeded in helium should theoretically be about 2 K at the end of the capillary but was previously determined to be about 20 K [120] from the gas packet expansion rate during free-flight to the laser interaction region. Even though the velocity selection through Rydberg excitation of a part of the gas packet via the pulse widths of the pulsed lasers of 10 ns (Excimer) and 3 ns to 5 ns (Pulsed dye lasers) results in a low velocity spread of $\sigma_v \sim 1\%$ [69], it does not reflect the translational temperature of the cloud of Rydberg atoms. A high temperature is not of significant concern for the surface experiment but is, as usual, of vital interest for the particle acceptance of a decelerator where, a reduced forward velocity of the initial gas packet is beneficial for increased acceptance.

It was considered in reference [120] that the quality of the hand-cut (sharp-edged) capillary in which the photolysis of ammonia occurs has a significant influence by introducing turbulences to the gas flow through the capillary. In trying to assess the influence of the capillary it was replaced with one of the same (quartz glass) material but with a tapered and smooth edge towards the skimmer, which would essentially be able to aid a second expansion after photolysis. This

capillary shape, as shown in Figure 3.3, is considered to be an ideal shape for a valve nozzle. In reference [157] it was found that for a tapered shape the supersonic disk exiting the orifice has a planar flow compared to a straight and sharp-edge orifice, where greatest differences are observed at short distances while the expansion dynamics in the far field are very similar, independent of the nozzle shape.

The expansion in this apparatus is not fully finished at the position of the capillary and skimmer, the terminal Mach numbers from section 2.3 are reached at distances of $L = 11.2\,\mathrm{cm}$ ($p_0 = 2\,\mathrm{bar}$) and $L = 18.2\,\mathrm{cm}$ ($p_0 = 5\,\mathrm{bar}$) which is far beyond the skimmer position at $L = 4.5\,\mathrm{cm}$. When the terminal Mach number from Equation 2.31 is reached, the gas is considered to be *frozen* along the expansion axis, the number of collisions within the gas constituents being insufficient to facilitate further cooling through collisional energy transfer. Several different initial pressures p_0 were tested from $2\,\mathrm{bar}$ to $6\,\mathrm{bar}$ but no appreciable differences in the field signal magnitude were observed apart from routine fluctuations. This implies that the dynamics of the gas expansion are mainly affected by processes in the capillary during and after photolysis rather than factors that are considered in the theory of supersonic expansion.

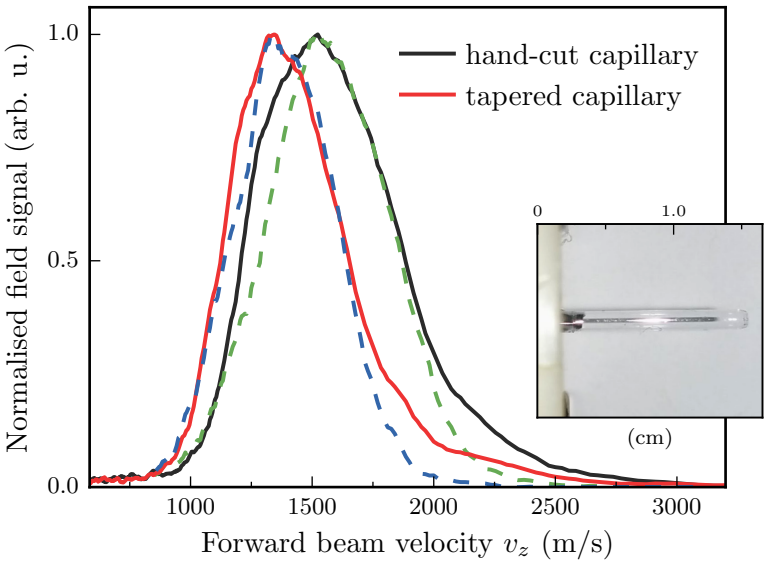

Figure 3.3: Amount of field ionisation signal for velocity selection from the supersonic gas packet (full lines) for different capillaries in which the hydrogen is produced through photodissociation. The capillary mounted to the face plate of the valve is shown in the inlet and has a tapered end instead of a rough, sharp edge. The experimental traces are overlaid with a trajectory simulation to estimate the temperature of the gas packet (dashed lines).

Figure 3.3 shows a comparison of the velocity distribution of the Rydberg atoms recorded via field ionisation for the sharp-edged and the tapered capillary. It can be seen, that the velocity

with the highest probability is reduced for the ideal capillary, from $1523\,\mathrm{m\,s^{-1}}$ to $1345\,\mathrm{m\,s^{-1}}$. Additionally, the temperature of the velocity distribution of the atoms is simulated with trajectories for a statistically created gas packet with an initial velocity spread $\sigma = \sqrt{kT/m}$. The temperature of the sharp capillary is here evaluated as 32 K and the tapered version as 22 K in contrast to the theoretical value of $\sim 2\,\mathrm{K}$. The maximum of the velocity distribution (tapered capillary), however, is close to the terminal velocity $1369\,\mathrm{m\,s^{-1}}$ from (2.33). The velocity spread in Figure 3.3 is determined from a signal recorded at polar angles to the beam axis, thereby probing the longitudinal temperature only secondarily. Furthermore, no discernible effect on the velocity distribution could be observed for different reservoir pressures. In conclusion, this suggests that the transverse dynamics of the supersonic expansion are altered through processes in the capillary.

The theoretical approach from section 2.3, after all, does not account for the geometry used here, a capillary mounted in front of a nozzle opening, and it is difficult to assess how this might affect the expansion. The hydrogen atoms are produced via excimer laser photodissociation

$$\mathrm{NH_3} + h\nu \rightarrow \mathrm{NH_2} + \mathrm{H}\,, \tag{3.2}$$

where the laser is focussed onto the end of the capillary. For photodissociation of larger molecules it was shown that the rotational cooling achieved low temperatures to attain satisfactory spectroscopic resolution [156]. Up to the point of photodissociation heavier ammonia is seeded in lighter helium. The case of seeding a heavier species in a light carrier gas has been studied intensively showing that the parallel temperature of the seed exceeds the one of the carrier [158]. In this case, the velocity mismatch could also be explained by a *velocity slip* in which the heavier gas is accelerated by the more abundant lighter carrier gas but does not reach the full velocity of the carrier [148, 152]. However, the heavier ammonia is only the precursor for the production of the detected hydrogen which is lighter than the carrier gas. This reverse case on the other hand, has received significantly less attention but experimental results and theory indicate that the parallel temperature of the lighter seeding gas is lower than the carrier gas [159, 160] which does not match the observations here nor does the assumed setup therein match the one of the expansion here.

For mixtures of heavy and light gases it was shown that the heavier particles concentrate on

the beam axis and the lighter particles expand radially at a higher velocity [161] which could be translated to a lower cooling efficiency for the lighter species. During the laser dissociation, the split-off hydrogen is likely to gain momentum which, when combined with the lesser equilibration with the carrier gas in the following expansion throughout the capillary, results in higher off-axis temperatures. The lower temperature observed with the tapered capillary could be explained by introducing a second, improved, stage of expansion when the gas exits the end of the capillary allowing better equilibration with the background gas mixture after photodissociation.

3.3 Rydberg excitation

The radiation required to excite ground state hydrogen atoms to a selected Rydberg state $|nkm\rangle$ has wavelengths in the ultraviolet (UV) and vacuum ultraviolet (VUV) range. The production of such radiation being coherent and tunable over a range of energies is not without challenge and is usually not directly attainable due to wavelength restrictions of optical components. An excimer laser, as used in the production of hydrogen can only be operated in a narrow wavelength window for a specific gas mixture and produces a beam of poor optical quality.

At low light intensity, the refractive index of optical media displays a linear response whereas at higher energy densities materials can deviate from this and display a nonlinear behaviour which can be utilised for frequency conversion. Within crystalline materials and rare gases, second (frequency doubling) and third (frequency tripling) harmonic conversion can be achieved respectively to produce the desired wavelengths [162]. Here, the dielectric polarisation $\mathbf{P}$ has contributions from higher order n, nonlinear, responses to the electric field $\mathbf{E^n}$ with electric susceptibility of the material χ^n.

3.3.1 VUV photon generation

In our apparatus, used for the measurements in section 1.6 and displayed in Figure 3.1, the excitation is carried out with a resonant two-photon transition. The VUV photon is produced through two steps of frequency conversion. While efforts to develop commercial VUV light sources continue to be made [163], to obtain wavelengths as low as necessary for the production of Lyman alpha (Ly-α) other measures have to be taken in our experiment. First, the Nd:YAG pumped dye laser produces UV radiation through second harmonic generation in a birefringent

beta barium borate (BBO) crystal at room temperature [164, 165] where a Pellin–Broca prism arrangement separates the wavelength fundamental. The beam is then focussed into a container filled with a mixture of krypton and argon that is directly mounted to the experimental chamber sealed by a lithium fluoride lens leaving the initially frequency doubled beam exiting the gas cell uncollimated while focussing the Lyman alpha radiation produced from frequency tripling in the rare gas mixture.

Third harmonic generation in rare gases

Generating frequency tripled light in a rare gas is a convenient way to produce tunable VUV radiation [166, 167]; the nonlinear process in the gas is induced through the high power density that a pulsed laser is able to deliver (typical pulse energy $15\,\mathrm{mJ}$ to $20\,\mathrm{mJ}$) and which is focussed into the rare gas cell ($f_{\mathrm{UV}} = 150\,\mathrm{mm}$ to $175\,\mathrm{mm}$). The tunability of the VUV output is demonstrated in Figure 3.4 for the $1s \rightarrow 2p$ transition in hydrogen as well as the spectroscopic selection of one of the fine structure doublet states through spin-orbit interaction which lifts the two $2p$ levels $^2\mathrm{P}_{1/2}$ and $^2\mathrm{P}_{3/2}$.

The data in Figure 3.4 is gathered from recording an ionisation signal with only the VUV laser intersecting the hydrogen atoms. Since the fundamental UV photons ($E > E(2p \rightarrow n = \infty)$) are not separated from the frequency tripled photons it is conceivable that a direct ionisation is occurring either through an excitation beyond the ionisation level E_{ion} via a VUV and a UV photon ($\mathrm{H} + h(\nu_{\mathrm{VUV}} + \nu_{\mathrm{UV}}) \rightarrow H^+$) or via two VUV photons ($\mathrm{H} + 2h\nu_{\mathrm{VUV}} \rightarrow H^+$). This direct signal appears earlier in the time of flight traces and can thereby easily separated from the field ionisation signal when the UV laser is engaged. The power of the VUV is adjusted with this direct signal so that no saturation of the field signal can be observed and the amount of direct ionisation is minimised.

The bandwidth of the dye lasers is stated as $0.0027\,\mathrm{nm}$ and the $2p$ doublet is split by $\sim 0.0005\,\mathrm{nm}$ ($0.37\,\mathrm{cm}^{-1}$) [168, 170] which leads to both spin-orbit components being populated. The laser was set to predominantly populate the $^2\mathrm{P}_{3/2}$ level but Figure 3.4 illustrates how much of the $^2\mathrm{P}_{1/2}$ level is populated at the same time. The width of the level (due to Doppler broadening) is very small, so this spectrum is dominated by the laser bandwidth within which almost the entire Gaussian for the $J = 1/2$ component from the bi-Gaussian fit is contained.

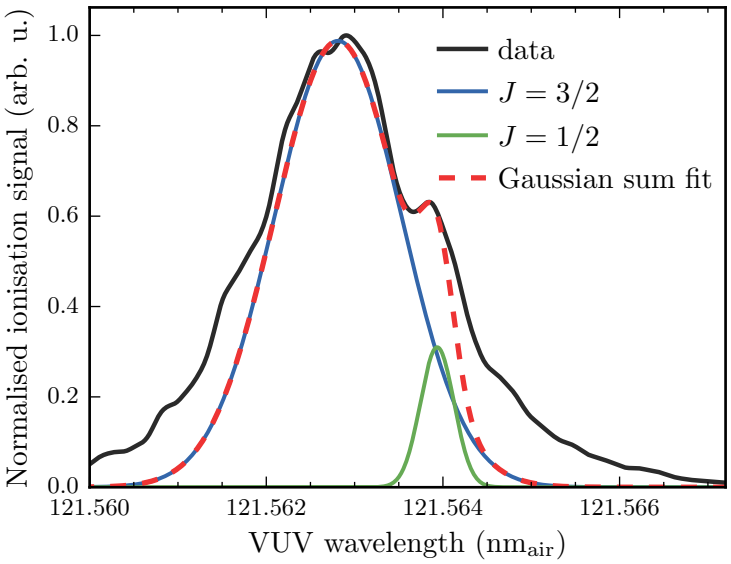

Figure 3.4: Signal from direct ionisation of hydrogen atoms scanned over the wavelength of a Nd:YAG pumped, frequency double dye laser that is passed through a rare gas mixture which produces the VUV Ly-α radiation necessary to excite atomic hydrogen. Through the $\sim 0.003\,\mathrm{nm}$ bandwidth of the laser either $2p$ doublet state gets excited resulting in a mixture of the fine structure components when the VUV wavelength is set to the maximum of a single component. These are decomposed as single Gaussian functions that are fitted to the wavelength data as the sum of the two to estimate the contribution of the J components. It should be noted that the displayed wavelengths are not representing the true Ly-α value of $121.5673\,\mathrm{nm}$ [168] but rather the mapped wavelength scale of the laser system through (calibrated) setpoints of the grating mechanism. The reference wavelength and the displayed wavelengths are given in air, a conversion below 2000 Å is not available [169].

When the VUV wavelength is tuned to the $J = 3/2$ level, the contributions from the $J = 1/2$ level can be estimated by the ratio of magnitudes of the single Gaussians which is 0.99 for the former and 0.31 for the latter component. This is in accordance with the ratio of the outermost Stark states for the fitting of wavelength scans in Figure 3.8.

The nonlinear response in pure inert gases has first been studied by determining the optical third-harmonic coefficients for the Kerr effect [171]. The intensity of the radiation produced through increased third-order susceptibility has been demonstrated to be enhanced by a factor of 10^6 by tripling in metallic vapours phase-matched in an inert buffer gas [172, 173]; the output photons, however, were in the UV range and the cell at a temperature significantly above room temperature. Another way of enhancing the power of the VUV output is to phase-match the production in a mixture of two rare gases, as done in the present experiment. It was shown that the conversion efficiency for Ly-α in phase-matched krypton is increased by two orders of magnitude compared to pure krypton [174]. The increased number density of krypton by

mixing it with another rare gas, a mixing of negatively and positively dispersive gases, and thereby improved conversion efficiency is discussed in detail in references [166, 174, 175].

In general, the conversion efficiency for third harmonic generation is about 10^{-6} to 10^{-7} [173] which implies that the number of hydrogen atoms being excited into a Rydberg state should be limited by the number of VUV photons since the two frequency doubled lasers are of comparable power, the loose focussing of the VUV radiation still leaves the power ratio unmatched in favour of the $2p \rightarrow ns$ transition. Thereby, attempts were undertaken to maximise the efficiency of the frequency tripling in the gas cell. The limitation for the conversion efficiency is set through absorption of VUV radiation in the gas mixture and the magnitude of the confocal beam parameter b; the lower b the earlier the VUV generation is saturated by dielectric breakdown of the gases [174].

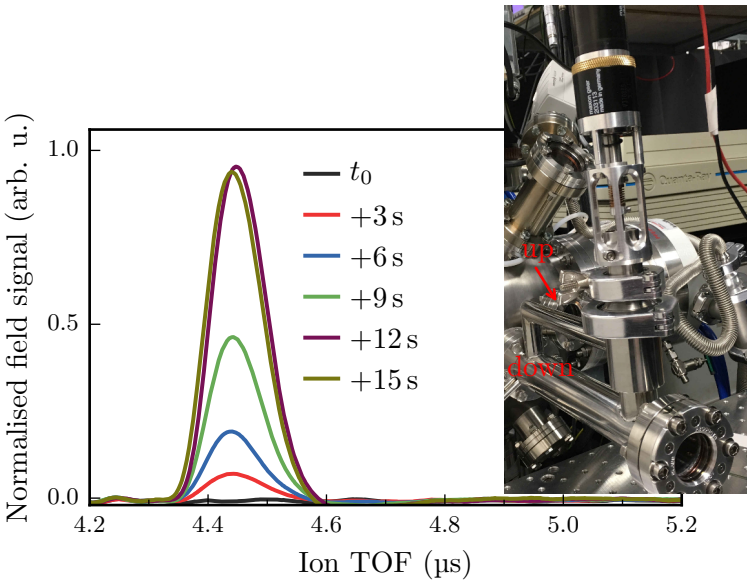

Figure 3.5: Demonstration of the fan that was installed in order to optimise the mixing of rare gases in a cell (tube) facilitating third harmonic generation to produce VUV radiation. Until the fan is engaged at t_0, the rare gas mixture has been mixing without external stirring for about 60 s. Subsequently it takes 10 s to 20 s until the measured Rydberg field ionisation signal equilibrates. Additionally marked are the laser viewports that are used for the regular surface ionisation experiment (down) and the decelerator experiment (up). In this image, only the *down* viewport is equipped with a gas cell used for frequency tripling.

First, by choosing a moderate b through the choice of UV lens focal length and increasing the partial pressure of krypton and consequently increasing the amount of phase-matching argon, the output power can be increased linearly with the amount of krypton in the pressure range where the cell is operated ($p_{\mathrm{Kr}} = 0.2\,\mathrm{bar}$ to $0.4\,\mathrm{bar}$). The ratio of the gases $p_{\mathrm{Kr}}/p_{\mathrm{Ar}}$ for optimal phase matching is $\sim 1 : 2.8$. Another issue is that the output power, as monitored by

the field ionisation signal, is sensitive to the mixing of the gases. The sensitivity and the breaking of the phase-matching condition has been examined for third harmonic conversion conducted in a cell and a gas jet which display significantly different gas flow dynamics [176]. The initial mixing of the two gases can be poor due to the low diffusion coefficient making it hard to find the optimal ratio and additionally it was observed that the conversion efficiency decreases over the course of hours. Since a permanent laminar flow, which yields high conversion efficiency over long periods of time as used in reference [177] is not attainable in this experiment, a fan was installed to stir the gases in the cell, see Figure 3.5. The device managed to greatly decrease the time necessary to settle the output power during the initial mixing phase which helped to finely adjust the partial gas pressures. However, it did not manage to recover the conversion efficiency when the gas mixture settled for more than 6 h, where the reasons can only be guessed, but a gradual contamination through improper seals seems likely.

A remark on the hubris of optimisation - when working with pulsed lasers

With the maximisation of the output power of the Lyman alpha radiation in mind, the frequency tripling scheme was duplicated in preparation for accommodating the Rydberg-Stark decelerator. For that, the excitation point, the point of intersection between molecular beam and the two lasers needed to be shifted away from the surface by using different vacuum chamber ports at different angles as marked in Figure 3.5. A second rare gas cell was built to allow either configuration (*down*: normal surface experiment and *up*: decelerator and surface experiment) to be operated as desired without breaking the vacuum. To maximise the number density of Rydberg atoms, the optical setup was carefully simulated and optimised with the ZEMAX software determining focal lengths and separations of the optical components involved. The (unfortunate) result of this prudent and elaborate planning can be observed in Figure 3.6.

Upon replacement of the LiF lens and selection of shorter focal lengths for the UV light focussed into the rare gas cell, the alignment was optimised manually. The spare LiF lenses were sourced from Crystaltechno Ltd at an affordable rate.

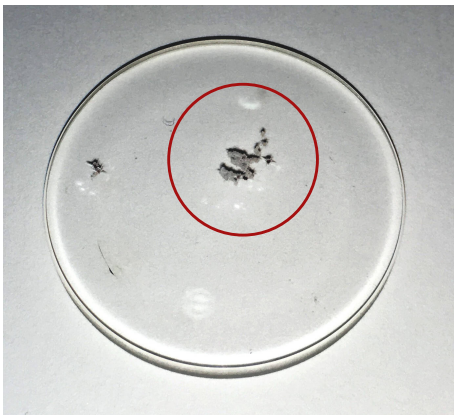

Figure 3.6: Burned lithium fluoride lens after several shots of focussed UV radiation with a focal length of $f = 500\,\mathrm{mm}$ used to collimate the beam into the rare gas cell for frequency tripling. It was not expected that at the calculated and optimised position of the lithium fluoride lens the still lower beam waist would exhibit a power density exceeding the damage threshold of the lithium fluoride crystal.

3.3.2 Stark state selection

The second step in the Rydberg excitation scheme is carried out with a frequency doubled dye laser of the same manufacturer as the one used for the generation of the VUV radiation (Sirah Cobra-Stretch pumped at $532\,\mathrm{nm}$ by a pulsed Continuum Surelite III Nd:YAG laser); in both the down- and up-configuration, the beams are counter propagated. The pulses of nanosecond duration are overlapped manually by monitoring the magnitude of a field ionisation signal on two-photon two-colour resonance. Usually, the investigation of surface ionisation is limited to principal quantum numbers $n = 20$ to 40 as shown in Figure 3.7. The upper limit is given by the bandwidth of the lasers and the bias that can be applied to the surface during excitation in order to achieve a Stark manifold for a single n that does not cross with a neighbouring manifold. The restriction for lower principal quantum numbers is caused by the potential magnitude necessary for field ionisation and extraction which cannot be achieved with the electronics in this experiment beyond $-5000\,\mathrm{V}$ (maximum field of $5000\,\mathrm{V\,cm^{-1}}$). Also, above $-3000\,\mathrm{V}$ significant noise in the time of flight traces is observed that overlays the ionisation signals.

The selection of a state from the manifold induced by the Stark effect as laid out in section 1.6, is done after Rydberg excitation in the presence of a constant bias field generated by a permanent potential bias applied to the surface mount and present during the subsequent ionisation processes. Figure 3.8 shows the result of a scan over the wavelength of the second step in the excitation scheme; the fitting of the wavelengths that represent the Stark state energies

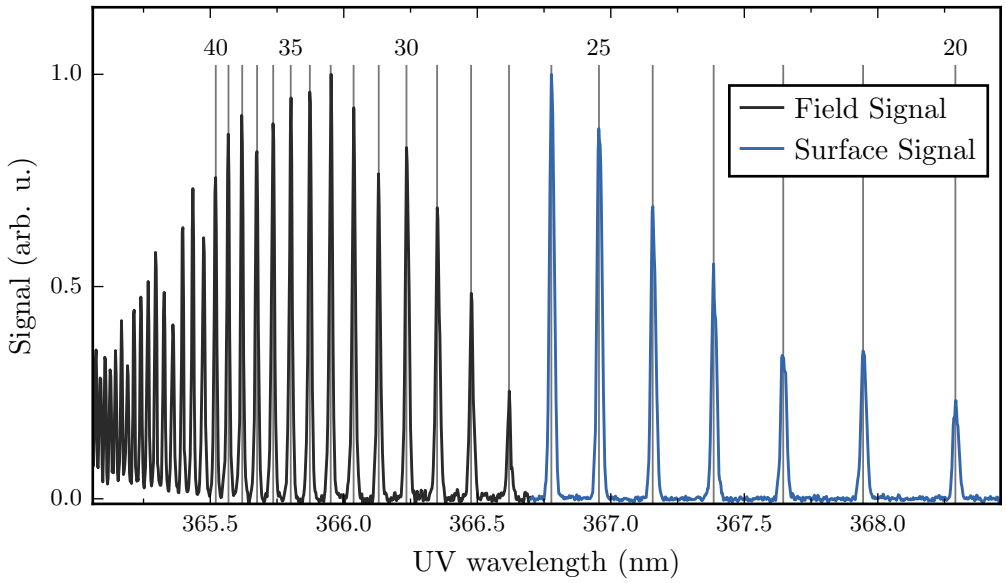

Figure 3.7: Field and surface ionisation signals recorded for wide-range wavelength scans for the second step in the Rydberg excitation scheme with a frequency doubled UV photon ($2p \rightarrow n$). The range of principal quantum numbers n that are typically covered in surface ionisation studies are fitted with the Rydberg formula in (1.1) for R_H marked as vertical lines.

is performed via Equation 1.7.

With regard to the discussion about the predominant fine structure component, the discussion about the wavelength selection will be done for the $J = 3/2$ as the starting point for the UV excitation. The perturbation of this level through the here applied electric fields is negligible, so that the transitions occur from spherical states to the parabolic Rydberg states [178]. It can be seen that, contrary to previous work displayed in Figure 1.9, a unique assignment to a certain Stark state is not without difficulty. Here, the polarisation of the two laser beams is crucial for the shape of the spectrum. The polarisation can either be parallel to the direction of the bias field during excitation (p-polarised, π) or perpendicular to the electric field (s-polarised, σ) where, *e.g.*, a combination σ-π denotes that the VUV radiation is perpendicular and the UV radiation is parallel.

Different polarisation combinations were tried and attempts undertaken to retrieve purer radiation with Glen-Taylor polarisers and to assert the best combination yielding greatest spectral resolution and signal intensity. With a coexistence of the $|m_l| = 0, \pm 1$ states in the $^2\mathrm{P}_{3/2}$ intermediate level, the transitions result in final populations of mainly $m_l = 0$ (π-π), $m_l = \pm 1$ (σ-π or π-σ) or $m_l = 0, \pm 2$ (σ-σ) [178]. The resulting spectrum in Figure 3.8 predominantly resembles a $\sigma - \sigma$ combination of polarisations from the theoretical spectra in reference [178].

Due to the number of Stark states being determined by the magnitude of m_l via (1.6), the most extreme Stark states in Figure 3.8, the most red-shifted and blue-shifted states $k = -34, 34$, have pure $m_l = 0$ character.

If the interest is in the extreme Stark states, as with the most blue-shifted low-field seeking states utilised for Rydberg-Stark deceleration, or in the study of surface ionisation dynamics for different electron polarisations, the intensity of transitions to these states is essential for a meaningful signal-to-noise ratio. An inverted distribution of intensities from Figure 3.8 would be achieved with a σ-π or π-π polarisation. As above, however, a near resemblance of this opposite spectrum was significantly lower in signal magnitude and thereby counterproductive for the intended purpose.

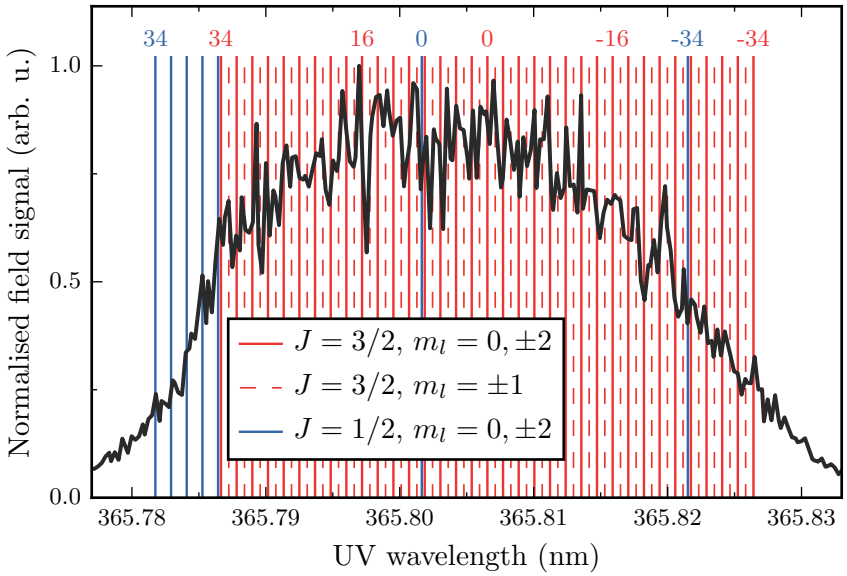

Figure 3.8: Stark spectrum of $n = 35$ recorded by monitoring the field ionisation signal at 1200 V cm^{-1} while scanning the UV wavelength, excitation occurs at a constant field of 19 V cm^{-1}. Marked are the transitions from the predominant fine structure component $^2P_{3/2}$ for $m_l = 0, \pm 2$ and $m_l = \pm 1$ parabolic Stark states while, for clarity, the contribution of the $^2P_{1/2}$ component is marked only for a few states and how they complement the wavelength scan and fitting process. The polarisation of the two lasers is chiefly perpendicular to the direction of the electric field.

Overall, it can be stated that resolution of the Stark states in Figure 3.8 carries a degree of ambiguity that should be accounted for when when comparing surface ionisation for different quantum numbers. There will always be a mixture of $m_l = 0$ and $m_l = \pm 2$ states present so that the additional $m_l = \pm 2$ components should be taken into consideration for the wave-packet propagation when experimental results are discussed in comparison to theoretical results. The uncertainty in the Stark states could be estimated as $k_{\text{real}} = k_{\text{fit}} \pm 2$ whose implications

are addressed in the next chapters. Another factor complicating the matter might be that the intensity of the Stark states is merely an effect of detection efficiency, especially for blue-shifted states.

Incomplete Stark manifold mapping through k-dependent ionisation threshold

As can be seen from the semi-empirical ionisation formula in Figure 1.2, increasingly higher fields are required to ionise Stark states with increasing k. This can require a field magnitude that is significantly larger than the classical ionisation limit required for a maximum red-shifted state to achieve an equivalent ionisation rate for the blue-shifted counterpart. This behaviour was confirmed by Delsart *et al.* where more than twice the field magnitude was applied to field-ionise the higher-energy Stark states in hydrogen [178], otherwise they would observe incomplete Stark spectra when trying to record all states with the same electric field magnitude. This issue in the context of the surface experiment will be discussed in the next section.

3.4 Ion extraction and detection

The ions from either ionisation process are removed from the interaction region with a pulsed field by applying a high voltage to a mesh mounted in front of the surface, the arrangement of mesh and surface ensures that the extraction field is homogeneous. The pulsed voltage supply is engaged a few microseconds after Rydberg excitation with the delay chosen to separate the field ionisation signal from the multi-photon ionisation signal and not having it overlap in the time of flight with surface signal.

In order to ensure that most of the ions are retrieved, previously an electrode stack was developed that combines a flight tube and ion optics to focus them onto the multi-channel plate (MCP) detector [179]. In this configuration, the extraction mesh was followed in line by a second mesh, a Wiley-McLaren configuration which improves the mass resolution of a mass spectrometer [180], two ion optics and a flight tube. The trajectories of ions in the presence of electrostatic electrodes as meshes and lenses can be compared to an optical setup of lenses with an optical axis defined by the symmetry of the circular extraction electrodes. As is demonstrated

in Figure 3.6, the performance of a double lens system can be hard to predict and prone to complications. This is especially relevant when the lens system is not operated with constant focal lengths. This is the situation for the extraction electrodes in the surface experiment where the first component, the extraction mesh, is scanned over a range of voltages in order to scan the extraction field, contrary to a typical time of flight of setup where the voltages on the extraction electrodes (extracting and repelling electrodes) can be optimised for detection [181]. Over the course of several experiments it became evident that the inherent layout of the previous combination of electrodes introduces ambiguity into the recorded data and does not perform well under all circumstances.

3.4.1 Revised detection system

The deficiencies of the previous detection setup are demonstrated in Figure 3.9 manifesting as incomplete Stark manifold mapping. For one, if all of the Stark states of higher energy are detected, the detectability of low k states is decreased and the spectrum can only be mapped incompletely leading to a great uncertainty in the assignment of Stark states. Additionally, at fields sufficiently high to ionise the high energy states it introduces features for mid-manifold states that appear to be anomalous. Second, from a mere practical perspective, in order to change the surface sample it was necessary to partially and cumbersomely dismantle the setup to get access to the surface holder introducing numerous complications.

To overcome the difficulties operating the surface experiment with this setup, a simpler replacement was designed. This consists of three electrode rings that are mounted as a stack in front of the MCP/phosphor-screen mount as shown in Figure 3.10 (a). The first electrode E1 is designed as a ring extended with a snoot towards the surface mount consisting of two conical cylinders sliding over each other to hold the extraction mesh without needing to attach it with epoxy. The three disk electrodes (E1, E2, E3) are operated in an einzel lens configuration where E2 is held at ground and E1 and E3 pulsed with a negative potential [182]. The electronics for the detection have been extended so that all electrodes are able to be pulsed. This was done in preparation for the deceleration experiment since external fields emanating from the detection electrodes would interfere with the excitation field at the shifted point of laser intersection. Since the only relevant species is hydrogen, mass resolution is not a concern here. This leaves this

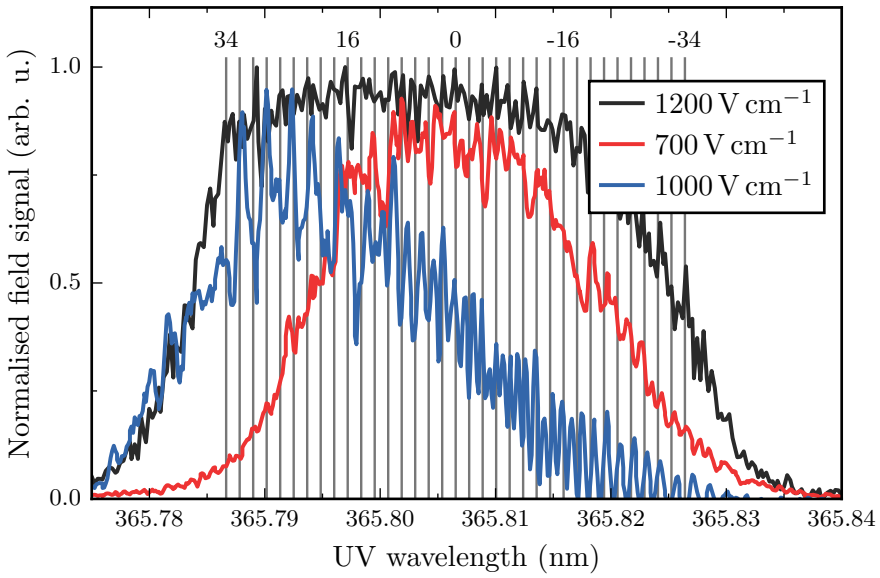

Figure 3.9: Comparison of UV wavelength scans for $n = 35$ with different detection setups and extraction fields. The traces at 700 V cm^{-1} (in red) and 1000 V cm^{-1} (in blue) were recorded with the previous detection stack as described in the text and exemplifying the problem of incompletely mapping the entire Stark spectrum with an insufficiently high extraction field. Additionally, at higher fields this setup introduces unphysical features as observed for the trace at 1000 V cm^{-1}. The black trace was recorded with an improved construction that is able to map the entire manifold at a constant field magnitude without distorting the spectrum. For guiding the eye, the boundaries of the complete spectrum are included with a fit for the Stark states from $J = 3/2$, $m_l = 0, \pm 2$ (grey lines).

construction with only one mesh at a transparency of 86% for extraction whereas the previous setup incorporated three meshes up to the detector decreasing the overall signal by about 40%.

A restriction posed on the detectability of the extracted ions is the size of the rectangular fibre couple (10×8mm) that is attached to the phosphor-screen which in turn is coupled to the MCP back plates (25 mm). The boundaries of the fibre can be estimated from Figure 3.10. This reduced effective area of the MCP front plate requires the ion beam to be focussed down on the centre of the plate. The performance and geometry of the new detection stack was simulated in SIMION® and heuristically optimised to detect all ions entering the snoot. The potential applied to electrode E3 is usually set to voltages ≤ -1000 V to focus the ion beam on the MCP within the field of view of the fibre coupling.

Experimentally, it was found that the surface signal is independent of the focussing voltage, affirming that the cloud of Rydberg atoms impacts the surface on the optical axis of the electrode stack which appears as a circular spot in Figure 3.10 (c). The field signal manifests itself as crescent-shaped cloud whose detectability is dependent on the magnitude of the focussing

voltage since it is not centred on the optical axis. This, however, is unavoidable as a higher delay would move the point of detection further towards the optical axis but overlay the ions from surface and field ionisation in time. To nonetheless ensure that all ions from surface ionisation are captured during the recording of a Stark spectrum, E3 is set to a high focussing voltage of $-2000\,\mathrm{V}$. A result with this improved detection is shown in Figure 3.8 and Figure 3.9 displaying a full Stark spectrum with no distortions. At voltages beyond $-2000\,\mathrm{V}$ and low extraction fields ($F < 150\,\mathrm{V\,cm^{-1}}$) the time of flight traces exhibit noise that can add to the integration within a time gate. Therefore, the focussing voltage during a scan over extraction voltages is set to maximally $-1300\,\mathrm{V}$.

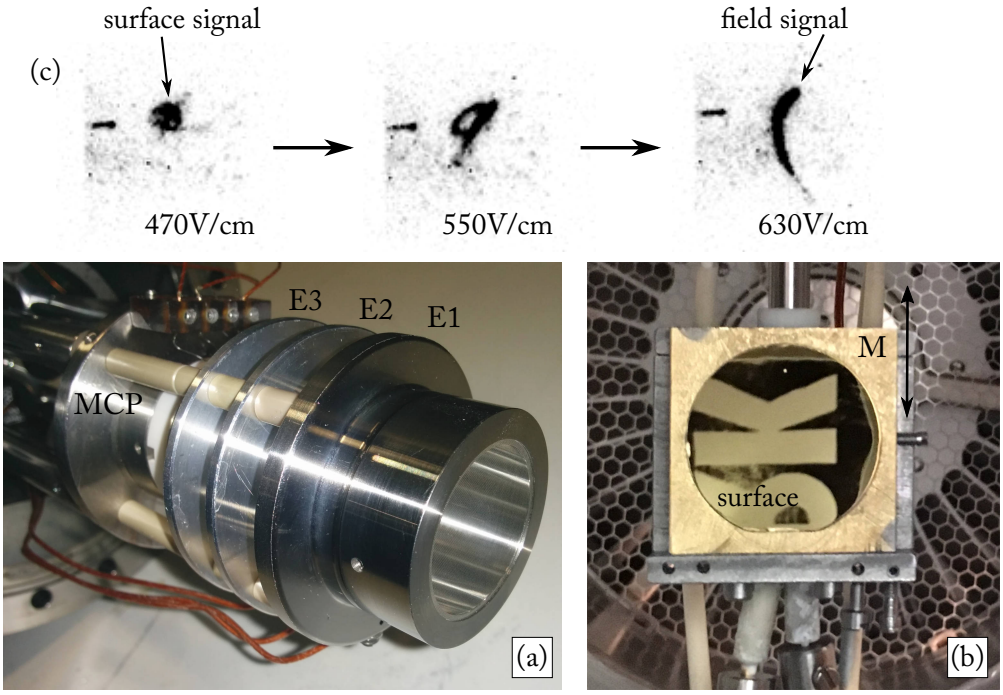

Figure 3.10: Improved detection setup principally designed as an extended einzel lens with electrodes E1 (detection mesh mount), E2 and E3 to direct ions onto a combined MCP/phosphor-screen assembly in (a). The stack of electrodes is mounted on a rail system connected to a linear motion feedthrough to adjust the surface-mesh separation. The surface is mounted on a detachable dovetail piece M that can be easily removed from the overall holder in (b). The sequence of camera images in (c) are recorded at different extraction fields as marked. It illustrates the transition from the surface ionisation signal (circular shaped) to the field ionisation signal (crescent shape) for $n = 35$; compare Figure 1.8 for the analogous transition in the time of flight traces.

Surface sample mounting

Complementing the effort in moving the excitation point away from the optical axis, a new surface holder was designed, shown in Figure 3.10 (b). The previous construction of a flat board with the sample block attached would have blocked the laser beams in the shifted configuration (up), the resulting point of excitation is approximately in the upper left corner of Figure 3.10 (b). The piece M that holds the actual surface sample gets slid on a block that is holding a heater element, thermocouple and potential bias connector, and is mounted on a translation stage. This mechanism enables movement of the holder in height, in the $(x,\ y)$ direction forward and sidewards and rotation around the z-axis of the chamber. The segment M being readily detachable allows a quick and unproblematic sample change that does not introduce the possibility of an accidental alteration of the geometric arrangement of the experimental components as well as not involving miniature parts needing to be dismantled inside the chamber. These could easily escape the operators hands and get into the inlet of the turbomolecular pump mounted below which can lead to a full destruction of the turbine and stator blades, a so called *cornflaking*. Despite this generating considerable attention, it is not a desirable introduction of downtime to an experiment.

3.4.2 Data recording

An important part of the experimental workflow is the gathering of the detected ion signals and its subsequent processing. As motivated earlier, the conclusiveness of a surface ionisation study as in section 1.6 depends on the comparison of the amount of surface signal expressed by integrated traces over the range of extraction voltages at different quantum numbers. To bring the surface signal to a common scale, a normalisation to the magnitude of the field signal magnitude is carried out. Thereby, it is evident that an accurate detection of the field signal, as laid out in the previous section, is essential to the data analysis.

Surface signal normalisation

The output of the fiber coupled to the MCP/phosphor-screen assembly is directed at a photomultiplier tube whose current is directly connected to a first (pre-)amplifier (gain $\times 5$) which is then further amplified by additional gain stages ($\times 10$). The signal from the amplifier is then

fed into a scope and recorded as signal over time (time of flight) where $t = 0$ is defined by a shared trigger source. The relevant parts of the time of flight traces are integrated over a time interval (gated) which is then registered as a single data point at certain extraction voltage.

Surface and field ionisation signal are of greatly different magnitude when recorded with the same gain which can lead to a saturation of the field signal when the surface signal is recorded with a higher MCP potential to achieve a sizeable signal magnitude. With the height of the field signal as the normalisation factor this can erroneously affect the normalised amount of surface signal when not accounted for. To decrease possible ambiguity in the data (per quantum number, for example), the field and surface traces are recorded separately and with a different number of gain stages where the surface trace gates are integrated at ten times the gain of the surface signal. The effect of saturation can be observed when comparing the wavelength scans (in black) from Figure 3.8 and Figure 3.9. Here, either channel was recording the same field ionisation process with the same time gates. Figure 3.9 shows the channel with the higher gain usually reserved for recording the surface signal which exhibits saturation compared to the trace in Figure 3.8.

Everyone loves automation

The integration of the time of flight traces and all signal processing is done externally by reading out the raw waveform data arrays from the scope with a customised software written in Python. The software provides a graphical user interface (GUI) that allows to set the time gating for the integration intervals and handles all data processing and plotting of the time of flight traces in widgets that are separated from the main code of the software. The GUI, shown in Figure 3.11 (a), remotely controls all peripheral devices in a centralised way, such as the delay generator that provides the synchronisation for all time-dependent actions in the experimental procedure or the gas-mixing fan from Figure 3.5. The object-oriented approach of the code allows to easily integrate additional devices into the control software.

Under normal conditions, a scan at otherwise identical settings is repeated at least three times and averaged for every extraction voltage. The data per extraction voltage is recorded with 10 to 20 shots of the gated time of flight traces that are averaged and integrated to collapse the amount of surface ion signal into a single data point. The consecutive data analysis is carried

out in a separate GUI, shown in Figure 3.11 (b), which handles the averaging and normalisation as well as the wavelength fitting procedure described in section 3.3, providing a consistent tool to ensure uniformity in the evaluation across various datasets. The source code for the software can be found under GitHub/mikekohlhoff.

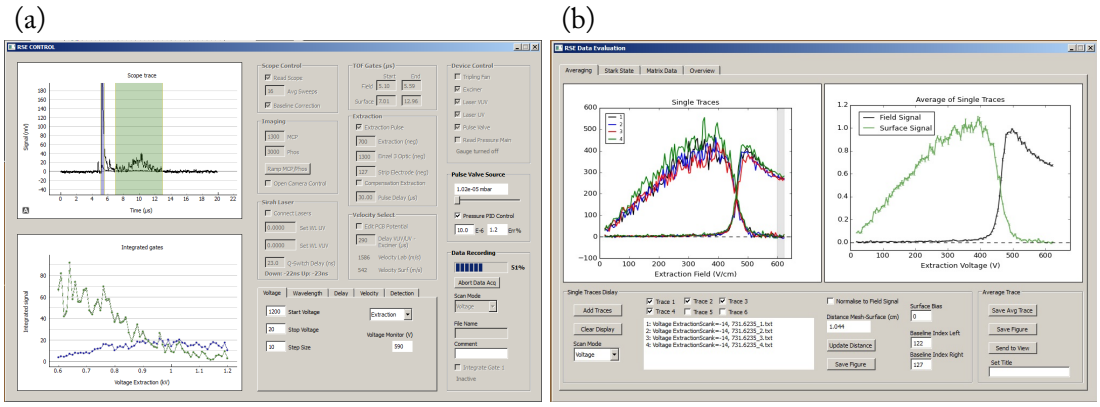

Figure 3.11: Screenshots of graphical user interface software written to control the Rydberg surface experiment in (a), unifying remote access for all experimental hardware, like the PID controller for the pulsed nozzle introduced in section 3.2. The software shown in (b) was designed to accommodate all relevant analysis and processing of the recorded data delivered from the experimental control software.

The experimental cycle starting with the pulsing of the gas expansion followed by Rydberg excitation and delayed detection is carried out at a repetition rate of 10 Hz limited by the Nd:YAG lasers pumping the dye lasers. A previous, more rudimentary, version of the experimental control written in LabVIEW was not capable of polling the data synchronously at this rate. This represents an unsatisfactory performance and should be expected to be within the realm of process control on a general-purpose operating system without resorting to a real-time data acquisition (DAQ) system.

A key to resolving this issue was to just have the (TCP/IP LAN) scope controller implemented in Python and to use a threading model that isolates the polling of data from the event handling of the user interface implemented in PyQt, a cross-platform application framework wrapped in Python. This mechanism is utilised for various other processes in the software that need to be decoupled from the main event loop. In essence, it involves the creation of a `QThread` object that connects the raw data returned from the scope readout to a routine that passes it to the processing widgets.

```
self.scopeThread = scopeThread(True, True)
self.scopeThread.dataReady.connect(self.dataAcquisition)
self.scopeThread.start()
```

Within this thread, the scope is armed to return a block of data when the acquisition of the time of flight traces is finished. A signal/slot mechanism is used to connect the control and the scope thread objects to each other which allows to communicate between them and pass on the data blocks from the scope.

```
class scopeThread(QtCore.QThread):
    def __init__(self, scopeRead=True, dispOff=False):
        QtCore.QThread.__init__(self)
        self.scope = LeCroyScopeControllerVISA()

    dataReady = QtCore.pyqtSignal(object)

    def run(self):
        while self.scopeRead:
            data = self.scope.armwaitread()
            self.dataReady.emit(data)
```

The full details of implementation can be reviewed at GitHub/mikekohlhoff.

With these steps it was possible to achieve a read-out rate for the scope of up to 20 Hz. Additionally, the custom software permits to operate the experiment in a fully automated way, introducing the capability to record greater amounts of data under optimised and more stable conditions.

Increased efficiency and long range free-metal-like charge transfer at graphene

As demonstrated by the results in section 1.6 for electronically structured Cu(100), the dynamics of the charge transfer from the bound Rydberg electron into a surface can be sensitive to the properties of the material itself. Whereas a metallic bulk surface is resonant for any energy of a Rydberg state, surface ionisation for the same metal can differ when the material has geometric constraints. The former case has been explored in multiple studies [67, 68, 69] whereas the findings for metallic thin films significantly differ [183]; electron confinement in a thin film results in a characteristically distinct behaviour from a free-electron metal in three dimensions. The low dimensionality of thin films modifies the wavefunction of the electron inside the bulk in amplitude and extension towards the vacuum side. Due to experimental limitations, the lowest film thickness in the latter investigation was of several monolayers which makes it highly intriguing to introduce a system with one-atom thickness.

The study of two-dimensional (2D) systems has historically been of great interest due to its richness of phenomena occurring when the motion of charge carriers is restricted in one dimension but are allowed to move freely in a plane and these systems display an intermediate character between low and high dimensionality. Since the isolation of the carbon allotrope graphene, which is made up of free-standing sheets that are one atom thick [184, 185], this first truly 2D crystallite material has been investigated extensively experimentally and theoretically while developing potential applications in an array of fields such as electronics [186, 187] for replacing conventional transistor [188], (electrochemical) energy storage [189, 190], materials and biomedicine [191, 192, 193].

What sets this remarkable material apart most is undoubtedly the plethora of extraordinary electronic properties. Starting with the band structure, graphene has a linear dispersion relation with the conduction and the valence band touching at the Dirac points, the **K** points of the Brillouin zone. Thereby, it is a semiconductor with zero bandgap but it can display metallic behaviour due to topological anomalies at zero energy that modify conductivity [194]; the position of the Fermi energy can be shifted by applying a gate voltage as demonstrated in [184]. Through this, the concentration and resistance of charge carriers is also affected, leading to a high carrier mobility in graphene [195]. Graphene can be described as a semimetal whose strong electron-electron many-body interactions contrast to ordinary metallic systems [196].

The study of the unique electronic properties, like observation of the quantum Hall effect at room temperature [197] or the behaviour of Dirac fermion quasi particles [198], is focussed on the in-plane properties of graphene while only few have concentrated on the electronic properties in the out-of-sheet z-direction. Mainly, the focus is here on the position of image potential states [199] which, in contrast to a bulk solid, are predicted to form a double (Rydberg) series of even- and odd-symmetry states whose wavefunctions have opposite parity with respect to reflection at the graphene plane [200]. The existence of this double series was confirmed experimentally via scanning tunneling microscopy of monolayer and bilayer graphene notwithstanding that the samples were not free-standing but epitaxially grown on a substrate [201]. In [200] it was further theorised that the existence of image states is the basis for the well known interlayer states in graphite [202, 203].

4.1 Graphene growth and sample surface topology

Making graphene of high quality, in sizeable pieces and considerable quantities is one of the challenges for it to be developed for large scale applications. This is a major focus of current research, with chemical vapour deposition (CVD) as the most promising approach for large-area synthesis [204]. Even though graphene products can by now be supplied by commercial vendors they do not deliver the properties that were desired for this study. The commercially available single layer films are normally made of flakes rather than a continuous film so that the Rydberg atoms in the gas packet would experience differently orientated graphene thin films.

For device fabrication, graphene is usually grown on metal substrates and then transferred

to semiconductors or dielectrics for further characterisation [205]. Here, the graphene sample has been grown on a copper foil (25 µm thick, 99.999%, Alfa Aesar) by CVD in collaboration with Grobert and coworkers. Prior to deposition the copper foil was cleaned and electropolished [206] followed by annealing. This yields a nearly full coverage of single layer graphene of predominantly monolayers with possibly up to 5 % bilayer coverage [207]. Different methods were employed to validate the quality of the monolayer as shown in Figure 4.1.

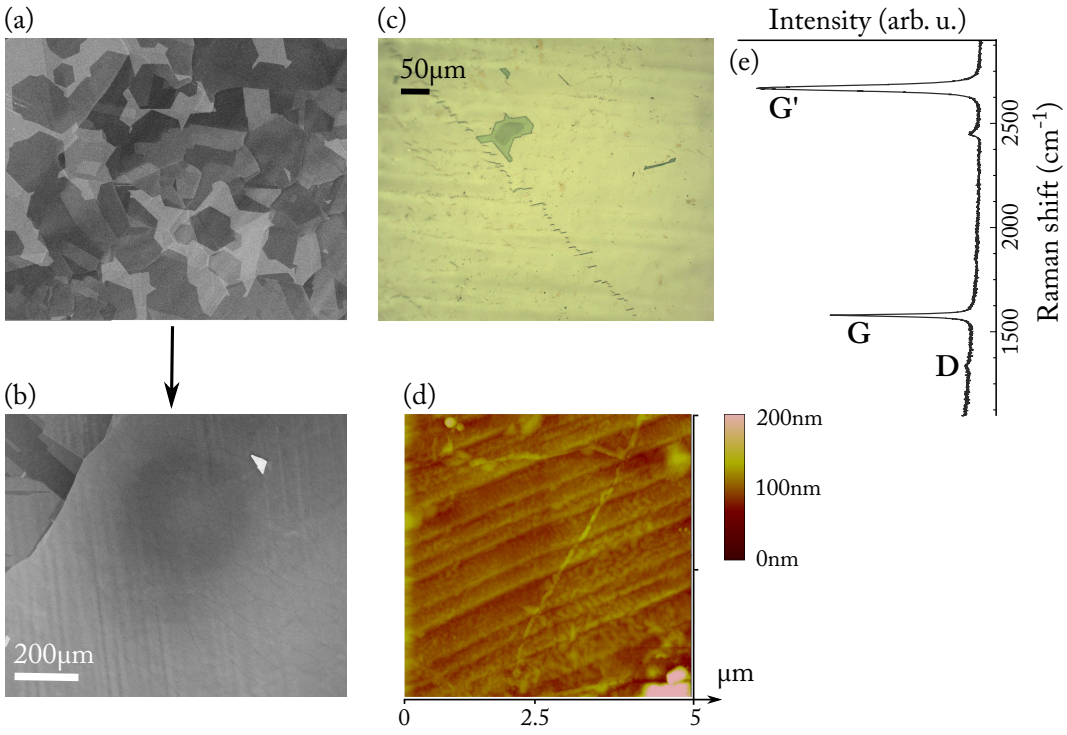

Figure 4.1: Sample characterisation with scanning electron microscopy of an incompletely grown graphene film in (a) and a fully grown film in (b) with crystal sizes of around 50 µm to 100 µm. The quality of the single layer can additionally be corroborated with a Raman spectrum in (e). The full coverage of the copper substrate was controlled optically in (c) displaying very few remaining spots of uncovered Cu substrate. An image of an atomic force microscopic (AFM) scan in (d) reveals the terrace structure of the copper foil. The high intensity feature in the lower right corner in (e) results from (post-)contamination of the sample which overall manifests itself in a comparatively poor quality of the AFM image.

A straightforward way to determine the coverage of graphene is optical microscopy which allows to distinguish between single-layer, bilayer and multilayer parts by observing grain boundaries [208]. The hole shown in Figure 4.1 (c) is one of a few over large surface areas; these are hard to avoid when a single-layer coverage is desired. Furthermore, the number of layers can be validated with Raman spectroscopy, where a single-layer is characterised by the near absence of

the **D** peak and the **G/G'** peaks roughly having a ratio of > 2; with increasing thickness the **G'** peak increases in width and loses its Lorentzian line shape [209]. The topology of the deposited film can be imaged with scanning electron microscopy (SEM), as in Figure 4.1 (a,b), covering larger areas of the surface. The two SEM images display the transition of individual graphene domains (dark hexagons) before they coalesce into a coherent film. Here, the synthesis was done for a slightly shorter time to get incomplete coverage and remaining copper domains can be seen in the upper left corner of the lower image (b). Note that these do not represent the actual sample used in this study but instead are SEM images taken from a sample grown with the same synthesis. The atomic force microscopy (AFM) image in 4.1 (d) is taken of the actual sample (after data collection) showing the structure of the copper foil to consist of micrometer sized crystal terraces characteristic for this material [207, 210]. In the case when graphene is transferred from the Cu substrate, single-crystal step edges can manifest itself as quasi-periodic nanoripples in the transferred film [211]. Here, the graphene film remains on the copper foil for the entire process of characterisation and measurements.

After film growth, the foil is quickly cooled and cut into place and glued to a surface holder block with silver paint (Agar Scientific G3629). As a reference sample for comparison without graphene, a foil sample was prepared identical to the initial steps of cleaning and annealing before graphene deposition. This graphene-free sample was also glued to a separate surface holder slider. Either sample was heated to $> 100\,^{\circ}\mathrm{C}$ in the Rydberg surface apparatus for an hour before measurements commence to remove possible contamination after CVD growth or by ambient air exposure.

Deposition on a Cu foil substrate was chosen for its established and well characterised procedure as well as being metallic and thereby comparable to previous results for free-metal gold. Note that only single crystal copper has a projected band gap as discussed earlier. Due to its inherent physical makeup, the properties of graphene can be strongly altered when interfaced with a metal substrate. CVD grown graphene on copper is only weakly interacting with the substrate, leading to a continuous pristine layer over atomic steps and edges without introducing defects [212] as well as preserving the characteristic electronic structure of graphene by weak adsorption onto the substrate [213]. The effects of doping graphene on the atomic scale have only recently been investigated in depth; however, in reference [213] the effects of even weak chemisorption on a metal substrate are discussed in shifting the Fermi level from the **K** points,

resulting in either electron or hole doping and finding that graphene is n-type doped on Cu.

4.2 Data evaluation and surface profile integration at high extraction fields

In order to cover a wider range of Rydberg state energies than in some previous studies, mid-manifold states with $k = 0, \pm 1$ were selected for principal quantum numbers from $n = 20$ to 40 as the probe state in this study. Data recording was carried out with the apparatus and its modifications as described in the previous section.

The lower the quantum number in question, the closer the ion will be produced towards the surface since the field ionisation high-field cutoff occurs at higher field strengths. Covering lower quantum numbers in the surface experiment requires extraction voltages up to $-4000\,\mathrm{V}$ ($4000\,\mathrm{V\,cm^{-1}}$ extraction field) at which significant noise development in the time of flight traces occurs, which can only be minimised so that for quantum numbers $n \geq 25$ the data evaluation is mostly straightforward as described in section 3.4 but has to be modified for lower quantum numbers. Usually, the surface ionisation profiles, which have a typical form as depicted in Figure 1.8, are baseline-corrected by subtracting an offset so that the high-field part (in the field ionisation regime) of the profile has zero intensity. This becomes increasingly difficult and ambiguous at higher extraction fields for $n \leq 25$.

Additionally, this problem gets more pronounced due to the way the time gating is set for recording the specific collisional velocities used here; surface ionisation for the graphene sample is recorded over a range of 19 Rydberg excitation delays (corresponding to 19 different velocity segments of the distribution) with a $10\,\mu\mathrm{s}$ increment. The data recording is automated so that the width of the time of flight gate for the surface ionisation is chosen to capture the signals at the earliest and the latest delay. Using this large gate width possibly increases the amount of recorded noise. The delay settings amount to a velocity range of $1070\,\mathrm{m\,s^{-1}}$ to $1840\,\mathrm{m\,s^{-1}}$ and the maximum and minimum delay were chosen to be at $10\,\%$ to $20\,\%$ of the maximum signal of the velocity distribution, which allowed a good signal-to-noise ratio. Traces for the reference Cu sample were recorded at just one velocity at about the maximum of the velocity distribution.

All surface and field ionisation profiles were recorded three times under equal conditions and

averaged, which makes about 1200 traces to be evaluated manually due to the aforementioned noise problems. In order to overcome this particular issue, a separate software was designed for this study to visualise the data evaluation. It is partially based on the software in 3.11 (b) and a screenshot is shown in Figure 4.2. Every trace can easily be reviewed within this GUI to carry out baseline correction, signal processing, normalisation, averaging, integration and error calculation for every n.

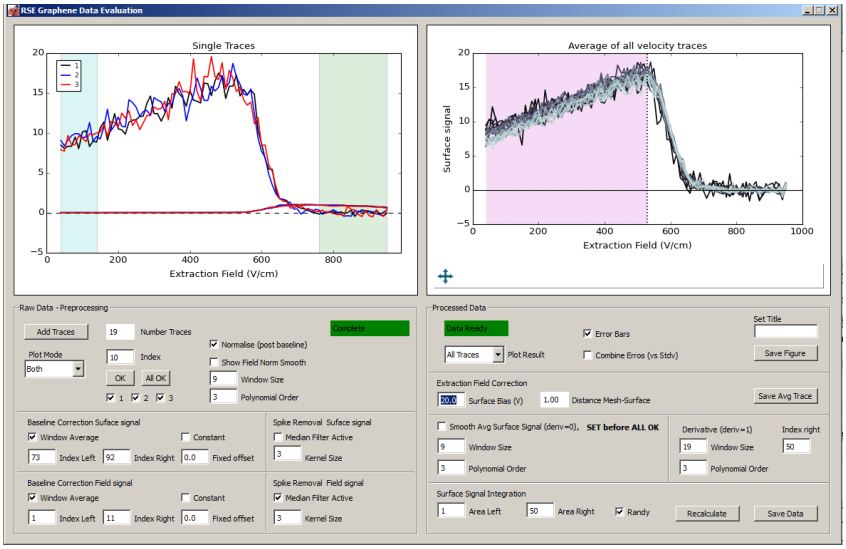

Figure 4.2: Graphical user interface used in this study to evaluate surface ionisation at graphene. The left panel displays the separate channels used for recording field and surface signal gates at different amplifications which in turn are integrated at a fixed extraction voltage to make up the characteristic profiles. Before the integration window of these profiles is chosen in the right panel the single velocity traces are processed per principal quantum number.

When the recorded surface signal profile does not return to a clear baseline, the value of the baseline is adjusted manually by a lookup offset which is taken from a series of surface gate scans for the chosen MCP voltages over the range of extraction voltages.

Usually, the entire surface ionisation profile is integrated over all extraction fields to be displayed as a single-valued integrated signal as a function of principal quantum number. To further determine the amount of integrated surface ionisation more precisely, the integration is alternatively carried out from the minimum extraction field to the maximum of the profile as depicted in Figure 4.2. This can further be motivated by the spread of the field values over which the field ionisation profile is dropping to zero which increases with decreasing n. Evaluating integrated surface integration over this transition field range between field and surface ionisation is conceivably less meaningful than the method chosen here.

For possibly general interest, the procedure of integration and the error calculation algorithm is done as follows. The integration of the surface time of flight gate and the resulting integration of the constructed surface ionisation profile (SIP) over the extraction field is implemented numerically with the trapezoidal rule between subsequent equidistant field values. More important when comparing relative quantities is the error propagation up to the forming of the integral. Initially, the data per extraction voltage in the SIP is recorded as a time gate integral with the standard deviation over multiple shots (10 in this study) as the error. Determining the error from these averaged integrated time gates can be done in different ways; for an overview see reference [214] from which multiple versions were implemented and compared. The version yielding the greatest error bars was eventually chosen for the entire data analysis. The error of the integral was calculated with a statistical approach by using the trapezoidal rule on a set of randomly generated traces with the error described before as standard deviation and then using the standard deviation of the set of integral values as the error of the given integral per quantum number.

4.3 Observation of increased detection efficiency at low extraction fields

Before comparing surface ionisation profiles and integrated profiles for different n and impact velocities, the non-zero ionisation that was observed at minimum extraction field is considered. This behaviour is markedly different from earlier studies with gold and copper [69, 97] and a comparison to the copper foil reference sample at the same conditions (gas packet forward velocity $v = 1353\,\mathrm{m\,s^{-1}}$) is shown in Figure 4.3. It could imply that ions are being formed at very large distances from the surface (*cf.* Equation 1.14).

Eliminating low-field noise

In the Rydberg surface experiment, the amount of detected signal can either be purely attributed to the surface ionisation process but equally, recorded ions in the H^+ ion mass gate can also stem from lasers striking metal electrodes producing photoelectrons, by electronic artefacts or scattered laser light striking the detector. As mentioned previously, at high potentials for the

focussing electrode E3 of the einzel lens construction, low-field noise can be observed which could be mistakenly be recorded as surface ionisation.

Figure 4.3 displays surface ionisation profiles for different focussing voltages. It can be seen that for voltages $\geq -1300\,\mathrm{V}$ significant amounts of noise are recorded for fields up to $200\,\mathrm{V\,cm^{-1}}$. The noise is dependent on the lasers being engaged and higher E3 voltages, making it conceivable that a certain combination of detection voltages creates a field distribution that allows to detect electrons from photoemission despite the MCP front plate being held at $\sim -1200\,\mathrm{V}$ to $-1400\,\mathrm{V}$ which has the E3 electrode closest to it. This appears unlikely at first but was validated with a trajectory simulation in SIMION® and it was determined that they do not originate from the interaction region but rather from the detection electrode stack possibly induced by scattered laser light. An alternative explanation could be that these photoelectrons may be accelerated and ionise gas molecules in their path to produce ions [215].

Since no change in the magnitude of the field signal below or above the noise-free threshold could be observed, the focussing voltage was set to $-1100\,\mathrm{V}$. The local limitation of the observed noise to low-field regions demonstrates that it is not the cause for increased detection efficiency.

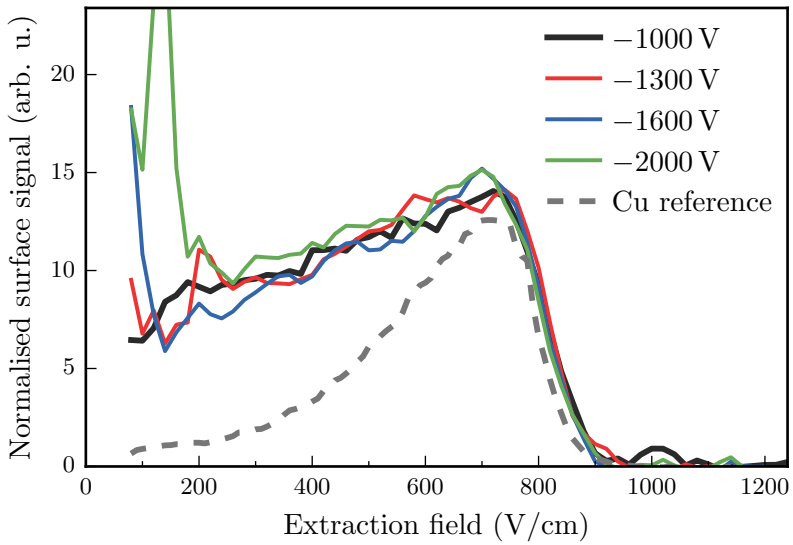

Figure 4.3: Single surface ionisation profiles for $n = 31$ mid-manifold Rydberg atoms impinging on a graphene film grown on Cu foil at different einzel lens focussing voltages to examine increased detection efficiency towards zero extraction fields in comparison to the reference sample (Cu foil without graphene). Due to the output limitations of the power supply, 0 V output cannot be achieved. A focussing voltage of $-1100\,\mathrm{V}$ was chosen permanently to avoid noise development below $200\,\mathrm{V\,cm^{-1}}$. Error bars are omitted for clarity.

As explained earlier, voltage biasing varies the work function of graphene but the overall

alteration of the material properties are still a subject of current research [216]. The surface bias voltage that is applied to the surface for Stark state selection and wavefunction polarisation maintenance is not switched during the experimental cycle but permanently engaged, whereas the extraction field to extract ions from surface ionisation is pulsed after Rydberg excitation and present during the process of surface ionisation. Thereby, in the current experimental configuration the graphene film can not be investigated without an electric field being present. However, equivalently to the previous argumentation, low-field ion detection efficiency might be affected by the magnitude of the surface potential bias.

Surface potential biasing effects

Figure 4.4 shows surface ionisation profiles for a variation of the surface bias field and no bias field present during Rydberg excitation. It can be seen that the amount of surface signal is highest in the field-free configuration and settles to a minimum signal for increasing excitation field for a field magnitude $\geq 40\,\mathrm{V\,cm^{-1}}$. Overall, all traces appear to settle at a similar signal magnitude towards minimum extraction field but differ in their magnitude at higher extraction fields. The likely reason for the appearance of the traces at non-zero surface bias fields is a mixing of red-shifted and blue-shifted Stark state components that have different ionisation dynamics [69] as is indicated by the broader field transition range of the $20\,\mathrm{V\,cm^{-1}}$ trace from field to surface ionisation. At lower (bias) excitation fields the density of Stark states within the laser bandwidth will be higher thereby simultaneously exciting multiple k-states. The high-field cutoff and maximum of the surface ionisation traces are shifting towards higher fields when k is increased with higher intensities for the red-shifted ($-k$) states over the blue-shifted ($+k$) states thereby forming the overall observed trace shape.

An equivalent understanding can be derived from the trace at $0\,\mathrm{V\,cm^{-1}}$. When no excitation field is present the l-degeneracy will not be lifted and a multitude of k-states will be excited and subsequently ionised [217]. Examining the trace at zero excitation field, an even wider spread at the onset of the signal can be observed suggesting the presence of a mixture of k-states whose field ionisation onset and surface ionisation magnitude will be different from that of a single Stark state resulting in the observed shape of the trace in comparison to the traces at a non-zero excitation field.

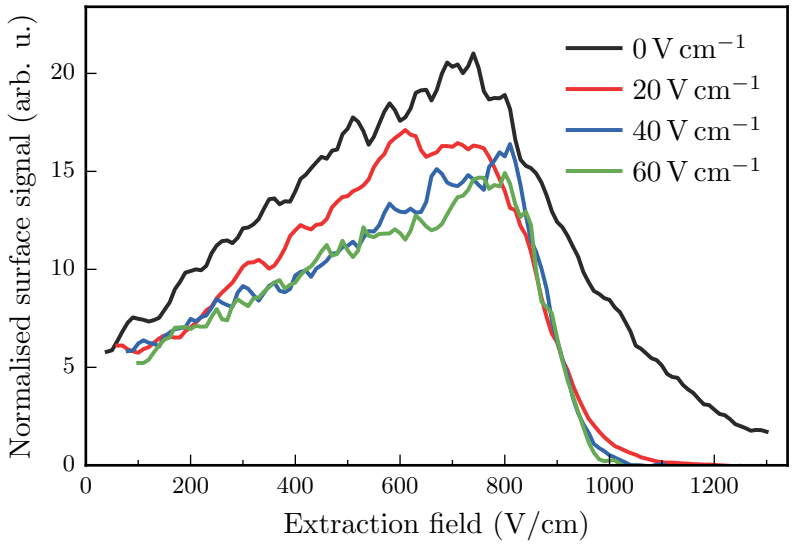

Figure 4.4: Single surface ionisation profiles for a $n = 30$ mid-manifold state at different surface biases by applying a positive bias to the surface holder and thereby the substrate on it. Under normal conditions the scans are carried out at a bias field of $46\,\mathrm{V\,cm^{-1}}$ ($d = 1\,\mathrm{cm}$) for $n = 30$. At $0\,\mathrm{V\,cm^{-1}}$ all extraction electrodes are turned off and Rydberg excitation is ideally occurring under field-free conditions. Again, error bars are omitted for clarity.

In conclusion it can be assessed that the surface voltage bias of the graphene film and the underlying substrate can be excluded as being responsible for the observed increased detection efficiency for the lowest extraction fields and be acknowledged as an unique feature of surface ionisation for the deposited graphene surface employed here.

4.4 Graphene sample robustness and reactivity

The data collection on the graphene sample was carried out over the course of two to three weeks in which the sample was held at ultrahigh-vacuum conditions with a base pressure as low as $5 \times 10^{-9}\,\mathrm{mbar}$ when idle and increasing up to $5 \times 10^{-8}\,\mathrm{mbar}$ to $1 \times 10^{-7}\,\mathrm{mbar}$ during supersonic valve operation. For a meaningful investigation it is crucial to assess the long-term stability of the graphene film under these conditions. The following mechanisms will also play a role in interpreting later results as a factor of exclusion.

It has previously been shown that the electric performance of graphene sheets is preserved after repeated cycles of bending induced stress [218]. For the production of novel field effect transistors the interface between graphene and, *e.g.*, metals has been studied intensively since defects on the atomic scale alter the properties of the material and impede device performance.

It was also demonstrated that highly energetic electrons and ions can induce small-scale defects in the regular carbon structure by knock-on atom displacement [219, 220] that then can transform a film to an amorphous sp^2 hybridised random arrangement of carbon atoms instead of leaving graphene perforated [221]. These polymorphic defects were shown to be able to heal themselves, that the vacancy holes can be filled if a nearby reservoir of loose carbon is available [222].

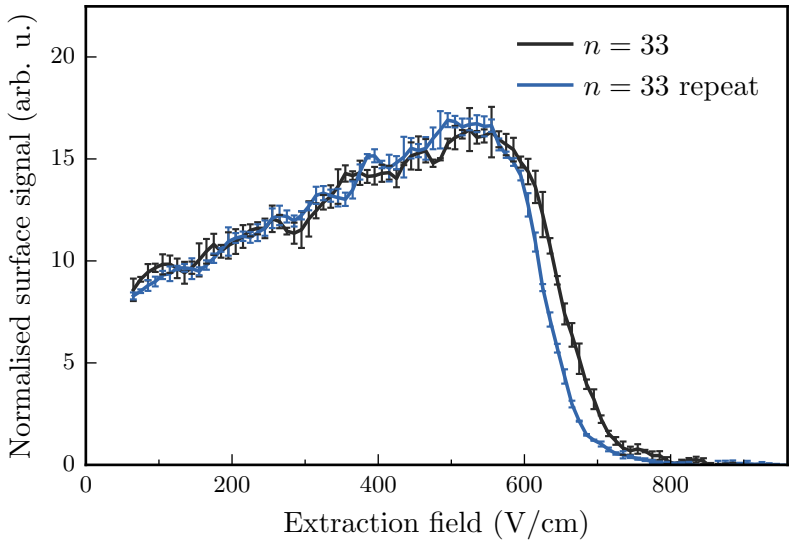

Figure 4.5: Surface ionisation profiles for a mid-manifold state recorded several days apart but under otherwise same conditions. The shift in the onset of the ionisation trace is likely due to a drift in the laser wavelength thereby exciting not the exactly same Stark states resulting in different field ionisation thresholds.

Despite the fact that graphite is chemically very inert it was demonstrated that graphene can undergo a reaction with low energy hydrogen ions from a plasma [223]. The obtained sp^3 hybridised hydrocarbon (graphane) has distinctly different electronic properties than graphene by removing conducting π orbitals and thereby creating an energy gap turning the semimetallic graphene into an insulator [224, 225]. The high sensitivity to chemisorption was also shown to realise a (reversible) semimetallic-to-metallic transition by iodine doping [226].

If a continuous exposure to ions (and photoelectrons) that are produced in either field or surface ionisation process and not extracted from the interaction region leads to a steady introduction of defects, the sample will lose or change its distinct surface ionisation profile over time. In order to address the possible deterioration of the film, a scan for the same state was performed about one week apart, shown in Figure 4.5. It can be seen that within error bars the surface ionisation traces coincide, inferring that no major changes occurred with the graphene

sample between the two measurements. By losing parts of the graphene film the underlying copper substrate should be exposed and the surface profiles start to resemble the shape of the copper reference trace in Figure 4.3.

Since not all photodissociated hydrogen atoms will be excited to a Rydberg state being able to be ionised, the possibility exists that these atoms react with graphene undergoing a semimetal-to-insulator transition. As shown later, however, the graphene sample displays metallic surface ionisation characteristics instead of behaving like an insulator which allows to also exclude this long-term effect taking place.

4.5 Increased free-metal-like behaviour

Due to a lack of understanding about the variability of the electronic properties of graphene through, *e.g.*, chemical doping, it is hard to classify under which circumstance the material displays characteristics of a metal, a semiconductor or an insulator. Moreover, the problem is possibly overlaid by quantum size effects introduced by the graphene thin film. Where the charge-transfer process involving a free-electron metal, as presented here in section 1.4, is highly understood and studied for ions and excited ground states as a resonant charge transfer (RCT), the constraints imposed on the electron motion along the surface normal should alter the dynamics of the charge transfer.

These quantum size effects have been observed for a metallic thin film theoretically in the static and dynamic case and experimentally for the dynamic case [183, 227]. In the latter study it was shown that the wavefunctions protruding from a thin film can increase electron transfer from the Rydberg state at long range displaying oscillations in the amount of surface ionisation over a range of n. Similarly, oscillations in the reflectivity of low-energy electrons from graphene on a copper substrate [228] and from thin graphite films [229] could be observed.

As shown in Figure 4.3 for $n = 31$ it can be seen that the electron transfer into the graphene film appears to significantly differ from the RCT at the Cu foil. This difference holds for the full range of quantum numbers investigated here; see Figure 4.6 for sample n values at constant collisional velocity. Overall, it can be observed that graphene exhibits higher magnitudes of surface ionisation signal over all extraction fields compared to Cu and displays non-zero surface ionisation at the lowest extraction field which increases for lower n due to the magnitude of

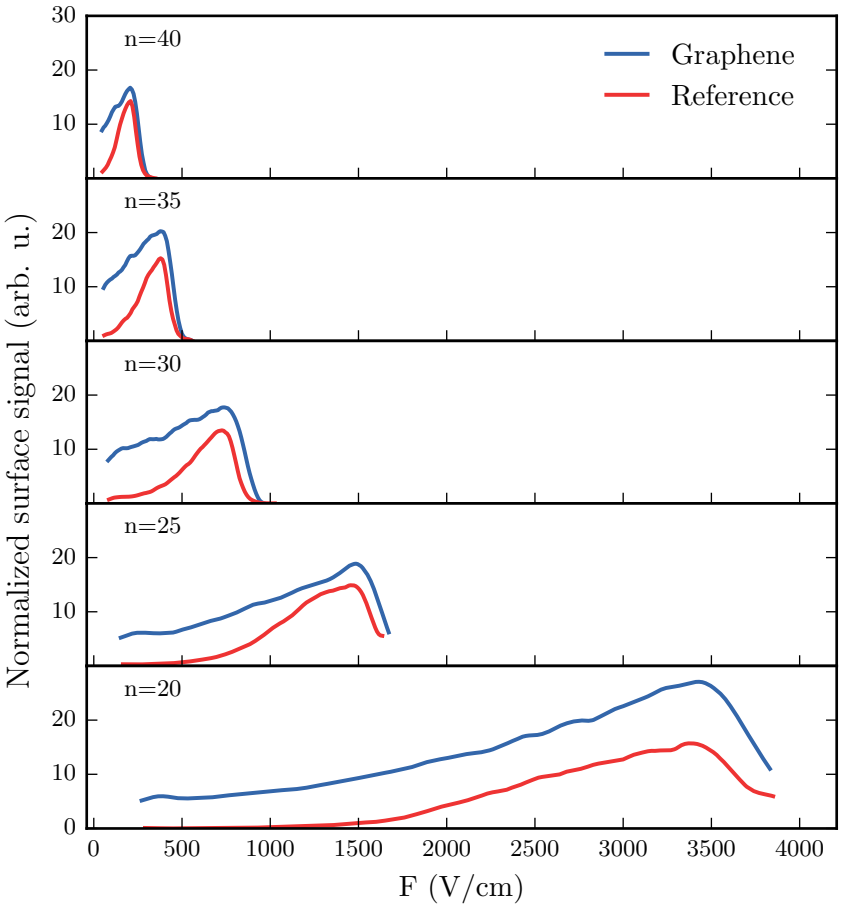

Figure 4.6: Comparison of Surface ionisation profiles of the graphene sample and the bare Cu foil it has been grown on for selected principal quantum numbers n, the increased detection efficiency can be observed for all n measured in this study. Traces for the graphene sample and the reference are shown for the same collisional velocity at $v_\perp = 463\,\mathrm{m\,s^{-1}}$.

the bias excitation field. But note that at higher n the spreading of the graphene and reference traces is greater for lower fields. In contrast, all Cu traces appear to draw towards zero ionisation at low field and also contrast in the shape of the traces between their maxima and the lowest extraction field. The data for $n = 20$ and $n = 25$ are not displayed beyond a high-field cut-off due to noise development as elaborated in section 4.2.

4.5.1 Resonance character of charge transfer

As previously demonstrated in section 1.6, the variability of the amount of surface ionisation with the velocity of the perpendicularly impinging Rydberg atoms can be used to reveal the sensitivity to the discrete image state spectrum of Cu(100). Whereas in [97] the selection was limited to four velocities, a greater number of velocities here should aid the detection of

discrete features in graphene, as for example probed previously with angle-resolved two-photon photoemission spectroscopy [199].

Figure 4.7 compares integrated surface ionisation profiles for graphene and copper at a single velocity as a function of principal quantum number. In accordance with Figure 4.6 it can be seen that for all n more surface ionisation occurs with graphene than Cu and that it follows a smooth trend. When looking at the respective integrals per n of the two traces, the mean of the ratio of the two is found as $r = 2.3 \pm 0.3$. Put simply, about two times as much surface ionisation is occurring (or is being detected) at the graphene sample.

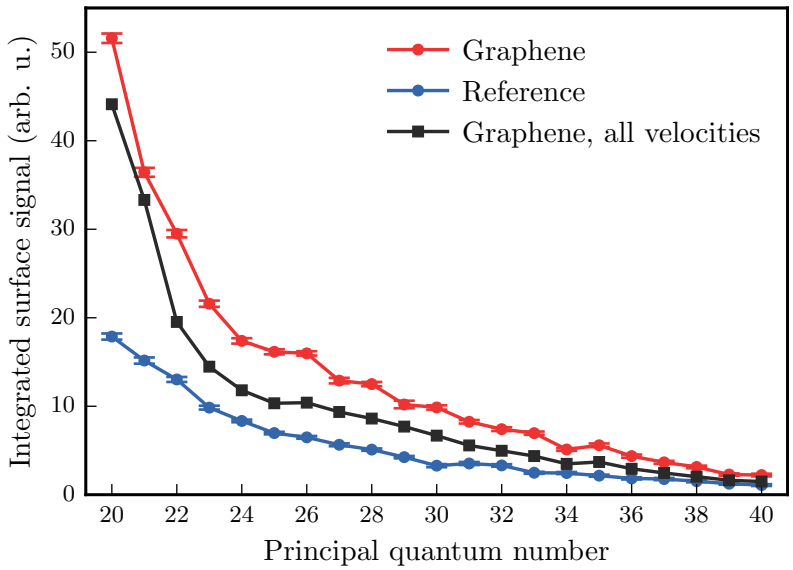

Figure 4.7: Integrated surface ionisation of graphene and Cu reference sample at constant impact velocity $v_\perp = 463\,\mathrm{m\,s^{-1}}$ as a function of principal quantum number (blue and red trace). The black trace shows the sum of integrated surface ionisation profiles for $v_\perp = 366\,\mathrm{m\,s^{-1}}$ to $630\,\mathrm{m\,s^{-1}}$. Note that the summed ionisation is on a different scale.

Examining the traces more closely only small deviations from the overall smooth trend can be observed. This trend is characteristic of a free-electron bulk surface as shown in Figure 1.10 for gold. The field ionisation threshold classically scales with n^{-4} thereby moving the surface ionisation high-field cutoff to higher fields and increasing the area for integration for decreasing n. If no discrete electronic feature of the surface material matches the energy range of the Rydberg state a monotonous function of n will be detected. Otherwise, pronounced non-monotonicity should be observed by resonant enhancement of charge-transfer. Evidently, deviations from a smooth free-metal-like trend should be amplified by summing up the integrated surface profiles per n when the velocity dependence is delivering an additional handle

on potential resonances, as is also depicted in Figure 4.7. Again, the curve for all velocity traces in sum resembles the shape for the known gold curve. For the reference sample, other than the data in Figure 4.8 all data for the pure Cu foil was recorded at a single velocity.

Collisional velocity effects

The velocity dependence was discussed in section 1.6 for resonant and non-resonant cases attributing a greater spread in ionisation with H atom velocity to a feature of resonance detection [97]. Also, it was argued that the variation with velocity can manifest itself differently in a resonant case, leading to a shape change in field regions where image and Rydberg states cross rather than an expansive increase in surface ionisation over the entire field range.

Figure 4.8 (a) examines the integrated surface ionisation for a fixed n as a function of impact velocity $v_\perp$. First, the ratio of ionisation at graphene and the Cu reference only varies slightly with velocity accounting for the ratio of ≈ 2. Also within the traces not much variation can be observed. Little variation is also found directly in the surface ionisation profiles for graphene in Figure 4.8 (b). Here, a shape in change is possibly only observed for lower collisional velocities. Considering that a lower signal intensity for slower parts of the gas packet ($v_\perp < 430\,\mathrm{m\,s^{-1}}$) could introduce a higher uncertainty in the normalisation process, the velocity dependence of graphene can be stated to be approximately constant over the velocity range, whereas for the Cu reference, ionisation is increasing with decreasing velocity as expected for a regular bulk metal.

The velocity dependence for graphene allows a twofold conclusion to be drawn. For one, a non-discrete resonant (or always resonant but not discretely resonance enhanced) charge transfer as for a regular metal would exhibit a uniform ion-detection increase with lower projectile velocity with regard to Equation 1.13 as ionisation occurs closer to the surface. This is demonstrated in Figure 4.8 for Cu. Using the variability of the velocity dependence straightforwardly as a conspicuous feature for (discrete) resonant enhancement of charge transfer, this would thereby infer that ionisation for graphene is "less resonant" than for Cu. This however, can easily be refuted by invoking the broadly increased ionisation for all n over all extraction fields.

As in the case for discrete image states of Cu(100), when ionisation occurs at greater distances from the surface, the velocity dependence can get more complicated and the probability of surface ionisation exhibits less variation with projectile velocity [98]. Therefore, it can be ten-

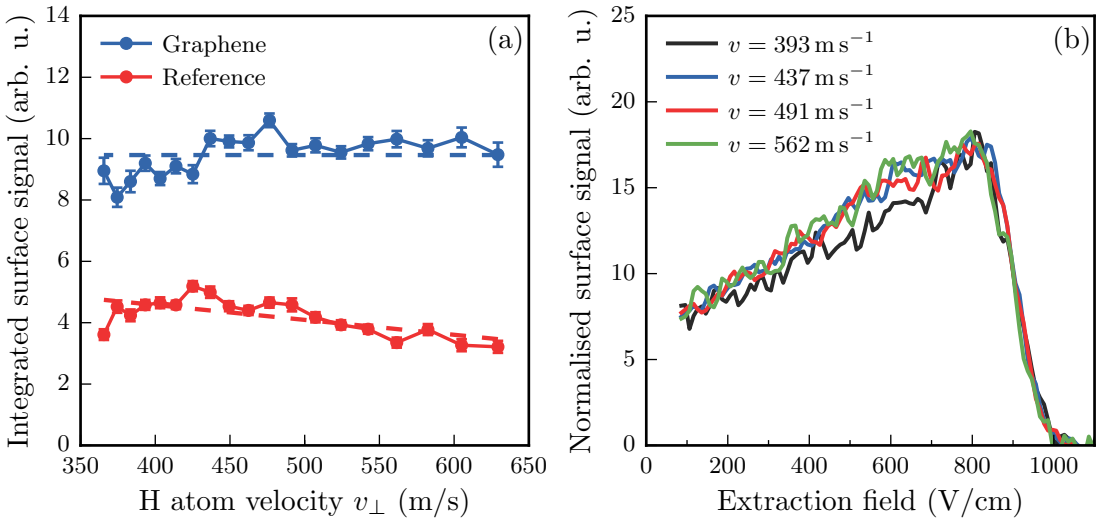

Figure 4.8: Integrated surface ionisation profiles for a $n = 30$ mid-manifold state as function of Rydberg H atom collisional velocity in perpendicular direction to the surface in (a). Dashed lines serve as guide to the eye for constant (graphene) and linear (Cu) data fits. The ratio of increased surface ionisation for graphene is occurring at a ratio of roughly 2 : 1. Example surface ionisation profiles for the graphene sample in (b) that are integrated as single value in (a).

tatively deduced that ionisation at the graphene film could take place at greater atom-surface separations, as will indeed be shown later, which possibly reduces the effects of the Rydberg atom collisional velocity and leads in turn to no pronounced variation of the integrated surface ionisation profiles as a function of impact velocity and subsequently as a function of principal quantum number. The observed charged transfer in graphene could be interpreted to be resonantly enhanced over all n, whereas in Cu(100), the resonant enhancement (where the integrated surface signal lies above the free-metal background, *cf.* Figure 1.10) occurs for discrete n.

4.5.2 Image state density and Fermi level shifts

The metallic nature of surface ionisation for graphene in conjunction with the resonance characteristics permits different explanations as to why an enhanced ionisation compared to a free-metal can be observed. On the one hand, graphene could have undergone a semimetal-to-metal transition which could (merely) justify the metallic performance. In this case, the Fermi level would need to have moved up which can be achieved through doping. For any (unintentional) doping process possibly taking place, only the n-type variant would be resulting in increased conductivity in contrast to p-type modifications via hydrogen [223]. Any impurity introduc-

tion and exposure to reactants are restricted to the abundance of elements in the gas expansion carrier gas. Treatment with NH_3 was reported to result in N-Doping but was achieved through annealing at 1100 °C [230], which can clearly be excluded here. Eventually, for doping to be invoked here, this only leaves the n-type doping induced through the Cu contact interface [213] to provide charge transfer channels for the Rydberg states. Yet this would merely account for the metallic character of the sample but not its increased amount of surface ionisation. If all Rydberg states would be resonant with an image state it could result in a broad enhancement of charge transfer.

The image plane of a free-standing sheet of graphene imparts two equivalent surfaces to the problem, where reflections in regard to this plane result in a double image state series with index $n^{\pm}$

$$E_n^{\pm} = -\frac{1}{16} \cdot \frac{1}{2(n_{\mathrm{img}} + a_n^{\pm})^2} \,, \tag{4.1}$$

where '+' and '−' refer to their parity and with a quantum defect a_n for the respective series [200]. As discussed in that reference, the free-electron, metal-like (unoccupied electronic states), properties of other carbon allotropes in nanotubes and fullerenes are predicted to originate from the hybridisation of the first even (+) image states. Here, the influence of the substrate was not included but acknowledged that it can modify the results in the gap between the graphene sheet and substrate. For monocrystalline Cu(111), two unoccupied interface surface states could be observed in the real-space between the bulk and the graphene sheet which stems from the hybridisation of an $n = 1$ image state and a quantum well state [231].

The image state energies in [200] were calculated by density-functional theory within a local-density approximation (LDA) [232] and an LDA approach that was extended with an image-potential, where the latter one was deemed to more accurately describe the Coulomb-like asymptotic potential form. Since no value for the quantum defect $a_n^{\pm}$ was given and could not be retrieved elsewhere, they were extrapolated in this work from the listed energy positions for the first three members of the double image state series in Table I in reference [200] through Equation 4.1. It then allowed extrapolation of the field-free image states to higher order, shown with the experimentally employed Rydberg states in Figure 4.9.

It can be seen that the density of image states is significantly increased when the two forms for determining $a_n^{\pm}$ are taken into account when compared to a single-crystal Cu. It can be

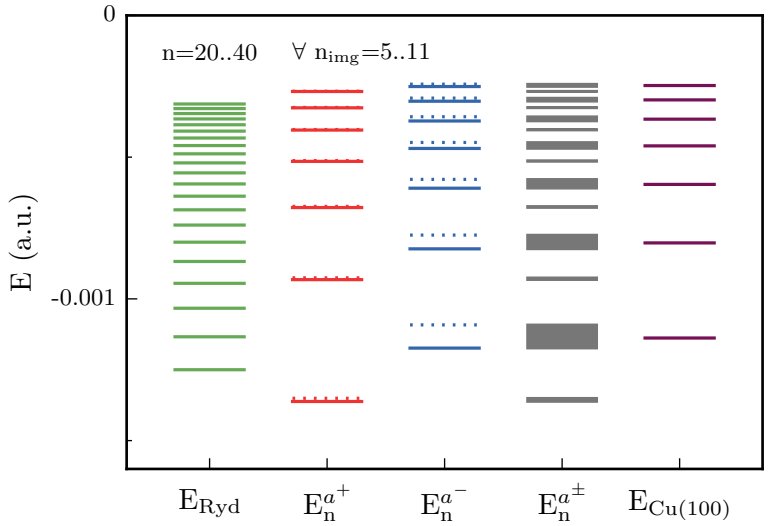

Figure 4.9: Energies in atomic units of the double series of image states in graphene with even (+) and odd (−) symmetry in comparison to the field-free Rydberg states. The quantum defect parameter $a^{\pm}$ was retrieved from reference [200] in which the energy positions were calculated in two forms (full versus dotted lines) that were respectively used for reconstructing $a^{\pm}$. For comparison, the energies of a single image state series for Cu are shown for terms $n_{\text{img}} = 5$ to 11 as displayed equally for the other series.

argued that a lack of features in the (summed) surface ionisation as a function of n in Figure 4.7 is due to a high density of image states that is beyond the effective resolution of the Stark state selection, so that the charge transfer occurs into a quasi-continuum of image states. This was similarly argued for thin films, where an increasing amount of monolayers results in a higher density of image states thereby resembling the ionisation trend of a bulk material [183]. Also, it was observed that the resonances at thin films in [183] displayed increased magnitudes of surface ionisation for lower thicknesses.

4.6 Long range surface ionisation

When discussing the velocity dependence in the previous section, it was hinted that the charge transfer event is shifted further away from the surface for graphene compared with the plain substrate. The magnitude of the extraction field that pulls away the resulting ion after surface ionisation can be used to estimate a distance via Equation 1.13. Visibly in Figure 4.6 it is shown that for graphene the surface profiles do not converge towards zero magnitude with zero extraction field, unlike the profiles observed for metals. Consequently, this would translate to an unphysical, infinite distance. To elucidate this further, the experiment was modified to

control the extraction voltage with a power supply of smaller output range ($\pm 10\,\mathrm{V}$) able to attain a genuinely $0\,\mathrm{V\,cm^{-1}}$ extraction field. The resulting surface profile over this reduced extraction field range passed through (the displayed) $0\,\mathrm{V\,cm^{-1}}$ extraction field before reaching zero surface ionisation signal, which indicates that field inhomogeneities shift the actual field magnitude away from the field magnitude calculated from the applied extraction mesh potential. All detection electrodes are pulsed in this experiment but not the ion imaging stack, so that fields emanating from the front MCP plate could conceivable be a source for stray fields in the interaction region.

Following the procedure from reference [233], stray fields were calculated by shifts in Rydberg spectra. The spectrum in Figure 3.7 is displayed incompletely omitting the full shape, which displays a convergence towards a horizontal trace of roughly constant intensity without Stark state resolution for high-energy photons and subsequently dropping to zero intensity due to the ionisation continuum. The inflection point of this ionisation edge was measured for several surface biases by which the actual shift in ionisation energy (in wavenumbers) can be calculated via $\Delta E(hc\,\mathrm{cm^{-1}}) = -6.12\sqrt{F(\mathrm{V/cm})},\ \ \Delta E = -2\sqrt{F(\mathrm{a.\,u.})}$.

A field offset was extrapolated from the zero of the ionisation energy shift, which was used to add to the recorded field axis plus a standard deviation determined from the measured output of the power supply and in total gives $\Delta F = 1.57\,\mathrm{V\,cm^{-1}}$. The result of this reconstructed field axis is shown in Figure 4.10 (b). The calculated distribution of ionisation distances is shown in Figure 4.10 (c) and strikingly displays that significant magnitudes of surface ionisation are extended up to 10 µm in stark contrast to the Cu reference, which converges at roughly 200 nm in accordance with the predicted value from the over-the-barrier model of $3.5n^2a_0$.

The observed length scales for the metallic reference here and the Cu(100) sample in section 1.6 can further be motivated by considering the extension z_e along the surface normal of the one-electron image state wavefunction that can be described by

$$\Psi_n^{\mathrm{Img}}(z_e) = z_e R_{n,l=0}\left(\frac{z_e}{4}\right), \tag{4.2}$$

with the hydrogenic radial wavefunction $R_{n,l=0}$ [234]. These wavefunctions can extend far into the vacuum by $\langle z_e\rangle_n^{\mathrm{Img}}$ and overlap with the wavefunctions of the Stark states [98]. Combining this extension with the classical size of the Rydberg orbital $\langle r_{\mathrm{Ryd}}\rangle$ can give an estimate for the

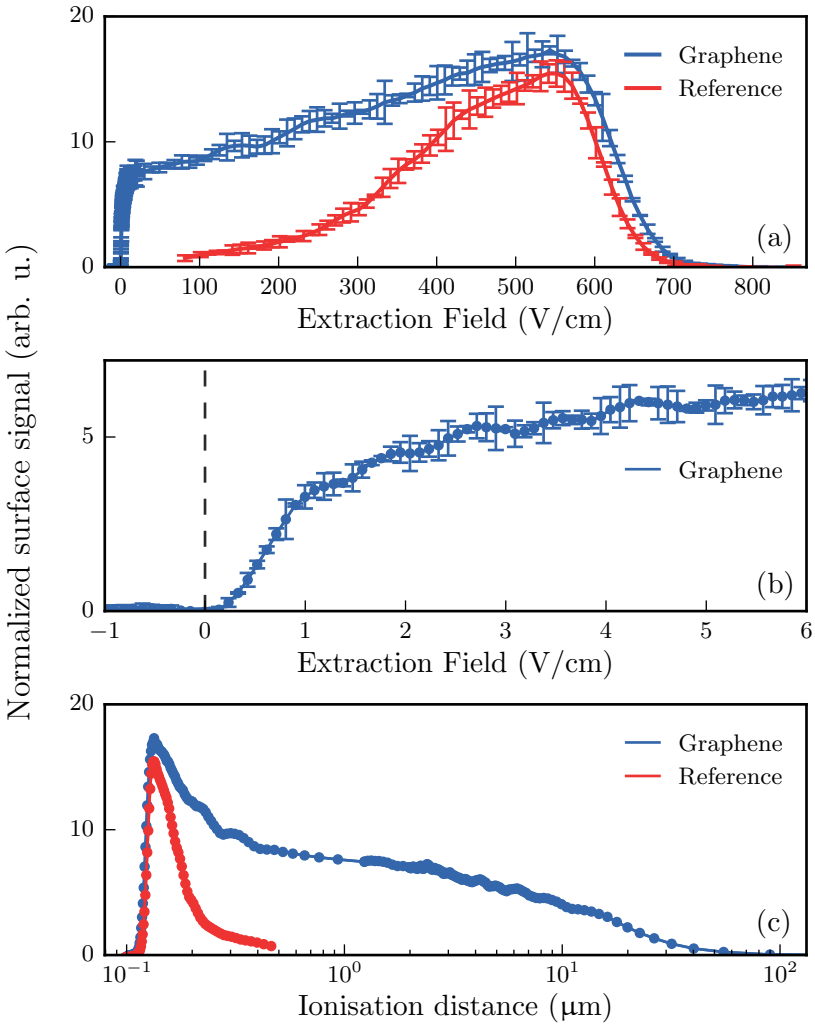

Figure 4.10: Surface ionisation profiles of a $n = 32$ mid-manifold state displaying increased surface ionisation at graphene in comparison to the Cu reference in (a). The extraction field range was extended for graphene in (b) to examine the increased ionisation at low-extraction fields, the trace for Cu is visibly converging towards zero magnitude. The field magnitude in (a) and (b) is converted to an ionisation distance via Equation 1.13 in (c).

resonance lengths in the investigated systems.

$$\langle z_e \rangle_n^{\mathrm{Img}} + \langle r_{\mathrm{Ryd}} \rangle = \left[6(n_{\mathrm{img}} + a_n)^2 + n_{\mathrm{Ryd}}^2 \right] a_0 \tag{4.3}$$

This gives, for instance, $\sim 1800 a_0 \approx 0.1\,\mu\mathrm{m}$ for $n_{\mathrm{img}} = 11$ and $n = 32$ which approximately matches the observed distances for Cu(100) and the Cu reference sample. However, this intuitive and simplifying estimate does not justify the observed lengths of charge transfer for graphene about one order of magnitude greater.

4.6.1 Excluding factors aiding enhanced detection

Equivalently to the previous argument in section 4.3, the increased detection efficiency could merely be an artefact owing to the nature of the sample. If local surface fields are able to generate field strengths that exceed the field ionisation threshold then ions detected below the field ionisation onset, as determined by the displayed extraction potential, will mistakenly be recorded as ions originating from surface ionisation. This apparent, increased low-field surface ionisation effect was studied by Pu *et al.*, where Rydberg atoms were incident on an electrode pattern of μm size that was alternately applied with a potential bias of $\sim \pm 1\,\mathrm{V}$.

The most obvious reason here could be the geometric nature of the sample deposited on a foil that shows creases on a macroscopic scale. These folds could create regions with different separations to the incoming Rydberg atoms. In effect, the Rydberg atom is ionised at a peak but then moves above a valley where it is extracted as if formed at much greater distance. This, however, is appropriate both for the graphene and the reference sample that are identical bar the deposited carbon and can thereby be excluded. When increased surface ionisation was observed with graphene, it should have been observed with the reference sample as well if this was just an effect of surface roughness.

Similarly, it could be argued that inherent topological features of the graphene sheet introduce a surface morphology that leads to the creation of locally strong stray fields. Random microscopic curvatures were found on a freely suspended graphene membrane that vary by $\pm 2°$ from the average surface normals and these corrugations have extensions of up to $1\,\mathrm{nm}$ [235, 236]. In another study for CVD grown graphene (on PET), strain-induced deformations of the films were found as wrinkles around nanometer-sized islands [237]. Again the comparison with the Cu foil substrate can be used, whose μm size terraces as shown in Figure 4.1 dominate the graphene sample's out-of-plane topology. If microscopic features of the graphene sheet as described were responsible for creating sufficiently strong stray fields, this effect would be even more pronounced for the pure Cu sample or the graphene sample would at least exhibit the same performance as the Cu reference.

Additionally, ionisation at greater distances was previously observed for nanoparticles and at doped silicon. In the former case, however, no connection was found that surface roughness is the source for this feature [179]. In the latter case, dopant charges modify the surface

potential in a regular manner and higher dopant densities were found to reduce the effect of increased ion detectability by decreased dopant spacings, thereby reducing the effective range of the perturbing dopant charges [83]. The potential energy landscape in graphene on Ru(0001) was found to form a periodic array of nanometer-sized potential wells that behave like quantum wells [238]. In [83] it was shown that beyond a certain dopant density, and thereby spacing, the ion detectability of the semiconductor surface resembles a bulk Au surface. The potential array in [238] is periodic on a length scale that is 10^2 to 10^3 smaller than the dopant spacing thereby allowing to exclude this reason as well.

Also, the role of the interface dipole that is formed at equilibrium through electron transfer from the graphene sheet to the metal contact as discussed in reference [213], remains a source of investigation but is very likely not to influence the surface ionisation dynamics at graphene. First, the metal side is connected to the surface holder which is positively potential biased, thereby the interface not in equilibrium, unable to form a permanent dipole of this sort. Second, the extraction field present during surface ionisation is expected to dominate the electric fields present in the interaction region. Third, the data in Figure 4.4 suggests that the surface biasing before pulsing of the ion extraction field has no effect on the surface ionisation dynamics of the graphene sheet. Beyond this point it can only be hypothesised how other potential effects, such as the formation of crack patterns in transferred sheets and fracture dynamics in 2D graphene lattices [205, 239], could contribute to the observed effect of surface ionisation at greater distances in graphene.

Summary

To conclude, it is observed that a graphene sample deposited on a copper foil exhibits a considerably different surface ionisation behaviour than the copper foil itself, which is used as a reference for a (regular) free-metal. In a free-metal, charge transfer into the surface is always resonant and the integrated surface ionisation profiles display a typical shape as function of the principal quantum number, which is smooth and shows no discrete features. This (metallic) trend is also observed for the graphene film but with higher magnitudes than the copper reference. This enhancement of the charge transfer above the background of a free-metal has also been observed previously for other discrete systems, theoretically and experimentally [183, 240]. Here, the

enhancement is explained with the Rydberg states being degenerate with a quasi-continuum of surface states that originate from a double series of image state, whose energy spacing is beyond the resolution of the Rydberg probes.

The greatest difference in surface ionisation between the graphene film and a metallic reference sample is observed for low extraction fields. By translating the electric field employed for extracting the ions stemming from surface ionisation to a distance from the surface, it is demonstrated that surface ionisation at the graphene sample extends to large distances of several micrometers. However, there is no obvious reason for this, at least on the basis of our current understanding of the graphene image states and the surface ionisation process of Rydberg atoms. A possibility is the large extension of the image states, which has been observed already for low principal quantum numbers by two-photon photoemission spectroscopy [100].

Velocity dependence of resonant Rydberg surface ionisation

As seen in the previous chapter for the graphene sample, the dependence of the surface ionisation magnitude on the collisional velocity $v_\perp$ of the Rydberg atoms can pose a challenge to a full understanding of the ionisation dynamics. This is especially true for electronically structured surface systems where the velocity dependence appears to significantly differ from a free-electron metal.

The difficulty of understanding the velocity dependence of surface ionisation becomes apparent when considering that the recorded ion signal is a convolution of the surface ionisation dynamics with the experimental methodology [73], resulting in a measurement of ion detection probability rather than directly observing the surface ionisation process. Specifically, a signal at a given extraction field indicates that ions are formed by surface ionisation at a spatial position with respect to the surface such that the ion could be extracted at that field. No signal does not indicate that there is no surface ionisation occurring at that field.

For example, the presence of the ion extraction field can increase the distant-dependent ionisation rate by lowering the height of the saddle point between atom and surface [241]. Equally, the velocity spread of the selected Rydberg atoms and the experimental geometry introduce a spread and shift in ionisation distances [96], where the experimental traces can be fitted semi-empirically as demonstrated via Equation 1.18 in [69]. The latter model was shown to be in good agreement for the most red-shifted ($-k_{\mathrm{max}}$) Stark states where the electron charge is orientated towards the surface. This case most resembles the classical treatment and is straightforward to illustrate by tunneling through the potential barrier formed towards the surface. Within the context of the decelerator to be introduced later and to operate in more intuitive territory, the theoretical predictions in this chapter are made for and the comparable experimental data taken with a gold surface.

5.1 Ionisation distance shift of charge transfer

The most obvious outcome of a reduced collisional velocity is the increased amount of time the Rydberg atom will spend when traversing a fixed distance increment ΔD, thereby expecting a shift towards greater distances at which surface ionisation occurs. The probability of this process as a function of distance D is calculated with the time-dependent wave-packet CWDVR technique introduced in section 2.2. The aim here is to investigate how the distribution of distances scales with increasing principal quantum number n. Earlier theoretical studies were restricted to lower n [73] thereby making it necessary to extrapolate the results from low n to the n-range experimentally available. As stated initially, the calculations are carried out with a surface potential modelled as a free-electron metal, the Jellium-model introduced in section 1.4.

5.1.1 Probe state selection

In order to compare the theoretical results to prospective data from the decelerator device (shifted excitation configuration, labelled here as *up*), it is advantageous that the initial quantum state for wave-packet propagation matches that which will be employed in the designed experimental geometry. The calculations are implemented with the maximum red-shifted Stark state $-k_{\max}$. In the geometry of the surface experiment (*down*) these states are orientated towards the surface. As explained in section 2.3, the high-dipole-moment state(s) employed for Rydberg-Stark deceleration are blue-shifted ($+k$), low-field seeking states which are vacuum orientated in the surface experiment. This is however only an apparent contradiction since the polarisation of the Rydberg atoms, compare Figure 1.2 for exemplary wavefunctions, is defined to the direction of the electric field and thereby at an arbitrary orientation in the lab frame. On the timescale of translational motion the Rydberg state polarisation is able to follow the field direction adiabatically such that states that are initially red-(blue-)shifted when formed could be rotated around so that they are blue-(red-)shifted with respect to the surface [7]. Evidently, the caveat to avoid in this process is the traversal of zero-field regions where the Rydberg Stark state would lose its quantisation axis and thereby electron polarisation.

On the other hand, as hinted at above, the red states are the most conclusive and easiest to interpret since the charge distribution is transfered from the spatial region between the ion and

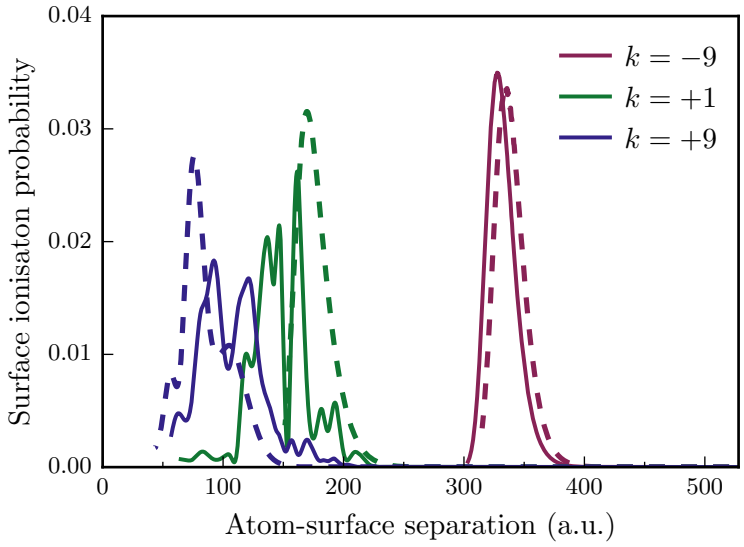

Figure 5.1: Surface ionisation probability as function of distance D from the surface calculated from wave-packet propagation for representative members of the $n = 10$, $m_l = 0$ Stark manifold at a constant velocity of $v_\perp = 463\,\mathrm{m\,s^{-1}}$. Compared are the propagation of the most red-shifted ($k = -9$), a mid-manifold ($k = +1$) and the most blue-shifted state ($k = +9$) in zero extraction field (solid lines) and at an ion-extraction field of 1×10^{-6} (a.u.), $5.14 \times 10^5\,\mathrm{V\,cm^{-1}}$ (dashed lines). The $k = -9$ Stark state at zero field is the state used for velocity dependent calculations.

the potential barrier directly towards the surface. The blue states, with their charge distribution located towards the vacuum side, have to pass the ion core towards the surface during charge transfer, likely leading to different ionisation dynamics as in the case of ionisation rates of Stark states in an electric field [75]. Mostly though, the Stark state specific dynamics are likely to be influenced by the way in which energy level crossings are traversed.

Zero-field adiabaticity

The different dynamics of red and blue states are illustrated in Figure 5.1 displaying the calculated surface ionisation probability as the electron density is transferred into the surface with decreasing distance as schematically depicted in Figure 2.1. The red state shows a smoothly increasing, Gaussian-like ionisation probability with a defined maximum in zero field (solid line) and for an applied ion-extraction field (dashed line) where the strength of the electric field is $F < 1/16n^4$. For the field applied, the Gaussian shape can also be observed for the mid-manifold state whereas the blue state shows deviations from this behaviour. These distortions are even more pronounced for the field-free case with blue and mid-manifold state significantly overlapping. For the red and the mid-manifold state, the traces display a behaviour as expected

with ionisation occurring closer to the surface with increasing k; note that the indicated distance is the separation of the ion core from the surface, rather than the atomic centre of mass. Also, ionisation is shifted towards greater distances in the non-zero electric field whereas the probability curves for respective red states do not differ greatly.

In section 1.4 it was discussed that interaction with the image charge perturbs the Rydberg levels leading to crossings which increase in number with decreasing atom-surface separation. Due to the density of states, blue-shifted states are more likely to encounter level crossings closer to the surface. In a purely homogeneous electric field the crossings occur diabatically in the hydrogen atom, but close to the surface the cylindrical symmetry is broken and the crossing can be partly adiabatic. At these crossings the initial wavefunction polarisation can get lost and ionise with mixed or exchanged polarisation. Thereby, the observed profiles for the blue and red state at zero extraction field can be explained by increased adiabaticity or by the traversal of more crossings due to Stark states lying closer together. That none of the electron density is lost but rather changes its polarisation is confirmed by the integral of all traces in Figure 5.1 as 0.999.

Thus, the selection of the maximally red-shifted state at zero field as the initial state for the calculations can (further) be motivated. It is assumed that the red state is sufficiently far away from the surface in the region of predominant ionisation such that less or no level crossings are encountered and that nonadiabatic effects are negligible. The comparison between the zero-field case and the applied field case suggests this is feasible since the profiles for the red states of either calculation are very similar in shape, magnitude and position of the maximum. Without an extraction field the ionisation dynamics may be described in an idealised, more "pure" way.

Determining of ionisation metrics

The velocity range over which the red states are propagated in the calculations is chosen to match the accessible range a decelerator device can span [242]; the forward velocities are $\{50,$ $100,$ $200,$ $400,$ $800,$ $1600,$ $3200,$ $6400\}\,\mathrm{m\,s^{-1}}$ where the perpendicular component is used in the calculations. An example for $n = 5$ is shown in Figure 5.2. It can be seen that with decreasing velocity the profiles shift towards greater distances with increasing maxima and thereby decreasing widths. These characteristics are extracted as demonstrated in Figure 5.2 and used to

compare the results for a range of principal quantum numbers from $n = 2$ to $n = 20$. Beyond $n = 20$ grid, sizes required to achieve convergence approach the memory limits of a workstation and the execution time for $v < 50\,\mathrm{m\,s^{-1}}$ exceeds reasonable run times. It was not attempted to run these calculations on a supercomputer, which should be able to process higher quantum numbers in significantly less time.

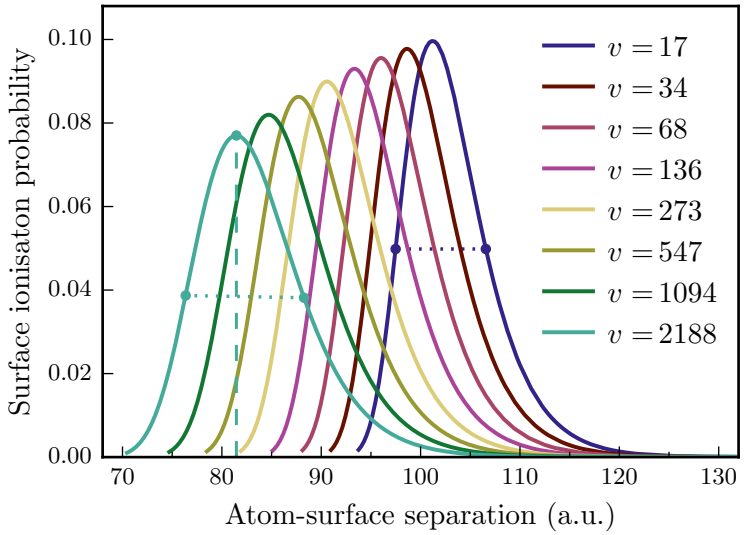

Figure 5.2: Wave-packet propagation of the most red-shifted $n = 5$, $k = -4$, $m_l = 0$ Stark state with no extraction field present for a set of collisional velocities. For evaluation three different features are extracted from these profiles: the distance position of the maximum (mode), the height of the maximum and the full width at half maximum marked accordingly for the $v = 2188\,\mathrm{m\,s^{-1}}$ trace.

When calculating the integral of all traces as shown in Figure 5.2 the value is constantly 0.999, which reflects a setting in the code that the calculations are terminated when a population of $10^{-3}\,\%$ of the initial electron density is reached. It thereby means that the great majority of the electron density escapes through the surface boundary into the metal.

With the Rydberg atom as a surface probe in mind, the change in the surface ionisation probability profiles can be used to aid the detection of discrete electronic features. If a far extending image state Ψ^n_{img} and a Rydberg state are in resonance over a specific distance range due to the differential variation of these energies with the atom-surface separation, the increased ionisation rate and smaller distance spread will make the atom more sensitive to the image state at a lower velocity since the interaction time between the two will be increased. It also allows to probe different distance regions by setting the velocity.

Ion core acceleration

Another approximation made in these calculations is the assumption that no forces are acting on the atom. However, when the electron density decreases during the ionisation process, the ion core will be less shielded so the atom gains a partial charge which can interact with its image charge resulting in an attractive force. The dynamics of electron and ion core as a compound system can be described with a mean-field (Ehrenfest) approach [243], the ion core moves in the average field of the electron, the expectation value of the electronic Hamiltonian. Results including this mean-field potential are displayed in Figure 5.3.

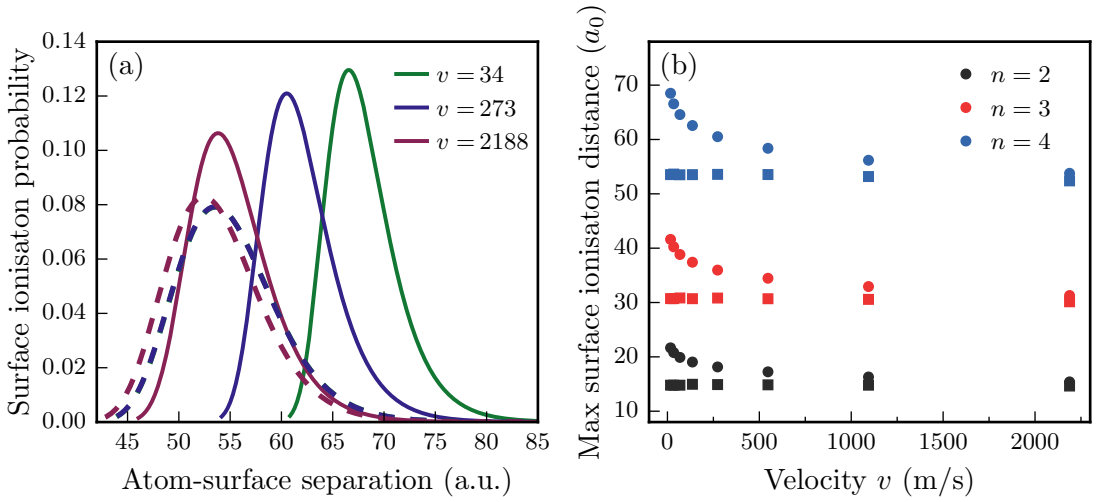

Figure 5.3: Comparison of velocity dependent wave-packet propagations for $n = 4$, $k = -3$, $m_l = 0$ at constant velocity (solid lines) and with the ion core accelerated (dashed lines) in (a). Panel (b) compares the distance at the maximum of the ionisation distribution for constant velocity (dots) and with mean-field acceleration (squares).

It can be seen that the velocity dependence is drastically altered with the mean-field approach. The force on the ion core leads to an acceleration towards the surface shortening the ionisation distances. Only for the highest velocity trace at $v = 2188\,\mathrm{m\,s^{-1}}$ is the ionisation probability shifted towards smaller distances compared to the lower velocity traces. The force on the ion core appears to equilibrate the probability distributions below a certain velocity.

It needs to be noted that under experimental conditions an applied extraction field is counteracting the force on the ion core. These fields are very high for low n so that wave-packet calculations need to be performed separately for a wide range of extraction field magnitudes were the effect of the force balancing to be studied systematically as well. Since this enlarges the parameter spaces beyond viability for the range of states examined here, it requires another

study solely devoted to this issue. It could be motivated that having neither effect included as zero-force on the ion core approximates a force balanced by the two opposing contributions as net-zero.

5.1.2 Ionisation distance scaling

From Figure 5.3 (b) with no force on the ion core, it can be seen that with increasing n, and thereby increasing orbital size, the mean ionisation distance steadily shifts towards greater distances at each velocity and also shifts towards greater distances for a constant n with decreasing velocity. In order to normalise for the size of the orbital, the distance axis can be scaled by n^2 as for the distance data displayed in Figure 5.4.

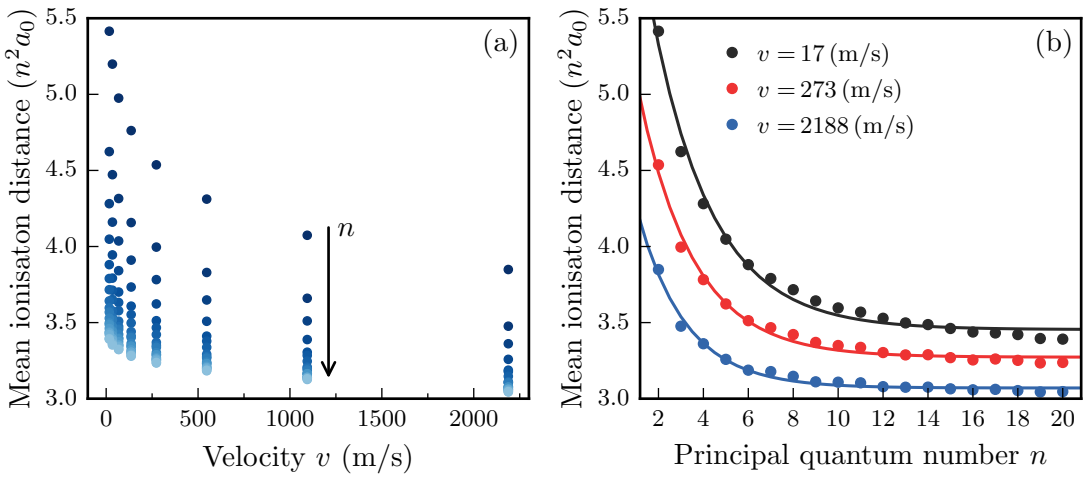

Figure 5.4: Ionisation distance scaled with the orbital size over collisional velocity for all principal quantum numbers of the $-k_{\max}$ state in (a). Distances at a constant velocity are decreasing from $n = 2$ (dark blue) to $n = 20$ (light blue). Selected constant velocities as a function of n overlaid with an exponential curve fit in (b).

For simplicity, the data evaluation assumes that the ionisation probability distribution profiles are symmetric and not slightly asymmetric so that the position of the maximum ionisation rate is equal to the mean distance (but strictly speaking the mode). The same goes for the width of the distribution which is determined as the width at half maximum height.

To investigate the velocity dependence of the ionisation distance for different principal quantum numbers, the distance data in Figure 5.4 (a) is displayed as function of n for selected velocities in (b). Additionally shown is an exponential least squares fit of the form $A \exp(-Bx) + C$ which best approximates the data. This model could be motivated to rep-

resent a relationship of the orbital size r and mean ionisation distance with varying velocity, where the factor A describes the distance $D_{r\to 0}$ and $C = D_{r\to\infty}$, with the dimensionless factor B controlling the scaling between distance and n. This relationship could be useful for extrapolating to higher n; the factors from the fitting function for all velocity sets are listed in Table 5.2.

Table 5.2: Fit parameters for exponential fit $f(n) = A\exp(-Bn) + C$ of principal quantum number n dependent data as displayed in Figure 5.4 for the respective data sets of collisional velocity v.

$v\,(\mathrm{m\,s^{-1}})$	$A\,(n^2a_0)$	B	$C\,(n^2a_0)$
17	3.96	0.34	3.45
34	3.65	0.38	3.41
68	3.34	0.39	3.37
136	3.06	0.40	3.32
273	2.75	0.41	3.27
547	2.46	0.43	3.22
1094	2.14	0.44	3.15
2188	1.89	0.47	3.07

As can be observed from Figure 5.4 (b), the scaled ionisation distance drops towards a minimum with increasing n. This scaled minimum distance appears to be independent of the orbital size for large Rydberg radii with only the velocity contributing. When examining the fitting coefficients more closely, the biggest changes are found for $v \leq 300\,\mathrm{m\,s^{-1}}$ with a linear correlation for higher velocities. For high n and $v \to 0$, the ionisation distance (C) converges towards the value of $3.48n^2a_0$ predicted from the over-the-barrier model.

Two conclusions can be drawn from these simulations of the idealised case of surface ionisation. First, greater changes in ionisation distance with n can be observed for lower velocities, which points towards a greater sensitivity to a resonant charge transfer and makes slow Rydberg atoms more appropriate as a probe state. Further, it can be noted that the n-dependent shift in ionisation distances can introduce a factor that needs to be considered when low principal quantum numbers in simulations are compared to experimental results with high-n Rydberg states.

Ionisation width and rate

When the velocity is decreased, the detection efficiency is affected twofold, judging by the preceding results. For a decreasing momentum of the remaining ion core after ionisation, the minimum detectable distance from (1.14) between ion and surface is decreased, leading to an increased detection efficiency indicated by more of the probability profile being in the region up to the minimum distance. This overlap can additionally be increased when the probability profile is shifted towards greater distances with decreasing velocity.

Using this argumentation, it can be further motivated that a decreased collisional velocity becomes an asset for utilising a Rydberg state as an electronic surface probe by considering the half width and maximum ionisation probability as shown in Figure 5.5.

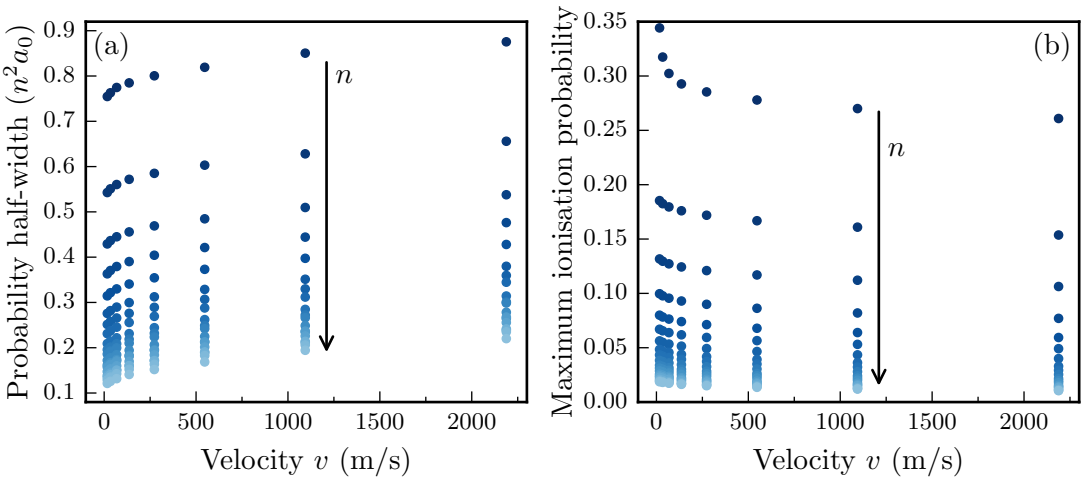

Figure 5.5: Wave-packet propagation results as in Figure 5.2 for the $-k_{\max}$, $m_l = 0$ state from $n = 2$ to $n = 20$ for a set of collisional velocities from which the full width at half maximum and maximum ionisation probability were extracted from each trace. The colour coding is set as before, showing the increasing n-range from $n = 2$ (dark blue) to $n = 20$ (light blue).

The scaled half-width displays an analogous behaviour as the mean distance in Figure 5.4 with traces of the same n showing decreasing half-width relative to the increasing orbital size, where traces of constant n show the reciprocal functional relationship. This means that it is more likely that the probability distribution lies within the detectable distance region, also increasing the amount of extracted ions. Equally, the traces appear to settle towards a minimum with increasing n. Since the integral of the probability is constant, the width and height of the distributions for different n and v are linked. It is thereby unsurprising that the (unscaled) maximum probability decreases with n and with velocity and the largest changes can be observed

for low n and low velocities. Overall, it appears that the probability distribution converges for surface ionisation at large principal quantum numbers. This makes it appealing to study low n at low velocities, which poses a challenging task experimentally.

5.2 Experimental investigation with limited velocity ranges by supersonic expansion

In order to provide a comparison to the velocity dependent calculations and to potential measurements performed with the decelerator, a (systematic) surface ionisation study was conducted with the velocity distribution that is attainable from a pulsed nozzle. The data in the previous section was calculated over a wide range of velocities to clearly show changes in the ionisation behaviour.

The difficulty of studying the process of Rydberg surface ionisation is in matching simulations and results from the Rydberg surface experiment. Foremost, the parameter spaces (principal quantum numbers, velocity, extraction field) of the modelling and those available from the experimental apparatus do not necessarily overlap and the geometry of theory and experiment are different with collisional angles at 90° and 20°, respectively. For atomically flat surfaces, however, the parallel velocity component is not expected to be of great relevance. Nevertheless, a real surface material is likely to be structured in some way contrary to the theoretical surface potential, which assumes a perfectly flat conductor. This structure can create variations of the surface potential whose root mean square field can reach values that can significantly alter the surface interactions, especially when the incidence angle is decreased [91, 244].

5.2.1 Gold sample preparation

For the measurements presented here a gold surface has been used, which, as a free-electron metal, can be described with the Jellium model for the surface potential as is also used for the wave-packet calculations before. The surface sample has been prepared by evaporation of gold on a silicon wafer which is then transferred onto the sample mount in the vacuum chamber; an image of the sample is shown in Figure 5.6. The roughness of the gold surface was determined via atomic-force microscopy (AFM) which gives a root mean squared roughness of 2 nm to

7 nm; the classical orbital size for the Rydberg states used here is 66 nm to 170 nm.

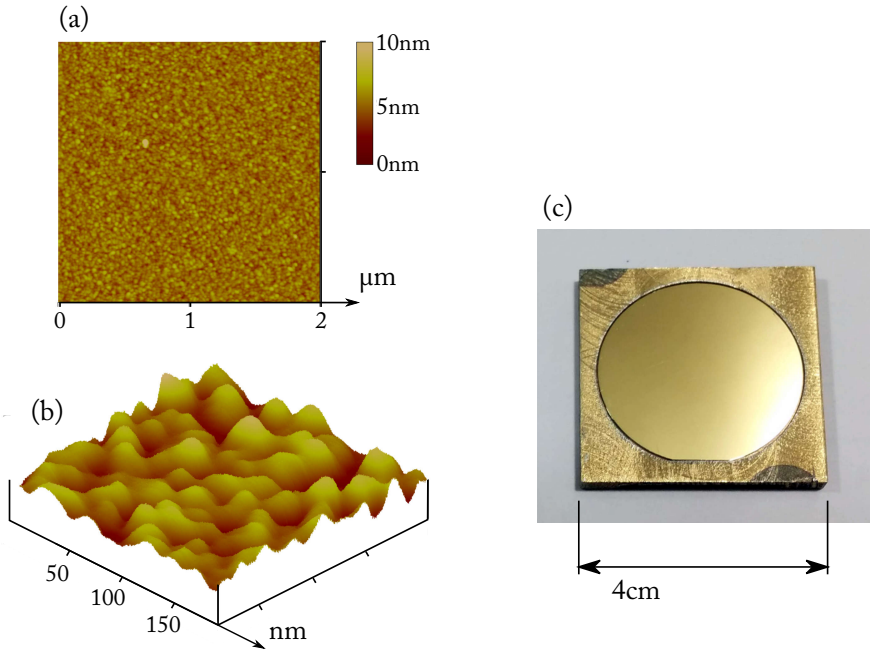

Figure 5.6: Gold surface sample used for all measurements in the text that refer to an Au sample. Gold has been evaporated on a silicon wafer mounted on a molybdenum holder in (c). A spare sample has been characterised by AFM spectroscopy in (a) and (b), note the different length scales.

In reference [91], the surface potentials were used to model the spread in surface ionisation versus extraction field of xenon with the over-the-barrier model (OTB). The corrugated surface potentials were reconstructed and used to model surface ionisation of hydrogen but did not create a good fit for experimentally observed traces [179]. A comparable gold surface was modelled therein and found to exhibit surface patch fields of magnitude 2 V cm^{-1} at a distance of 600 nm. It was concluded that the presence of patch fields cannot simply explain the spread in ionisation distances and generally that surface roughness is not the source of it.

5.2.2 Molecular beam velocity selection

A variation of the impact velocity can be achieved by delay-selecting a part of the velocity distribution as generated by the pulsed valve operated with different seeding gases as depicted in Figure 3.1. Velocity distributions for purely expanded NH_3 and 20% NH_3 seeded in helium, neon and argon are shown in Figure 5.7. It can be observed that only the pure ammonia beam and seeding in He deliver usable beam intensities as measured by Rydberg field ionisation. It

has to be considered that the signal magnitude from surface ionisation is approximately reduced further by a factor of 10 compared to the field ionisation rendering seeding in Ne and Ar virtually unusable.

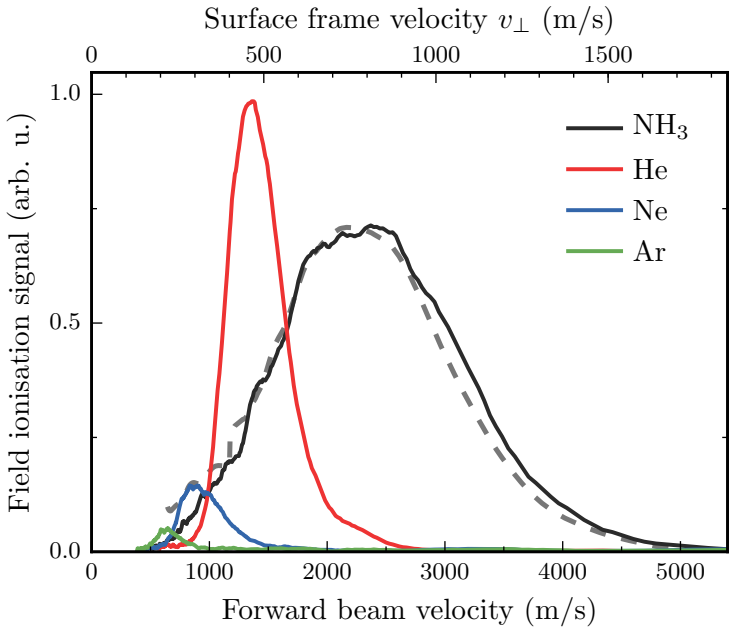

Figure 5.7: Signal intensity of direct field ionisation of a pure NH_3 molecular beam and of mixtures of 20% NH_3 in the respective rare gases normalised to the maximum intensity of the He beam. The velocity is determined from the delay of the Rydberg excitation and is approximately given in the frame of the beam axis as "forward"; an uncertainty arises since beam axis and direction of laser propagation are at an azimuthal angle φ=20 as displayed in Figure 3.1 and a polar angle θ=45. Additionally shown is the perpendicular component of the forward velocity. A trajectory fit for the NH_3 velocity distribution is included, with a spread $\sigma = \sqrt{kT/m}$ for $T = 82\,\mathrm{K}$ (dashed line).

The likely reason for the low intensity in the case of neon and argon is the separation of the lighter hydrogen with an enrichment of the carrier gas on the beam axis [161, 245], which is greatly intensified with the (unusually) long flight path of the gas packet from the orifice to the interaction region. This diffusive depletion of the lighter species on the jet axis diminishes the availability of lower velocities but would still leave large accessible velocity ranges at higher velocities, particularly for the pure ammonia beam. The overall aim, however, is to attain lower velocities, most of all regarding the particle acceptance of a decelerator, which is aided by a decreased (transverse) temperature of the gas packet that is significantly lower for the helium seeded beam. Despite a smaller usable velocity interval, the density of hydrogen atoms at lower velocities is greater when seeding in helium compared to the pure ammonia beam. This is also beneficial for the operation of the decelerator; a likely loss of particles is mitigated by a higher

number density of initial particles. Since the results here were also intended to provide a basis for comparison to measurements performed with the decelerator, the majority of data was recorded with hydrogen produced from ammonia seeded in helium.

5.2.3 Stark state selection uncertainty

The resolution of the Stark states is addressed in section 3.3 as an estimated $k_{\text{real}} = k_{\text{fit}} \pm 2$, *i.e.*, the determined k-state could be off by one towards lower or higher energy. Since the measure for comparing surface ionisation is often the integrated ionisation profile, this issue is addressed by comparing the Stark spectrum for $n = 28$ in Figure 5.8. Generally, the traces in (a) show the same qualitative behaviour as previous measurements for gold [69].

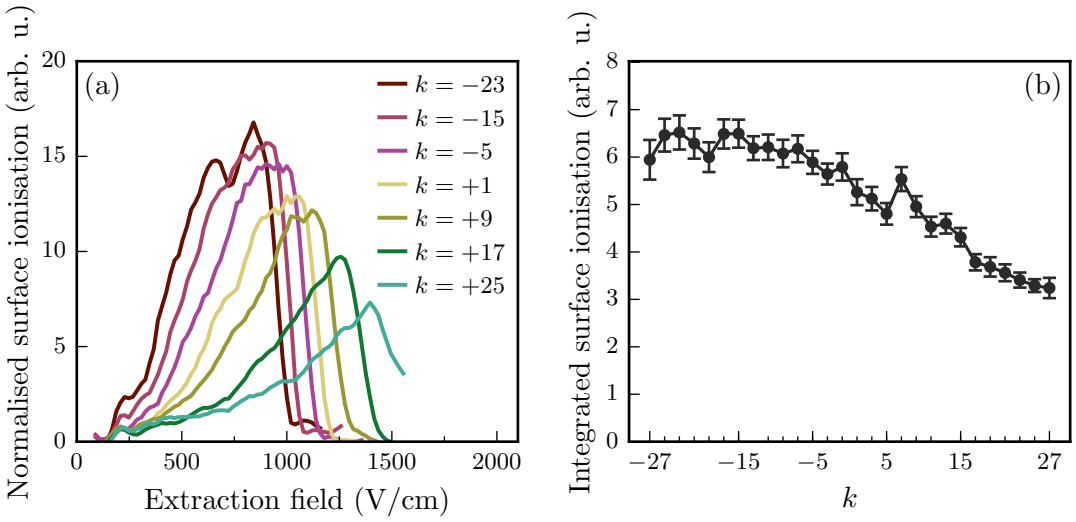

Figure 5.8: Surface ionisation profiles for various Stark states of $n = 28$ with $-k_{\text{max}} = -27$ to $+k_{\text{max}} = 27$ in (a). Traces are non-zero at high extraction fields due to high-field noise. Profiles are integrated up to the field value of the maximum before the onset of field ionisation in (b). Note that the data here was recorded with the newly designed extraction setup introduced in section 3.4.

With increasing k, the onset of surface ionisation is shifted to higher extraction fields reflecting the shift of the field ionisation threshold for more blue-shifted Stark states. All traces converge at approximately the same minimum field value, but progress differently with increasing field towards the high-field cutoff. The maximum that is then reached decreases with increasing k. The change of the integral from these trace shifts is depicted in Figure 5.8 (b) and does not result in an overall constant amount of integrated surface ionisation. Following the trend of the maxima of the k-traces, the integrated ionisation is decreasing with increasing k

and the ratio of the maximum and the minimum amount is ~ 2.

A linear regression of the data in Figure 5.8 gives a slope of -0.064 which results in a change of ± 0.128 in integrated surface ionisation for neighbouring Stark states with $\Delta k = \pm 2$. If this change in consecutive k states was included as an uncertainty in surface ionisation integrals due to ambiguous labelling, the error, at least in this case for $n = 28$, would amount to $\epsilon \approx 2.5\%$.

5.2.4 Reduced surface ionisation variability with collisional velocity

To investigate the velocity dependence systematically, surface ionisation was recorded for 31 delay settings with an increment of $\Delta t_{\mathrm{Ryd}} = 5\,\mu\mathrm{s}$ for a maximum red-shifted, mid-manifold and maximum blue-shifted Stark state of principal quantum numbers $n = 30, 35, 40$. Data was also taken for $n = 25$ but with a smaller velocity range due to technical complications and hence is not presented for comparison. The data for $n = 25$, however, shows the same trend as the other n presented below.

Figure 5.9 (a) representatively displays selected surface ionisation profiles for $n = 30$, $k = -1$ of data recorded with the described gold surface. Most notably in these profiles is a lower change with the collisional velocity in the normalised ionisation magnitude compared to earlier measurements. Previously, a pronounced increase in detection efficiency could be observed for a decreased velocity of the hydrogen projectiles [69], which is to be expected for a reduced momentum of the remaining ion core after the event of surface ionisation by Equation 1.13.

Since the experimental apparatus was already modified to some extent at this point, as presented earlier in section 3.2 to 3.4, it is conceivable that these changes in data recording in some manner contribute to this observation. In order to verify this, Figure 5.9 (b) depicts the maximum magnitude of the field ionisation signal over the range of hydrogen beam velocities. It can be seen that this curve follows the intensity of the molecular beam with a maximum matching the curve shown in Figure 5.7. These maxima are used to normalise the surface ionisation profiles to a common scale. Thereby it can be concluded that the data recording works as desired and the magnitude of the surface ionisation profiles are a valid representation.

To further investigate the velocity dependence of different states $|n, k\rangle$ and velocities, the integrated surface ionisation traces are chosen to be the central metric of comparison. The collisional velocity should affect the extraction profiles broadly by increased or reduced extraction

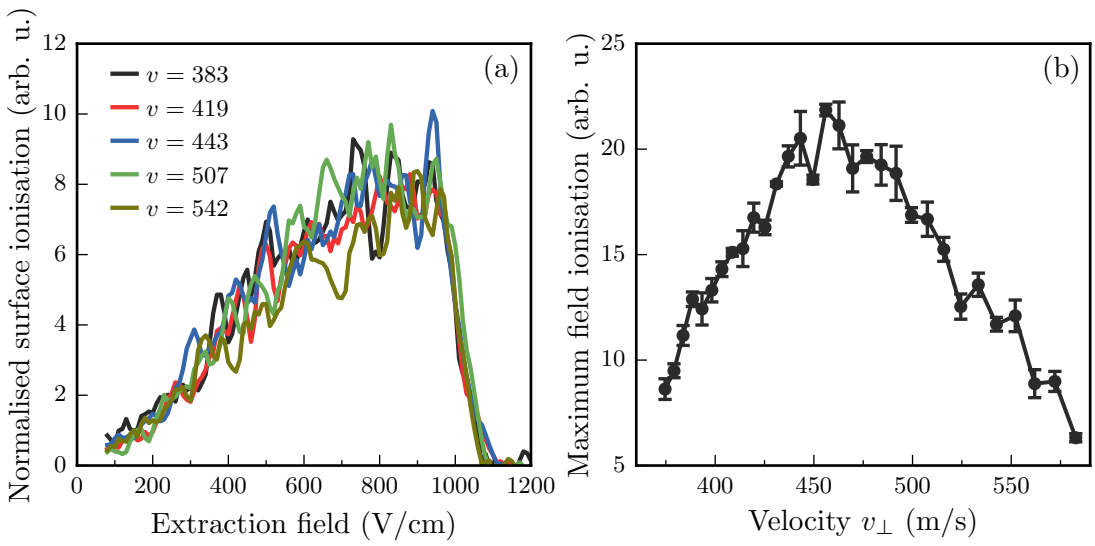

Figure 5.9: Selected normalised surface ionisation profiles for $n = 30$, $k = -1$ recorded in sequence over a range of collisional velocities v given in the surface frame ($v_\perp$ in $\mathrm{m\,s^{-1}}$) and selected from a beam of 20% ammonia seeded in helium in (a). The respective unnormalised maxima of the field ionisation signal are displayed in (b) for the whole range of collisional velocities. The field ionisation maxima in (b) are used to normalise the surface ionisation traces in (a).

efficiency over the whole range of extraction fields. Figure 5.10 shows integrated surface ionisation profiles for the different Stark states per principal quantum numbers over the range of velocities. The low spread in the traces over extraction field translates into the traces for the extreme and midrange members of the Stark manifold alike.

First, it can be seen that the intensity of the integrated surface ionisation for the most blue-shifted states exceeds the magnitude of the most red-shifted and the mid-manifold states for all n whereas the differences between the mid-manifold and the red states are not very pronounced. This trend is in contrast to the one discernible in Figure 5.8 where the magnitude of the surface ionisation signal for the red state is roughly double that of the blue state. It has to be noted that the experimental data presented in this section was recorded with the previous detection setup which suffered from a reduced detectability for field ionisation of blue-shifted states. Since the normalisation is carried out through the recorded intensity of the field ionisation signal, it is legitimate to assume that a systematically lower field signal for the blue states results in a higher normalised surface signal. It again underlines that this part of the experiment needed to be revised.

Since this effect of detection efficiency of the field signal is most pronounced for the Stark states within a manifold, it appears more conclusive to compare the data for the respective Stark

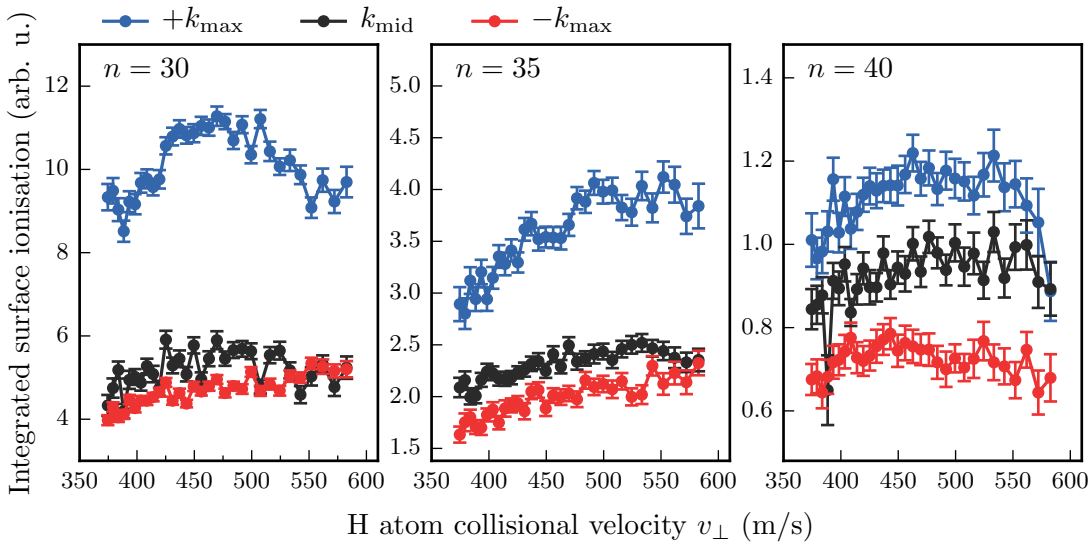

Figure 5.10: Integrated surface ionisation profiles for three different principal quantum numbers recorded over a range of collisional velocities for the maximum blue-shifted ($+k_{\mathrm{max}}$), a mid-manifold and the maximum red-shifted ($-k_{\mathrm{max}}$) Stark state. The velocity selection is achieved through delaying the Rydberg excitation of a molecular beam packet of 20% ammonia seeded in helium; ions are extracted not with the electrode stack shown in Figure 3.10 but a previous setup.

states to each other as depicted in Figure 5.11 and disregard the relative intensities of $k_i(n)$. In this way it can be seen that the integrated surface ionisation signal decreases with principal quantum number for all k states with larger differences between $n = 30$ and $n = 35$ than between $n = 35$ and $n = 40$, which is the behaviour as expected from the reduced integral caused by the field ionisation threshold shifting to lower field magnitudes for increasing n. Within the traces integrated surface ionisation appears to either decrease or be constant with decreasing collisional velocity. This apparent decrease is contrary to what might be expected from previous studies.

The data were recorded sequentially with increasing laser delay, thereby the maximum velocity was recorded first with continuously decreasing hydrogen atom velocity. The experimental apparatus was furthermore operated without the PID feedback loop to keep the source pressure of the molecular beam vacuum chamber constant. As shown in Figure 3.2, the field signal decreases with time. Since the velocity scans run over longer periods, this will affect both the amount of ions recorded from field and surface ionisation. Ideally, a variable signal strength should be compensated by the normalisation process. It could be argued that the ratio of ions produced from either ionisation process forms a linear relationship but that the charge multiplication at the microchannel plates (MCP) is nonlinear whereas the normalisation assumes a

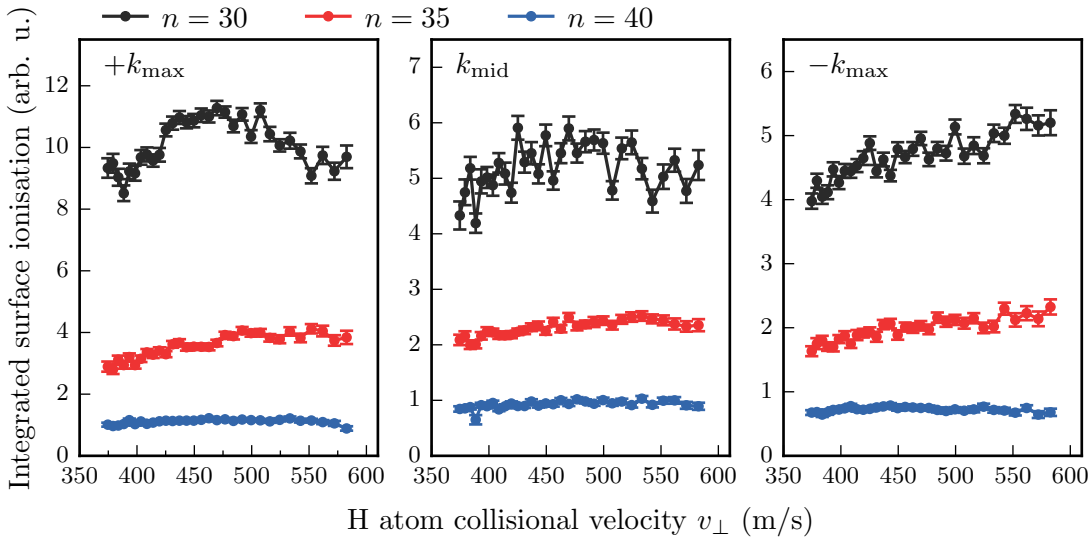

Figure 5.11: Data from Figure 5.10 rearranged for the maximum blue-shifted ($+k_{\max}$), mid-manifold (k_{mid}) and maximum red-shifted ($-k_{\max}$) Stark state per principal quantum number n.

linear relationship. For one, space-charge effects can cause saturation leading to a nonlinear pulse height distribution (pulse count rate over pulse height), but it was also shown that at increased event rates, the incoming flux of ions, MCPs exhibit a variable gain leading to nonlinear characteristics for the effective detection efficiency [246, 247].

Following this argument, the k traces in Figure 5.11 are constant with collisional velocity indicating that the error bars shown underestimate the true experimental fluctuations. The PID controller was installed in response to this degree of uncertainty introduced by the poor long-term stability of the Rydberg number density. It also demonstrates the experimental challenges of surface ionisation studies in systematically covering a larger parameter space.

Increased collisional velocities

To tentatively investigate an extended velocity range towards higher velocities, several scans were recorded with a gas packet generated from expansion of pure ammonia since the selectable range of velocities from the helium seeded beam is small relative to the mean velocity. This allows to cover a greater range of collisional velocity as illustrated in Figure 5.7.

Figure 5.12 shows scans of three different velocities $v_\perp$ for a mid-manifold $k = 0$ and the maximum red-shifted $k = -34$ state of the $n = 35$ manifold. Due to a higher intensity of the mid-manifold state, a usable molecular beam density could be attained for velocities further from the maximum of the velocity distribution. Traces were also recorded for $k = 34$ but not

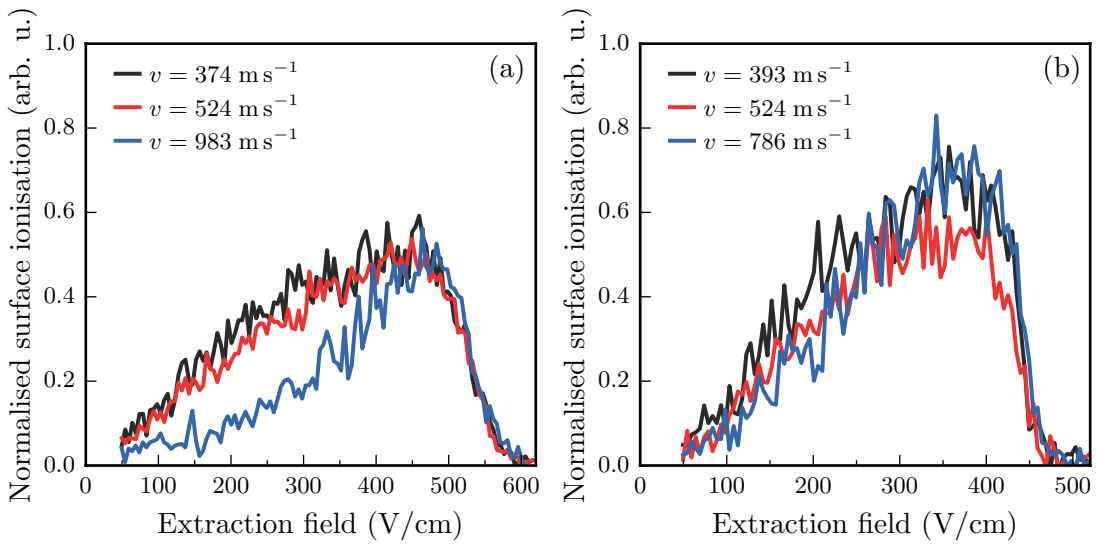

Figure 5.12: Surface ionisation profiles recorded for $n = 35$, $k = 0$ in (a) and $k = -34$ in (b), where the hydrogen atom velocities were selected from a molecular beam of pure NH_3. Displayed is the perpendicular component of the collisional velocity. The analogous behaviour of reduced variability with velocity in the magnitude of the traces over all extraction fields as observed for $k = -34$ is also exhibited by the surface ionisation profiles of $k = 34$ for the same collisional velocities (not shown here).

shown for them displaying qualitatively the same behaviour as $k = -34$. As before, the red state surface ionisation does not exhibit great variations with decreased velocity; a minor decrease of surface ionisation with increased velocity can be observed at lower extraction fields. A similar observation can be made for the $k = 0$ where a marked difference is noticeable for the (greater) highest velocity. In either case a shape change rather than a broad decrease appears to occur for the highest velocity.

In the case for the mid-manifold state, the maximum velocity from the pure ammonia expansion is ~ 3 greater than the minimum collisional velocity from helium seeding where the spread amounts to ~ 2. One the one hand, this range of velocities is possibly too narrow to observe any velocity dependent effects when comparing the velocity spread in Figure 5.4. On the other hand, it is also conceivable that the velocity dependence is yet best modelled with the meanfield acceleration included. In Figure 5.3 (a) it can be seen that a shift towards shorter surface separations, leading to reduced ion detectability at lower extraction fields, is only occurring for the highest impact velocity.

To ultimately examine the effects of the velocity of the hydrogen atoms projectiles undergoing surface ionisation, several steps need to be taken. First, the wave-packet propagation cal-

culations including the ion core acceleration need to be repeated for the whole parameter space spanned by collisional velocity and extraction field. Second, to rid the experimental results from ambiguities, all factors affecting the magnitude of (normalised) surface ionisation, such as the gas packet density and ion extraction dynamics, need to be further explored and comprehended. Third, it is likely that an extension of the velocity range to higher and especially to lower values will aid the understanding of the velocity dependence.

In summary, the Rydberg surface ionisation measurements at a gold surface presented here do not show much velocity dependence for a mid-manifold and extreme members of the Stark manifold alike. In comparison with previous work on Cu(100), this suggests that it is only when there are isolated resonance effects that the experiments are sensitive to the velocity dependence, despite the predictions of the theory (without inclusion of ion acceleration).

Towards an extended impact velocity range via a chip-based decelerator

From section 5.2 it becomes clear that an extended range of collisional velocities for a Rydberg atom approaching a surface contributes to the understanding of Rydberg surface ionisation itself. Furthermore, with the results for electronically structured Cu(100) in section 1.6, varying the collisional velocity can aid in identifying electronic features of the surface system, specifically for lower velocities. An illustrative and qualitative motivation for a reduced velocity of the hydrogen Rydberg atoms utilised as an electronic probe can also be drawn spectroscopically from the energy-time uncertainty

$$\Delta E \, \Delta t \geq \frac{\hbar}{2} \, , \tag{6.1}$$

by which a maximally increased interaction time Δt (through a minimised probe projectile velocity) reduces the transit-time broadening of a measurement. This can lead to a more precise response of the probe to the sample, which, in the context of the Rydberg atom approaching a surface, makes it conceivable to increase the likelihood of capturing discrete electronic features of the surface. Although at this stage other experimental factors are more likely to limit the "resolution" of the Rydberg atom probe such as the earlier described process Stark state selection.

Quantum size effects in the resonant charge transfer (RCT) between an H^- ion and a thin metal film are predicted to disappear in the case of increased collisional velocities where the RCT becomes indistinguishable from a semi-infinite metal surface [227]. The interaction characteristics are washed out because the charge transfer is finished before the electron can sense the finite size of the film. This possibly also applies to the graphene film sample in section

4.5, so that the measurements could show different characteristics with a reduced collisional velocity.

Similarly, the dynamics of electron transfer between a negatively charged ion and a Cu(100) surface are shown to be very different at low and high collisional velocities and are attributed to the finite time in which the electron passes into the metal and probes the band structure [117].

With the goal to develop the Rydberg surface experiment towards employment in further surface studies, not only an adjustable impact velocity would be advantageous but also the mitigation of factors that exacerbate the interpretation of surface ionisation measurements. Ideally, an extension of the apparatus as described in section 3.1 would fulfil the following objectives:

(1) Selective velocity control where decreased collisional velocities are especially crucial to maximise the interaction time between the Rydberg state and the surface.
(2) Mechanical control that allows one to perpendicularly direct the atoms towards the surface target to better match experimental data with theory and also reduce averaging effects by parallel traversal of the surface. This also allows a smaller spot size of the incident beam on the surface.
(3) Separation of the Rydberg species of interest from the trailing background gases from the supersonic expansion that could deposit as adsorbates on the surface.
(4) An arrangement that manages to hold the Rydberg atoms at a fixed separation D above the surface.

The overall aim thereby, to make the Rydberg surface experiment more sensitive and cleaner, is best achieved with a decelerator that accomplishes the stated criteria.

6.1 Rydberg-Stark decelerator design

Over the last decade several techniques to slow down Rydberg atoms and molecules have been developed by Merkt and coworkers; for a detailed overview see reference [248]. These devices include a four electrode arrangement that works as an atom mirror in which inhomogeneous electric fields are generated via time-dependent exponentially decaying kilovolt electrode potentials. This setup allowed for the deceleration and trapping of hydrogen Rydberg atoms in two dimensions [249, 250]. An extended version eventually created a three-dimensional on-axis trap that was successfully loaded with hydrogen Rydberg atoms and molecules with transverse

temperatures of $\sim$ 150 mK, where trapping times were limited by collisions with the background gas from the pulsed nozzle trailing the hydrogen species [251, 252, 253]. Eventually, their efforts led to a setup of 15 electrodes that accomplished an initial on-axis deceleration, 90° deflection and off-axis trapping of hydrogen Rydberg atoms [7]. Additionally, the apparatus was enclosed in a thermal shield connected to a pulse-tube cryorefrigerator to cool down the environment to 7.5 K for studying the lifetimes of trapped atoms [242].

These three-dimensional electrode configurations generate the inhomogeneous fields necessary for deceleration and deflection in the same way. Moving potential wells and traps are created by applying potentials that exponentially decay over time, thus they can in principle be classified as single-stage Rydberg-Stark decelerators. On the other hand, Stark and Zeeman decelerators for ground state atoms and molecules work on the basis of multiple stages that can either be operated by a sequence of electric or magnetic field gradients [254, 255] or with a genuinely movable three-dimensional trap design [256, 257]. The latter sequence of potentials was borrowed from a chip device that was developed by Meijer and coworkers, in which a micrometer-sized array of 1254 electrodes was used to decelerate and trap CO molecules by Meek *et al.* [258, 259], essentially forming a two-dimensional Stark decelerator on a chip. Here, an oscillating potential sequence creates potential wells that travel above the surface of the substrate and are able to trap low-field seeking (LFS) states in the wells rather than being slowed down by a travelling electric-field gradient [260].

The operational principle was adopted by Hogan *et al.* for decelerating and trapping hydrogen Rydberg atoms [242], whereby the number of stages could be reduced to 11 electrodes of millimeter size since only small electric field magnitudes are necessary to effectively remove kinetic energy from the moving Rydberg atoms with higher dipole moment. Furthermore, Hogan *et al.* patterned the electrodes on a printed circuit board (PCB), an easy to process template for various electrode layouts [261, 262] compared to the micrometer-sized array made of gold electrodes deposited on a glass substrate used by Meek *et al.*.

6.1.1 Printed circuit board architecture

The flexibility of the PCB architecture, physical constraints of the apparatus and the requirement to have either mode of the surface experiment accessible (regular surface experiment *down* and

with the Rydberg excitation point shifted to accommodate the decelerator *up*) made the design from reference [242] a suitable choice; see Figure 3.5 for an illustration of the used viewports in the respective configurations. The original design developed by Hogan *et al.* was comprised of 11 electrodes that are $0.5\,\mathrm{mm}$ wide and have a centre-to-centre spacing $d_z = 1\,\mathrm{mm}$ along the z-direction. The electrodes are spaced in parallel over the PCB surface with a length of $10\,\mathrm{mm}$ in the x-direction with enlarged end pieces in one direction for potential application and shaping of the resulting field distribution.

The electrode dimensions in [242] were chosen so that the resulting electric field traps accommodate the dimension of the Rydberg atom cloud constrained by the widths of the excitation laser beams. These spacings were adopted for the decelerator introduced here, but extended to 23 electrodes made from copper with an overall length of $25\,\mathrm{mm}$ in the z-direction; the construction is shown in Figure 6.1. The device is fitted between the surface sample holder and the extraction mesh, which are $10\,\mathrm{mm}$ apart. The design introduced here was meant to serve as the first stage of several prototypes that eventually fully satisfy the initially stated objectives. For example, off-axis guiding could be achieved by bending the PCB board so that the decelerator simultaneously acts as a deflector [37].

The point of Rydberg excitation is shifted away from the centre of the vacuum chamber in front of the centre of the surface in Figure 6.1 (a) and occurs between two parallel plates, where the lower plate is held at a constant positive potential and the upper one is grounded to create a homogeneous electric field. Since the shifted point of intersection between the Rydberg excitation laser beams and the molecular beam is not adjustable but fixed through the position and size of ports on the vacuum chamber, the decelerator was extended in length by increasing the number of electrodes to have the chip stretching from the point of Rydberg excitation to the midpoint of the circular surface sample. The basis set for creating the desired field distribution is six electrodes applied with the oscillating potentials, so that the sequence of electrodes can be continued successively to any total number of electrodes; see reference [263] for a 44-electrode decelerator.

Since the two-dimensional layout leads to a saddle point in the y-direction, the traps are not closed in this direction. For atoms escaping the traps and for atoms from the initial cloud that are not accepted by the decelerator, an aperture is installed at the end of the decelerator where the location is chosen to be before the position on the z-axis where the electric field

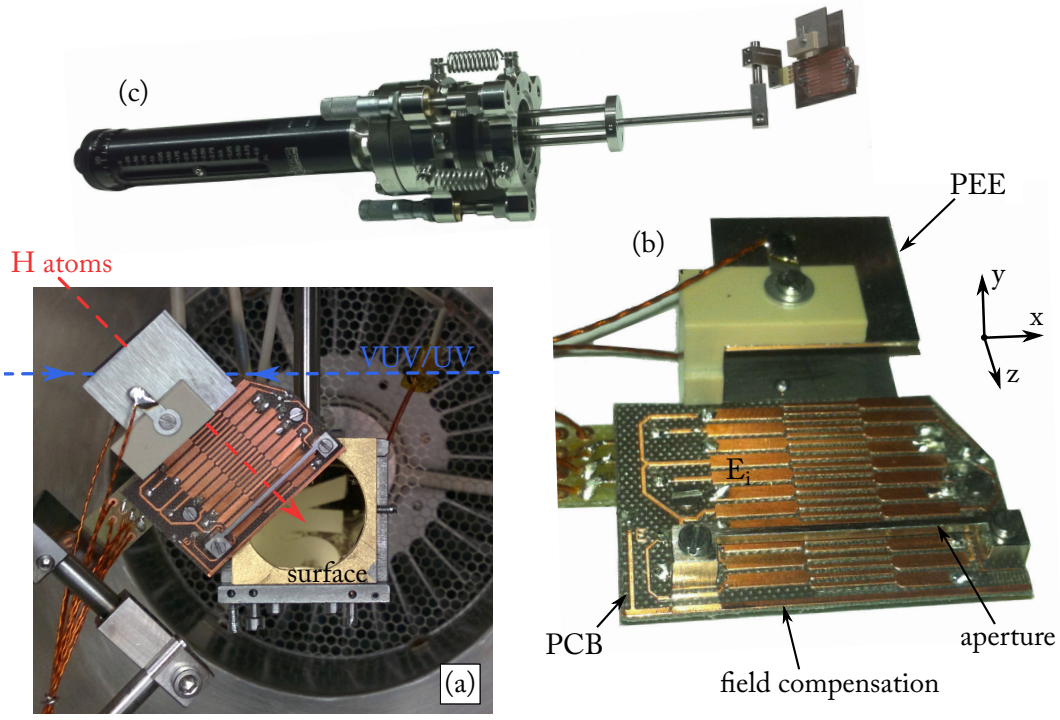

Figure 6.1: Construction of a two-dimensional decelerator that is interfaced with the Rydberg surface experiment in (a). The pattern of electrodes E_i is milled on a printed circuit board (PCB) and additionally equipped with a pair of parallel plates (PEE) for Rydberg excitation of hydrogen atoms with counter propagating laser beams, an aperture and a strip electrode across the PCB for electric field compensation in (b). The decelerator is mounted on a linear motion feedthrough in (c) that allows to retract the device from the interaction region as well as manipulation in all three dimensions.

configuration loses its trapping geometry. The aperture can be seen in Figure 6.1 (a) and (b). At the end of the PCB a single strip electrode is provided, which can be pulsed during extraction for field modification purposes.

6.1.2 Oscillating potential sequence and moving traps

The field distribution generated by the repeating sets of six electrodes is depicted in Figure 6.2 (b) and (c). In the zy-plane, potential wells are formed that act as a trap for LFS Rydberg states and they exhibit a well defined minimum with nearly circular shape near the trap centre. The minimum of the traps is set at $\sim 0.7\,\mathrm{mm}$ above the surface of the PCB and repeats every $3d_z$ ($3\,\mathrm{mm}$) so that a multitude of minima is formed along the z-direction. Along the chip normal the electric field displays a saddle point at $\sim 1.2\,\mathrm{mm}$ whose field magnitude depends on the maximum potential applied to the electrodes. It thereby defines the trap depth in this direction. The spacing between the chip and the lower edge of the aperture is chosen to be

above the saddle point at 1.5 mm

The static multipole configuration depicted in Figure 6.2 (b) and (c) is retrieved at constant potentials. When the potentials are oscillated with a frequency ω of the form

$$U_i = (-1)^i U_0[1 + cos(\omega t + \phi_i)] \tag{6.2}$$

with ($i = 1-6$), as shown in Figure 6.2 (a), the field minimum moves along the chip surface with a constant velocity $v_z = 3d_z\,\omega/(2\pi)$. The potential span from peak to peak of the potentials is $2U_0$. The sinusoidal potentials are phase-shifted by $\phi_i = (i-1)2/3\pi$ so that electrodes $\{1, 4\}$, $\{2, 5\}$ and $\{3, 6\}$ have the same potential shapes but of opposite magnitude [264].

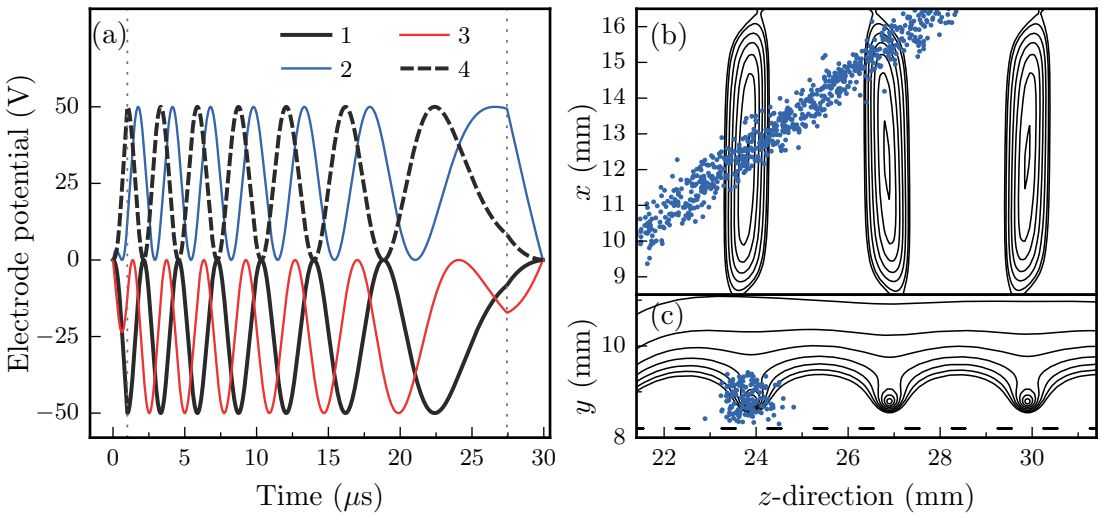

Figure 6.2: Oscillating potential sequence for a set of six electrodes repeatedly patterned on a printed circuit board with a phase shift of $2/3\pi$ for consecutive electrodes and a magnitude of $U_0 =$ 25 V in (a). For clarity, sequences for electrode 5 and 6 are omitted. Grey dotted lines mark linear potential ramps at the beginning and the end of the potential sequence. The initial frequency ω_0 for the incoming velocity of 1345 m s^{-1} is chirped to generate traps moving at a final velocity of 100 m s^{-1}. The resulting electric field distribution generated by the potentials at the end of the initial ramping at 1 µs is depicted up to 80 V cm^{-1} in (b) and (c) with contours in steps of 10 V cm^{-1}. The chip starts at 20.5 mm with a total length of 25 mm. Additionally shown are the initial particle clouds from the trajectory simulations (blue circles) as a slice in the middle of the chip between the electrode end caps in (c) and in full width in (b) at the height of the minima at about 0.7 mm above the PCB that is positioned at 8.2 mm. Compare the beam angles in Figure 6.1 for the 45° between the z-axis of the decelerator and the excitation laser beams resulting in the orientation of the gas packet.

At a constant frequency, the traps move with a constant velocity along the chip, guiding Rydberg atoms in them. When a linear chirp is applied to the frequency $\omega(t) = \omega_0 + kt$, the

velocity of the traps can either be increased or decreased, thereby accelerating or decelerating particles that are trapped in them by an acceleration a_z in the z-direction, such that the potentials oscillate over time of the form $\omega(t) = \omega_0 + (2\pi/3d_z)a_z t$ with the frequency ω_0 that corresponds to the initial velocity v_{in}. To hold particles above the chip, the potential sequence merely needs to be interrupted by a phase where all electrodes are held at a constant potential [242].

The distance between the formation of the first and last stable potential minimum sets the distance available here for deceleration at $19.1\,\mathrm{mm}$. At the beginning and the end of the potential sequence, a linear ramp towards the maximum magnitude U_0 is applied and is marked accordingly in Figure 6.2 (a), which was shown to increase the phase-space acceptance of the device [242]. These times are not included in the deceleration phase of the sequence; the generation of the potential sequences is set up so that the deceleration time is calculated from the constant z-position of the first minimum to the last minimum, merely adding the ramping times to the overall sequence.

Potential waveform generator electronics

In order to create the (analog) oscillating potentials that are applied to the PCB electrodes, an arbitrary waveform generator was constructed based on a 32-channel high-speed digital I/O PCI card with a sample rate of 20 MHz. This approach enables direct integration with the centralised control PC at significantly reduced cost compared to an external function generator. The Nyquist limit, by which the sampling frequency that reconstructs the analog waveform output needs to be at least twice the highest frequency of the waveform, is sufficiently undercut since the potential frequency ω is at most $400\,\mathrm{kHz}$ so that bandwidth limitation during signal generation is of no concern. Also, an external waveform generator is usually limited to an analog output of ± 5 V or 10 V, not covering the whole DC range needed for creating the electric field traps by U_0, requiring an amplifier in any case downstream of the waveform generation.

Here, the digital-to-analog conversion and amplification are carried out differently, as schematically shown in Figure 6.3 (a). The potential waveforms are generated in the control software in a separate thread for the three different positive channels with a depth of 10-bit per channel. The assignment of the ten bits of calculated magnitude A_i per time step as defined by

the sample rate ($A_i^{\max} = 1023$) are done via bitwise operations ("bitwise or" and bit shifts) on the 32-bit output port as demonstrated in the following for one channel in simplified form.

```
left = np.uint32(PCBPot[1,:])
self.DOOut = np.zeros(np.size(left), dtype=np.uint32)

# buffer entry at each sample rate step
# left[i] = PCB potential magnitude A(ti)
for i in np.arange(0, np.size(left)):
    self.DOOut[i] = self.DOOut[i] | left[i] << 16 | right[i] << 4
    # set clock bit alternatingly
    self.DOOut[i] = self.DOOut[i] | np.fmod(i+1,2) << self.__clockBit

# write buffer to port
self.__DIOCard.WritePort(ctypes.c_void_p(self.__DOOut.ctypes.data))
```

The waveform potential arrays are constructed in the software, loaded into the memory of the PCI card and the port written every time a trigger pulse is received in a sequence as shown in Figure 6.3 (b). The full code implementation of the waveform generator module can be found under GitHub/mikekohlhoff.

The 10 TTL pulses per channel produced by the PCI card are subsequently recombined in designated digital-to-analog (DA) converter chips to be output as a voltage. In order to have the magnitude of the waveform potentials variable, the amplification of the DA converted signal is not fixed. This step is combined with a first amplification stage in the same instrument up to a maximum of $U_0^{\max} = \pm 10\,\mathrm{V}$. A further (fixed) amplification stage is housed in a separate device that is hard-wired to a feedthrough that connects all electrodes of the decelerator inside the vacuum chamber.

The first, variable, amplification stage can be regulated from $0-100\%$ which is further scaled by the second stage of amplification. The chips used in the first stage, however, were revealed to be bandwidth-limited beyond a certain gain, which limits the overall output to $U_0 = \pm 25\,\mathrm{V}$. This is deemed to be sufficient for the range of quantum numbers envisioned to be used here in comparison to reference [242].

Despite its initial attractiveness for systematic device integration and great material cost savings, the author does not encourage the reproduction of commercially available electronics.

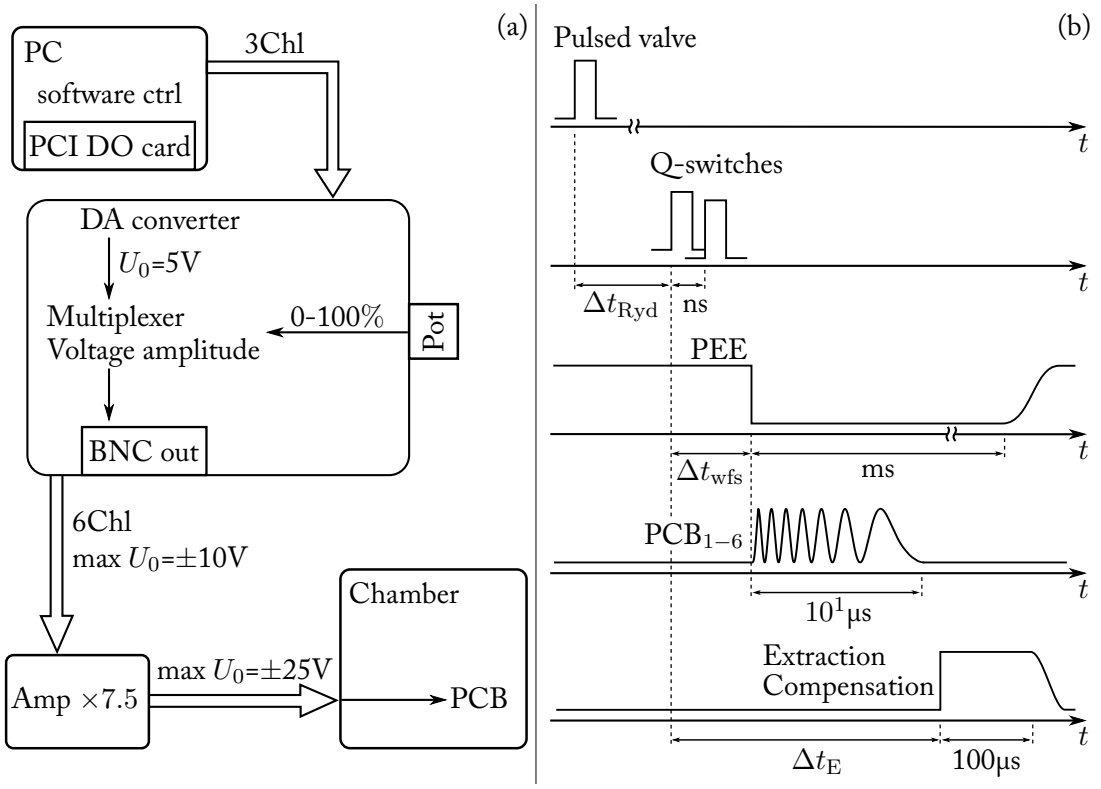

Figure 6.3: Essential building blocks of the in-house constructed arbitrary waveform generator used to generate the six channels of oscillating potentials applied to the PCB decelerator in (a). Three digital-to-analog (DA) chips convert the output of the PCI card into a voltage; through the multiplexer the positive and negative (inverted) channel of same shape share one DA converter. The same board amplifies the converted analog signal up to 20 V peak-to-peak magnitude $2U_0$, which is further amplified with a separate external amplifier that is mounted to an electrical feedthrough connecting the sets of PCB electrodes. The overall potential magnitude is controlled with a potentiometer (Pot) during the first amplification stage. The experimental sequence of electrode switching and timing in (b) shows the order in which the waveform potentials are generated relative to the main trigger signal of the pulsed valve at 10 Hz. The waveforms are delayed by Δt_{wfs} and the pulsing of the extraction and compensation electrodes by Δt_{E} after Rydberg excitation.

6.2 Implementation into surface experiment

The first step in installing the decelerator is to shift the point of Rydberg excitation out of the interaction region of the *down*-configuration and use the hereby established alignment of the molecular beam and the laser beams to subsequently spatially arrange the decelerator construction. The PCB electrodes are aligned along the axis of the molecular beam and the performance of the decelerator is assessed with the field ionisation signal before trying to receive a decelerated surface ionisation signal.

6.2.1 Shifted Rydberg excitation

Since the excitation point is shifted away from the optical axis of the detection electrode stack, all (detection) electrodes in the experiment are pulsed in a sequence so that no electrode potentials are permanently present during Rydberg excitation at the changed position (other than stray fields emanating from the microchannel plates and phosphor screen detector). The voltages applied for extraction would perturb the much smaller potentials used for the decelerator and create inhomogeneous electric fields that deflect the Rydberg atoms.

The prospective point of Rydberg excitation with the decelerator in place is shifted from the original excitation position by $\sim 4\,\mathrm{cm}$, away from the surface. The resulting flight time of the Rydberg atoms until field ionisation for the helium seeding used here is $\sim 30\,\mu\mathrm{s}$. To investigate the effect of the increased time of flight towards the surface (it was previously $\sim 5\,\mu\mathrm{s}$), field and surface ionisation profiles are recorded in the original and the shifted alignment. The data shown in Figure 6.4 has been recorded without a bias field present during Rydberg excitation to better compare the results, thus exciting and detecting a mixture of k-states.

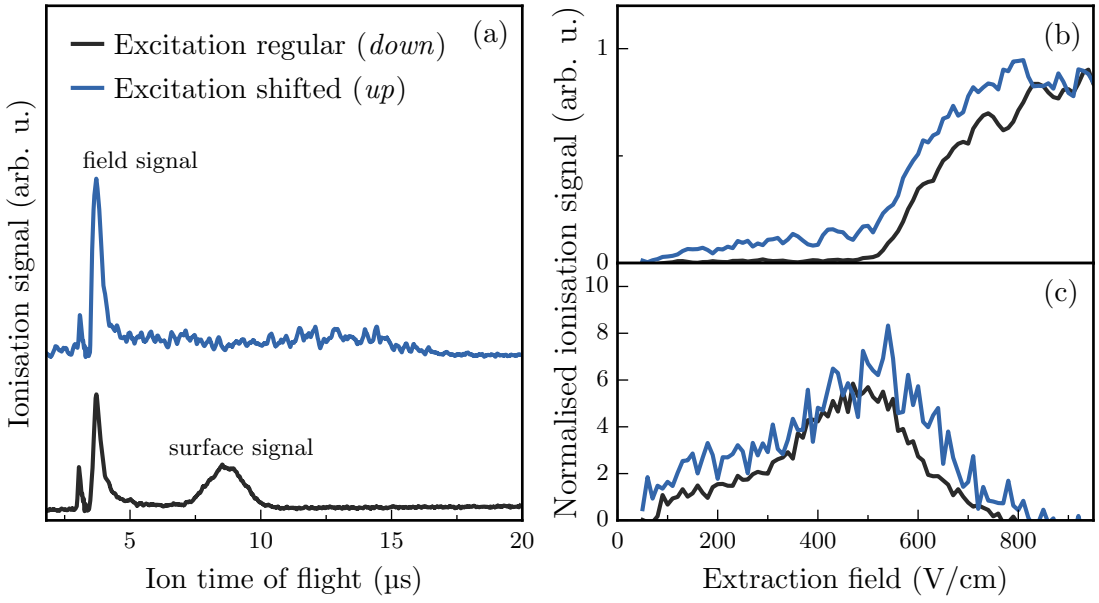

Figure 6.4: Comparison of the ionisations signals in the original configuration (down) and the shifted intersection of molecular beam and Rydberg excitation lasers of $n = 35$ with no bias field present. Panel (a) depicts the recorded scope traces at an intermediate extraction field of $600\,\mathrm{V\,cm^{-1}}$ between surface and field ionisation. Ion time of flight traces are arbitrarily shifted for clarity. The accordingly marked signals are time gated, integrated and normalised as shown for the field signal in (b) and the surface signal in (c). The peak before the field ionisation peak in (a) is due to the pulsed extraction electronics.

It can be seen from Figure 6.4 (a) that the field ionisation signal exhibits a sharp structure

in either alignment (*i.e.* with the original orientation or with the decelerator in place), whereas the usually distinguishable surface signal is spread out over a greater time gate for the shifted excitation point. The narrow distribution of the field signal in both cases is due to immediate ionisation of all atoms that are within the detection region of the surface, while the ions from surface ionisation are produced successively upon approach. It can also be observed that the field trace for the longer flight time in (b) displays non-zero signal over the entire extraction field range. It is conceivable that the longer exposure to the thermal environment of the chamber increases the probability that black-body transitions to a spectrum of higher lying states occurs, which have increasingly lower field ionisation thresholds.

The spread in the surface ionisation signal is not surprising considering the earlier determined temperature of the gas packet of 22 K ($v_{\mathrm{transverse}} \approx 400\,\mathrm{m\,s^{-1}}$) in the approximate molecular beam frame. For one, this introduces a significant spread in the flight times towards the surface which results in widely different arrival times with lower intensities, assuming the number of initially excited Rydberg atoms is approximately equal. Full width at half maxima from time of flight traces via delayed extraction are $\sim 12\,\mu\mathrm{s}$ (down) and $\sim 22\,\mu\mathrm{s}$ (up). On the other hand, this likely also leads to hydrogen Rydberg trajectories not entering the interaction region and thereby not getting detected; the amount of field signal in the shifted configuration is about five times lower than that recorded in the original configuration. The existence of stray fields in the interaction region is demonstrated in section 4.6, which can also be a source of losing trajectories available to detection. Nonetheless, the normalised surface traces from both configurations are in good agreement, higher amounts of noise can be attributed to the extended time gate and an overall lower ion signal-to-noise ratio resulting from the lower Rydberg beam intensity.

In the experimental configuration it is difficult to assess the loss of Rydberg population through radiative decay processes. There must, however, be some losses occurring; it is just not possible to determine the amount, but it appears not to be a principal obstacle for sufficient numbers of Rydberg atoms arriving at the surface. Considering that the lifetime of a Stark state is increased in an electric field [5], this prospect gets even more reassuring.

Installation of the decelerator

The next step involves mounting the decelerator as shown in Figure 6.1 (a) by aligning the PCB surface and electrodes along the axis of the molecular beam that passes below the knife-edge aperture at the end of the chip without obstruction. Despite the laser beams passing the rectangular electrodes and the decelerator mount without clipping, their presence introduces significant amounts of noise, especially at low extraction fields, primarily stemming from the VUV radiation whose stray high energy photons are likely to easily ionise materials along the beam path when passing by closely. In order to minimise any noise generated by the laser beams, the alignment of the PCB is optimised with respect to the laser position, with the overall power of the VUV radiation reduced.

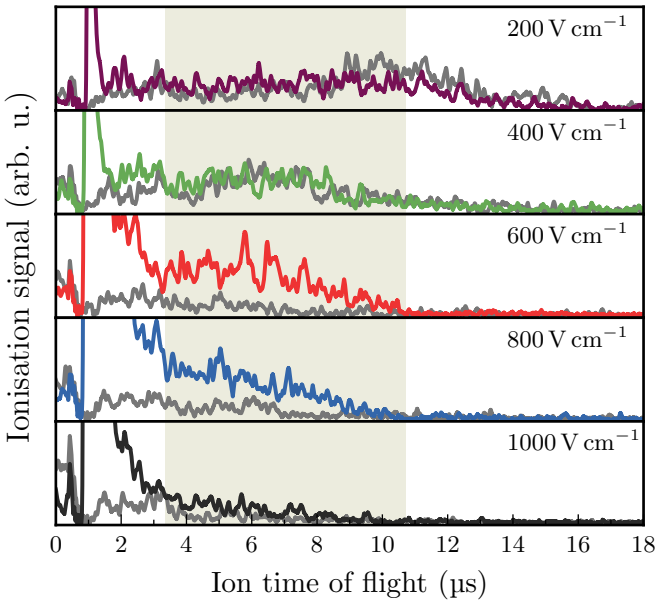

Figure 6.5: Ion time of flight traces detected from field and surface ionisation of $n = 35$ at different extraction fields (coloured traces) and the respective baselines (grey traces). The field signal occurs at about 1 µs, greatly exceeding the magnitude of the surface signal. The baseline is recorded with only the excimer laser for hydrogen production turned off. The surface signal gate for integration (as used in Figure 6.6) is marked with the shaded area. Noise development at low extraction fields can be observed at later times, overlapping with the surface time gate.

Additional to an expected partial blocking of the Rydberg atom cloud through the PCB holder, the noise-reducing adjustments lead to a further reduction of the field signal intensity of roughly $1 : 10$ in comparison to the original configuration. Time of flight traces shown in Figure 6.5 demonstrate the difficulty of recording all ions stemming from surface ionisation, and to distinguish the surface ionisation events from the background signal in this configu-

ration due to a broadly spread ionisation signal, low signal-to-noise ratio and irregular noise. The reduced intensity might introduce a high degree of uncertainty when comparing surface ionisation measurements to each other.

With an appropriate time gating, a field and surface ionisation profile of $n = 35$ analogous to the measurement in Figure 6.4 is presented for the shifted excitation point (but with the decelerator mount aligned) in Figure 6.6. The field ionisation trace in Figure 6.6 exhibits the same increased detection efficiency for lower extraction fields as before, whereas the surface trace displays decreased ionisation at lower extraction fields that is near constant $< 400\,\mathrm{V\,cm^{-1}}$. Comparing the corresponding traces from Figure 6.5 it is reasonable to assume that this part of the profile is a result of increased noise and surface ionisation ceases at higher fields than suggested in (b).

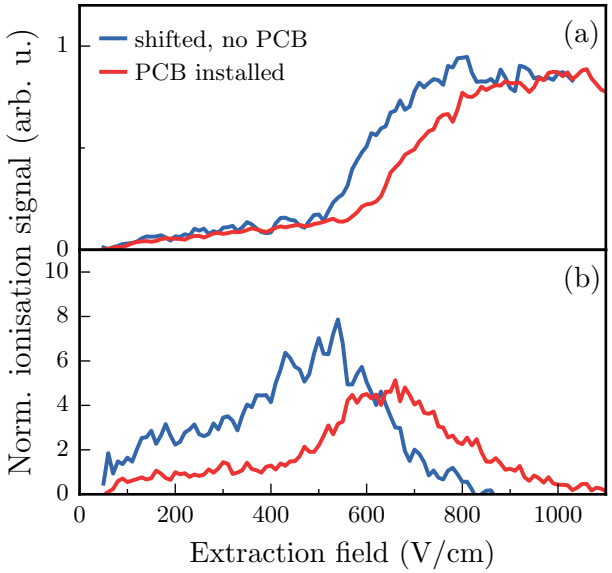

Figure 6.6: Field ionisation in (a) and surface ionisation signal in (b) compared for $n = 35$ with no bias field present in the shifted configuration (up) without the decelerator present and in the same arrangement with the PCB decelerator installed. The chip is aligned with the molecular beam running in parallel to the chip and passing through the aperture unhindered.

Moreover, both field and surface profile are shifted by about $100\,\mathrm{V\,cm^{-1}}$ towards higher extraction fields. Particularly, the surface trace shows a wider transition field range from field to surface ionisation. These observations strongly suggest that the extraction field as displayed is actually lower due to a modification of the field distribution in the interaction region. The introduction of further components between the extraction mesh and the surface holder results in a perturbation of the homogeneous extraction field.

6.2.2 Extraction field compensation

The homogeneous electric field distribution for ion extraction is paramount to the analysis and comparison of surface ionisation measurements since the field strength is used to infer the distance at which ionisation occurs. To reduce the effect of field inhomogeneities, the strip electrode in Figure 6.1 (field compensation) is pulsed alongside the ion extraction electrodes. The interest here lies in the field region closest to the surface where surface ionisation occurs. For this spatial region, an optimisation is carried out to minimise the spread of the local electric field by applying a potential to the strip electrode. The size of the region is chosen to match the projected width of the moving potential trap onto the surface; the height is 1 mm. Without the decelerator electrodes, the field spread σ_E in this region at an extraction mesh potential of 1000 V is $\sigma_E = 0.7\,\mathrm{V\,cm^{-1}}$, whereas $\sigma_E = 161.2\,\mathrm{V\,cm^{-1}}$ in the presence of the PCB.

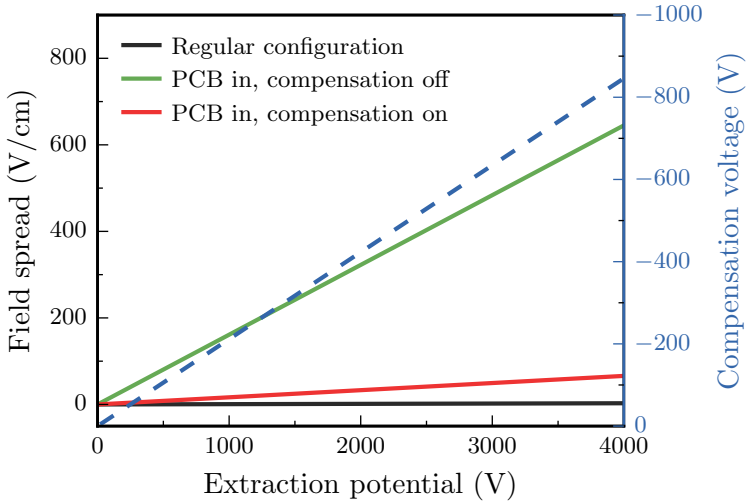

Figure 6.7: Electric field spreads for an area above the surface for the regular Rydberg surface experiment (extraction mesh and grounded surface holder) and with the introduction of the decelerator, as a function of extraction potential applied to the mesh. The compensation strip electrode is either grounded (*off*) or applied with a voltage that is calculated from an optimisation to reduce the field spread (*on*, dashed blue line).

Here, different ways of compensating the field inhomogeneities are possible by either pulsing a compensation electrode, the metallic aperture, the surface holder or a combination thereof. Different combinations were examined beforehand, where the configuration delivering the smallest field spread showed to be the strip electrode with the aperture and surface grounded.

The strip electrode extends along the full width of the deceleration electrodes, rendering the problem symmetrical along the surface parallel so that the electrode grid is designed in two dimensions with a resolution of 20 grid units per millimeter. The optimisation is performed

using the MATLAB® function `patternsearch` by minimising σ_E expressed through a target function:

```
spread = @(efield) abs(max(efield) - min(efield));
[optimPot optimSpread] = patternsearch(@spread);
```

The respective field spreads and the result of the optimisation are displayed in Figure 6.7. With the compensation electrode engaged, the electric field spread in the surface interaction region is reduced to $\sigma_E = 16.5\,\mathrm{V\,cm^{-1}}$ at an extraction potential of 1000 V.

The calculated potentials are loaded into the control software and the power supplies set by looking up the corresponding value for the applied extraction mesh potential. A comparison of surface and field ionisation scans with the compensation enabled are shown in Figure 6.8 for the calculated compensation potential, and double and half the theoretical value.

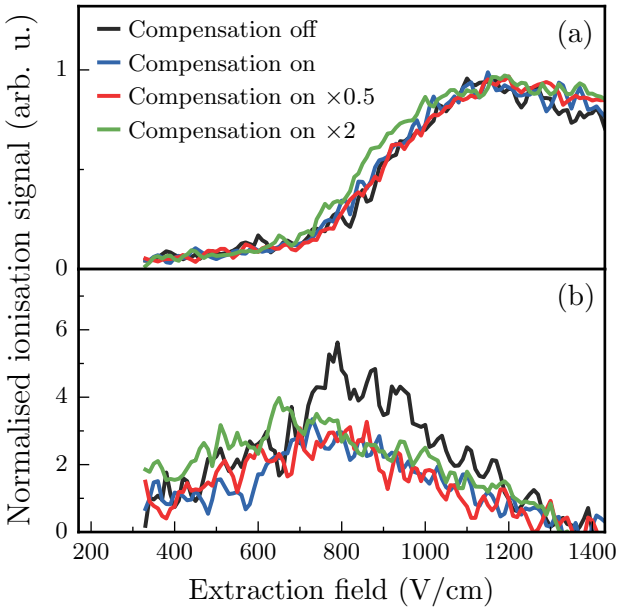

Figure 6.8: Comparison of field ionisation in (a) and surface ionisation in (b) of $n = 35$ for the compensation electrode disabled and enabled at different multiples of the calculated compensation voltage applied. Here, the extraction field is still given as the homogeneous electric field assuming no further electrodes between extraction mesh and surface.

The field trace exhibits no real difference with and without (simple) compensation; only for the doubled compensation potential can a slight shift of the field ionisation threshold towards lower fields be observed. A more significant difference is however observed for the surface ionisation traces, which confirms the target of designing the field compensation for a region of surface ionisation rather than the field regions of field ionisation. For the single and double compensation potential, the surface profiles resemble the trace from Figure 6.6: a shift of the

maximum of the profile towards lower extraction field regions with increased detection efficiency at lower fields for the doubled compensation potential. Overall, a decreased magnitude for all three settings can be seen during field compensation. It is possible that the presence of the compensation potential is introducing increased transverse velocities to the extracted ions which escape the detection mesh. After all, the local optimisation occurs in regard to field homogeneity not ion extraction efficiency.

Since the width of the transition between field and surface ionisation is not visibly affected by the compensation procedure, it suggests that the global field inhomogeneities are still sufficiently high, by which field and surface ionisation are occurring simultaneously over a range of applied extraction potentials. That the result of the field compensation is more discernible at the doubled output further suggests deficiencies in the field modelling. First, the dimensions in the simulations are likely to not fully match the spacing of the externally aligned chip and surface in the experiment. Second, the idealised electrode geometry in the model does not account for rough edges, from which stray fields can emanate, further enhancing field inhomogeneities. Third, the resolution of the potential grid might be too coarse to adequately model the electric field distribution close to the surface.

Despite these limitations it is satisfying that the detection of a surface ionisation signal could be achieved and optimised with the decelerator in place.

6.3 Experimental performance

During installation of the decelerator, no Stark states are selected as no bias field is present at the time of laser excitation. The next step involves operating the full electrode and pulse sequence as depicted in Figure 6.3 (b). The target here is to characterise the performance of the decelerator via evaluation of the field ionisation signal and then move on to record surface ionisation. To gain a better understanding of the influence of experimentally adjustable and accessible parameters while operating the decelerator, some of the parameters are simulated in advance.

6.3.1 Parameter space dependencies

The trajectory simulations are carried out with the electrode geometry modelled in two dimensions along the z-axis in the middle of the chip. Despite the acceleration of the code introduced in section 2.3, a three dimensional grid that contains all electrodes requires impractical computational times in order to examine multiple parameters. As depicted in Figure 6.2 (c), a $0.25\,\mathrm{mm}$ wide segment of the three dimensional initial cloud is projected onto the yz-plane and propagated through the decelerator. In the simulations, the origin of the cloud is moved to the midpoint in the z-direction of the excitation electrodes and the height fixed at the y-coordinate of the trap minima. The temperature and forward velocity of the Rydberg atom cloud are set to $22\,\mathrm{K}$ and $v_z = 1345\,\mathrm{m\,s^{-1}}$ respectively, as determined for the tapered capillary in section 3.2 and used for all simulations shown in Figure 6.9. The particles are counted in a plane behind the decelerator at constant a z-position, relative to the number of initial particles, yielding the transmission T.

The starting point for all simulations and the experimental cycle is to optimise the onset of the waveform potentials relative to the incoming cloud of Rydberg atoms. The first stable electric field minimum is formed $12.75\,\mathrm{mm}$ away from the midpoint of the atom cloud during Rydberg excitation which corresponds to the maximum in transmission at $9.5\,\mu\mathrm{s}$ in Figure 6.9 (a), and which is used henceforth for all other simulations.

It would also be possible to engage the waveform potentials when the cloud is at the next minimum in the sequence at multiples of $3d_z$ further along the z-axis. First, this shortens the available length of the chip for the deceleration sequence which would increase the acceleration of the traps and the force exerted on the atoms in the moving traps. When the moving and accelerating traps are chosen as the frame of reference, an additional term $U_{\mathrm{pseudo}} = -ma_{\mathrm{trap}}z$ alters the potential energy landscape experienced by the atoms resulting from a constant pseudo-force ma_{trap} in the positive z-direction in the accelerated frame [264]. This leads to a distortion of the symmetric traps with a tilting and opening in the forward direction with increasing acceleration [248]. Second, the later onset of the traps would let the atoms traverse over the chip while no PCB electrode potentials are applied which can lead to the atoms entering regions of zero field, resulting in a loss or mixing of the initially prepared Stark state.

Operating with the velocity of the traps set to the velocity of the incoming atoms, no accel-

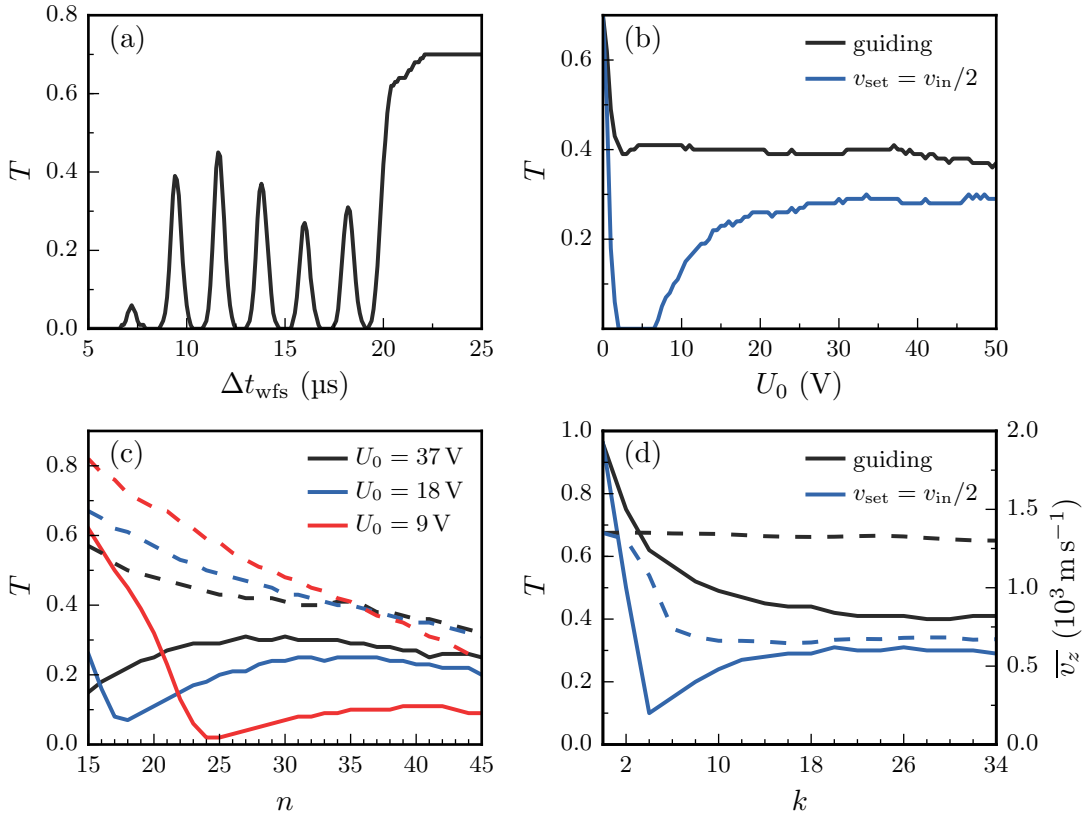

Figure 6.9: Trajectory simulations for various parameters that are adjustable in the experimental cycle from Figure 6.3 (b) given as transmission T of the initial number of particles, comparing guiding-mode ($v_{\mathrm{set}} = v_{\mathrm{in}}$) and a deceleration sequence with a final velocity $v_{\mathrm{set}} = 673\,\mathrm{m\,s^{-1}}$. Variation of the delay Δt_{wfs} between Rydberg excitation and the onset of the oscillating potentials in guiding-mode only in (a), variation of the potential magnitude U_0 in (b) of $n = 35$, $k = 34$. Transmission as function of principal quantum number n, $+k_{\mathrm{max}}$ in (c) for three different potential magnitudes U_0 for deceleration (solid line) and at constant velocity (dashed lines). Variation of the low-field seeking Stark states of $n = 35$ from $+k_{\mathrm{max}}$ to $k = 0$ in (d) and the corresponding average velocities in the z-direction $\overline{v_z}$ (dashed lines) of all detected particles.

eration is exerted on the Rydberg atoms so the pseudoforce is not present. This guiding-mode is compared to a deceleration sequence in which the final velocity is set to half the initial velocity as in Figure 6.9 (b), which shows that transmission is nearly constant in either case for $U_0 > 20\,\mathrm{V}$ and the guiding-mode for $U_0 > 5\,\mathrm{V}$. Below 20 V, transmission in guiding-mode increases with decreasing potential magnitude due to a weakening force on the atoms up to a maximum value of $\sim 70\%$ detected particles. The same value is also reached for the deceleration sequence but with a minimum around 5 V.

The uncertainty of the Stark state assignment has been discussed before and is demonstrated in Figure 6.9 (d) to not be a problem for the performance of the decelerator: at $n = 35$, transmission is nearly constant for $k \geq 22$. For lower Stark states, transmission is increased in

guiding-mode since the decreasing dipole moment $(3/2nk)$ leads to a weaker interaction with the electric field. For the decelerated sequence, an increase of transmitted particles is observed for $k > 4$. The decreased interaction with the decelerator for low Stark states is additionally corroborated with the forward velocity of the arriving particles. The set velocity is only reached for $k \geq 10$; no reduction of the velocity is observed for $k = 0, 2$ as the particles pass through the device without their trajectories being altered.

In both guiding-mode and deceleration for the Stark states, the amount of detected particles increases to 95% for $k = 0$. This increased transmission compared to (a) and (b) is due to the inhomogeneous fields formed between the excitation plates and the electrodes at the beginning of the decelerator, which are not experienced for zero dipole moment but for the maximum blue-shifted states in (a) and (b), likely leading to a deflection in the y-direction. Since parts of the initial cloud collide with the chip holder, 100% transmission is never achieved.

Also, the choice of principal quantum number from the experimentally available range of 20 to 40 appears to not exceedingly affect the transmission rates for $n \geq 30$ and $U_0 \gtrsim 20\,\mathrm{V}$ for the deceleration sequence. The results for the constant velocity sequence, on the other hand, exhibit a nearly linear decrease in the number of transmitted particles with increasing dipole moment of the Rydberg state, with the dependence on U_0 also smaller with increasing n. It suggests that the higher forces exerted on the Rydberg atoms leads to a higher number of ejected particles, and that for high principal quantum numbers a (maximal) potential magnitude of $U_0 = 25\,\mathrm{V}$, as delivered by the electronics, is sufficient for efficient operation of the device.

6.3.2 Partially reduced transmission in guiding-mode

Measurements for engaged waveform potentials are conducted for $n = 35$ and an approximate Stark state of $k = 28$. The splitting of the Stark states results in a lower intensity compared to the degenerate superposition populated at zero field, particularly for the outermost low-field seeking state. Since it has been shown that the selection of a lower Stark state does not overly affect the performance of the decelerator, the higher intensity state $k = 28$ is chosen. Generally, it is observed that the field ionisation signal drops in intensity by about 30% with a selected Stark state, which is consistent with the relative intensities of the Stark spectrum and the field-free field ionisation signal.

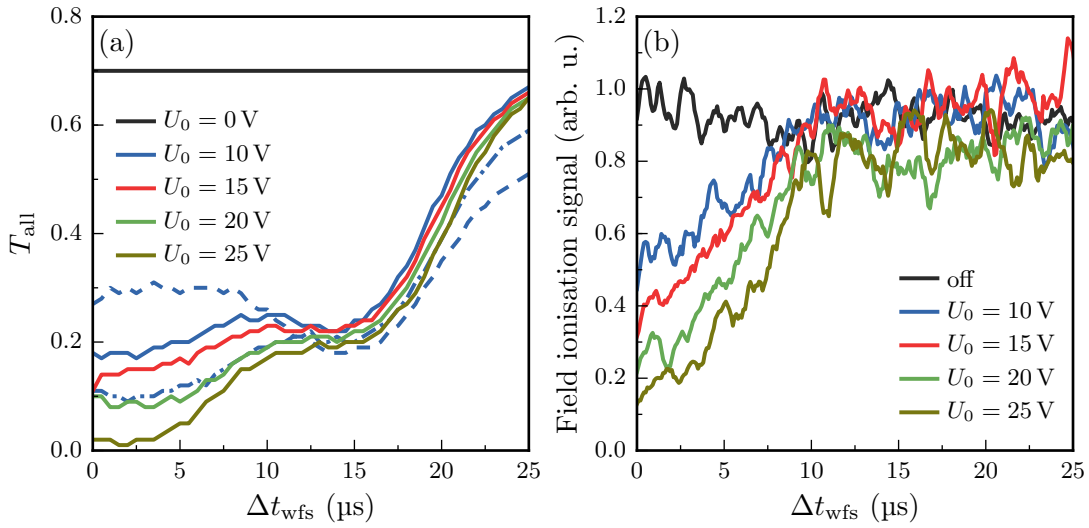

Figure 6.10: Simulated arrival of all particles in the detection region as function of the waveform potential switching Δt_{wfs} relative to Rydberg excitation in (a); contrast this to Figure 6.9 (a) for the loss of horizontal resolution. Additionally shown is a simulation at $U_0 = 10\,\mathrm{V}$ where the initial cloud of atoms is shifted by $0.25\,\mathrm{mm}$ upwards (dashed line) and downwards (dash-dot). Recorded field ionisation signal as function of waveform potential delay for different potential magnitudes U_0 in (b), signal intensities are normalised to the maximum of the trace with the amplifier turned to zero output ('off').

In the initial phase of operation, the reduction in the field signal transmission at a constant velocity of the moving traps is targeted by trying to receive a signal structure as in Figure 6.9 (a), where at later delay times the atom cloud has entirely passed the chip and is not affected by the trapping potentials. The extraction delay t_E is chosen to engage when the Rydberg cloud has passed the decelerator and is within the interaction/detection region. Scans for different waveform potential magnitudes as function of the waveform potential delay are shown in Figure 6.10 (b). It can be observed that the transmission is reduced for delay times $\leq 10\,\mu\mathrm{s}$ to $15\,\mu\mathrm{s}$, after which the signal appears nearly constant. However, the traces do not exhibit a pronounced structure.

The previously presented simulations have been carried out specifically to investigate various parameters with a centred slice of the initial particle distribution with little spread in the z-axis. When the whole cloud as depicted in Figure 6.2 (b) is used, no transmission maxima can be distinguished. Also, all particles arriving behind the chip are counted here whereas previously only particles that passed through the aperture were marked as detected. Due to the nature of the experimental detection not being in line with the decelerator axis, all particles entering the detection region will be field-ionised and recorded.

Up to about 12 µs, the simulations display a dependence on the trapping potentials akin to the experimental signal, with little variation beyond 15 µs. For a proper comparison, the differences in alignment included in the model and the experiment need to be addressed. First, a shift of the excitation point horizontally towards the chip results in a change in the delay time of $\approx \pm 0.75\,\mu\mathrm{s/mm}$, so that the delay times in Figure 6.10 (b) are conceivably greater than displayed by 1 µs to 3 µs. Second, a shift of the excitation point vertically is examined in (a) at $U_0 = 20\,\mathrm{V}$, which modifies the intensities in the beginning and at the end of the delay traces. Here, the whole cloud is shifted parallel to the chip surface whereas in the experiment it is possible that successive external alignments of the device result in an angle between beam axis and chip surface. It is thereby conceivable that the partial mismatch between simulation and experiment at higher delay times is based on a (combination of) different experimental atom beam alignment and different detection geometries than that specified in the simulations.

6.3.3 Insufficient time of flight changes for deceleration sequences

Proceeding to apply the chirped frequency deceleration potential sequences, Δt_{wfs} is assigned the theoretical value at which the midpoint of the cloud is at the position of the first trap. Albeit not all initial particles will be accepted and decelerated by the potential sequence, different flight times of undecelerated and decelerated particles can be appropriately time-gated to select the decelerated ensemble. Figure 6.11 (b) shows the recorded time of flight traces for different final velocities of the potential sequence. The field ionisation signal is recorded relative to the time of Rydberg excitation by varying the extraction delay. If the potential sequence serves to, at least partially, decelerate particles, the time of flight distribution would be expected to shift towards greater values or be modified from its shape in guiding mode.

Despite a small shift of the maxima in Figure 6.11 (b), only minor differences in the time of flight traces can be observed. The maxima of the respective distributions are positioned at the following delay times:

$v_{\mathrm{set}}\,(\mathrm{m\,s^{-1}})$	v_{in_1}	1000	600	200	v_{in_2}
$\Delta t_E\,(\mu\mathrm{s})$	30.95	30.12	30.31	32.37	31.71

An apparent shift towards longer flight times emerges for the traces at $v_{\mathrm{set}} = 1000\,\mathrm{m\,s^{-1}}$, $600\,\mathrm{m\,s^{-1}}$ and $200\,\mathrm{m\,s^{-1}}$ but is inconsistent in comparison to the constant velocity traces.

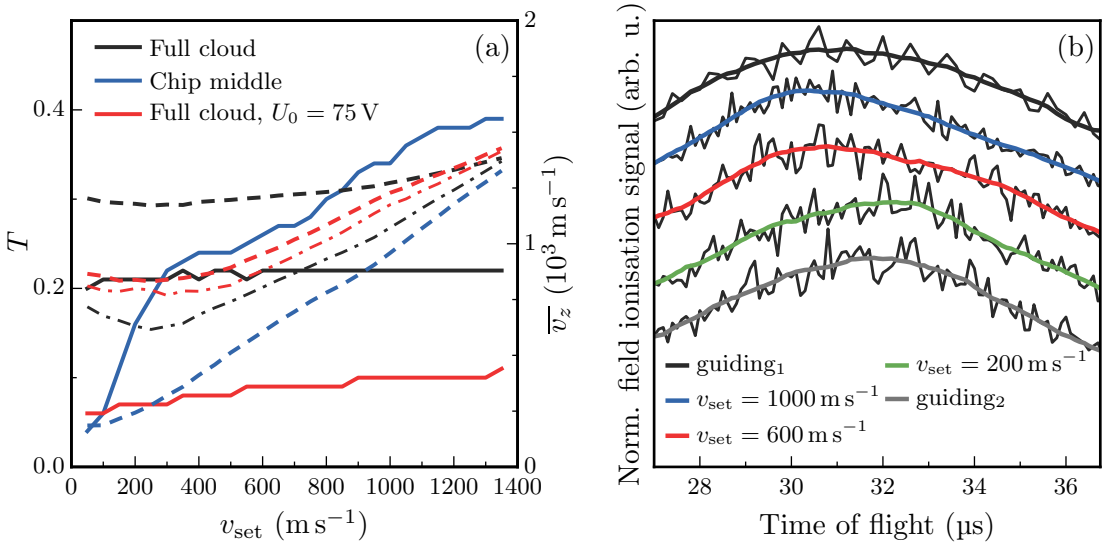

Figure 6.11: Simulated transmission T (solid lines) and final average velocity in the z-direction $\overline{v_z}$ (dashed, dash-dot lines) of initial particles at $n = 35$, $k = 34$ decelerated with potential sequences at $U_0 = 25\,\mathrm{V}$ and $75\,\mathrm{V}$ for final velocities v_{set} in (a). For the full cloud, dashed lines correspond to all particles arriving in the detection region whereas dash-dot lines count only particles below the aperture on the molecular beam axis. Experimental time of flight traces of $n = 35$, $k = 28$ are depicted as a function of delayed pulsed field detection (Δt_E) for various set final velocities at $U_0 = 25\,\mathrm{V}$. Traces labelled with *guiding*$_1$ and *guiding*$_2$ are recorded before (1) and after (2) the set of deceleration sequences were applied at a constant velocity of $1345\,\mathrm{m\,s^{-1}}$. For clarity, these traces are normalised by their maxima and stacked by an offset.

The shift simultaneously occurs with a change in shape of the traces towards smaller ($v_{\mathrm{set}} = 1000\,\mathrm{m\,s^{-1}}$, $600\,\mathrm{m\,s^{-1}}$) and greater ($v_{\mathrm{set}} = 1000\,\mathrm{m\,s^{-1}}$, v_{in_2}) delay times. Since the traces were recorded in sequence, this variation might be discarded as a systematic experimental drift and not an actual change in the flight times.

Reasons for the inefficiency of the decelerator in this configuration can be found in the trajectory simulation results in Figure 6.11 (a). Whereas the selected width of particles (0.5 mm) displays a near linear decrease in the average velocity of arriving particles with set velocity, the full (experimental) cloud at $U_0 = 25\,\mathrm{V}$ reaches a minimum average value of about $1150\,\mathrm{m\,s^{-1}}$. This average value of the full cloud is of all particles that arrive in the detection region; for the particles on the trap axis (below the aperture) a minimum average velocity of about $600\,\mathrm{m\,s^{-1}}$ is reached. The difference in average velocity between the two particle counts, above and below the aperture, decreases with increasing potential magnitude U_0 where a minimum velocity of $850\,\mathrm{m\,s^{-1}}$ is attained for the full cloud. At the same time, this decreases the overall fraction of particles from the full cloud that arrive at the detection plane; at $U_0 = 25\,\mathrm{V}$ the transmission

is nearly constant whereas at 75 V it is about half and decreasing with decreasing set velocities. Nonetheless, this theoretical improvement is not attainable with the waveform generator employed in these experiments. The insignificant change in numbers of (all) arriving particles and only small change in average velocity at $U_0 = 25$ V can be used to explain the small differences in the experimentally observed time of flight traces.

The transmission rates illustrate that within the limitations of the designed decelerator, only a small portion of the initial particles are efficiently decelerated. With the current pulsed detection geometry it is not possible to distinguish these decelerated species from the large background of undecelerated and deflected particles. All particles within the detection region will be ionised during the voltage pulse for extraction without a position, and thereby time, sensitive separation.

At this point, a major redesign of the existing decelerator by physically separating incoming and outgoing particles through various apertures, the installation of a detection setup to be in line with the molecular beam axis for better characterisation and an upgrade of the potential waveform amplifier electronics would be necessary which, unfortunately, was not within the time scope of the project. These modifications would make the decelerated species more distinguishable from the undecelerated particles but result in overall low numbers of detectable particles, which has been shown to be challenging in recording a well-defined surface ionisation signal with a viable signal-to-noise ratio. The greatest improvement in the decelerator performance is expected from the elimination of the angle between the Rydberg excitation lasers and the molecular beam, which requires even more extensive changes of the experimental apparatus that are not feasible at this point.

Nevertheless it must be recognised that this was the first attempt to integrate a Rydberg decelerator into a surface ionisation apparatus. The experiments presented here enabled an evaluation of the first-generation design, and the lessons learnt should guide future efforts in this direction for new generations of machines.

Conclusions and directions

Rydberg atoms successfully probed electronically discrete high-lying image states in the projected bandgap of Cu(100) by resonantly enhanced charge transfer of the Rydberg electron [97], suggesting that they offer a new approach for further investigating surfaces. The hydrogen atoms employed here are especially useful for this purpose, since their wavefunction orientation is not scrambled upon approach to the surface so that their quantum state does not change relative to the surface [69].

Previously, the study of surface systems has been extended to geometrically confined systems where surface ionisation at an iron thin film displays a resonance character that varies with film thickness up to a minimum thickness of several monolayers [183]. A nearly perfect thin film of one monolayer, however, can be achieved with the two-dimensional material graphene.

Semi-metal monolayer graphene

The energy gap in graphene can be modified by various factors, enabling it to exhibit characteristics of a thin film that is either metallic or an insulator [184, 265]. Surface ionisation measurements performed at a constant collisional velocity for mid-manifold Stark states (as a function of principal quantum number) display a dependency which strongly resembles a free-electron metal such as gold – but with approximately twice the magnitude of detected signal. For the Cu(100) sample, an additional handle on the resonance dynamics was introduced by varying the impact velocity of the Rydberg atoms, which has been predicted to differently impact resonant and non-resonant charger transfer [98]. However, no distinct resonant features are observed for graphene which allows to classify the charge transfer dynamics to be metallic in nature at higher efficiency. The reason for this behaviour is theorised to be the high density of image states that are formed by a double series whose energy spacing is below the resolution of the Rydberg surface experiment. The spatially far-extending image states are likely contributing to the observed increased detection of surface ionisation at greater atom-surface separations up to

micrometers, which exceeds the copper reference sample by more than one order of magnitude.

The origin of the enhanced efficiency at graphene requires further theoretical investigation for a comprehensive understanding. Complementary experiments could be carried out with monolayer hexagonal boron nitride (h-BN), which displays a large bandgap and is sufficiently similar to graphene in structure but electronically distinct from it to reveal the influence of the monolayer and the variable energy spacing of valence and conduction band on the charge transfer dynamics in comparison [266, 267, 268]. It could help to distinguish the role of the image state density in the presence of a thin film when the bandgap of the film is fixed and the metallic behaviour not variable.

With modifications made to improve the long-term signal stability of the apparatus, measurements over a large range of collisional velocities can now be conducted in less time and in a more reproducible manner. This aids comparison between normalised and integrated surface ionisation signals for different quantum states.

Velocity dependence at gold surface

For a gold surface, charge transfer from the Rydberg state is always resonant since the conduction band is degenerate with the Rydberg series. A gold surface system is investigated theoretically using a wave-packet propagation approach for the maximum red-shifted Stark state whose electron density is directed towards the surface. The distance from the surface at which ionisation occurs gradually shifts to greater scaled distances (in $n^2 a_0$) for increasing principal quantum number n and increasing velocity; at large orbital radii ($n > 20$) the ionisation distance becomes dependent only on the velocity. The calculations are carried out without acceleration of the ion core included, which appears to shorten and equilibrate the ionisation distance when the collisional velocity decreases.

The results can be considered as preliminary, as a further study of the same range of Stark states and velocities with the mean-field acceleration and the extraction field values included is necessary to draw final conclusions. Nevertheless, a potentially useful scaling relationship for n and velocity has been derived that can be used for extrapolating to higher n regimes.

The minimal variability observed for the mean-field included calculations is verified experimentally in this work for a set of principal quantum numbers and Stark states – in contrast to

earlier experiments for a gold surface [69], where the contrasting trends are possibly connected to the different manner in which surface ionisation is recorded. Only for largely different collisional velocities can a marked difference be observed in the relative amount of surface ionisation.

Since expansion from a supersonic valve delivers a rather narrow velocity distribution that is particularly limited towards lower velocities, a chip-based decelerator is combined with the surface experiment to extend the range of available collisional velocities. A wider range of atom velocities is hoped to better address the ambiguities in the velocity dependence.

Decelerator design review

The constructed and installed travelling potential well decelerator is, within the parameters available from the existing apparatus, not able to efficiently decelerate a sufficient number of particles to observe a velocity decrease by pulsed field ionisation detection, or for the ultimate target of recording ions from the surface ionisation of decelerated Rydberg atoms as a function of velocity.

To make the chip decelerator work in the current configuration, several steps need to be taken beyond an improvement of the electronics and parts of the decelerator. To better characterise the performance of the device, a second detector is necessary to appropriately capture the atoms coming off the device rather than the pulsed mesh that is located partially above the decelerator itself. A separate and simultaneously available detection scheme would allow for the optimisation of the deceleration sequence and subsequently record surface ionisation in the original (detection) configuration.

Also, a shortening of the distance between the pulsed valve and Rydberg excitation should result in much less depletion of the hydrogen atoms on the beam axis when heavier seeding gases are in use. The reduced velocity of these gas packets could either be used to directly probe the surface without a decelerator at first, and at the same time aid the particle acceptance of the decelerator.

On the other hand, the idea behind the two-dimensional design is to accommodate operation in the original configuration alongside the added device. Without experimental or apparatus constraints, another decelerator design could better attain the objectives of dual deceleration and deflection.

For example, the surface sample could be mounted directly on a chip that holds a decelerator transmission line with one detector off the chip perpendicular to the beam direction, similar to devices that have been developed by Hogan and coworkers. When a second electrode plate is introduced on top of the board holding the decelerator electrodes, a second microchannel plate stack could detect surface ionisation, as well as *in situ* pulsed field detection, through a hole in the upper plate [269]. Another option is a three-dimensional electrode configuration for off-axis trapping [7], which could be interfaced with a surface sample while the on-axis geometry can be used to characterise the efficiency of the decelerator itself. In either case, the difficulty will be in interfacing the surface with an electrode configuration in which it is still possible to create a homogeneous electric field for ion extraction and where all ions produced from surface ionisation are captured. Extensive simulations are recommended prior to construction of the next generation of device.

Rydberg atom surface probes

With graphene, another distinct surface sample has been added to the portfolio of investigated surfaces. From the similarities and differences in the surface ionisation dynamics at Cu(100), iron thin films and graphene, a framework of Rydberg surface ionisation as a tool in surface analysis of image states can already be developed. The variety of surface interfaces can be extended to dielectrics, which are abundant in quantum optics, or superconducting materials, where collective interactions give rise to the existence of quasiparticles (which may manifest itself in broadly distinctive charge transfer dynamics).

As demonstrated in this thesis, progress has been made – both conceptually and technically – towards a full understanding of the complex process of charge transfer from a Rydberg atom into a surface. Some questions remain unanswered and further investigation is needed, but there is sufficient optimism that it will be possible to overcome these hurdles and develop Rydberg atoms into reliable surface probes.

References

[1] G. Grass, The Tin Drum, Secker & Warburg, 1959, p. 25.

[2] H. Bethe and E. Salpeter, Quantum Mechanics of One- and Two-Electron Atoms, Springer-Verlag OGH, 1957.

[3] A. Bokulich, "Bohr's Correspondence Principle", The Stanford Encyclopedia of Philosophy, ed. by E. N. Zalta, 2014.

[4] T. F. Gallagher, Rydberg Atoms, Cambridge University Press, 1994.

[5] C. Seiler, J. A. Agner, P. Pillet, and F. Merkt, "Radiative and collisional processes in translationally cold samples of hydrogen Rydberg atoms studied in an electrostatic trap", J. Phys. B: At., Mol. Opt. Phys. **49**, 094006 (2016).

[6] C. J. Foot, Atomic Physics, 1st ed., Oxford Master Series in Atomic, Optical and Laser Physics, Oxford University Press, USA, 2005.

[7] C. Seiler, S. D. Hogan, H. Schmutz, J. A. Agner, and F. Merkt, "Collisional and Radiative Processes in Adiabatic Deceleration, Deflection, and Off-Axis Trapping of a Rydberg Atom Beam", Phys. Rev. Lett. **106**, 073003 (2011).

[8] Theodosiou, "Lifetimes of alkali-metal - atom Rydberg states", Phys. Rev. A **30**, 2881 (1984).

[9] W. A. Chupka, "Factors affecting lifetimes and resolution of Rydberg states observed in zero-electron-kinetic-energy spectroscopy", J. Chem. Phys. **98**, 4520 (1993).

[10] F. Merkt, "Molecules in high Rydberg states", Annu.Rev.Phys.Chem. **48**, 657 (1997).

[11] T. P. Softley, "Applications of molecular Rydberg states in chemical dynamics and spectroscopy", Int. Rev. Phys. Chem. **23**, 1 (2004).

[12] F. Merkt and T. P. Softley, "Rotationally resolved zero-kinetic-energy photoelectron spectrum of nitrogen", Phys. Rev. A **46**, 302 (1992).

[13] U. Hollenstein, R. Seiler, H. Schmutz, M. Andrist, and F. Merkt, "Selective field ionization of high Rydberg states: Application to zero-kinetic-energy photoelectron spectroscopy", J. Chem. Phys. **115**, 5461 (2001).

[14] D. Comparat and P. Pillet, "Dipole blockade in a cold Rydberg atomic sample [Invited]", Journal of the Optical Society of America B **27**, A208 (2010).

[15] A. Reinhard, T. C. Liebisch, B. Knuffman, and G. Raithel, "Level shifts of rubidium Rydberg states due to binary interactions", Phys. Rev. A **75**, 1 (2007).

[16] D. P. Fahey, T. J. Carroll, and M. W. Noel, "Imaging the dipole-dipole energy exchange between ultracold rubidium Rydberg atoms", Phys. Rev. A **91**, 062702 (2015).

[17] T. J. Carroll, K. Claringbould, A. Goodsell, M. J. Lim, and M. W. Noel, "Angular dependence of the dipole-dipole interaction in a nearly one-dimensional sample of Rydberg atoms", Phys. Rev. Lett. **93**, 153001 (2004).

[18] L. Béguin, A. Vernier, R. Chicireanu, T. Lahaye, and A. Browaeys, "Direct measurement of the van der waals interaction between two rydberg atoms", Phys. Rev. Lett. **110**, 263201 (2013).

[19] M. D. Lukin, M. Fleischhauer, R. Cote, L. M. Duan, D. Jaksch, J. I. Cirac, and P. Zoller, "Dipole Blockade and Quantum Information Processing in Mesoscopic Atomic Ensembles", Phys. Rev. Lett. **87**, 037901 (2001).

[20] D. Tong, S. M. Farooqi, J. Stanojevic, S. Krishnan, Y. P. Zhang, R. Côté, E. E. Eyler, and P. L. Gould, "Local blockade of Rydberg excitation in an ultracold gas", Phys. Rev. Lett. **93**, 063001 (2004).

[21] E. Urban, T. a. Johnson, T. Henage, L. Isenhower, D. D. Yavuz, T. G. Walker, and M. Saffman, "Observation of Rydberg blockade between two atoms", Nature Physics **5**, 110 (2008).

[22] A. Gaëtan, Y. Miroshnychenko, T. Wilk, A. Chotia, M. Viteau, D. Comparat, P. Pillet, A. Browaeys, and P. Grangier, "Observation of collective excitation of two individual atoms in the Rydberg blockade regime", Nature Physics **5**, 115 (2009).

[23] S. Baur, D. Tiarks, G. Rempe, and S. Dürr, "Single-Photon Switch Based on Rydberg Blockade", Phys. Rev. Lett. **112**, 073901 (2014).

[24] W. Anderson, J. Veale, and T. Gallagher, "Resonant Dipole-Dipole Energy Transfer in a Nearly Frozen Rydberg Gas", Phys. Rev. Lett. **80**, 249 (1998).

[25] I. Mourachko, D. Comparat, F. de Tomasi, A. Fioretti, P. Nosbaum, V. M. Akulin, and P. Pillet, "Many-Body Effects in a Frozen Rydberg Gas", Phys. Rev. Lett. **80**, 253 (1998).

[26] T. G. Walker and M. Saffman, "Zeros of Rydberg–Rydberg Föster interactions", J. Phys. B: At., Mol. Opt. Phys. **38**, S309 (2005).

[27] T. Vogt, M. Viteau, J. Zhao, A. Chotia, D. Comparat, and P. Pillet, "Dipole blockade at förster resonances in high resolution laser excitation of rydberg states of cesium atoms", Phys. Rev. Lett. **97**, 083003 (2006).

[28] N. Saquet, A. Cournol, J. Beugnon, J. Robert, P. Pillet, and N. Vanhaecke, "Landau-zener transitions in frozen Pairs of rydberg atoms", Phys. Rev. Lett. **104**, 133003 (2010).

[29] S. Ravets, H. Labuhn, D. Barredo, L. Beguin, T. Lahaye, and A. Browaeys, "Coherent dipole-dipole coupling between two single Rydberg atoms at an electrically-tuned Forster resonance", Nat Phys **10**, 914 (2014).

[30] H. Saßmannshausen, F. Merkt, and J. Deiglmayr, "Pulsed excitation of Rydberg-atom-pair states in an ultracold Cs gas", Phys. Rev. A **92**, 032505 (2015).

[31] M. Saffman, T. G. Walker, and K. Molmer, "Quantum information with Rydberg atoms", Rev. Mod. Phys. **82**, 2313 (2010).

[32] T. Kazimierczuk, D. Fröhlich, S. Scheel, H. Stolz, and M. Bayer, "Giant Rydberg excitons in the copper oxide Cu_2O", Nature **514**, 343 (2014).

[33] T. E. Wall, A. M. Alonso, B. S. Cooper, A. Deller, S. D. Hogan, and D. B. Cassidy, "Selective Production of Rydberg-Stark States of Positronium", Phys. Rev. Lett. **114**, 173001 (2015).

[34] E. A. Hinds, K. S. Lai, and M. Schnell, "Atoms in micron-sized metallic and dielectric waveguides", Philos. Trans. R. Soc. London. Ser. A Math. Phys. Eng. Sci. **355**, 2353 (1997).

[35] V. Sandoghdar, C. I. Sukenik, E. A. Hinds, and S. Haroche, "Direct measurement of the van der Waals interaction between an atom and its images in a micron-sized cavity", Phys. Rev. Lett. **68**, 3432 (1992).

[36] V. Bendkowsky, B. Butscher, J. Nipper, J. P. Shaffer, R. Löw, and T. Pfau, "Observation of ultralong-range Rydberg molecules", Nature **458**, 1005 (2009).

[37] P. Allmendinger, J. Deiglmayr, J. A. Agner, H. Schmutz, and F. Merkt, "Surface-electrode decelerator and deflector for Rydberg atoms and molecules", Phys. Rev. A **90**, 043403 (2014).

[38] M. Schlagmüller, T. C. Liebisch, F. Engel, K. S. Kleinbach, F. Böttcher, U. Hermann, K. M. Westphal, A. Gaj, R. Löw, S. Hofferberth, T. Pfau, J. Pérez-Ríos, and C. H. Greene, "Ultracold Chemical Reactions of a Single Rydberg Atom in a Dense Gas", Phys. Rev. X **6**, 031020 (2016).

[39] H. Saßmannshausen and J. Deiglmayr, "Observation of Rydberg-Atom Macrodimers: Micrometer-Sized Diatomic Molecules", Phys. Rev. Lett. **117**, 083401 (2016).

[40] T. Niederprüm, O. Thomas, T. Eichert, C. Lippe, J. Pérez-Ríos, C. H. Greene, and H. Ott, "Observation of pendular butterfly Rydberg molecules", Nature Communications **7**, 12820 (2016).

[41] G. Günter, H. Schempp, M. Robert-de-Saint-Vincent, V. Gavryusev, S. Helmrich, C. S. Hofmann, S. Whitlock, and M. Weidemüller, "Observing the dynamics of dipole-mediated energy transport by interaction-enhanced imaging", Science **342**, 954 (2013).

[42] T. Peyronel, O. Firstenberg, Q.-Y. Liang, S. Hofferberth, A. V. Gorshkov, T. Pohl, M. D. Lukin, and V. Vuletić, "Quantum nonlinear optics with single photons enabled by strongly interacting atoms", Nature **488**, 57 (2012).

[43] O. Firstenberg, T. Peyronel, Q.-Y. Liang, A. V. Gorshkov, M. D. Lukin, and V. Vuletić, "Attractive photons in a quantum nonlinear medium", Nature **502**, 71 (2013).

[44] D. Jaksch, J. I. Cirac, P. Zoller, S. L. Rolston, R. Côté, and M. D. Lukin, "Fast quantum gates for neutral atoms", Phys. Rev. Lett. **85**, 2208 (2000).

[45] C. Monroe, "Quantum information processing with atoms and photons", Nature **416**, 238 (2002).

[46] H. Kübler, J. P. Shaffer, T. Baluktsian, R. Löw, and T. Pfau, "Coherent Excitation of Rydberg Atoms in Thermal Vapor Microcells", Nature Photonics **4**, 112 (2010).

[47] S. D. Hogan, J. A. Agner, F. Merkt, T. Thiele, S. Filipp, and A. Wallraff, "Driving Rydberg-Rydberg Transitions from a Coplanar Microwave Waveguide", Phys. Rev. Lett. **108**, 063004 (2012).

[48] A. Wallraff, D. I. Schuster, A. Blais, L. Frunzio, R.-S. Huang, J. Majer, S. Kumar, S. M. Girvin, and R. J. Schoelkopf, "Strong coupling of a single photon to a superconducting qubit using circuit quantum electrodynamics", Nature **431**, 162 (2004).

[49] R. Barends, J. Kelly, A. Megrant, D. Sank, E. Jeffrey, Y. Chen, Y. Yin, B. Chiaro, J. Mutus, C. Neill, P. O'Malley, P. Roushan, J. Wenner, T. C. White, A. N. Cleland, and J. M. Martinis, "Coherent Josephson Qubit Suitable for Scalable Quantum Integrated Circuits", Phys. Rev. Lett. **111**, 080502 (2013).

[50] M. H. Devoret and R. J. Schoelkopf, "Superconducting circuits for quantum information: an outlook", Science **339**, 1169 (2013).

[51] A. Tauschinsky, R. M. T. Thijssen, S. Whitlock, H. B. van Linden van den Heuvell, and R. J. C. Spreeuw, "Spatially resolved excitation of Rydberg atoms and surface effects on an atom chip", Phys. Rev. A **81**, 063411 (2010).

[52] J. M. Obrecht, R. J. Wild, and E. A. Cornell, "Measuring electric fields from surface contaminants with neutral atoms", Phys. Rev. A **75**, 062903 (2007).

[53] R. Gerritsma, S. Whitlock, T. Fernholz, H. Schlatter, J. a. Luigjes, J. U. Thiele, J. B. Goedkoop, and R. J. C. Spreeuw, "Lattice of microtraps for ultracold atoms based on patterned magnetic films", Phys. Rev. A **76**, 033408 (2007).

[54] H. Hattermann, M. Mack, F. Karlewski, F. Jessen, D. Cano, and J. Fortágh, "Detrimental adsorbate fields in experiments with cold Rydberg gases near surfaces", Phys. Rev. A **86**, 022511 (2012).

[55] J. Reichel and V. Vuletic, Atom Chips, Wiley VCH, 2011.

[56] J. M. Wylie and J. E. Sipe, "Quantum electrodynamics near an interface", Phys. Rev. A **32**, 2030 (1985).

[57] G. Barton, "Van der Waals shifts in an atom near absorptive dielectric mirrors", Proc. R. Soc. London A Math. Phys. Eng. Sci. **453**, 2461 (1997).

[58] R. P. Abel, C. Carr, U. Krohn, and C. S. Adams, "Electrometry near a dielectric surface using Rydberg electromagnetically induced transparency", Phys. Rev. A **84**, 023408 (2011).

[59] J. D. Carter and J. D. D. Martin, "Energy shifts of Rydberg atoms due to patch fields near metal surfaces", Phys. Rev. A **83**, 032902 (2011).

[60] J. D. Carter, O. Cherry, and J. D. D. Martin, "Electric-field sensing near the surface microstructure of an atom chip using cold Rydberg atoms", Phys. Rev. A **86**, 053401 (2012).

[61] A. Osterwalder and F. Merkt, "Using High Rydberg States as Electric Field Sensors", Phys. Rev. Lett. **82**, 1831 (1999).

[62] V. Zhelyazkova and S. D. Hogan, "Probing interactions between Rydberg atoms with large electric dipole moments in amplitude-modulated electric fields", Phys. Rev. A **92**, 011402 (2015).

[63] J. E. Lennard-Jones, "Processes of adsorption and diffusion on solid surfaces", Trans. Faraday Soc. **28**, 333 (1932).

[64] D. Gray, Z. Zheng, K. Smith, and F. Dunning, "Ionization of K (nd) Rydberg-state atoms at a surface", Phys. Rev. A **38**, 1601 (1988).

[65] N. A. Nguyen, B. K. Dey, M. Shapiro, and P. Brumer, "Coherent Control in Nano-lithography: Rydberg Atoms", J. Phys. Chem. A **108**, 7878 (2004).

[66] C. Fabre, M. Gross, J. M. Raimond, and S. Haroche, "Measuring atomic dimensions by transmission of Rydberg atoms through micrometre size slits", J. Phys. B: At., Mol. Opt. Phys. **16**, L671 (1983).

[67] G. R. Lloyd, S. R. Procter, and T. P. Softley, "Ionization of Hydrogen Rydberg Molecules at a Metal Surface", Phys. Rev. Lett. **95**, 133202 (2005).

[68] S. B. Hill, C. B. Haich, Z. Zhou, P. Nordlander, and F. B. Dunning, "Ionization of Xenon Rydberg Atoms at a Metal Surface", Phys. Rev. Lett. **85**, 5444 (2000).

[69] E. So, M. Dethlefsen, M. Ford, and T. P. Softley, "Charge transfer of Rydberg H atoms at a metal surface", Phys. Rev. Lett. **107**, 093201 (2011).

[70] K. Kazansky, G. Borisov, and J.-P. Gauyacq, "Wave-packet propagation approach in the theory of charge transfer in projectile–metal surface interactions", Nucl. Instruments Methods Phys. Res. Sect. B Beam Interact. with Mater. Atoms **157**, 21 (1999).

[71] F. Dunning, H. Dunham, C. Oubre, and P. Nordlander, "Behavior of Rydberg atoms at surfaces: energy level shifts and ionization", Nucl. Instruments Methods Phys. Res. Sect. B Beam Interact. with Mater. Atoms **203**, 69 (2003).

[72] J. Sjakste, A. G. Borisov, and J. P. Gauyacq, "Ionization of Rydberg atoms colliding with a metal surface", Phys. Rev. A **73**, 042903 (2006).

[73] E. So, M. T. Bell, and T. P. Softley, "Wave-packet propagation study of the charge-transfer dynamics of Rydberg atoms with metal surfaces", Phys. Rev. A **79**, 012901 (2009).

[74] J. D. Bekenstein and J. B. Krieger, "Stark Effect in Hydrogenic Atoms: Comparison of Fourth-Order Perturbation Theory with WKB Approximation", Phys. Rev. **188**, 130 (1969).

[75] R. J. Damburg and V. V. Kolosov, "A hydrogen atom in a uniform electric field", J. Phys. B: At., Mol. Opt. Phys. **12**, 2637 (1979).

[76] K. Ganesan and K. T. Taylor, "Rydberg states of the hydrogen atom near a metal surface", J. Phys. B: At., Mol. Opt. Phys. **29**, 1293 (1996).

[77] Y. Alhassid, E. A. Hinds, and D. Meschede, "Dynamical symmetries of the perturbed hydrogen atom: The van der Waals interaction", Phys. Rev. Lett. **59**, 1545 (1987).

[78] R. O. Jones, P. J. Jennings, and O. Jepsen, "Surface barrier in metals: a new model with application to W (001)", Phys. Rev. B **29**, 6474 (1984).

[79] P. Jennings, R. Jones, and M. Weinert, "Surface barrier for electrons in metals", Phys. Rev. B **37**, 6113 (1988).

[80] M. Iñarrea, V. Lanchares, J. Palacián, A. Pascual, J. Salas, and P. Yanguas, "Rydberg hydrogen atom near a metallic surface: Stark regime and ionization dynamics", Phys. Rev. A **76** (2007).

[81] J. Burgdörfer, P. Lerner, and F. W. Meyer, "Above-surface neutralization of highly charged ions: The classical over-the-barrier model", Phys. Rev. A **44**, 5674 (1991).

[82] H. Dunham, S. Wethekam, J. Lancaster, and F. Dunning, "Ionization of xenon Rydberg atoms at Si(100) surfaces", Nucl. Instruments Methods Phys. Res. Sect. B Beam Interact. with Mater. Atoms **256**, 46 (2007).

[83] G. Sashikesh, M. S. Ford, and T. P. Softley, "Ionization of Rydberg H_2 molecules at doped silicon surfaces", J. Chem. Phys. **138**, 114308–114308 (2013).

[84] G. Sashikesh, E. So, M. Ford, and T. Softley, "Surface ionisation of molecular H_2 and atomic H Rydberg states at doped silicon surfaces", Mol. Phys. **112**, 2495 (2014).

[85] G. E. McCown, C. R. Taylor, and C. A. Kocher, "Excited-state atomic beam studies of submonolayer adsorption on a fine mesh", Phys. Rev. A **38**, 3918 (1988).

[86] M. A. Cazalilla, N. Lorente, R. D. Muiño, J.-P. Gauyacq, D. Teillet-Billy, and P. M. Echenique, "Theory of Auger neutralization and deexcitation of slow ions at metal surfaces", Phys. Rev. B **58**, 13991 (1998).

[87] E. A. McCormack, E. So, M. Dethlefsen, M. S. Ford, and T. P. Softley, "Detection of electrons in the surface ionization of H Rydberg atoms and H_2 Rydberg molecules", J. Phys. B: At., Mol. Opt. Phys. **45**, 015204 (2012).

[88] J. J. C. Geerlings, L. F. T. Kwakman, and J. Los, "Local work function effects in the neutralization of alkali ions scattered from cesiated surfaces", Surf. Sci. **184**, 305 (1987).

[89] S. Wethekam, H. Dunham, J. Lancaster, and F. Dunning, "Charge-transfer rates for xenon Rydberg atoms at a metal surface", Phys. Rev. A **73**, 032903 (2006).

[90] D. Neufeld, H. Dunham, S. Wethekam, J. Lancaster, and F. Dunning, "Ionization of xenon Rydberg atoms at Au(111) surfaces: Effect of stray fields", Phys. Rev. B **78**, 115423 (2008).

[91] Y. Pu, D. D. Neufeld, and F. B. Dunning, "Ionization of Rydberg atoms at metallic surfaces: Influence of stray fields", Phys. Rev. A **81**, 042904 (2010).

[92] P. Nordlander and F. B. Dunning, "Interaction of Rydberg atoms with a metal surface in the presence of an external electric field", Phys. Rev. B **53**, 8083 (1996).

[93] G. R. Lloyd, S. R. Procter, E. A. McCormack, and T. P. Softley, "Ionization of H_2 Rydberg molecules at a metal surface", J. Chem. Phys. **126**, 184702–184702 (2007).

[94] E. A. McCormack, M. S. Ford, and T. P. Softley, "Level Crossings in the Ionization of H_2 Rydberg Molecules at a Metal Surface", J. Phys. Chem. A **114**, 11175 (2010).

[95] J. Hanssen, C. F. Martin, and P. Nordlander, "Dynamics of Rydberg atoms near metal surfaces in the presence of an electric field", Surf. Sci. **423**, L271 (1999).

[96] N. N. Nedeljković and D. K. Božanić, "Ionization dynamics via ion-collection field of Rydberg atoms approaching metal surfaces", Phys. Rev. A **81**, 032902 (2010).

[97] J. A. Gibbard, M. Dethlefsen, M. Kohlhoff, C. J. Rennick, E. So, M. Ford, and T. P. Softley, "Resonant Charge Transfer of Hydrogen Rydberg Atoms Incident on a Cu(100) Projected Band-Gap Surface", Phys. Rev. Lett. **115**, 093201 (2015).

[98] E. So, J. A. Gibbard, and T. P. Softley, "Ionization of Rydberg H atoms at band-gap metal surfaces via surface and image states", J. Phys. B: At., Mol. Opt. Phys. **48**, 175205 (2015).

[99] D. Straub and J. Himpsel, "Spectroscopy of image-potential states with inverse photoemission", Phys. Rev. B **33**, 2256 (1986).

[100] U. Höfer, I. L. Shumay, C. Reuß, U. Thomann, W. Wallauer, and T. Fauster, "Time-Resolved Coherent Photoelectron Spectroscopy of Quantized Electronic States on Metal Surfaces", Science **277**, 1480 (1997).

[101] P. Wahl, M. A. Schneider, L. Diekhöner, R. Vogelgesang, and K. Kern, "Quantum Coherence of Image-Potential States", Phys. Rev. Lett. **91**, 106802 (2003).

[102] J. A. Gibbard, "Rydberg ionisation into confined and discrete systems", PhD thesis, University of Oxford, 2015.

[103] B. Bahrim, P. Kurpick, U. Thumm, and U. Wille, "Electron dynamics and level broadening in slow atomic interactions with metal surfaces and thin metallic films", Nucl. Instruments Methods Phys. Res. Sect. B-Beam Interact. with Mater. Atoms **164**, 614 (2000).

[104] U. Thumm, P. Kürpick, and U. Wille, "Size quantization effects in atomic level broadening near thin metallic films", Phys. Rev. B **61**, 3067 (2000).

[105] L. D. Landau and L. M. Lifshitz, Quantum Mechanics, 2nd ed., Pergamon Press, 1965.

[106] J. W. Gadzuk, "Theory of atom-metal interactions:: I. Alkali atom adsorption", Surf. Sci. **6**, 133 (1967).

[107] M. Remy, "Theory Concerning the Interaction of an Alkali Atom and a Metallic Surface", J. Chem. Phys. **53**, 2487 (1970).

[108] P. Nordlander, "Lifetimes of negative-ion states near metal surfaces", Phys. Rev. B **46**, 2584 (1992).

[109] V. Ermoshin and A. Kazansky, "Wave packet study of H– decay in front of a metal surface", Physics Letters A **218**, 99 (1996).

[110] J. Gauyacq and A. Borisov, "Charge transfer in atom-surface collisions: Effect of the presence of adsorbates on the surface", J. Phys. Condens. Matter **10**, 6585 (1998).

[111] J. C. Nordlander, P. and Tully, "Energy Shifts and Broadening of Excited Hydrogen-Atom Levels in the Vicinity of a Metal Surface", Phys. Rev. Lett. **61**, 990 (1988).

[112] D. Teillet-Billy and J. P. Gauyacq, "Position and width of a negative ion state in front of a surface: formation of C-(4S) ions by electron capture", Surf. Sci. **239**, 343 (1990).

[113] A. Borisov, D. Teillet-Billy, and J. Gauyacq, "Energy shift and broadening of H levels in front of a metal surface", Nuclear Instruments and Methods in Physics Research B **78**, 49 (1993).

[114] A. G. Borisov, R. Zimny, D. Teillet-Billy, and J. P. Gauyacq, "Energy and lifetime of one-electron multicharged-ion states in front of an Al surface", Phys Rev A **53**, 2457 (1996).

[115] P. Nordlander, "Energies and lifetimes of atomic Rydberg states near metal surfaces", Phys. Rev. B **53**, 4125 (1996).

[116] W. P. Reinhardt, "Complex Coordinates in the Theory of Atomic and Molecular Structure and Dynamics", Annual Review of Physical Chemistry **33**, 223 (1982).

[117] A. G. Borisov, A. K. Kazansky, and J. P. Gauyacq, "Finite Time Effect in the Charge Transfer Process during an Ion-Metal Surface Collision", Phys. Rev. Lett. **80**, 1996 (1998).

[118] J. R. Rubbmark, M. M. Kash, M. G. Littman, and D. Kleppner, "Dynamical effects at avoided level crossings: A study of the Landau-Zener effect using Rydberg atoms", Phys. Rev. A **23**, 3107 (1981).

[119] C. Leforestier, R. H. Bisseling, C. Cerjan, M. D. Feit, R. Friesner, A. Guldberg, A. Hammerich, G. Jolicard, W. Karrlein, H. D. Meyer, N. Lipkin, O. Roncero, and R. Kosloff, "A comparison of different propagation schemes for the time dependent Schrödinger equation", J. Comput. Phys. **94**, 59 (1991).

[120] E. So, "Interaction of Rydberg hydrogen atoms with metal surfaces", PhD thesis, University of Oxford, 2011.

[121] J. Lill, G. Parker, and J. Light, "Discrete variable representations and sudden models in quantum scattering theory", Chemical Physics Letters **89**, 483 (1982).

[122] J. C. Light and T. Carrington Jr., "Discrete-Variable Representations and their Utilization", Advances in Chemical Physics, John Wiley & Sons, Inc., 2007, 263.

[123] A. M. Cohen, "An Algebraic Approach to Certain Differential Eigenvalue Problems", Linear Algebra Appl **240**, 183 (1996).

[124] D. Baye, M. Hesse, and M. Vincke, "The unexplained accuracy of the Lagrange-mesh method", Phys. Rev. E **65**, 026701 (2002).

[125] K. M. Dunseath, J.-M. Launay, M. Terao-Dunseath, and L. Mouret, "Schwartz interpolation for problems involving the Coulomb potential", J. Phys. B: At., Mol. Opt. Phys. **35**, 3539 (2002).

[126] M. Abramowitz and I. A. Stegun, Handbook of Mathematical Functions With Formulas, Graphs and Mathematical Tables, tenth printing, vol. 55, National Bureau of Standards Applied Mathematics Series, Dover Publications, 1972.

[127] A. R. Barnett, "COULFG: Coulomb and Bessel functions and their derivatives, for real arguments, by Steed's method", Comput. Phys. Commun. **27**, 147 (1982).

[128] W. H. Press, S. A. Teukolsky, W. T. Vetterling, and B. B. Flannery, Numerical Recipes in FORTRAN, Cambridge University Press, 1992.

[129] J. A. Fleck, J. R. Morris, and M. D. Feit, "Time-dependent propagation of high energy laser beams through the atmosphere", Applied physics **10**, 129 (1976).

[130] G. Strang, "Accurate partial difference methods I: Linear cauchy problems", Archive for Rational Mechanics and Analysis **12**, 392 (1963).

[131] R. Kosloff, "Time-dependent quantum-mechanical methods for molecular dynamics", The Journal of Physical Chemistry **92**, 2087 (1988).

[132] D. E. Manolopoulos, "Derivation and reflection properties of a transmission-free absorbing potential", The Journal of Chemical Physics **117**, 9552 (2002).

[133] T. Gonzalez-Lezana, E. J. Rackham, and D. E. Manolopoulos, "Quantum reactive scattering with a transmission-free absorbing potential", The Journal of Chemical Physics **120**, 2247 (2004).

[134] T. Seideman and W. H. Miller, "Calculation of the cumulative reaction probability via a discrete variable representation with absorbing boundary conditions", The Journal of Chemical Physics **96**, 4412 (1992).

[135] E. Lavert-Ofir, Y. Shagam, A. B. Henson, S. Gersten, J. Kłos, P. S. Zuchowski, J. Narevicius, and E. Narevicius, "Observation of the isotope effect in sub-kelvin reactions.", Nat. Chem. **6**, 332 (2014).

[136] A. B. Henson, S. Gersten, Y. Shagam, J. Narevicius, and E. Narevicius, "Observation of Resonances in Penning Ionization Reactions at Sub-Kelvin Temperatures in Merged Beams", Science **338**, 234 (2012).

[137] W. Paul, "Electromagnetic traps for charged and neutral particles", Rev. Mod. Phys. **62**, 531 (1990).

[138] W. D. Phillips, "Nobel Lecture: Laser cooling and trapping of neutral atoms", Rev. Mod. Phys. **70**, 721 (1998).

[139] H. L. Bethlem, G. Berden, and G. Meijer, "Decelerating Neutral Dipolar Molecules", Phys. Rev. Lett. **83**, 1558 (1999).

[140] S. Y. van de Meerakker, N. Vanhaecke, and G. Meijer, "Stark deceleration and trapping of OH radicals", Annual Review of Physical Chemistry **57**, 159 (2006).

[141] K. A. E. Meyer, L. L. Pollum, L. S. Petralia, A. Tauschinsky, C. J. Rennick, T. P. Softley, and B. R. Heazlewood, "Ejection of Coulomb Crystals from a Linear Paul Ion Trap for Ion–Molecule Reaction Studies", The Journal of Physical Chemistry A **119**, 12449 (2015).

[142] T. Breeden and H. Metcalf, "Stark Acceleration of Rydberg Atoms in Inhomogeneous Electric Fields", Phys. Rev. Lett. **47**, 1726 (1981).

[143] D. Townsend, A. L. Goodgame, S. R. Procter, S. R. Mackenzie, and T. P. Softley, "Deflection of krypton Rydberg atoms in the field of an electric dipole", J. Phys. B: At., Mol. Opt. Phys. **34**, 439 (2001).

[144] E. Vliegen, H. J. Wörner, T. P. Softley, and F. Merkt, "Nonhydrogenic Effects in the Deceleration of Rydberg Atoms in Inhomogeneous Electric Fields", Phys. Rev. Lett. **92**, 033005 (2004).

[145] E. Vliegen and F. Merkt, "Normal-Incidence Electrostatic Rydberg Atom Mirror", Phys. Rev. Lett. **97**, 033002 (2006).

[146] S. Y. T. van de Meerakker, H. L. Bethlem, N. Vanhaecke, and G. Meijer, "Manipulation and Control of Molecular Beams", Chemical Reviews **112**, 4828 (2012).

[147] D. R. Miller, "Free Jet Sources", Atomic and Molecular Beam Methods, ed. by G. Scoles, vol. 1, Oxford University Press, 1988, p. 14.

[148] M. D. Morse, "Supersonic Beam Sources", Atomic, Molecular, and Optical Physics: Atoms and Molecules, ed. by F. Dunning and R. Hulet, Experimental Methods in the Physical Sciences pt. 2, Academic Press, 1996, p. 21.

[149] H. Haberland, U. Buck, and M. Tolle, "Velocity distribution of supersonic nozzle beams", Review of Scientific Instruments **56**, 1712 (1985).

[150] H. Ashkenas and F. S. Sherman, "The Structure and Utilization of Supersonic Free Jets in Low Density Wind Tunnels", Rarefied Gas Dynamics, Volume 2, ed. by J. H. de Leeuw, 1965, p. 84.

[151] J. B. Anderson, R. P. Andres, and J. B. Fenn, "Supersonic Nozzle Beams", Advances in Chemical Physics, vol. 10, John Wiley & Sons, Inc., 1966, p. 275.

[152] J. B. Anderson, "Molecular Beams from Nozzle Sources", Molecular beams and low density gasdynamics, ed. by P. P. Wegener, vol. 4, New York, Marcel Dekker, Inc., 1974, p. 1.

[153] V. I. Arnold, Mathematical Methods of Classical Mechanics, 2nd ed., vol. 60, Springer-Verlag New York, 1989.

[154] G. Benettin and A. Giorgilli, "On the Hamiltonian interpolation of near-to-the identity symplectic mappings with application to symplectic integration algorithms", Journal of Statistical Physics **74**, 1117 (1994).

[155] S. Y. T. van de Meerakker, H. L. Bethlem, and G. Meijer, "Taming molecular beams", Nature Physics **4**, 595 (2008).

[156] S. Willitsch, J. Dyke, and F. Merkt, Helv. Chim. Acta **86**, 1152 (2003).

[157] H. R. Murphy and D. R. Miller, "Effects of nozzle geometry on kinetics in free-jet expansions", The Journal of Physical Chemistry **88**, 4474 (1984).

[158] R. Campargue, "Progress in overexpanded supersonic jets and skimmed molecular beams in free-jet zones of silence", J. Phys. Chem. **88**, 4466 (1984).

[159] A. Lebehot, J. Kurzyna, V. Lago, M. Dudeck, and R. Campargue, "Laser Sustained Plasma Free Jet and Energetic Atom Beam of Pure Argon or Oxygen Seeded Argon Mixture", Atomic and Molecular Beam Methods, ed. by R. Campargue, Springer-Verlag Berlin Heidelberg, 2001, p. 237.

[160] A. Miffre, M. Jacquey, M. Büchner, G. Trénec, and J. Vigué, "Parallel temperatures in supersonic beams: Ultracooling of light atoms seeded in a heavier carrier gas", J. Chem. Phys. **122** (2005).

[161] J. B. Anderson, "Separation of Free Jets Gas Mixtures in", AIChE J. **13**, 1188 (1967).

[162] K. J. S. Eikema and W. Ubach, "Precision laser spectroscopy in the extreme ultraviolet", Handbook of High-Resolution Spectroscopy, ed. by M. Quack and F. Merkt, John Wiley and Sons, Inc, 2011.

[163] M. Yanagihara, M. Z. Yusop, M. Tanemura, S. Ono, T. Nagami, K. Fukuda, T. Suyama, Y. Yokota, T. Yanagida, and A. Yoshikawa, "Vacuum ultraviolet field emission lamp utilizing KMgF3 thin film phosphor", APL Materials **2** (2014).

[164] A. Borsutzky, R. Brünger, C. Huang, and R. Wallenstein, "Harmonic and sum-frequency generation of pulsed laser radiation in BBO, LBO, and KD*P", Applied Physics B **52**, 55 (1991).

[165] G. C. Bhar, U. Chatterjee, A. M. Rudra, P. Kumbhakar, R. K. Route, and R. S. Feigelson, "Generation of tunable 187.9–196-nm radiation in β-Ba_2BO_4", Opt. Lett. **22**, 1606 (1997).

[166] R. Mahon, T. J. McIlrath, and D. W. Koopman, "Nonlinear generation of Lyman-alpha radiation", Applied Physics Letters **33**, 305 (1978).

[167] R. Wallenstein, "Generation of narrowband tunable VUV radiation at the Lyman-α wavelength", Optics Communications **33**, 119 (1980).

[168] A. Kramida, Yu. Ralchenko, J. Reader, and and NIST ASD Team, NIST Atomic Spectra Database (ver. 5.3), [Online]. Available: `http://physics.nist.gov/asd` [2016, October 13]. National Institute of Standards and Technology, Gaithersburg, MD. 2015.

[169] D. C. Morton, "Atomic data for resonance absorption lines. I - Wavelengths longward of the Lyman limit", Ap. J. Suppl. **77**, 119 (1991).

[170] P. W. Atkins and R. Friedman, Molecular Quantum Mechanics, 4th ed., Oxford University Press, 2005.

[171] G. H. C. New and J. F. Ward, "Optical Third-Harmonic Generation in Gases", Phys. Rev. Lett. **19**, 556 (1967).

[172] S. E. Harris and R. B. Miles, "Proposed Third-Harmonic Generation in Phase-Matched Metal Vapors", Applied Physics Letters **19**, 385 (1971).

[173] J. F. Young, G. C. Bjorklund, A. H. Kung, R. B. Miles, and S. E. Harris, "Third-Harmonic Generation in Phase-Matched Rb Vapor", Phys. Rev. Lett. **27**, 1551 (1971).

[174] R. Hilbig and R. Wallenstein, "Enhanced production of tunable VUV radiation by phase-matched frequency tripling in krypton and xenon", IEEE Journal of Quantum Electronics **17**, 1566 (1981).

[175] A. Kung, J. Young, and S. Harris, "Generation of 1182-Å radiation in phase-matched mixtures of inert gases", Applied Physics Letters **22**, 301 (1973).

[176] A. L'Huillier, L. A. Lompré, M. Ferray, X. F. Li, G. Mainfray, and C. Manus, "Third-Harmonic Generation in Xenon in a Pulsed Jet and a Gas Cell", EPL (Europhysics Letters) **5**, 601 (1988).

[177] B. Cronin, M. G. D. Nix, R. H. Qadiri, and M. N. R. Ashfold, "High resolution photofragment translational spectroscopy studies of the near ultraviolet photolysis of pyrrole", Phys. Chem. Chem. Phys. **6**, 5031 (2004).

[178] C. Delsart, L. Cabaret, C. Blondel, and R.-J. J. Champeau, "Two-step high-resolution laser spectroscopy of the Stark substates of the n=44 level in atomic hydrogen", J. Phys. B: At., Mol. Opt. Phys. **20**, 4699 (1987).

[179] M. G. B. Dethlefsen, "Charge transfer processes of atomic hydrogen Rydberg states near surfaces", PhD thesis, University of Oxford, 2013.

[180] W. C. Wiley and I. H. McLaren, "Time-of-Flight Mass Spectrometer with Improved Resolution", Review of Scientific Instruments **26**, 1150 (1955).

[181] C. J. Rennick, J. Lam, W. G. Doherty, and T. P. Softley, "Magnetic Trapping of Cold Bromine Atoms", Physical Review Letters **112**, 023002 (2014).

[182] H. Liebl, Applied Charged Particle Optics, Springer-Verlag Berlin Heidelberg, 2008.

[183] J. A. Gibbard and T. P. Softley, "Handshake electron transfer from hydrogen Rydberg atoms incident at a series of metallic thin films", The Journal of Chemical Physics **144**, 234703 (2016).

[184] K. S. Novoselov, A. K. Geim, S. V. Morozov, D. Jiang, Y. Zhang, S. V. Dubonos, I. V. Grigorieva, and A. A. Firsov, "Electric Field Effect in Atomically Thin Carbon Films", Science **306**, 666 (2004).

[185] K. S. Novoselov, D. Jiang, F. Schedin, T. J. Booth, V. V. Khotkevich, S. V. Morozov, and A. K. Geim, "Two-dimensional atomic crystals", Proc. Natl. Acad. Sci. U.S.A. **102**, 10451 (2005).

[186] H. Lu, A. Lipatov, S. Ryu, D. J. Kim, H. Lee, M. Y. Zhuravlev, C. B. Eom, E. Y. Tsymbal, A. Sinitskii, and A. Gruverman, "Ferroelectric tunnel junctions with graphene electrodes.", Nature communications **5**, 5518 (2014).

[187] I. Jurewicz, A. Fahimi, P. E. Lyons, R. J. Smith, M. Cann, M. L. Large, M. Tian, J. N. Coleman, and A. B. Dalton, "Insulator-Conductor Type Transitions in Graphene-Modified Silver Nanowire Networks: A Route to Inexpensive Transparent Conductors", Advanced Functional Materials **24**, 7580 (2014).

[188] F. Schwierz, "Graphene transistors", Nature Nanotechnology **5**, 487 (2010).

[189] R. Raccichini, A. Varzi, S. Passerini, and B. Scrosati, "The role of graphene for electrochemical energy storage.", Nature Materials **14**, 271 (2015).

[190] E. Quesnel et al., "Graphene-based technologies for energy applications, challenges and perspectives", 2D Mater. **2**, 30204 (2015).

[191] A. K. Geim and K. S. Novoselov, "The rise of graphene.", Nature Materials **6**, 183 (2007).

[192] A. K. Geim, "Graphene: Status and Prospects", Science **324**, 1530 (2009).

[193] "Graphene steps into biomedicine", Nature Materials **15**, 485 (2016).

[194] T. Ando, Y. Zheng, and H. Suzuura, "Dynamical Conductivity and Zero-Mode Anomaly in Honeycomb Lattices", Journal of the Physical Society of Japan **71**, 1318 (2002).

[195] K. Bolotin, K. Sikes, Z. Jiang, M. Klima, G. Fudenberg, J. Hone, P. Kim, and H. Stormer, "Ultrahigh electron mobility in suspended graphene", Solid State Communications **146**, 351 (2008).

[196] D. A. Siegel, C.-H. Park, C. Hwang, J. Deslippe, A. V. Fedorov, S. G. Louie, and A. Lanzara, "Many-body interactions in quasi-freestanding graphene", Proc. Natl. Acad. Sci. **108**, 11365 (2011).

[197] K. S. Novoselov, Z. Jiang, Y. Zhang, S. V. Morozov, H. L. Stormer, U. Zeitler, J. C. Maan, G. S. Boebinger, P. Kim, and A. K. Geim, "Room-Temperature Quantum Hall Effect in Graphene", Science **315**, 1379 (2007).

[198] K. S. Kim, A. L. Walter, L. Moreschini, T. Seyller, K. Horn, E. Rotenberg, and A. Bostwick, "Coexisting massive and massless Dirac fermions in symmetry-broken bilayer graphene", Nature Materials **12**, 887 (2013).

[199] K. Takahashi, M. Imamura, I. Yamamoto, J. Azuma, and M. Kamada, "Image potential states in monolayer, bilayer, and trilayer epitaxial graphene studied with time- and angle-resolved two-photon photoemission spectroscopy", Phys. Rev. B **89**, 155303 (2014).

[200] V. M. Silkin, J. Zhao, F. Guinea, E. V. Chulkov, P. M. Echenique, and H. Petek, "Image potential states in graphene", Phys. Rev. B **80**, 121408 (2009).

[201] S. Bose, V. M. Silkin, R. Ohmann, I. Brihuega, L. Vitali, C. H. Michaelis, P. Mallet, J. Y. Veuillen, M. Alexander Schneider, E. V. Chulkov, P. M. Echenique, and K. Kern, "Image potential states as a quantum probe of graphene interfaces", New Journal of Physics **12**, 023028 (2010).

[202] M. Posternak, A. Baldereschi, A. J. Freeman, E. Wimmer, and M. Weinert, "Prediction of electronic interlayer states in graphite and reinterpretation of alkali bands in graphite intercalation compounds", Physical Review Letters **50**, 761 (1983).

[203] G. Csányi, P. B. Littlewood, A. H. Nevidomskyy, C. J. Pickard, and B. D. Simons, "The role of the interlayer state in the electronic structure of superconducting graphite intercalated compounds", Nature Physics **1**, 42 (2005).

[204] K. V. Emtsev, A. Bostwick, K. Horn, J. Jobst, G. L. Kellogg, L. Ley, J. L. McChesney, T. Ohta, S. a. Reshanov, J. Röhrl, E. Rotenberg, A. K. Schmid, D. Waldmann, H. B. Weber, and T. Seyller, "Towards wafer-size graphene layers by atmospheric pressure graphitization of silicon carbide.", Nature Materials **8**, 203 (2009).

[205] K. S. Kim, Y. Zhao, H. Jang, S. Y. Lee, J. M. Kim, K. S. Kim, J.-H. Ahn, P. Kim, J.-Y. Choi, and B. H. Hong, "Large-scale pattern growth of graphene films for stretchable transparent electrodes", Nature **457**, 706 (2009).

[206] S. V. Gils, C. L. Pen, A. Hubin, H. Terryn, and E. Stijns, "Electropolishing of Copper in H_3PO_4 Ex Situ and In Situ Optical Characterization", J. Electrochem. Soc. **154**, C175 (2007).

[207] X. Li, W. Cai, J. An, S. Kim, J. Nah, D. Yang, R. Piner, A. Velamakanni, I. Jung, E. Tutuc, S. K. Banerjee, L. Colombo, and R. S. Ruoff, "Large-area synthesis of high-quality and uniform graphene films on copper foils.", Science **324**, 1312 (2009).

[208] D. L. Duong, G. H. Han, S. M. Lee, F. Gunes, E. S. Kim, S. T. Kim, H. Kim, Q. H. Ta, K. P. So, S. J. Yoon, S. H. S. J. Chae, Y. W. Jo, M. H. Park, S. H. S. J. Chae, S. C. Lim, J. Y. Choi, and Y. H. Lee, "Probing graphene grain boundaries with optical microscopy", Nature **490**, 235 (2012).

[209] A. C. Ferrari, J. C. Meyer, V. Scardaci, C. Casiraghi, M. Lazzeri, F. Mauri, S. Piscanec, D. Jiang, K. S. Novoselov, S. Roth, and A. K. Geim, "Raman Spectrum of Graphene and Graphene Layers", Phys. Rev. Lett. **97**, 187401 (2006).

[210] K. Kertész, A. A. Koós, A. T. Murdock, Z. Vértesy, P. Nemes-Incze, P. J. Szabó, Z. E. Horváth, L. Tapasztó, C. Hwang, N. Grobert, and L. P. Biró, "Polarized light microscopy of chemical-vapor-deposition-grown graphene on copper", Appl. Phys. Lett. **100** (2012).

[211] G. X. Ni, Y. Zheng, S. Bae, H. R. Kim, A. Pachoud, Y. S. Kim, C. L. Tan, D. Im, J. H. Ahn, B. H. Hong, and B. Özyilmaz, "Quasi-periodic nanoripples in graphene grown by chemical vapor deposition and its impact on charge transport", ACS Nano **6**, 1158 (2012).

[212] H. I. Rasool, E. B. Song, M. J. Allen, J. K. Wassei, R. B. Kaner, K. L. Wang, B. H. Weiller, and J. K. Gimzewski, "Continuity of graphene on polycrystalline copper", Nano Lett. **11**, 251 (2011).

[213] G. Giovannetti, P. A. Khomyakov, G. Brocks, V. M. Karpan, J. Van Den Brink, and P. J. Kelly, "Doping graphene with metal contacts", Phys. Rev. Lett. **101**, 026803 (2008).

[214] K. Tatebe, Combining Multiple Averaged Data Points And Their Errors, 2005, URL: `http://isi.ssl.berkeley.edu/~tatebe/whitepapers/Combining%20Errors.pdf` (visited on 11/08/2016).

[215] N. Mirsaleh-Kohan, W. D. Robertson, and R. N. Compton, "Electron ionization time-of-flight mass spectrometry: Historical review and current applications", Mass Spectrometry Reviews **27**, 237 (2008).

[216] M. Freitag, H.-Y. Chiu, M. Steiner, V. Perebeinos, and P. Avouris, "Thermal infrared emission from biased graphene.", Nature Nanotechnology **5**, 497 (2010).

[217] M. G. Littman, M. M. Kash, and D. Kleppner, "Field-Ionization Processes in Excited Atoms", Phys. Rev. Lett. **41**, 103 (1978).

[218] M. H. Kang, L. O. Prieto López, B. Chen, K. Teo, J. A. Williams, W. I. Milne, and M. T. Cole, "Mechanical Robustness of Graphene on Flexible Transparent Substrates", ACS Appl. Mater. Interfaces, 22506 (2016).

[219] K. Nordlund, J. Keinonen, and T. Mattila, "Formation of Ion Irradiation Induced Small-Scale Defects on Graphite Surfaces", Phys. Rev. Lett. **77**, 699 (1996).

[220] A. Hashimoto, K. Suenaga, A. Gloter, K. Urita, and S. Iijima, "Direct evidence for atomic defects in graphene layers.", Nature **430**, 870 (2004).

[221] J. Kotakoski, A. V. Krasheninnikov, U. Kaiser, and J. C. Meyer, "From point defects in graphene to two-dimensional amorphous carbon", Phys. Rev. Lett. **106**, 105505 (2011).

[222] R. Zan, Q. M. Ramasse, U. Bangert, and K. S. Novoselov, "Graphene re-knits its holes", Nano Letters **12**, 3936 (2012).

[223] D. C. Elias, R. R. Nair, T. M. G. Mohiuddin, S. V. Morozov, P. Blake, M. P. Halsall, A. C. Ferrari, D. W. Boukhvalov, M. I. Katsnelson, A. K. Geim, and K. S. Novoselov, "Control of graphene's properties by reversible hydrogenation: evidence for graphane.", Science **323**, 610 (2009).

[224] J. O. Sofo, A. S. Chaudhari, and G. D. Barber, "Graphane: A two-dimensional hydrocarbon", Phys. Rev. B **75**, 153401 (2007).

[225] D. W. Boukhvalov, M. I. Katsnelson, and A. I. Lichtenstein, "Hydrogen on graphene: Electronic structure, total energy, structural distortions and magnetism from first-principles calculations", Phys. Rev. B **77**, 037425 (2008).

[226] Z. Wu, Y. Han, R. Huang, X. Chen, Y. Guo, Y. He, W. Li, Y. Cai, and N. Wang, "Semimetallic-to-metallic transition and mobility enhancement enabled by reversible iodine doping of graphene.", Nanoscale **6**, 13196 (2014).

[227] E. Y. Usman, I. F. Urazgil'din, A. G. Borisov, and J. P. Gauyacq, "Quantum size effect in the resonant electron transfer between an ion and a thin metal film", Phys. Rev. B **64**, 205405 (2001).

[228] N. Srivastava, Q. Gao, M. Widom, R. M. Feenstra, S. Nie, K. F. McCarty, and I. V. Vlassiouk, "Low-energy electron reflectivity of graphene on copper and other substrates", Phys. Rev. B **87**, 245414 (2013).

[229] H. Hibino, H. Kageshima, F. Maeda, M. Nagase, Y. Kobayashi, and H. Yamaguchi, "Microscopic thickness determination of thin graphite films formed on SiC from quantized oscillation in reflectivity of low-energy electrons", Phys. Rev. B **77**, 075413 (2008).

[230] B. Guo, Q. Liu, E. Chen, H. Zhu, L. Fang, and J. R. Gong, "Controllable N-doping of graphene", Nano Letters **10**, 4975 (2010).

[231] S. Pagliara, S. Tognolini, L. Bignardi, G. Galimberti, S. Achilli, M. I. Trioni, W. F. van Dorp, V. Ocelík, P. Rudolf, and F. Parmigiani, "Nature of the surface states at the single-layer graphene/Cu(111) and graphene/polycrystalline-Cu interfaces", Phys. Rev. B **91**, 195440 (2015).

[232] J. P. Perdew and A. Zunger, "Self-interaction correction to density-functional approximations for many-electron systems", Phys. Rev. B **23**, 5048 (1981).

[233] T. Thiele, S. Filipp, J. A. Agner, H. Schmutz, J. Deiglmayr, M. Stammeier, P. Allmendinger, F. Merkt, and A. Wallraff, "Manipulating Rydberg atoms close to surfaces at cryogenic temperatures", Phys. Rev. A **90**, 013414 (2014).

[234] T. Klamroth, P. Saalfrank, and U. Höfer, "Open-system density-matrix approach to image-potential dynamics of electrons at Cu(100): Energy- and time-resolved two-photon photoemission spectra", Phys. Rev. B **64**, 035420 (2001).

[235] J. C. Meyer, A. K. Geim, M. I. Katsnelson, K. S. Novoselov, D. Obergfell, S. Roth, C. Girit, and A. Zettl, "On the roughness of single- and bi-layer graphene membranes", Solid State Commun. **143**, 101 (2007).

[236] J. C. Meyer, A. K. Geim, M. I. Katsnelson, K. S. Novoselov, T. J. Booth, and S. Roth, "The structure of suspended graphene sheets", Nature **446**, 60 (2007).

[237] Z. Li, I. A. Kinloch, R. J. Young, K. S. Novoselov, G. Anagnostopoulos, J. Parthenios, C. Galiotis, K. Papagelis, C. Y. Lu, and L. Britnell, "Deformation of Wrinkled Graphene", ACS Nano **9**, 3917 (2015).

[238] B. Borca, S. Barja, M. Garnica, D. Sánchez-Portal, V. M. Silkin, E. V. Chulkov, C. F. Hermanns, J. J. Hinarejos, A. L. Vázquez de Parga, A. Arnau, P. M. Echenique, and R. Miranda, "Potential Energy Landscape for Hot Electrons in Periodically Nanostructured Graphene", Phys. Rev. Lett. **105**, 036804 (2010).

[239] P. R. Budarapu, B. Javvaji, V. K. Sutrakar, D. Roy Mahapatra, G. Zi, and T. Rabczuk, "Crack propagation in graphene", Journal of Applied Physics **118**, 064307 (2015).

[240] J. A. Gibbard and T. P. Softley, "Resonant charge transfer of hydrogen Rydberg atoms incident at a metallic sphere", J. Phys. B: At., Mol. Opt. Phys. **49**, 114004 (2016).

[241] F. Dunning, S. Wethekam, H. Dunham, and J. Lancaster, "Charge transfer rates for xenon Rydberg atoms at metal and semiconductor surfaces", Nucl. Instruments Methods Phys. Res. Sect. B Beam Interact. with Mater. Atoms **258**, 61 (2007).

[242] S. D. Hogan, P. Allmendinger, H. Saßmannshausen, H. Schmutz, and F. Merkt, "Surface-Electrode Rydberg-Stark decelerator", Phys. Rev. Lett. **108**, 063008 (2012).

[243] J. C. Tully, "Mixed quantum-classical dynamics", Faraday Discuss. **110**, 407 (1998).

[244] D. D. Neufeld, Y. Pu, and F. B. Dunning, "Probing stray surface electric patch fields using Rydberg atoms", Nuclear Instruments and Methods in Physics Research B **269**, 1288 (2011).

[245] S. DePaul, D. Pullman, and B. Friedrich, "A pocket model of seeded supersonic beams", The Journal of Physical Chemistry **97**, 2167 (1993).

[246] G. Fraser, M. Pain, J. Lees, and J. Pearson, "The operation of microchannel plates at high count rates", Nuclear Instruments and Methods in Physics Research Section A: Accelerators, Spectrometers, Detectors and Associated Equipment **306**, 247 (1991).

[247] B. Brehm, J. Grosser, T. Ruscheinski, and M. Zimmer, "Absolute detection efficiencies of a microchannel plate detector for ions", Measurement Science and Technology **6**, 953 (1995).

[248] Hogan, Stephen D., "Rydberg-Stark deceleration of atoms and molecules", EPJ Techn Instrum **3**, 2 (2016).

[249] E. Vliegen and F. Merkt, "Stark deceleration of hydrogen atoms", J. Phys. B At. Mol. Opt. Phys. **39**, L241 (2006).

[250] E. Vliegen, S. D. Hogan, H. Schmutz, and F. Merkt, "Stark deceleration and trapping of hydrogen Rydberg atoms", Phys. Rev. A **76**, 023405 (2007).

[251] S. D. Hogan and F. Merkt, "Demonstration of Three-Dimensional Electrostatic Trapping of State-Selected Rydberg Atoms", Phys. Rev. Lett. **100**, 043001 (2008).

[252] S. D. Hogan, C. Seiler, and F. Merkt, "Rydberg-State-Enabled Deceleration and Trapping of Cold Molecules", Phys. Rev. Lett. **103**, 123001 (2009).

[253] C. Seiler, S. D. Hogan, and F. Merkt, "Trapping cold molecular hydrogen", Phys. Chem. Chem. Phys. **13**, 19000 (2011).

[254] N. Vanhaecke, U. Meier, M. Andrist, B. H. Meier, and F. Merkt, "Multistage Zeeman deceleration of hydrogen atoms", Phys. Rev. A **75**, 031402 (2007).

[255] L. Scharfenberg, H. Haak, G. Meijer, and S. Y. T. van de Meerakker, "Operation of a Stark decelerator with optimum acceptance", Phys. Rev. A **79**, 023410 (2009).

[256] A. Osterwalder, S. A. Meek, G. Hammer, H. Haak, and G. Meijer, "Deceleration of neutral molecules in macroscopic traveling traps", Phys. Rev. A **81**, 051401 (2010).

[257] S. A. Meek, M. F. Parsons, G. Heyne, V. Platschkowski, H. Haak, G. Meijer, and A. Osterwalder, "A traveling wave decelerator for neutral polar molecules", Rev. Sci. Instrum. **82**, 093108 (2011).

[258] S. A. Meek, H. L. Bethlem, H. Conrad, and G. Meijer, "Trapping Molecules on a Chip in Traveling Potential Wells", Phys. Rev. Lett. **100**, 153003 (2008).

[259] S. A. Meek, H. Conrad, and G. Meijer, "Trapping Molecules on a Chip", Science **324**, 1699 (2009).

[260] N. Vanhaecke, D. Comparat, and P. Pillet, "Rydberg decelerator using a travelling electric-field gradient", J. Phys. B: At., Mol. Opt. Phys. **38**, S409 (2005).

[261] P. Lancuba and S. D. Hogan, "Guiding Rydberg atoms above surface-based transmission lines", Phys. Rev. A **88**, 043427 (2013).

[262] P. Lancuba and S. D. Hogan, "Transmission-line decelerators for atoms in high Rydberg states", Phys. Rev. A **90**, 053420 (2014).

[263] P. Allmendinger, J. A. Agner, H. Schmutz, and F. Merkt, "Deceleration and trapping of a fast supersonic beam of metastable helium atoms with a 44-electrode chip decelerator", Phys. Rev. A **88**, 043433 (2013).

[264] S. A. Meek, H. Conrad, and G. Meijer, "A Stark decelerator on a chip", New J. Phys. **11**, 055024 (2009).

[265] K. S. Novoselov, A. K. Geim, S. V. Morozov, D. Jiang, M. I. Katsnelson, I. V. Grigorieva, S. V. Dubonos, and A. A. Firsov, "Two-dimensional gas of massless Dirac fermions in graphene", Nature **438**, 197 (2005).

[266] G. Giovannetti, P. A. Khomyakov, G. Brocks, P. J. Kelly, and J. Van Den Brink, "Substrate-induced band gap in graphene on hexagonal boron nitride: Ab initio density functional calculations", Phys. Rev. B **76**, 073103 (2007).

[267] C. R. Dean, a. F. Young, I. Meric, C. Lee, L. Wang, S. Sorgenfrei, K. Watanabe, T. Taniguchi, P. Kim, K. L. Shepard, and J. Hone, "Boron nitride substrates for high-quality graphene electronics.", Nature Nanotechnology **5**, 722 (2010).

[268] G. Cassabois, P. Valvin, and B. Gil, "Hexagonal boron nitride is an indirect bandgap semiconductor", Nature Photonics **10**, 262 (2016).

[269] P. Lancuba and S. D. Hogan, "Electrostatic trapping and in situ detection of Rydberg atoms above chip-based transmission lines", J. Phys. B: At., Mol. Opt. Phys. **49**, 074006 (2016).